UC Santa Barbara

UC Santa Barbara Electronic Theses and Dissertations

Title

Measuring, Understanding, and Controlling Heteroatom Distributions in Layered and Zeolite Boro- and Alumino-silicate Frameworks

Permalink

https://escholarship.org/uc/item/8wg0h19g

Author

Hsieh, Ming-Feng

Publication Date

2014

Peer reviewed|Thesis/dissertation

eScholarship.org Powered by the California Digital Library
University of California

UNIVERSITY OF CALIFORNIA

Santa Barbara

Measuring, Understanding, and Controlling Heteroatom Distributions in Layered and Zeolite Boro- and Alumino-silicate Frameworks

A dissertation submitted in partial satisfaction of the

requirements for the degree Doctor of Philosophy in Chemical Engineering

by

Ming-Feng Hsieh

Committee in charge:

Professor Bradley F. Chmelka, Chair

Professor Ram Seshadri

Professor Baron Peters

Professor Michael J. Gordon

December 2014

The dissertation of Ming-Feng Hsieh is approved.

_____

Professor Ram Seshadri

_____

Professor Baron Peters

_____

Professor Michael J. Gordon

_____

Professor Bradley F. Chmelka, Committee Chair

October 2014

Measuring, Understanding, and Controlling Heteroatom Distributions in Layered and Zeolite Boro- and Alumino-silicate Frameworks

Copyright © 2014

by

Ming-Feng Hsieh

ACKNOWLEDGEMENTS

First of all, I would like to acknowledge my Ph.D. advisor, Prof. Bradley F. Chmelka, for his great support during my graduate school career. His research enthusiasm and guidance has consistently motivated me to explore possibilities in diverse disciplines, part of which have been considered exceedingly difficult to understand. Despite the fact that many of our ideas and trials did not succeed, we were still able to make significant contributions in certain research topics. In particular, I thank him for his meticulous teaching as for how to effectively communicate scientific results, ideas, and hypotheses to others. Also, I would like to thank my Ph.D. committee members, Prof. Michael Gordon, Prof. Baron Peters, and Prof. Ram Seshadri for their scientific insights that helped develop my research projects.

Secondly, I would like to acknowledge the hard-working, intelligent, and fun members of the Chmelka research group. In particular, I am very grateful to work with Dr. Ramzy Shayib, Dr. Robert Messinger, Dr. Ben Smith, Dr. Justin Jahnke, Dr. Donghun Kim, Dr. Steve Donaldson, Dr. Louis Jones, Dr. Nate George, Trent Tovar, Rahul Sangodkar, Matt Aronson, Matt Idso, Niels Zusblatt, Vahagn Yeranossian, Zach Berkson, Katherine Brune, Howie Dobbs, Thomas Farmer, David Phan, and Lane Allison. These wonderful people have made my life in graduate school not only fruitful but also entertaining. Additionally, I would like to thank the wonderful team of collaborators in France: Dr. Sylvian Cadars, Dr. Mounesha Garaga, Dr. Zalfa Nour, Dr. Michael Deschamps, and Dr. Dominique Massiot for their great NMR lessons and assistance. Furthermore, I would like to express my sincere gratitude to a number of UCSB professionals for their general assistance and insightful

guidance in designing experiments: Dr. Jerry Hu, Jaya Nolt, Shamon Walker, Joe Doyle, Dr. Amanda Strom, Dr. Youli Li, Miguel Zepeda, Mark Cornish, and Dr. Stephan Kraemer.

During my graduate school career, the most impressive experience would be the summer in 2012. I was very fortunate to have an opportunity to be a research intern at the Chevron Energy Technology Company where I was able to meet several industrial professionals. This unexpected journey trained me to look at catalysts from multiple angles. I particularly thank Dr. Stacey Zones for his great guidance not only in research but also in life. His sense of humor and "California" style inspired me to enjoy zeolite chemistry. Also, I am very grateful to work with Dr. Cedrick Mahieux who helped improve my understanding of fundamental chemistry and experimental design. Furthermore, I would like to thank Dr. Dan Xie for his thoughtful teaching in X-ray diffraction techniques. I would like to acknowledge Dr. Georgie Scheuerman, Dr. Charlie Wilson, and Dr. Bob Saxton for their support of the whole program. Dr. Bob Saxton's energetic management style was very enjoyable. Additionally, I would like to express my sincere gratitude to Dr. Cong-Yan Chen, Dr. Saleh Elomari, Timi Singa, Annabelle Benin, Anthony Nelson, Maryam Delder, Dr. Kaustav Chaudhuri, Dr. Tom Rea, Dr. Tracy Davis, Dr. Howard Lacheen, Dr. Adeola Ojo, Dr. Michael Cheng, Dr. Richard Dutta, Dr. Bi-Zeng Zhan, Dr. Mingting Xu, Maria Anaya, and Wendy Smith.

At last, I would like to end my acknowledgements by thanking my family for their love and support. Without them, it would not be possible for me to complete this Ph.D. program.

VITA OF MING-FENG HSIEH

EDUCATION

Ph.D., University of California, Santa Barbara 2009 – 2014
Chemical Engineering
Research Advisor: Professor Bradley F. Chmelka
Thesis: Measuring, Understanding, and Controlling Heteroatom Distributions in Layered and Zeolite Boro- and Alumino-silicate Frameworks

Bachelor of Science, National Taiwan University 2004 – 2008
Chemical Engineering

PROFESSIONAL EMPLOYMENT

Research Intern, Chevron Energy Technology Company Jun. 2012 – Sep. 2012
Teaching Assistant, University of California, Santa Barbara Spring 2012

PUBLICATIONS

X. Fang, Z. Liu, **M.F. Hsieh**, M. Chen, P. Liu, C. Chen, N. Zhang, Hollow Mesoporous Aluminosilica Spheres with Perpendicular Pore Channels as Catalytic Nanoreactors, *ACS Nano*, **2012**, *6*, 4434-4444.

S.I. Zones, A. Benin, S-J Hwang, D. Xie, S. Elomari, **M.F. Hsieh**, Studies of Aluminum Reinsertion into Borosilicate Zeolites with Intersecting Channels of 10- and 12-Ring Channel Systems, *Journal of the American Chemical Society*, **2014**, *136*, 1462-1471.

M.N. Garaga, **M.F. Hsieh**, Z. Nour, M. Deschamps, D. Massiot, B.F. Chmelka, S. Cadars, Local Environments of Boron Heteroatoms in Non-Crystalline Layered Silicates, in preparation.

M.F. Hsieh, M.N. Garaga, Z. Nour, M.T. Aronson, S. Cadars, B.F. Chmelka, Aluminum Heteroatom Distributions in Surfactant-Directed Aluminosilicates, in preparation.

M.F. Hsieh, C.M. Lew, S.I. Zones, B.F. Chmelka, Controlling Aluminum Site Distributions in Delaminated Zeolite SSZ-70 by Isomorphous Substitution of Boron with Aluminum, in preparation.

D. Xie, S. Smeets, C. Baerlocher, **M.F. Hsieh**, M.T. Aronson, W. Wan, X. Zhou, B.F. Chmelka, S.I. Zones, L.B. McCusker, Structure Determination of the Layered Zeolite Catalyst SSZ-70, in preparation.

M.F. Hsieh, S.I. Zones, B.F. Chmelka, Influences of Structure-Directing Species on Boron Site Distributions in Borosilicate Zeolite SSZ-70 Catalysts, in preparation.

SELECTED PRESENTATIONS

M.F. Hsieh, C.M. Lew, S.I. Zones, and B.F. Chmelka, Measuring boron heteroatom distributions in borosilicate zeolite catalysts, 247th ACS national meeting, Dallas, TX, March, 2014 (Oral Presentation)

M.F. Hsieh, M.N. Garaga, Z. Nour, M.T. Aronson, S. Cadars, S.I. Zones, and B.F. Chmelka, Measuring and understanding heteroatom distributions in borosilicate zeolite catalysts, Materials Research Outreach Program (MROP), Santa Barbara, CA, February, 2014 (Poster Presentation)

M.F. Hsieh, M.N. Garaga, Z. Nour, M.T. Aronson, S. Cadars, S.I. Zones, and B.F. Chmelka, Nanoscale Characterization of Heteroatom Distributions in Boro- and Alumino-Silicate Frameworks, American Institue of Chemical Engineers (AIChE) Annual Meeting, San Francisco, CA, November, 2013 (Oral Presentation)

M.F. Hsieh, Measuring and Controlling Heteroatom Distributions in Zeolite Catalysts, 6th UCSB Chemical Engineering Graduate Student Symposium, Santa Barbara, CA, October, 2013 (Oral Presentation)

M.F. Hsieh, M.N. Garaga, Z. Nour, M.T. Aronson, S. Cadars, S.I. Zones, B.F. Chmelka, Boron and Aluminum Heteroatom Structures and Distributions in Surfactant-Directed Silicate Frameworks, Pacific Coast Catalysis Society Meeting, Santa Barbara, CA, September, 2012 (Poster Presentation)

ABSTRACT

Measuring, Understanding, and Controlling Heteroatom Distributions in Layered and Zeolite Boro- and Aluminosilicate Frameworks

by

Ming-Feng Hsieh

Site-specific heteroatom incorporation imparts catalytic and adsorption properties to silicate-based catalysts (e.g., zeolites and clays), leading to diverse technologically important industrial processes. In such applications, reactions are typically catalyzed at Brønsted acid sites associated with H^+ cations that balance the anionic charges near framework heteroatom species (generally aluminum) in heteroatom-containing silicate frameworks. Despite the fact that the catalytic and adsorption properties of these catalysts have been observed to be greatly influenced by several factors, such as heteroatom type, contents, and distributions, the associated fundamental understanding of heteroatom site distributions is still very limited and has been elusive. This is partially due to lack of experimental methods that can probe the complicated order and disorder around heteroatom sites even in well-ordered crystalline silicate frameworks. Among various characterization methods, solid-state nuclear magnetic resonance (NMR) spectroscopy can be considered as a promising technique because of its high sensitivity to electronic environments of NMR-active nuclei, which allows their molecular proximities and connectivities to be established.

Herein, newly modified two-dimensional (2D) NMR techniques were applied to probe specific covalent site connectivities between framework boron or aluminum heteroatoms and their nearby silicate sites in zeolite and layered boro- and alumino-silicate materials. The established site connectivities, in conjunction with crystallography, enable the determination of boron or aluminum heteroatom site distributions. We applied the new 2D NMR methods to boron- or aluminum-containing surfactant-directed silicates and zeolite SSZ-70, aiming for understanding similarities and differences between boron and aluminum incorporation. Interestingly, boron atoms are shown to be preferentially incorporated into specific silicate sites in most cases, whereas aluminum atoms appear to be non-selectively distributed among different silicate sites in all cases. Such observations may suggest that boron and aluminum species participate differently in the formation of boro- and aluminosilicates, respectively.

Based on the molecular understanding of boron and aluminum siting learned from these materials, a synthesis protocol to control heteroatom siting in zeolite catalysts is proposed using borosilicate zeolite SSZ-70 (B-SSZ-70) as an example. The protocol begins with the preparation of B-SSZ-70 that was delaminated to increase its external surface area for reactions involving bulky molecules, during which boron siting was monitored ex-situ at different synthesis stages. The results show that boron site distributions were retained during the course of post-synthetic treatments. Subsequently, the framework boron species in the delaminated B-SSZ-70 were post-synthetically exchanged with aluminum atoms. Notably, as expected, the reinserted aluminum species are concluded to be located at certain silicate sites on external surface sites. This is very different from the aluminum siting in Al-SSZ-70 (i.e., Al is everywhere). Overall, these analyses, methods, and synthesis protocols

are expected to provide insights into the local environments of heteroatoms and their distributions in zeolite catalysts, which would enable rational zeolite synthesis with engineered heteroatom site distributions.

TABLE OF CONTENTS

Chapter 1: Introduction

1.1 Motivation

Catalysts play an important role in many chemical reactions by lowering the activation energy for reactants to reach transition states, leading to higher reaction rates compared to uncatalyzed reactions under the same conditions.[1] Accordingly, catalysts are widely used in the petrochemical, fine chemical, pharmaceutical, agricultural, and energy industries.[2–4] The global catalyst market, with such broad and important applications, was estimated to be $29.5 billion in 2010, and it is expected to continuously grow due to increasing demand in different aspects, such as refineries using crude oil with complicated compositions to satisfy more stringent environmental regulations.[5] Consequently, a minor improvement in catalyst properties would make a significant economic impact, and this prospect has motivated the catalysis community to synthesize new catalysts and to optimize the performance and properties of existing catalysts. Furthermore, increasing environmental awareness has attracted more attention on development of "green" catalysts. Therefore, developing environmentally benign catalysts with improved properties has become an important goal amongst the science and engineering communities.

A majority of industrial processes are based on acid catalysts, such as cracking, isomerization, and disproportionation.[2,3,6–8] However, in these and other industrial applications, acid catalysts were designed for high product yields without thoughtful consideration of their environmental impact. For instance, concentrated hydrofluoric acid (HF), sulfuric acid (H_2SO_4) and other homogeneous acid catalysts are commonly used in these traditional processes, because of their high activity and selectivity at relatively low

operating costs.[4,9,10] However, their hazardous properties can have serious health and environmental effects. Also, homogeneous acid catalysts are typically in the same phase as reactants and products, and therefore they require difficult and expensive separation and recycling processes that must comply with increasingly stringent environmental regulations. These undesirable properties have motivated the development and optimization of *hetero*geneous catalysts that can directly replace homogenous catalysts in traditional catalytic processes.

Compared to homogeneous catalysts, heterogeneous catalysts function in a different phase from reactants and products, where catalysts are commonly in the solid phase and interact with reactants and products in liquid and/or gas phase(s). This allows heterogeneous catalysts to be more easily separated from reactants and products. However, there are other fundamental aspects of heterogeneous catalysis that need improvement. For example, lower reaction activity and less tunable catalytic properties, as compared to homogeneous catalysts, limit the widespread application of heterogeneous catalysts. Therefore, more work is needed to optimize the properties of heterogeneous catalyst to enhance selectivity and activity under a variety of chemical reaction conditions.

1.2 Silica-alumina-based solid acid catalysts

1.2.1 Amorphous solid acids

The chemical compositions of most common solid acid catalysts are generally tuned by varying silica (SiO_2) and alumina (Al_2O_3) contents, and such silica-alumina based materials are divided into two categories: 1) amorphous or 2) crystalline, based on their degree of long-range structural order. Unlike crystalline solid acids, amorphous silica-alumina

materials have disordered frameworks, although their chemical composition could be very similar to that of crystalline types. Such structural disorder typically leads to lower thermal and chemical stability than crystalline solid acids.[4,6,11] Nevertheless, amorphous silica-alumina catalysts can be synthesized with ordered mesoporosities (2 to 50 nm). These larger and tunable pore sizes enable reactions involving bulky molecules that would otherwise not be possible with nanoporous (<2 nm) crystalline aluminosilicates (*i.e.*, zeolites) due to mass transfer resistances.[4,12–14] Specific examples of mesoporous silica-alumina, such as M41S and SBA-type, can be synthesized in lamellar, cubic, hexagonal, and other mesophases with a wide range of mesopore diameters.[13,15–18] Furthermore, these mesoporous silica-alumina materials have surface areas up to 1000 m^2/g (or even higher), providing a greater number of accessible acid sites for reactions.[13]

In addition to tunable mesophases and pore sizes, amorphous silica-alumina materials often have Brønsted and Lewis acid sites. Brønsted acidity is believed to arise from silanol groups (Si-OH), whereas Lewis acidity results from electron-deficient aluminum species. Brønsted and Lewis acidity could be partially tuned by judiciously changing chemical compositions and/or framework morphologies, designed for a variety of catalytic and adsorption applications. Despite weaker Brønsted acidity compared to zeolites, silica-alumina are generally used as co-catalysts and/or binders of zeolite catalysts in fluid catalytic cracking (FCC) processes.[4] Recently, some investigations have demonstrated the potential of utilizing mesoporous silica-alumina as catalysts in several model reactions, such as alkylation of aromatics[19] and propene oligomerization.[20]

1.2.2 Nanoporous crystalline solid acids

Another class of solid acids is crystalline aluminosilicates typically known as zeolites. Zeolites constitute a substantial fraction of commercial solid acid catalysts because of their high thermal and chemical stabilities, strong acidities, and confined framework structures, all of which contribute to high activity and shape selectivity in various reactions at high operating temperatures.[4,6,8,21] Zeolite frameworks are composed of corner-sharing tetrahedral sites (T-sites), most of which are silicon (Si) atoms covalently bonded to four neighboring Si atoms via bridging oxygen atoms (*i.e.*, silicon-oxygen tetrahedra, >95 wt%). Interestingly, the interconnected T-sites can be arranged in different nano-scale geometries to construct a variety of three-dimensional (3D) networks with uniformly shaped cavities and nanopores (typically <1 nm). To date, more than 200 different zeolite structures have been reported, and each structural type is given a distinct three letter code by the International Zeolite Association (IZA).[22] More importantly, isomorphic substitution of Si atoms by aluminum (Al) or other trivalent heteroatoms (*e.g.*, boron, B) produces framework negative charges that are balanced by cations, such as sodium ions or protons. These charge-balancing cations (protons especially) are the key elements that impart catalytic and adsorption properties to zeolites.

For solid acid catalytic applications, aluminum-substituted zeolites with protons (H^+) as charge-balancing cations are usually desired, because of the strong Brønsted acidity that results from such a composition.[23–25] The Brønsted acid sites refer to bridging hydroxyl groups between framework Si and Al sites, as shown in Figure 1. Proton-form zeolites can be utilized to catalyze various industrial reactions, such as alkylation of aromatics, hydrocarbon cracking, and isomerization.[4,6,11,21] Currently, zeolite Y, ZSM-5, Beta,

Mordenite, and Ferrierite are the most commonly used zeolite catalysts for commercial applications, whose framework structures are depicted in Figure 2.[26] The main structural features of these zeolites and their representative industrial processes will be briefly discussed below.

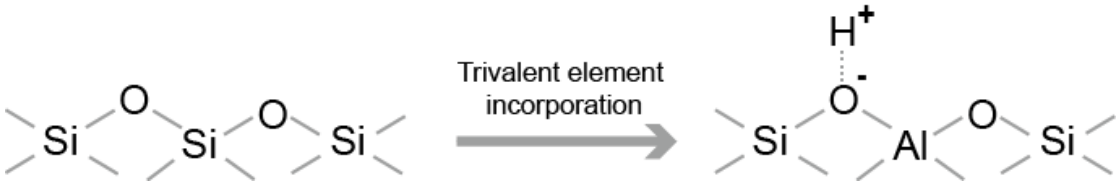

Figure 1. Schematic diagram of how a Brønsted acid site is formed via trivalent heteroatom incorporation (*e.g.*, Al or B) into four-coordinate sites in zeolites.

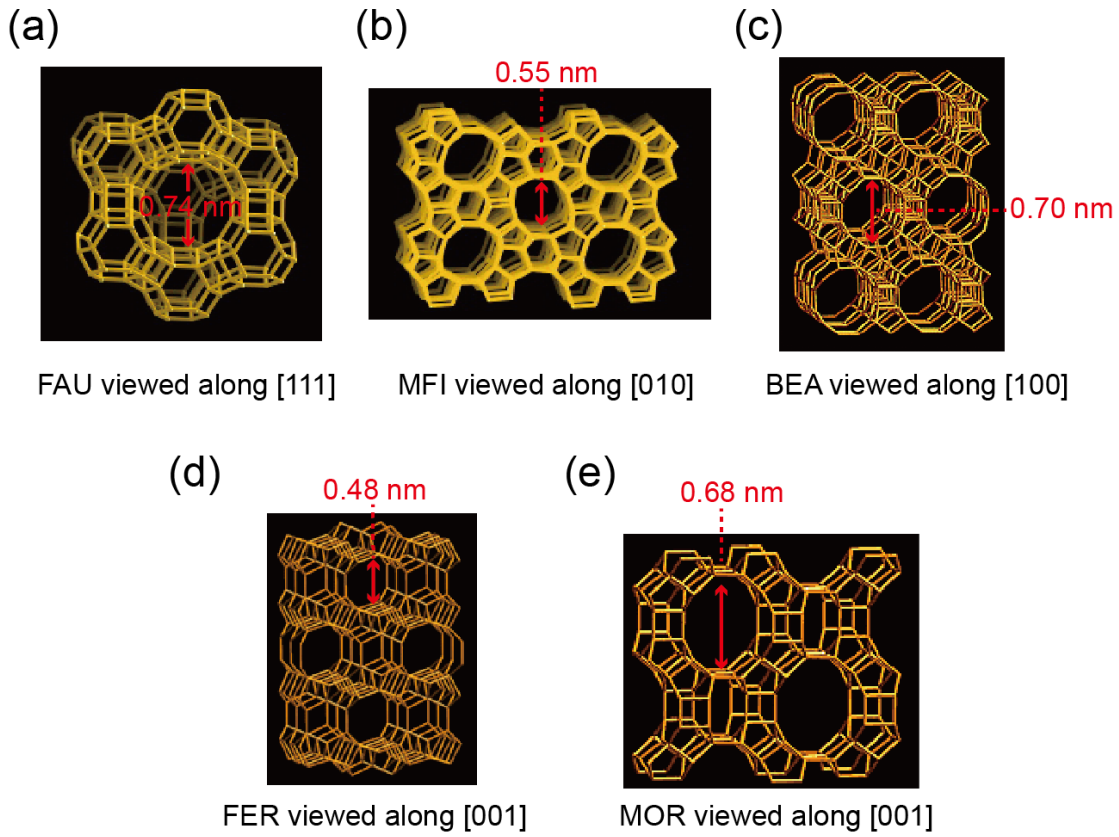

Figure 2. Schematic diagrams of several industrially important zeolite frameworks: (a) zeolite Y (FAU), (b) ZSM-5 (MFI), (c) zeolite Beta (BEA), (d) ferrierite **(**FER), and (e) mordenite (MOR) with approximate pore diameters.

Zeolite Y (three letter code: FAU) has two cage environments (*i.e.*, sodalite and super cages) with Si/Al molar ratio of 2 or higher, and it is often dealuminated to produce ultra-stable zeolite Y (USY), which greatly improves its thermal and chemical stability. USY is commercially used in FCC units to convert crude oil to light distillates (*e.g.*, gasoline, diesel).[4] In contrast, ZSM-5 (MFI) is often used to catalyze hydrocarbon isomerization and alkylation of small hydrocarbons, including methanol-to-gasoline (MTG).[27] The applicability of ZSM-5 in these reactions is mainly due to its unique framework structure, which contains two kinds of intersecting channels that are built by 10-member-ring (10-MR) with slightly different diameters (0.53 x 0.56 nm and 0.51 x 0.55 nm). Interestingly, the channels of ZSM-5 allow faster diffusion of benzene, monosubstituted benzenes, and para-xylene than meta- and ortho-disubstituted benzenes, resulting in superior shape selectivity for mono- and para-disubstituted benzenes in ZSM-5 catalyzed reactions. A representative industrial application is the selective toluene disproportionation process.[28] Zeolite Beta (BEA) possesses two types of channels, both of which are formed by 12-MR with slightly different diameters (0.55 x 0.55 nm and 0.76 x 0.64 nm). Due to the relatively large pores of zeolite Beta, diffusion of aromatics and *tert*-butyl group containing molecules is expected to be faster and easier with respect to zeolites with small and medium pore sizes. Such superior diffusion properties are important for cumene synthesis by alkylation of benzene with propene, as applied to the Polimeria Europa-ENI[29] and the UOP Q-Max processes.[30]

Different from zeolite Y and Beta yet similar to ZSM-5, ferrierite (FER) is considered a medium-pore zeolite because there are two kinds of intersection channels, formed by 10-MR (0.42 x 0.54 nm) and 8-MR (0.35 x 0.48 nm). As expected, these structural features present severe diffusion limitation for *tert*-butyl group-containing molecules and aromatics,

leading to applications involving small hydrocarbons, such as the *n*-butylene skeletal isomerization to isobutylene (a gasoline reformulation relevant process).[31] Finally, mordenite (MOR) is characterized by roughly straight channels (12-MR, 0.65 x 0.70 nm) and side pockets (8-MR, 0.34 x 0.48 nm). According to the discussion above, we can anticipate that *tert*-butyl group-containing molecules and aromatics are able to diffuse into the main channels rather than side pockets, which is still true even when excess *n*-hexane is used during adsorption tests.[32] Similar to Ferrierite, Mordenite is the basic component of commercial catalysts for skeletal isomerization of C4-C6 paraffin.[33] Interestingly, the main 12-MR channels of mordenite also facilitate diffusion of monosubstituted benzenes, whereas ortho-disubstituted benzenes are hindered. This suggests that mordenite catalyzes selective conversion of aromatics. An industrial application is the Dow-Kellogg cumene synthesis process, where dealuminated mordenite is used.[30] Collectively, these various industrial applications demonstrate the strong dependence of zeolite catalytic and adsorption properties on the framework structures.

Combinations of amorphous and crystalline solid acid catalysts reveal opportunities for developing heterogeneous solid acid catalysts with targeted catalytic and adsorption properties, aiming to replace traditional homogeneous catalysts ultimately. While heterogeneous solid acid catalysts have currently been employed in a number of industrial processes, their catalytic properties still need improvement, such as how acidity could be tailored via catalyst preparation. However, this requires a better understanding of how solid acidity originates and how acidity could be altered to influence catalytic and adsorption properties. Here, my thesis will discuss relevant issues in zeolite catalysts with emphasis on

identifying Al and B heteroatom locations in zeolite frameworks, because their distributions are believed to affect acidity and catalytic performances of zeolites.

1.3 Molecular origins of acid sites in zeolites

Although zeolites are used in many important industrial processes, a molecular-level understanding of zeolite acidity and how acidity may be controlled still remain elusive. In addition, despite the fact that some evidence of catalytic properties under the influence of acid site locations in zeolites were reported,[34–36] to the best of our knowledge, such dependence of acidities on catalytic and adsorption properties have not been generalized to all types of zeolite catalysts. Part of the limited understanding can be attributed to the difficulty in probing and characterizing acid sites in zeolite frameworks, which are more complicated than homogeneous catalysts. While a general understanding of acidities in zeolites had been proposed,[37] identifying and ideally controlling acid site distributions are still very challenging to achieve in zeolite synthesis. As discussed before, Brønsted acid sites result from H^+ species that are present to charge balance negative charges near framework Al atoms (Figure 1). Catalytic and adsorption properties of such H^+ species were observed to be greatly influenced by the local zeolite structures and their compositions.[38] For example, for a given framework Al site in zeolites, its resulting acid strength depends on the first and the second coordination shell structures around the specific Al site.[39–41] It should be noticed that the next-nearest-neighboring (NNN) T-sites (12 in total) could be all substituted with Al atoms without violating the Lowenstein's rule (Figure 3), which pertains to no covalent bonds between two adjacent Al atoms via bridging oxygen atoms (*i.e.*, Al-O-Al).[42,43]

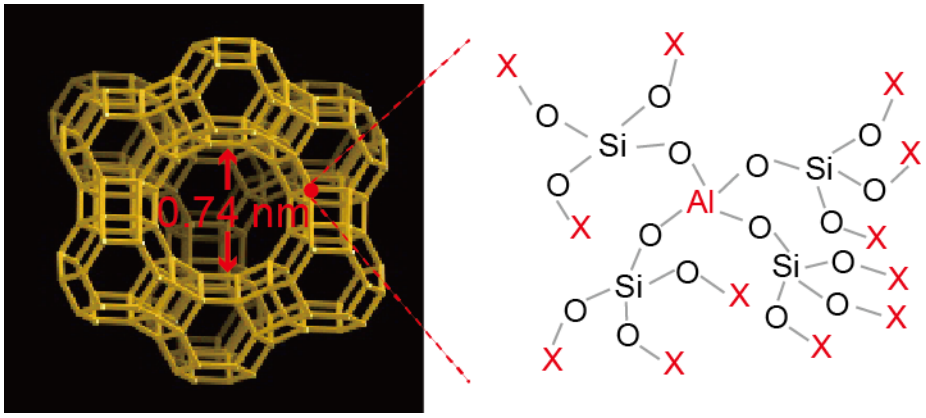

Figure 3. Schematic diagram of next-nearest-neighboring (NNN) T-sites for a given framework aluminum site in a zeolite Y, where X could be either a silicon or an aluminum atom. Note that the bond lengths and angles are not precise and used for illustration only.

Following this rule, it can be anticipated that a central Al site could have 12 Al sites in its NNN at most, which would dramatically affect the stability and activity of the corresponding Brønsted acid sites.[39–41] This is supported by the observation that increased number of Al sites would lower the stability of zeolite frameworks and also reduce the associated acidity of bridging hydroxyl groups.[44–46] It is therefore hypothesized that the strongest Brønsted acidity in zeolites could be reached when a completely isolated four-coordinate Al site is present in frameworks (*i.e.*, no other Al atoms in its NNN), which would yield a Si/Al molar ratio to be around 10. However, the overall Brønsted acidity would decrease if Al concentration is further reduced.[38,47,48] Additionally, the amount of Al incorporation into frameworks is greatly governed by the types of zeolites. While the hypothesis was nicely proposed, precise correlations between acidity and local compositions of zeolite frameworks have been still challenging to establish, partially due to complicated zeolite crystallization processes that have not been fully understood. This is also because of characterization methods that have limited capacity for interrogating Al site distributions.

1.3.1 Directing the formation of zeolite framework structures

As mentioned earlier, zeolites have been extensively used in industrial processes, all of which utilize synthetic zeolites.[49] Typically, synthetic zeolites are prepared by mixing silica and aluminum- or other heteroatom-containing sources in water together with a structure-directing agent (SDA) and a mineralizing agent (hydroxides or fluorides). The whole mixture is subsequently aged at certain temperatures for a period of time to form a gel, which is heated hydrothermally at elevated temperatures (~100 to 200 °C) for several hours up to days or even weeks.[23–25,50] The main function of mineralizing agents is to facilitate the hydrolysis and condensation reactions between chemical reagents to develop zeolite products via crystal nucleation and growth. The framework structure of the final zeolite products is greatly influenced by types of SDA and initial compositions of reaction gel (*e.g.*, H_2O/SiO_2 and SiO_2/Al_2O_3 molar ratios), each of which will be briefly discussed below.

Initially, zeolites were synthesized using inorganic alkali and alkaline earth metal cations as SDAs under alkaline conditions (pH > 11). For these syntheses at high pH, the high concentration of hydroxide (OH^-) serves as a mineralizing agent. These conditions and compositions generally result into low silica zeolites, such as zeolite A, X, and Y.[23] While these low silica zeolites were excellent materials for ion-exchange and separation treatments, their high Al concentrations reduce the stability of zeolite frameworks, which limits their catalytic applications. Later on, Mobil researchers in the 1970s pioneered the use of organic quaternary ammonium molecules as SDAs in zeolite synthesis. The organic quaternary ammonium molecules are relatively larger and more hydrophobic than alkali and alkaline earth metal cations, which in general require a smaller number of negative charges (*e.g.*, four-coordinate Al species) for charge balancing. Furthermore, the alkyl groups of organic

SDAs could be synthetically varied to tune their hydrophobicity. Depending on the type of organic quaternary ammonium SDA used in the syntheses, high silica zeolites with different frameworks can be obtained. For example, the use of tetraethyl- and tetrapropyl ammonium hydroxides typically leads to the formation of BEA and MFI, respectively[51,52] (see Figure 4). Interestingly, the combination of alkyl ammoniums and alkyl amines results into new chemical compositions of the previously determined zeolite frameworks.[53,54] In addition to hydroxides, fluorides were introduced as another type of mineralizing agent in zeolite preparations, which expanded the compositions and structures of synthetic zeolites.[55,56] The presence of fluorides eliminates the need of hydroxides and allows zeolite synthesis to proceed under pH neutral conditions. More importantly, fluoride-mediated zeolite synthesis enables the discovery of new zeolite structures with low framework densities, as well as siliceous counterparts of previously identified aluminosilicate zeolites.[55]

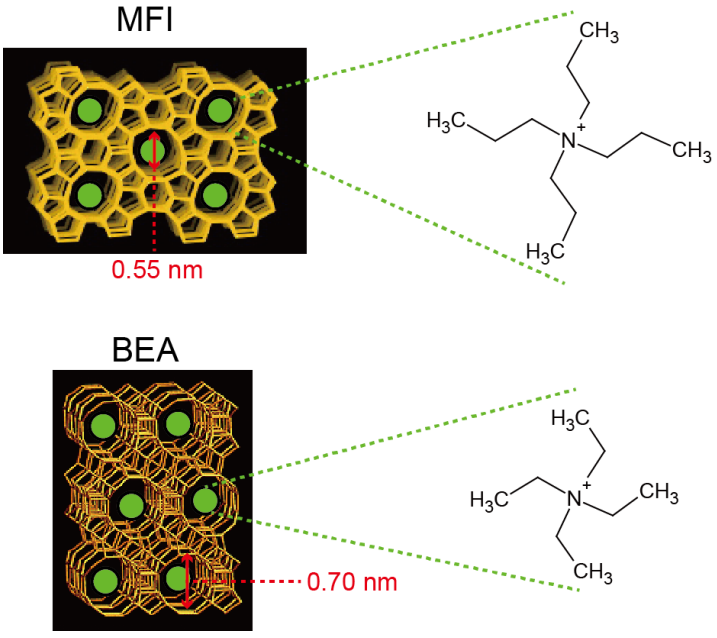

Figure 4. Schematic diagram of zeolites MFI and BEA with their corresponding structure-directing agents (SDAs): tetrapropylammonium and tetraethylammonium, respectively.

In addition to the type of SDA species used, the chemical compositions of the starting reactant mixture greatly influences the final zeolite product. For example, the same SDA (*N*,*N*,*N*-trimethyladamantammonium) could result in 3 distinct framework structures with different micropore volumes, depending on the H_2O/SiO_2 molar ratios in reactant mixture (Figure 5).[57–59] Similar examples are observed in the case of imidazolium derivatives as SDA, where the same alkyl imidazolium may not yield the same zeolite framework across various H_2O/SiO_2 ratios.[60] Similar research topics can be found in other referecnes.[50,61–63]

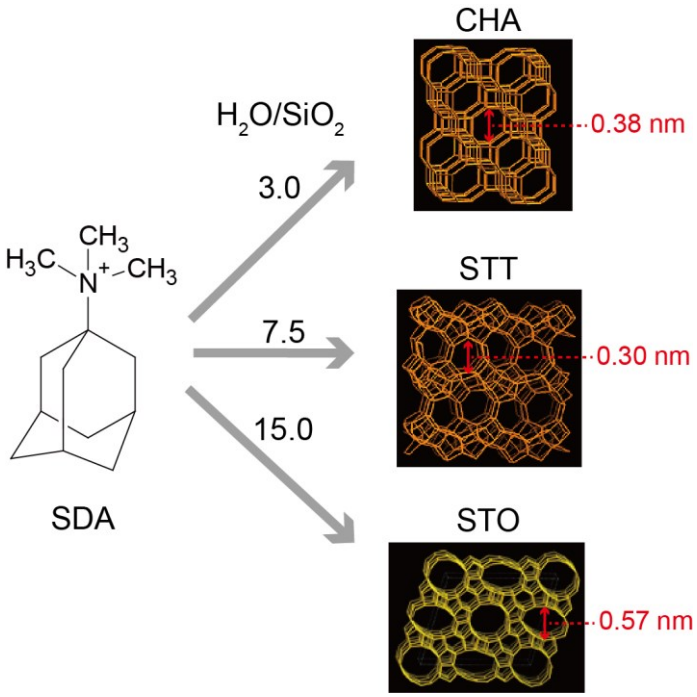

Figure 5. Schematic diagram regarding the influence of H_2O/SiO_2 ratios in reactant on phase selectivities in zeolite synthesis.

1.3.2 Heteroatom incorporation into zeolite frameworks

Heteroatom incorporation is known to impart catalytic activities and adsorption properties to zeolite catalysts. For example, the number of heteroatoms incorporated in the zeolite framework will influence the overall acidity, possibly leading to different reaction

rates.[64,65] On the other hand, various types of heteroatoms can be used in zeolite syntheses and will impart unique reaction activity to heteroatom-containing zeolite catalysts. For example, aluminum (Al) is commonly used due to its resulting strong Brønsted acidity that can catalyze industrially important reactions.[6] In contrast, boron (B) atom incorporation did not initially receive too much attention, mainly because borosilicates exhibit much weaker acidity than aluminosilicates, insufficient to catalyze most reactions.[66] However, it has been recently reported that borosilicates can be chemically exchanged to other heteroatoms, such as Al or Titanium (Ti), via post-synthetic treatments.[67–72] Also, certain zeolite frameworks may be synthesized as borosilicate phases only.[73–79] In addition to Al and B atoms, other heteroatoms are often introduced for specific applications. For example, Ti-containing zeolites (*e.g.*, TS-1) can be used in oxidation reactions,[80–84] whereas iron- and copper-incorporated zeolites with small pores can be implemented in automobiles for selective catalytic reduction (SCR).[85–89] With Tin (Sn) heteroatom incorporation, zeolites exhibit Lewis acidity, which extends the application of zeolites to biomass conversion processes.[90–93] Additionally, the substitution of Si atoms by germanium (Ge) has led to the discovery of new zeolites with interesting framework structures.[61,94–96] The continued development and understanding of heteroatom incorporation conditions and compositions is expected to further expand the catalytic applications of zeolites.

Although the importance of heteroatom incorporation has been acknowledged, it is still very challenging to identify their exact locations in zeolite frameworks and to rationalize how to alter their locations. This may be attributed to the characterization methods have limited abilities to probe heteroatom siting. In this thesis, new two-dimensional (2D) nuclear magnetic resonance (NMR) techniques will be described. These new NMR methods,

together with crystallography, allow heteroatom distributions in ordered frameworks to be directly measured, which had been impossible to achieve. Al and B were first chosen for demonstration, in part because Al and B have more friendly nuclear properties than other heteroatoms (*e.g.*, Sn or Ti) for NMR investigations, such as their superior NMR signal sensitivities. Additionally, Al and B heteroatom incorporation affects the macroscopic catalytic properties of zeolites, as previously discussed. Furthermore, it would be very interesting to investigate their similarities and differences. Based on the molecular understanding of Al and/or B heteroatom distributions in zeolites, it may be possible to synthesize alumino- and borosilicates with desired Al and B siting, respectively. Ultimately, such capabilities would allow zeolite properties to be tailored for specific catalytic applications.

1.3.3 Characterization of zeolite framework structures

Confined space in zeolite structures is known to provide shape selectivity in catalytic and adsorption reactions.[6,11,97,98] A detailed understanding of these framework topologies is important for the improvement of zeolites in existing processes, as well as for exploring new potential applications. X-ray diffraction (XRD), which provides long-range periodic order of crystalline frameworks, is one of the most common methods used to characterize zeolite structures. The direct comparison of XRD patterns with those in a structural database[22] allows the framework types of new zeolite materials to be identified. Additional structural information, such as site connectivities, may be obtained through refinements.[99–101] Another common characterization method, electron microscopy (*e.g.*, transmission electron microscopy (TEM) and scanning electron microscopy (SEM)) enables the direct

observation of zeolite morphologies, from which zeolite crystal sizes can be estimated.[102] Recent developments in microscopy have combined with electron diffraction and is considered a powerful tool in determining unknown zeolite structures.[103,104] In addition, zeolite structural features can be indirectly probed by using hydrocarbon adsorption and acid-catalyzed model reactions.[105–107] For example, zeolites with small, medium, and large pore sizes and various cavities exhibit different hydrocarbon uptake rates during the same adsorption reactions.[107,108] Likewise, zeolites with different pore mouth and cavity sizes have different cracking conversion rates of the same hydrocarbons.[106,109–111]

As a complementary method to those described above, solid-state nuclear magnetic resonance (NMR) spectroscopy is highly sensitive to short-range order of elements of interest (*e.g.*, ^{1}H, ^{11}B, ^{27}Al, and ^{29}Si) in ordered and disordered environments, which is very challenging for diffraction to establish.[112–114] Specifically, different ^{1}H, ^{11}B, ^{27}Al, and ^{29}Si species in zeolites can be identified via one-dimensional (1D) NMR measurements.[112,115,116] More importantly, their homonuclear or heteronuclear interactions can be unambiguously identified by applying two-dimensional (2D) NMR methods.[117] The resulting insights can be used to establish zeolite structures and to estimate molecular proximities between organic SDA and boro-/aluminosilicate frameworks.[118–120] The combination of various characterization methods used here, as summarized in Table 1, is expected to provide insights for zeolite structure determination and improve the understanding of zeolite synthesis.

Table 1. Characterization methods often used to understand properties of zeolites.

Method	Insight
XRD	Long-range order, extent of crystallinity, and zeolite phases
Electron microscopy (SEM and TEM)	Crystal sizes and morphology
Adsorption and reaction testing	Pore sizes and accessibility to cavities
Solid-state NMR spectroscopy	Short-range order, molecular proximity, and molecular site connectivities

1.4 Research objectives

The overall goal of this thesis is to measure, understand, and ideally control B and Al heteroatom distributions in layered and zeolite boro- and aluminosilicate frameworks, respectively. Our main approach to this challenging problem is the application of advanced solid-state 2D NMR methods, as well as systematic synthesis methods by varying chemical compositions that include Al, B contents and the type of SDA species. These new NMR techniques were first tested on two types of surfactant-directed silicates that exhibit distinct degrees of framework condensation. Consequently, there are various numbers of T-sites in the two systems for B and Al heteroatom incorporations. For the first time, B heteroatom distributions in semi-crystalline borosilicate frameworks are directly probed and further established with the new NMR methods (Ch. 2). The resulting boron siting is then compared with Al atom distributions in the surfactant-directed aluminosilicate counterparts, aiming to understand similarities and differences between B and Al incorporations (Ch. 3). The same 2D NMR techniques were subsequently applied to one specific zeolite (*i.e.*, SSZ-70) with the intention of identifying the locations of B and Al species in crystalline boro- (B-SSZ-70) and aluminosilicates (Al-SSZ-70), respectively. Before analyses of B and Al atom

distributions, this complicated zeolite structure were analyzed in great detail via advanced 2D NMR methods (Ch. 4). Interestingly, B-SSZ-70 zeolites could be synthesized via similar yet distinct organic SDAs, which spur the interest in understanding how SDAs influence final boron heteroatom distributions (Ch. 5). In addition, zeolite SSZ-70 can be delaminated to expose a great number of accessible acid sites for catalysis. Furthermore, boron species in borosilicate zeolites could be chemically exchanged with aluminum to increase their Brønsted acidity. Together, zeolite B-SSZ-70 was chosen for delamination, where boron atom siting was monitored *ex-situ* from as-made to delaminated B-SSZ-70 (UCB-4). With the understanding of Al reinsertion and SSZ-70 structure, reinserted Al atoms are expected to locate at some T-sites. The Al atom distribution in Al-reinserted UCB-4 was next compared with aluminosilicate zeolite SSZ-70 (Al-SSZ-70). This offers an opportunity to "direct" Al heteroatom distributions in zeolite catalysts (Ch. 6). Finally, all lessons learned from these different research projects are summarized for future references (Ch. 7).

1.5 References

1. http://goldbook.iupac.org/C00876.html.

2. Clark, J. H. Solid acids for green chemistry. *Acc. Chem. Res.* **35,** 791–797 (2002).

3. Wilson, K. & Clark, J. H. Solid acids and their use as environmentally friendly catalysts in organic synthesis. *Pure Appl. Chem.* **72,** 1313–1319 (2000).

4. Busca, G. Acid catalysts in industrial hydrocarbon chemistry. *Chem. Rev.* **107,** 5366–5410 (2007).

5. *Market Report: Global Catalyst Market*. (2011).

6. Corma, A. From Microporous to Mesoporous Molecular Sieve Materials and Their Use in Catalysis. *Chem. Rev.* **97,** 2373–2419 (1997).

7. Tanabe, K. & Holderich, W. F. Industrial application of solid acid–base catalysts. *Appl. Catal. A Gen.* **181,** 399–434 (1999).

8. Davis, M. E. Ordered porous materials for emerging applications. *Nature* **417,** 813–821 (2002).

9. Feller, A. & Lercher, J. A. Chemistry and Technology of Isobutane/Alkene Alkylation Catalyzed by Liquid and Solid Acids. *Adv. Catal.* **48,** 229–295 (2004).

10. Zhao, Z.-K., Qiao, W.-H., Li, Z.-S., Wang, G.-R. & Cheng, L.-B. Friedel–crafts alkylation of α-methylnaphthalene in the presence of ionic liquids. *J. Mol. Catal. A Chem.* **222,** 207–212 (2004).

11. Corma, A. State of the art and future challenges of zeolites as catalysts. *J. Catal.* **216,** 298–312 (2003).

12. García-Martínez, J., Johnson, M., Valla, J., Li, K. & Ying, J. Y. Mesostructured zeolite Y—high hydrothermal stability and superior FCC catalytic performance. *Catal. Sci. Technol.* **2,** 987 (2012).

13. Kresge, C. T. & Roth, W. J. The discovery of mesoporous molecular sieves from the twenty year perspective. *Chem. Soc. Rev.* **42,** 3663–70 (2013).

14. Perego, C. & Millini, R. Porous materials in catalysis: challenges for mesoporous materials. *Chem. Soc. Rev.* **42,** 3956–76 (2013).

15. Zhao, D., Huo, Q., Feng, J., Chmelka, B. F. & Stucky, G. D. Nonionic Triblock and Star Diblock Copolymer and Oligomeric Surfactant Syntheses of Highly Ordered, Hydrothermally Stable, Mesoporous Silica Structures. *J. Am. Chem. Soc.* **120,** 6024–6036 (1998).

16. Zhao, D. *et al.* Triblock copolymer syntheses of mesoporous silica with periodic 50 to 300 angstrom pores. *Science* **279,** 548–52 (1998).

17. Kresge, C. T., Leonowicz, M. E., Roth, W. J., Vartuli, J. C. & Beck, J. S. Ordered mesopourous molecular sieves synthesized by a liquid-crystal template mechanism. *Nature* **359,** 710–712 (1992).

18. Beck, J. S. *et al.* Molecular or Supramolecular Templating : Defining the Role of Surfactant Chemistry in the Formation of Microporous and Mesoporous Molecular Sieves. *Chem. Mater.* **6,** 1816–1821 (1994).

19. Perego, C. *et al.* Mesoporous silica-aluminas as catalysts for the alkylation of aromatic hydrocarbons with olefins. *Microporous Mesoporous Mater.* **27,** 345–354 (1999).

20. Flego, C. *et al.* Reaction and deactivation study of mesoporous silica–alumina (MSA) in propene oligomerisation. *J. Mol. Catal. A Chem.* **204,** 581–589 (2003).

21. Martínez, C. & Corma, A. Inorganic molecular sieves: Preparation, modification and industrial application in catalytic processes. *Coord. Chem. Rev.* **255,** 1558–1580 (2011).

22. http://www.iza-structure.org/databases/.

23. Barrer, R. M. *Hydrothermal Chemistry of Zeolites*. (Academic Pr, 1982).

24. Cundy, C. S. & Cox, P. A. The hydrothermal synthesis of zeolites: history and development from the earliest days to the present time. *Chem. Rev.* **103,** 663–702 (2003).

25. Cundy, C. S. & Cox, P. A. The hydrothermal synthesis of zeolites: Precursors, intermediates and reaction mechanism. *Microporous Mesoporous Mater.* **82,** 1–78 (2005).

26. Zones, S. I. Translating new materials discoveries in zeolite research to commercial manufacture. *Microporous Mesoporous Mater.* **144,** 1–8 (2011).

27. Keil, F. J. Methanol-to-hydrocarbons: process technology. *Microporous Mesoporous Mater.* **29,** 49–66 (1999).

28. Halgeri, A. B. & Das, J. Recent advances in selectivation of zeolites for para - disubstituted aromatics. *Catal. Today* **73,** 65–73 (2002).

29. http://www.eni.com/it_IT/home.html.

30. Schmidt, R. J. Industrial catalytic processes—phenol production. *Appl. Catal. A Gen.* **280,** 89–103 (2005).

31. Rossini, S. The impact of catalytic materials on fuel reformulation. *Catal. Today* **77,** 467–484 (2003).

32. Bevilacqua, M. *et al.* An FTIR study of the accessibility of the protonic sites of H-mordenites. *Phys. Chem. Chem. Phys.* **4,** 4575–4583 (2002).

33. Weyda, H. & Köhler, E. Modern refining concepts—an update on naphtha-isomerization to modern gasoline manufacture. *Catal. Today* **81,** 51–55 (2003).

34. Jones, A. J., Carr, R. T., Zones, S. I. & Iglesia, E. Acid strength and solvation in catalysis by MFI zeolites and effects of the identity, concentration and location of framework heteroatoms. *J. Catal.* **312,** 58–68 (2014).

35. Ogura, M. *et al.* Stabilization of bare divalent Fe(II) cations in Al-rich beta zeolites for superior NO adsorption. *J. Catal.* **315,** 1–5 (2014).

36. Schallmoser, S. *et al.* Impact of the local environment of Brønsted acid sites in ZSM-5 on the catalytic activity in n-pentane cracking. *J. Catal.* **316,** 93–102 (2014).

37. Van Santen, R. A. & Kramer, G. J. Reactivity Theory of Zeolitic Broensted Acidic Sites. *Chem. Rev.* **95,** 637–660 (1995).

38. Xu, B., Bordiga, S., Prins, R. & van Bokhoven, J. a. Effect of framework Si/Al ratio and extra-framework aluminum on the catalytic activity of Y zeolite. *Appl. Catal. A Gen.* **333,** 245–253 (2007).

39. Mikovsky, R. J. & Marshall, J. F. Random aluminum-ion siting in the faujasite lattice. *J. Catal.* **44,** 170–173 (1976).

40. Pine, L. A., Maher, P. J. & Wachter, W. A. Prediction of cracking catalyst behavior by a zeolite unit cell size model. *J. Catal.* **476,** 466–476 (1984).

41. Beagley, B., Dwyer, J., Fitch, F. R., Mann, R. & Walters, J. Aluminum Distribution and Properties of Faujasites. Basis of Models and Zeolite Acidity. *J. Phys. Chem.* **88,** 1744–1751 (1984).

42. Larin, A. V. The Loewenstein rule: the increase in electron kinetic energy as the reason for instability of Al-O-Al linkage in aluminosilicate zeolites. *Phys. Chem. Miner.* **40,** 771–780 (2013).

43. Loewenstein, W. The distribution of aluminium in the tetrahedra of silicates and aluminates. *Am. Mineral.* **39,** 92–96 (1954).

44. Freude, D., Hunger, M. & Pfeifer, H. 1H MAS NMR studies on the acidity of zeolites. *Chem. Phys. Lett.* **128,** 62–66 (1986).

45. Barthomeuf, D. & Beaumont, R. X, Y, aluminum-deficient, and ultrastable faujasite-type zeolites: III. Catalytic activity. **30,** 288–297 (1973).

46. Kramer, G. J. & van Santen, R. A. Theoretical determination of proton affinity differences in zeolites. *J. Am. Chem. Soc.* **115,** 2887–2897 (1993).

47. Wang, Q. L., Giannetto, G. & Guisnet, M. Dealumination of zeolites III. Effect of extra-framework aluminum species on the activity, selectivity, and stability of Y zeolites in n-heptane cracking. *J. Catal.* **130,** 471–482 (1991).

48. Corma, A., Melo, F. V & Rawlence, D. Effect of the nonuniform dealumination on the acidity and catalytic activity of faujasite : Part 2 . Accessibility of acid sites. *Zeolites* **12,** 261–264 (1992).

49. Chen, N. Y., Degnan, T. F. & Smith, C. M. *Molecular Transport and Reaction in Zeolites: Design and Application of Shape Selective Catalysis*. 328 (Wiley, 1994).

50. Corma, A. & Davis, M. E. Issues in the Synthesis of Crystalline Molecular Sieves: Towards the Crystallization of Low Framework-Density Structures. *ChemPhysChem* **5,** 304–313 (2004).

51. Rohrbaugh, W. J., Rohrman, A. C. & Wood, J. D. The framework of zeolite beta. *Zeolites* **8,** 446–452 (1988).

52. Kokotailo, G. T., Lawton, S. L., Olson, D. H. & Meier, W. M. Structure of synthetic zeolite ZSM-5. *Nature* **272,** 437–438 (1978).

53. Zones, S. I., Hwang, S. J. & Davis, M. E. Studies of the synthesis of SSZ-25 zeolite in a "mixed-template" system. *Chemistry* **7,** 1990–2001 (2001).

54. Zones, S. I. & Hwang, S.-J. Synthesis of High Silica Zeolites Using a Mixed Quaternary Ammonium Cation, Amine Approach: Discovery of Zeolite SSZ-47. *Chem. Mater.* **14,** 313–320 (2002).

55. Camblor, M. A., Villaescusa, L. A. & Diaz-Cabanas, M. J. Synthesis of all-silica and high-silica molecular sieves in fluoride media. *Top. Catal.* **9,** 59–76 (1999).

56. Flanigen, E. M. & Patton, R. L. Silica polymorph and process for preparing same. (1978).

57. Zones, S. I., Darton, R. J., Morris, R. & Hwang, S.-J. Studies on the role of fluoride ion vs reaction concentration in zeolite synthesis. *J. Phys. Chem. B* **109,** 652–61 (2005).

58. Burton, A. W., Zones, S. I. & Elomari, S. The chemistry of phase selectivity in the synthesis of high-silica zeolites. *Curr. Opin. Colloid Interface Sci.* **10,** 211–219 (2005).

59. Wagner, P. *et al.* Guest/Host Relationships in the Synthesis of the Novel Cage Based Zeolites SSZ-35, SSZ-36, and SSZ-39. *J. Am. Chem. Soc.* **122,** 263–273 (2000).

60. Archer, R. H., Zones, S. I. & Davis, M. E. Imidazolium structure directing agents in zeolite synthesis: Exploring guest/host relationships in the synthesis of SSZ-70. *Microporous Mesoporous Mater.* **130,** 255–265 (2010).

61. Moliner, M., Rey, F. & Corma, A. Towards the rational design of efficient organic structure-directing agents for zeolite synthesis. *Angew. Chem. Int. Ed. Engl.* **52,** 13880–13889 (2013).

62. Jackowski, A., Zones, S. I., Hwang, S.-J. & Burton, A. W. Diquaternary ammonium compounds in zeolite synthesis: cyclic and polycyclic N-heterocycles connected by methylene chains. *J. Am. Chem. Soc.* **131,** 1092–100 (2009).

63. Zones, S. I. *et al.* The fluoride-based route to all-silica molecular sieves; a strategy for synthesis of new materials based upon close-packing of guest–host products. *Comptes Rendus Chim.* **8,** 267–282 (2005).

64. Dědeček, J., Sobalík, Z. & Wichterlová, B. Siting and Distribution of Framework Aluminium Atoms in Silicon-Rich Zeolites and Impact on Catalysis. *Catal. Rev. - Sci. Eng.* **54,** 135–223 (2012).

65. Stach, H. *et al.* Mordenite acidity: dependence on the silicon/aluminum ratio and the framework aluminum topology. 2. Acidity investigations. *J. Phys. Chem.* **96,** 8480–8485 (1992).

66. Chen, C. Y. & Zones, S. I. Reforming of FCC Heavy Gasoline and LCO with Novel Borosilicate Zeolite Catalysts. *Stud. Surf. Sci. Catal.* **135,** 159 (2001).

67. Zones, S. I. *et al.* Studies of Aluminum Reinsertion into Borosilicate Zeolites with Intersecting Channels of 10- and 12-Ring Channel Systems. *J. Am. Chem. Soc.* **57,** 1462−1471 (2014).

68. Ouyang, X. *et al.* Single-Step Delamination of a MWW Borosilicate Layered Zeolite Precursor under Mild Conditions without Surfactant and Sonication. *J. Am. Chem. Soc.* **57,** 1449−1461 (2014).

69. Zones, S. I., Chen, C. Y., Benin, A. & Hwang, S.-J. Opportunities for selective catalysis within discrete portions of zeolites: The case for SSZ-57LP. *J. Catal.* **308,** 213–225 (2013).

70. Chen, C.-Y. & Zones, S. I. Method for heteroatom lattice substitution in large and extra-large pore borosilicate zeolites. (2002).

71. Ogino, I. *et al.* Heteroatom-Tolerant Delamination of Layered Zeolite Precursor Materials. *Chem. Mater.* **25,** 1502–1509 (2013).

72. Chen, C. Y. & Zones, S. I. From Borosilicate to Gallo- and Aluminosilicate Zeolites : New Methods for Lattice Substitution via Post-Synthetic Treatment. *Stud. Surf. Sci. Catal.* **135,** 211 (2001).

73. Vortmann, S., Marler, B., Gies, H. & Daniels, P. Synthesis and crystal structure of the new borosilicate zeolite RUB-13. *Microporous Mater.* **4,** 111–121 (1995).

74. Li, Y. & Zou, X. SU-16: a three-dimensional open-framework borogermanate with a novel zeolite topology. *Angew. Chem. Int. Ed. Engl.* **44,** 2012–2015 (2005).

75. Elomari, S., Burton, A. W., Ong, K., Pradhan, A. R. & Chan, I. Y. Synthesis and Structure Solution of Zeolite SSZ-65. *Chem. Mater.* **19,** 5485–5492 (2007).

76. Wagner, P. *et al.* Electron Diffraction Structure Solution of a Nanocrystalline Zeolite at Atomic Resolution. *J. Phys. Chem. B* **103,** 8245–8250 (1999).

77. Elomari, S., Burton, A., Medrud, R. C. & Grosse-Kunstleve, R. The synthesis, characterization, and structure solution of SSZ-56: An extreme example of isomer specificity in the structure direction of zeolites. *Microporous Mesoporous Mater.* **118,** 325–333 (2009).

78. Burton, A. *et al.* The synthesis, characterization, and structure solution of SSZ-58: a novel two-dimensional 10-ring pore zeolite with previously unseen double 5-ring subunits. *J. Am. Chem. Soc.* **125,** 1633–1642 (2003).

79. Burton, A. & Elomari, S. SSZ-60: a new large-pore zeolite related to ZSM-23. *Chem. Commun. (Camb).* 2618–9 (2004). doi:10.1039/b410010g

80. Wu, P. A Novel Titanosilicate with MWW Structure: II. Catalytic Properties in the Selective Oxidation of Alkenes. *J. Catal.* **202,** 245–255 (2001).

81. Fan, W., Wu, P., Namba, S. & Tatsumi, T. A titanosilicate that is structurally analogous to an MWW-type lamellar precursor. *Angew. Chem. Int. Ed. Engl.* **43,** 236–40 (2004).

82. Wu, P. *et al.* Methodology for synthesizing crystalline metallosilicates with expanded pore windows through molecular alkoxysilylation of zeolitic lamellar precursors. *J. Am. Chem. Soc.* **130,** 8178–87 (2008).

83. Taramasso, M., Perego, G. & Notari, B. Preparation of porous crystalline synthetic material comprised of silicon and titanium oxides. (1983).

84. Notari, B. Microporous Crystalline Titanium Silicates. *Adv. Catal.* **41,** 253–334 (1996).

85. Moden, B., Donohue, J. M., Cormier, W. E. & Li, H.-X. The Uses and Challenges of Zeolites in Automotive Applications. *Top. Catal.* **53,** 1367–1373 (2010).

86. Fritz, a. & Pitchon, V. The current state of research on automotive lean NOx catalysis. *Appl. Catal. B Environ.* **13,** 1–25 (1997).

87. Chen, H.-Y. & Sachtler, W. M. . Activity and durability of Fe/ZSM-5 catalysts for lean burn NOx reduction in the presence of water vapor. *Catal. Today* **42,** 73–83 (1998).

88. Brandenberger, S., Kröcher, O., Tissler, A. & Althoff, R. The State of the Art in Selective Catalytic Reduction of NO x by Ammonia Using Metal-Exchanged Zeolite Catalysts. *Catal. Rev. - Sci. Eng.* **50,** 492–531 (2008).

89. Liu, Z. & Ihl Woo, S. Recent Advances in Catalytic DeNO X Science and Technology. *Catal. Rev. - Sci. Eng.* **48,** 43–89 (2006).

90. Moliner, M., Román-Leshkov, Y. & Davis, M. E. Tin-containing zeolites are highly active catalysts for the isomerization of glucose in water. *Proc. Natl. Acad. Sci. U. S. A.* **107,** 6164–8 (2010).

91. Román-Leshkov, Y. & Davis, M. E. Activation of Carbonyl-Containing Molecules with Solid Lewis Acids in Aqueous Media. *ACS Catal.* **1,** 1566–1580 (2011).

92. Bermejo-Deval, R., Gounder, R. & Davis, M. E. Framework and Extraframework Tin Sites in Zeolite Beta React Glucose Di ff erently. *ACS Catal.* **2,** 2705–2713 (2012).

93. Bermejo-Deval, R. *et al.* Metalloenzyme-like catalyzed isomerizations of sugars by Lewis acid zeolites. *Proc. Natl. Acad. Sci. U. S. A.* **109,** 9727–32 (2012).

94. Moliner, M., Martinez, C. & Corma, A. Synthesis Strategies for Preparing Useful Small Pore Zeolites and Zeotypes for Gas Separations and Catalysis. *Chem. Mater.* **26,** 246–258 (2014).

95. Corma, A., Navarro, M. T., Rey, F., Rius, J. & Valencia, S. Pure polymorph C of zeolite beta synthesized by using framework isomorphous substitution as a structure-directing mechanism. *Angew. Chem. Int. Ed. Engl.* **40,** 2277–2280 (2001).

96. Paillaud, J.-L., Harbuzaru, B., Patarin, J. & Bats, N. Extra-large-pore zeolites with two-dimensional channels formed by 14 and 12 rings. *Science* **304,** 990–992 (2004).

97. Degnan, T. F. The implications of the fundamentals of shape selectivity for the development of catalysts for the petroleum and petrochemical industries. *J. Catal.* **216,** 32–46 (2003).

98. Corma, A. Inorganic Solid Acids and Their Use in Acid-Catalyzed Hydrocarbon Reactions. *Chem. Rev.* **95,** 559–614 (1995).

99. Xie, D., McCusker, L. B. & Baerlocher, C. Structure of the borosilicate zeolite catalyst SSZ-82 solved using 2D-XPD charge flipping. *J. Am. Chem. Soc.* **133,** 20604–10 (2011).

100. McCusker, L. B. & Baerlocher, C. Solving the Structures of Polycrystalline Materials: from the Debye-Scherrer Camera to SwissFEL. *Chim. Int. J. Chem.* **68,** 19–25 (2014).

101. McCusker, L. B. & Baerlocher, C. Using electron microscopy to complement X-ray powder diffraction data to solve complex crystal structures. *Chem. Commun. (Camb).* 1439–51 (2009).

102. Liu, Z. *et al.* A review of fine structures of nanoporous materials as evidenced by microscopic methods. *Reprod. Syst. Sex. Disord.* **62,** 109–46 (2013).

103. Su, J. *et al.* Structure analysis of zeolites by rotation electron diffraction (RED). *Microporous Mesoporous Mater.* (2013).

104. Willhammar, T., Yun, Y. & Zou, X. Structural Determination of Ordered Porous Solids by Electron Crystallography. *Adv. Funct. Mater.* n/a–n/a (2013).

105. Zones, S. I. *et al.* Indirect assessment of unknown zeolite structures through inference from zeolite synthesis comparisons coupled with adsorption and catalytic selectivity studies. *J. Catal.* **250,** 41–54 (2007).

106. Zones, S. . & Harris, T. . The Constraint Index test revisited: anomalies based upon new zeolite structure types. *Microporous Mesoporous Mater.* **35-36,** 31–46 (2000).

107. Chen, C. *et al.* Characterization of shape selective properties of zeolites via hydroisomerization of n-hexane. *Microporous Mesoporous Mater.* **164,** 71–81 (2012).

108. Archer, R. H. *et al.* Physicochemical Properties and Catalytic Behavior of the Molecular Sieve SSZ-70. *Chem. Mater.* **22,** 2563–2572 (2010).

109. Carpenter, J. R., Yeh, S., Zones, S. I. & Davis, M. E. Further investigations on Constraint Index testing of zeolites that contain cages. *J. Catal.* **269,** 64–70 (2010).

110. Davis, T. M. *et al.* The importance of channel intersections in the catalytic performance of high silica stilbite. *J. Catal.* **298,** 84–93 (2013).

111. Frillette, V. J., Haag, W. O. & Lago, R. M. Catalysis by crystalline aluminosilicates: Characterization of intermediate pore-size zeolites by the "Constraint Index."*J. Catal.* **67,** 218–222 (1981).

112. Fyfe, C. A., Feng, Y., Grondey, H., Kokotailo, G. T. & Gies, H. One- and Two-Dimensional High-Resolution Solid-State NMR Studies of Zeolite Lattice Structures. *Chem. Rev.* **91,** 1525–1543 (1991).

113. Brouwer, D. H. *et al.* A general protocol for determining the structures of molecularly ordered but noncrystalline silicate frameworks. *J. Am. Chem. Soc.* **135,** 5641–5655 (2013).

114. Brouwer, D. H. Structure solution of network materials by solid-state NMR without knowledge of the crystallographic space group. *Solid State Nucl. Magn. Reson.* **51-52,** 37–45 (2013).

115. Hwang, S.-J., Chen, C.-Y. & Zones, S. I. Boron Sites in Borosilicate Zeolites at Various Stages of Hydration Studied by Solid State NMR Spectroscopy. *J. Phys. Chem. B* **108,** 18535–18546 (2004).

116. Jiang, Y., Huang, J., Dai, W. & Hunger, M. Solid-state nuclear magnetic resonance investigations of the nature, property, and activity of acid sites on solid catalysts. *Solid State Nucl. Magn. Reson.* **39,** 116–41 (2011).

117. Shayib, R. M. *et al.* Structure-directing roles and interactions of fluoride and organocations with siliceous zeolite frameworks. *J. Am. Chem. Soc.* **133,** 18728–18741 (2011).

118. Hedin, N. *et al.* Structure of a surfactant-templated silicate framework in the absence of 3d crystallinity. *J. Am. Chem. Soc.* **126,** 9425–32 (2004).

119. Christiansen, S. C. *et al.* Molecularly ordered inorganic frameworks in layered silicate surfactant mesophases. *J. Am. Chem. Soc.* **123,** 4519–4529 (2001).

120. Janicke, M. T. *et al.* Low Silica MCM-41 Composites and Mesoporous Solids. *Chem. Mater.* **11,** 1342–1351 (1999).

Chapter 2: Local Environments of Boron Heteroatoms in Non-Crystalline Layered Silicates

2.1 Abstract

Boron heteroatom distributions are shown to be significantly different in two closely related layered borosilicates synthesized by subtly different alkylammonium surfactant species. The complicated order and disorder near framework boron sites in both borosilicates were characterized at the molecular-level by using a combination of multi-dimensional solid-state nuclear magnetic resonance (NMR) spectroscopy techniques and first-principles calculations. Notably, two-dimensional solid-state *J*-mediated (through-bond) $^{11}B\{^{29}Si\}$ NMR analyses provide direct and local information on framework boron sites that are covalently bonded to silicon sites through bridging oxygen atoms. The resolution and identification of distinct ^{11}B-O-^{29}Si site pairs, in conjunction with framework structures, allows determination of boron heteroatom distributions in the layered borosilicate frameworks, which are shown to be distinct for materials synthesized with $C_{16}H_{33}N^{+}Me_3$ and $C_{16}H_{33}N^{+}Me_2Et$ structure-directing surfactant species. The analyses reveal that the boron atoms are shown to be non-selectively distributed among different types of silicon sites in the layered $C_{16}H_{33}N^{+}Me_3$-directed borosilicate framework, whereas boron atoms are preferentially incorporated into one type of specific incompletely condensed sites in the $C_{16}H_{33}N^{+}Me_2Et$-directed borosilicate material. Interestingly, framework boron species appear to induce framework condensation of their next-nearest-neighbor silicon sites in the $C_{16}H_{33}N^{+}Me_3$-directed borosilicate. By comparison, boron species do not appear to

significantly alter short-range order of their nearby silicon sites in the $C_{16}H_{33}N^{+}Me_2Et$-directed borosilicate. These molecular-level insights are supported by density functional theory (DFT) calculations, which show the distinct influences of boron atoms on the $C_{16}H_{33}N^{+}Me_3$- and $C_{16}H_{33}N^{+}Me_2Et$-directed borosilicate frameworks, consistent with the experimental observations. The differences in boron site distributions and local boron-induced structural transformations for the two surfactant-directed borosilicates appear to be due to the different extents of cross-linking of the siliceous frameworks. The understanding of order and disorder near framework ^{11}B sites, as well as the ^{11}B site distributions in borosilicates is expected to be correlated with associated acidity, reaction activity, and other material properties of borosilicate catalysts.

2.2 Introduction

Porous materials, such as mesoporous silica and zeolites, have attracted significant attention since the last two decades, because of their diverse industrial applications including ion exchangers,[1–3] adsorbents,[4–6] separation membranes,[7,8] or heterogeneous catalysts.[9–11] These applications substantially rely on properties that are in part attributed to presence of heteroatoms (*e.g.*, Al, B, Ga) in silica- or silicate-based materials. Therefore, to rationally alter heteroatom site distributions in heteroatom-containing silicate or silica frameworks is expected to optimize catalytic properties of these materials.[12–14] However, this has been a major challenge in Materials Science, in part because characterization of heteroatom siting is extremely difficult. Even in porous materials with well-ordered structures, such as zeolites, it is still very challenging to precisely identify locations of heteroatoms in structures, based on average long-range order established via diffraction

methods, except for some types of heavy heteroatoms (*e.g.*, Fe or Ti).[15–17] This problem could be mitigated if single crystals with sufficient crystal sizes are available for diffraction measurements, from which reliable refinements could yield information on heteroatom site distributions (*e.g.*, B, Fe and Ga) in zeolites.[18,19] Nevertheless, determination of heteroatom siting in ordered silicate frameworks using diffraction techniques still remains significantly challenging for other heteroatoms, such as ^{27}Al, because ^{27}Al and ^{29}Si have very close scattering factors.[20]

While solid-state nuclear magnetic resonance (NMR) spectroscopy provides molecular-level insights that in principle could characterize local environments of heteroatoms and their distributions in heteroatom-containing silicates, limited NMR spectral resolution has often led to ambiguous answers to such difficult questions.[21,22] Previous investigations often suggest near-random[19] or poorly preferential distributions of heteroatoms in heteroatom-containing zeolites.[12,22–26] Zeolites with ideal 3-dimensional (3D) structures are composed of tetrahedral sites (T-sites) that are bonded to other four T-sites via bridging oxygen atoms, which primarily lead to distinct ^{29}Si environments (designated as Q^4 ^{29}Si) in solid-state ^{29}Si NMR spectroscopy. The Q^n notation is used to describe bonding configurations of T-sites, where n refers to the number of connected T-sites for a given T-site. Interestingly, despite the fact that Q^4 ^{29}Si environments in 3D zeolites are all chemically and structurally similar and only exhibit subtle differences in Si-O-Si bond angles and Si-O bond lengths, ^{29}Si NMR spectroscopy can identify these very similar yet distinct Q^4 ^{29}Si species due to their molecular-level properties. However, heteroatoms inserted into these Q^4 ^{29}Si sites appear to result into ^{29}Si NMR signatures extremely difficult to distinguish from each other, resulting into the difficulty in determining precise locations

of heteroatoms in frameworks. To the best of our knowledge, it does not appear to be strong driving force, at least from thermodynamic perspective, for heteroatoms preferentially inserted into specific crystallographic sites in heteroatom-containing silica(te)s. This may explain that there are no reports of high-silica zeolites, where ^{27}Al or other heteroatoms could be incorporated selectively into certain framework sites. In rare cases, where heteroatoms occupy one specific framework site in zeolites (*e.g.*, ^{11}B in borosilicate zeolite MCM-70[27], ^{27}Al in scolecite[20]), this particular site is occupied exclusively only by heteroatoms, and the other sites are all Si.

In this context, an alternative route for controlling heteroatom distributions in zeolites could begin with silicate precursors that possess structurally distinguishable ^{29}Si environments. This is the case of layered silicates,[28,29] whose molecularly-ordered frameworks, very similar to zeolites, are nevertheless less condensed and contain T-sites connected to only three other T-sites via bridging oxygen atoms (designated as Q^3 ^{29}Si). Interestingly, Q^3 and Q^4 ^{29}Si species exhibit very different ^{29}Si NMR frequency ranges: Q^3 (*ca.* -92 to -103 ppm) and Q^4 ^{29}Si sites (*ca.* -105 to -120 ppm). While Q^3 ^{29}Si sites are often considered as structural defects in zeolites with the remarkable exception of SSZ-74 that has ordered Si vacancies,[30] Q^3 ^{29}Si environments are indeed part of framework structures in layered silicates.[31–36] Furthermore, some of layered silicates can transform into structurally related 3D zeolites via framework condensation of Q^3 Si sites in adjacent layers.[32,33,37–39]

Among different types of layered silicates, surfactant-directed layered silicates[40,41] are excellent model systems to test the possibility of establishing and controlling heteroatom locations as well as the potential of being new 3D zeolite precursors. Here, we focus on the surfactant-directed layered silicates that self-assemble into mesoscopically-ordered phases

in presence of alkylammonium surfactants with chemical formula $CH_3(CH_2)_{15}$-$N^+R_1R_2R_3$ (R_1, R_2 and R_3 = Me or Et).[40] Interestingly, hydrophobic properties of surfactant headgroups can be tuned to form different silicate structures with two and five distinct ^{29}Si sites for $C_{16}H_{33}\mathbf{Me_3}N^+$ and $C_{16}H_{33}\mathbf{Me_2Et}N^+$ surfactant molecules, respectively. Additionally, the ^{29}Si sites in these surfactant-directed silicates lead to sharp and well-resolved ^{29}Si NMR signals, which would facilitate challenging characterization of heteroatom site distributions in heteroatom-containing silicates. Another interest of these surfactant-directed layered silicates is because they may be considered the first historical step prior to mesostructured zeolites developed by Ryoo and co-workers.[8,42–44] The synthesis of zeolite nanosheets, in particular, can be viewed as an extended synthesis of the surfactant-directed layered silicates investigated here, where judicious designed alkylammonium surfactants with multiple headgroups were employed to crystalize layered zeolite frameworks with thicker wall thickness (*ca.* 2 nm), as compared to layered silicates (< 1 nm).[41,42,45] However, the large number of distinct ^{29}Si sites in these zeolite MFI nanosheets does not lead to sufficiently separated ^{29}Si NMR signals, very different from $C_{16}H_{33}\mathbf{Me_3}N^+$- and $C_{16}H_{33}\mathbf{Me_2Et}N^+$-directed layered silicates that are the focus of this work.

While Al heteroatoms were previously shown to be incorporated in the $C_{16}H_{33}\mathbf{Me_3}N^+$-directed layered silicates, locations of the ^{27}Al sites could not be unambiguously established.[46,47] In addition to ^{27}Al atoms, boron (^{11}B) atoms can be incorporated into zeolite frameworks, although they result into much weaker solid acidity than ^{27}Al-induced ones. Nevertheless, such relatively weak acidity can catalyze reactions that require modest solid acidity.[48,49] Furthermore, certain zeolite frameworks could be only synthesized in associated borosilicate forms. These observations spur a number of investigations of borosilicate

syntheses with the intention of discovering new zeolite topologies.[49–58] More interestingly, ^{11}B species in large-pore borosilicate zeolites (*e.g.*, SSZ-24 and SSZ-31) can be chemically exchanged to ^{27}Al species via isomorphic substitution to prepare ^{27}Al-reinserted zeolites with enhanced solid acidity.[59–63]

Here, ^{11}B atom site distributions in $C_{16}H_{33}\mathbf{Me_3}N^+$- and $C_{16}H_{33}\mathbf{Me_2Et}N^+$-directed layered borosilicates are established and shown to be significantly different. Specifically, the complicated order and disorder near ^{11}B sites were probed using a combination of solid-state multi-dimensional NMR techniques and density functional theory (DFT) calculations. Our main objectives are to demonstrate that preferential ^{11}B atom distributions in borosilicates may be achieved and to provide molecular-level insights into local environments nearby ^{11}B species, both of which were approached by identifying molecular interactions involving ^{11}B atoms as well as Q^3 and Q^4 ^{29}Si and ^{1}H species in both $C_{16}H_{33}\mathbf{Me_3}N^+$- and $C_{16}H_{33}\mathbf{Me_2Et}N^+$-directed borosilicates. Importantly, our results reveal significantly different ^{11}B site distributions in the two surfactant-directed borosilicates synthesized under otherwise compositions and conditions. Such understanding is expected to provide key elements to establish relationships between local structures and associated catalytic activity of borosilicate zeolite catalysts at the molecular-level.

2.3 Experimental

2.3.1 Materials.

Cetyltrimethylammonium bromide ($C_{16}H_{33}\mathbf{Me_3}NBr$, ≥96.0%, Sigma-Aldrich), cetyldimethylethylammonium bromide ($C_{16}H_{33}\mathbf{Me_2Et}NBr$, ≥98%, Sigma-Aldrich), tetramethylammonium hydroxide (TMAOH, 25 wt% in water, Sigma-Aldrich), boric acid

(Sigma-Aldrich), hydrofluoric acid (HF, 48 wt% in water, Sigma-Aldrich), nitric acid (HNO_3, ACS reagent and 70%), amorphous silica (SiO_2, CAB-O-SIL M5 scintillation grade, ACROS ORGANICS) and methanol (ACS grade, VWR®) were purchased and directly used without any further purification. 99% ^{29}Si-enriched SiO_2 was purchased from CortecNet (France). Syntheses of layered surfactant-directed borosilicates follow the molar composition of 1.0 SiO_2: 0.2 B_2O_3: 0.7 TMAOH: 113.4 H_2O: 9.9 CH_3OH: 0.7 surfactants (either $C_{16}H_{33}Me_3NBr$ or $C_{16}H_{33}Me_2EtNBr$). Surfactants were first dissolved in deionized water. TMAOH and CH_3OH were subsequently added and the solution stirred for 30 min, after which silica precursors (either SiO_2 or recondensed $^{29}SiO_2$) were added, and the reaction media stirred for a week. Boric acid was then added for 2 h to obtain synthesis gels, which were later transferred into a Teflon™-lined Parr™ 4745 stainless-steel reactor, well-sealed and heated at 135 °C under static conditions for 2 ($C_{16}H_{33}$**Me$_3$**N^+-directed borosilicates) and 7 days ($C_{16}H_{33}$**Me$_2$Et**N^+-directed borosilicates). After the hydrothermal treatment, the as-synthesized layered surfactant-directed borosilicates were collected using vacuum filtration and washed with deionized water. The products were dried at 90 °C overnight before characterization.

Recondensed $^{29}SiO_2$ was prepared by dissolving ^{29}Si-enriched SiO_2 in 1M TMAOH solution (pH ~ 14) under reflux 95 °C and stirring conditions for 19 days. The ^{29}Si-enriched silica was subsequently recovered by adding concentrated HBr acid solution to obtain precipitate gels (pH of 7 - 8), which were subsequently collected by vacuum filtration. The precipitated gels were purified by deionized water, high-speed centrifugation, and removal of excess water. The purified silica source (designated as recondensed $^{29}SiO_2$) was dried at 90 °C for several days prior to syntheses of borosilicates.

2.3.2 Characterization

Elemental analyses. Bulk Si/B ratios were obtained using inductively coupled plasma (ICP) analysis (Thermo iCAP 6300 model). Before ICP analysis, the as-synthesized layered materials were calcined at 550 °C for 12 hours to remove organic surfactants, and the resulting calcined materials were dissolved with 2 wt % HF and 3 wt % HNO_3 acid solution under vigorous stirring conditions for several days. The CHN results were provided by the analytical lab in the Marine Science Institute (MSI) at UCSB using the CEC440HA model from Exeter Analytical, Inc.

Solid-state one-dimensional (1D) ^{11}B, ^{29}Si and two-dimensional (2D) $^{11}B\{^{1}H\}$ HETCOR NMR experiments were performed on a Bruker Avance (III) 750 and 400 NMR spectrometers operating at 17.6 (^{1}H, ^{11}B, and ^{29}Si Larmor frequencies of 750.12, 240.66, and 149.01 MHz, respectively) and 9.4 T (^{1}H, ^{11}B, and ^{29}Si frequencies of 400.17, 128.38, and 79.49 MHz, respectively). 1D $^{29}Si\{^{1}H\}$ CP-MAS experiments were collected at room temperature, 17.6 T, and under magic-angle-spinning (MAS) conditions of 10 kHz using a 4 mm probehead along with a cross-polarization (CP) contact time of 8 ms and a recycle delay of 2 s. 4096 and 128 transients were used for ^{29}Si-non-labled and ^{29}Si enriched materials, respectively. 1D ^{11}B echo-MAS experiments were performed at 17.6 T under MAS conditions of 14 kHz along with a recycling delay of 2 s and a double frequency sweep (DFS)[64] preparation sequence to enhance ^{11}B signal. Heteronuclear ^{1}H decoupling at a nutation frequency of 50 kHz with small-phase-incremental-alternation-with-64-steps (SPINAL64)[65] was utilized during acquisition for both ^{29}Si and ^{11}B NMR experiments. Transverse dephasing time measurements were performed with 7 increments to obtain a

series of half-echo delays between 0 and 12 ms, each of which was collected using 1024 scans. Heteronuclear ^{1}H decoupling (SPINAL64) at a nutation frequency of 60 kHz alternatively turned on and off during the echo (and kept on during the acquisition).

Two-dimensional (2D) ^{11}B{^{1}H} HETCOR NMR spectra were collected at room temperature, 17.6 T, and under MAS conditions of 14 kHz using a 4 mm probehead. The magnetization was transferred from ^{1}H to ^{11}B by using adiabatic passage through Hartmann-Hahn condition.[66] CP contact time of 1.0 and 0.1 ms were used for the $C_{16}H_{33}Me_3N^+$- and $C_{16}H_{33}Me_2EtN^+$- directed layered borosilicates, respectively. The signal in the 2D ^{1}H dimension was accumulated over 96 increments with 176 transients each for the $C_{16}H_{33}Me_3N^+$-directed materials and 128 increments with 64 transients each for the $C_{16}H_{33}Me_2EtN^+$-directed materials. Heteronuclear ^{1}H decoupling at a nutation frequency of 70 kHz was applied during acquisition. Both spectra were collected using a recycling delay of 2 s.

2D ^{11}B{^{29}Si} dipolar- and *J*-mediated HMQC spectra were collected on ^{29}Si-enriched materials under MAS conditions of 10 kHz at room temperature and 9.4 T using a 3.2 mm triple-resonance probehead. The heteronuclear dipolar couplings between ^{11}B and ^{29}Si species were reintroduced in dipolar-mediated ^{11}B{^{29}Si} HMQC experiments via a $R4^2_1$ symmetry-based dipolar recoupling scheme[67–70] at a ^{29}Si nutation frequency of 20 kHz ($2\nu_R$). The recoupling durations were set to 6.0 ms (10 symmetry cycles of 6 rotor periods each) before and after the evolution period. The second ^{29}Si dimension was collected with a recycling delay of 2.17 s and 96 increments, each of which contained 1024 transients, leading to total experimental time of 61 h. The half-echo delay before and after the evolution period in the ^{11}B{^{29}Si} *J*-mediated HMQC[71] experiments were experimentally

optimized to 10.0 and 12.5 ms for the $C_{16}H_{33}N^{+}Me_3$- and $C_{16}H_{33}N^{+}Me_2Et$-directed layered borosilicates, respectively. The indirect dimensions were collected with 32 increments (2304 scans each) for the $C_{16}H_{33}N^{+}Me_3$-direct materials and 96 increments (768 transients each) for the $C_{16}H_{33}N^{+}Me_2Et$-direct materials. A recycling delay of 3 s was used in 2D $^{11}B\{^{29}Si\}$ *J*-mediated HMQC collected on the $C_{16}H_{33}N^{+}Me_3$- and $C_{16}H_{33}N^{+}Me_2Et$-direct materials, resulting in experimental durations of 62 and 63 h, respectively. Heteronuclear ^{1}H decoupling with the SPINAL64 sequence at a nutation frequency of *ca.* 60 kHz was applied during the whole sequence. ^{29}Si and ^{11}B NMR chemical shifts were referenced to tetramethylsilane (TMS) and BF_3OEt_2, respectively.

Error calculations for the transverse dephasing time measurements were conducted with a Monte Carlo approach, by repeating the same fit on 512 sets of data points generated by adding random noise to the experimental data set added. The standard deviation of the added random noise was fixed to the standard deviation between the experimental points and the best fit. The reported errors correspond to the standard deviation of the fitted data over the 512 fits.

X-ray diffraction. The mesostructures and local-range order were characterized using small-angle (SAXS) and wide-angle (WAXS) X-ray diffractions. SAXS patterns were collected using a Riguku SMART lab diffractometer and a Cu Kα radiation (λ = 1.5405 Å) generated at 44 kV and 40 mA. The scanning angle range of a SAXS pattern was from 0.5 to 10° 2Θ and the step size was set to 0.5 °/min. Furthermore, WAXS patterns were collected using a Philips XPERT Pro diffractometer and a Cu Kα radiation (λ = 1.5405 Å) generated at 45 kV and 40 mA. The materials were scanned at a step size of 4 °/min between 2Θ angle ranges from 10 to 45°.

DFT Calculations were conducted with CASTEP,[72] a code based on Density Functional Theory that uses a plane-wave approach and periodic boundary conditions. Geometry optimizations were conducted using PBE as an exchange correlation functional,[73] a cut-off energy of 650 eV, and the default "on-the-fly" "ultrasoft" pseudopotentials[74] of Materials Studio 5.5 (see Table A1) with convergence thresholds of 10^{-5} eV/atom for the total energy, $3x10^{-2}$ eV/Å for the maximum ionic force, and 10^{-3} Å for the maximum ionic displacement. During the geometry optimization, unit cells were kept frozen, while all the atoms inside were allowed to relax in order to minimize both the forces on the atoms and on the unit cell. Depending on the model size, different Monkhorst-Pack[75] (MP) grid was used to sample the Brillouin zone so as to give a k-spacing less than 0.04 $Å^{-1}$ in the *a*, *b*, *c* directions. For example, a 4×4×1 MP grid is used when calculation was made on one unit cell (10 or 8 Si atoms depending on the material), whereas MP grids of size 4×2×1, 2×4×1, 2×2×1, and 3×1×1 were used for the 1×2×1, 2×1×1, 2×2×1, and 1×3×1 supercells, respectively.

Calculations of NMR shielding values were performed using the Gauge Including Projector Augmented Wave (GIPAW) approach[76] method implemented in CASTEP using the same conditions for cut-off energy and MP grid as for geometry optimizations. Reliable absolute chemical shift values may be obtained from correlation plots between experimental isotropic chemical shifts and calculated isotropic chemical shielding for an appropriate series of reference compounds in order to cover a large domain of chemical shifts for each type of nuclei. Here, we used for ^{29}Si and ^{11}B chemical shifts calculations the compounds listed in Table A2, which gave rise to the correlation plots shown in Figure A1. The correlation equations were respectively: $\delta_{iso}(ppm) = -0.920\ \sigma_{iso} + 288.45$ for ^{29}Si, and $\delta_{iso}(ppm) = -1.004\ \sigma_{iso} + 95.31$ for ^{11}B.

2.4 Results and Discussion

The locations of boron (^{11}B) atoms are exceedingly difficult to elucidate, because they exhibit less extents of long-range order than crystalline structures. Such characteristics in general make diffraction based analyses, sensitive to long-range framework order, less suitable for these tasks. For example, powder X-ray diffraction (XRD) patterns of as-synthesized $C_{16}H_{33}\mathbf{Me_3}N^+$- and $C_{16}H_{33}\mathbf{Me_2Et}N^+$-directed borosilicates with *ca*. 99% ^{29}Si enrichment show small- (Figure 1a, c) and high-angle reflections (Figure 1b, d) in both borosilicate materials, indicating a high degree of mesoscopic lamellar order and long-range framework order, respectively. These results are very similar to the closely related $C_{16}H_{33}\mathbf{Me_3}N^+$- and $C_{16}H_{33}\mathbf{Me_2Et}N^+$-directed siliceous frameworks,[40,41,45] although the elemental analyses indeed reveal presence of ^{11}B contents in the two borosilicates (Table 1), where $C_{16}H_{33}\mathbf{Me_3}N^+$- and $C_{16}H_{33}\mathbf{Me_2Et}N^+$-directed borosilicate materials are shown to have Si/B ratios of 142 and 52, respectively. Based on the XRD and elemental analyses, ^{11}B incorporation does not appear to induce substantial changes of long-range order in $C_{16}H_{33}\mathbf{Me_3}N^+$- and $C_{16}H_{33}\mathbf{Me_2Et}N^+$-directed layered borosilicates, as compared to their siliceous counterparts. However, it is not possible to unambiguously establish the locations of ^{11}B atoms in the two borosilicate materials here by using XRD analyses only. Consequently, distributions of ^{11}B sites, as well as their interactions with structure-directing surfactant species and silicon (^{29}Si) framework sites have still remained elusive.

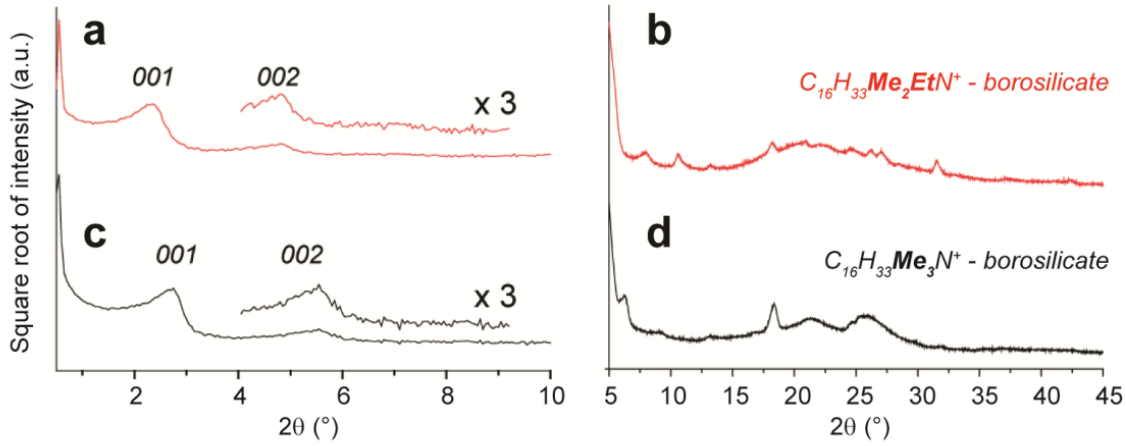

Figure 1. (a, c) Small- and (b, d) wide-angle powder X-ray diffraction patterns of as-synthesized (a, b) $C_{16}H_{33}\mathbf{Me_2}EtN^+$- (Si/B ~52) and (c, d) $C_{16}H_{33}\mathbf{Me_3}N^+$-directed layered borosilicates (Si/B ~142) with *ca.* 99% ^{29}Si enrichment.

Table 1. Summary for elemental analyses of $C_{16}H_{33}\mathbf{Me_2Et}N^+$- and $C_{16}H_{33}\mathbf{Me_3}N^+$-directed layered borosilicates.

Material	Atomic content (wt%)					Si/B	surfactant per Q^3 unit
	C	H	N	Si	B		
$C_{16}H_{33}\mathbf{Me_3}N^+$-borosilicate	37.5	7.4	2.5	18.4	0.05	142	0.64
$C_{16}H_{33}\mathbf{Me_2Et}N^+$-borosilicates	42.1	7.4	2.7	17.7	0.13	52	0.71

Same as the XRD analyses that show a high degree of similarity between $C_{16}H_{33}\mathbf{Me_3}N^+$- and $C_{16}H_{33}\mathbf{Me_2Et}N^+$-directed layered borosilicates and siliceous materials, 1D ^{29}Si{^{1}H} CP-MAS NMR of $C_{16}H_{33}\mathbf{Me_3}N^+$- and $C_{16}H_{33}\mathbf{Me_2Et}N^+$-directed layered borosilicates reveals two and five ^{29}Si species, as shown in Figure 2a and c, respectively. Interestingly, the 1D ^{29}Si NMR analyses appear to be identical to the associated siliceous counterparts, where $C_{16}H_{33}\mathbf{Me_3}N^+$- and $C_{16}H_{33}\mathbf{Me_2Et}N^+$-directed layered silicates have two and five distinct ^{29}Si framework sites, respectively.[40,41] The results indicate that short-range molecular order of the borosilicate and siliceous frameworks are very similar. Furthermore, the narrow ^{29}Si

NMR spectral widths (full-width-at-half-maximum (FWHM): 0.8 to 1.5 ppm) in Figure 2a, c show highly uniform local ^{29}Si environments present in both surfactant-directed borosilicates. Specifically, $C_{16}H_{33}\mathbf{Me_3}N^+$-directed borosilicate has one Q^3 and one Q^4 ^{29}Si species, designated as Si1 and Si2, respectively, with the Q^3/Q^4 ratio of 0.50. By comparison, two Q^3 (Si1 and 2) and three Q^4 ^{29}Si species (Si3, 4, and 5) are present in the $C_{16}H_{33}\mathbf{Me_2Et}N^+$-directed borosilicate with the approximate Q^3/Q^4 ratio of 0.67. Nevertheless, the 1D ^{29}Si NMR analyses do not enable information on ^{11}B species in both surfactant-directed borosilicate materials.

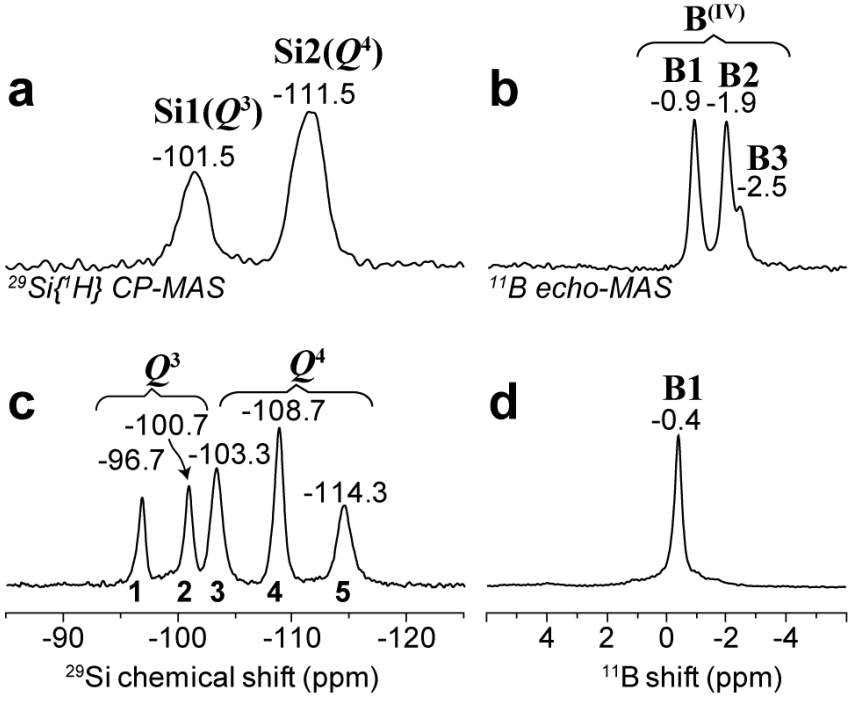

Figure 2. Solid-state 1D (left) ^{29}Si{^{1}H} CP-MAS and (right) ^{11}B echo-MAS NMR spectra of (a-b) $C_{16}H_{33}\mathbf{Me_3}N^+$- (Si/B ~142) and (c-d) $C_{16}H_{33}\mathbf{Me_2Et}N^+$-directed layered borosilicates (Si/B ~52), respectively. The spectra were all collected at 17.6 T and room temperature. Distinct ^{29}Si and ^{11}B species with their corresponding chemical shifts are described in detail in each MAS NMR spectrum. [Courtesy: Dr. Mounesha Garaga]

In contrast with XRD and ^{29}Si NMR analyses, ^{11}B NMR spectroscopy provides local information on ^{11}B species in borosilicates. For example, 1D ^{11}B echo-MAS reveals three and one four-coordinate ^{11}B sites in the $C_{16}H_{33}\mathbf{Me_3}N^+$- and $C_{16}H_{33}\mathbf{Me_2Et}N^+$-directed layered borosilicates, as evidenced by various ^{11}B NMR signals (FWHM: 0.3 to 0.5 ppm) in Figure 2b and d, respectively. These results are consistent with the understanding of $C_{16}H_{33}\mathbf{Me_3}N^+$- and $C_{16}H_{33}\mathbf{Me_2Et}N^+$-directed silicate structures composed of four-coordinate framework ^{29}Si sites only. Therefore, ^{11}B species would become four-coordinated when incorporated into these two framework structures. In this regard, ^{11}B incorporation is expected to modify the host inorganic structures, primarily because of different sizes between ^{29}Si and ^{11}B atoms. To support such a hypothesis, the elemental analyses (*i.e.*, Si/B ratios) were used to estimate a possible fraction of ^{29}Si NMR signals that result from ^{29}Si sites near ^{11}B species, and the detailed description and results are summarized in Table A3. Specifically, the results indicate that more than 15% of the ^{29}Si NMR signals would be affected if substantial influences of ^{11}B sites on their neighboring ^{29}Si species exist in the $C_{16}H_{33}\mathbf{Me_2Et}N^+$-directed borosilicate (*e.g.*, the perturbation range: at least 5 Å). However, this estimation is in stark contrast with the 1D ^{29}Si NMR spectrum (Figure 2c), showing that the $C_{16}H_{33}\mathbf{Me_2Et}N^+$-directed borosilicate has very similar ^{29}Si environments to its siliceous analog. Such facts suggest that framework ^{11}B species exhibit highly localized influences on their nearby ^{29}Si neighbors (very likely less than 5 Å), consistent with the 1D ^{11}B NMR spectrum (Figure 2d) that only shows one ^{11}B signal at -0.4 ppm (FWHM: 0.3 ppm). The ^{11}B NMR analyses demonstrate well-defined ^{11}B environments and suggest that ^{11}B atoms seem to incorporate into one type of ^{29}Si sites in the $C_{16}H_{33}\mathbf{Me_2Et}N^+$-directed borosilicate. Very different from the case of $C_{16}H_{33}\mathbf{Me_2Et}N^+$-directed borosilicate, 1D ^{11}B NMR

analyses provide solid evidence that framework ^{11}B species induce structural changes in the $C_{16}H_{33}\mathbf{Me_3}N^+$-directed borosilicate frameworks. Specifically, three ^{11}B signals at -0.9, -1.9, and -2.5 ppm are identified by the 1D ^{11}B NMR (Figure 2b), all of which correspond to three distinct four-coordinate ^{11}B sites and designated as B1, B2, and B3, respectively. However, the presence of the three ^{11}B species obviously exceeds the number of distinct framework ^{29}Si sites available for ^{11}B incorporation, indicating that structural rearrangements occur in the $C_{16}H_{33}\mathbf{Me_3}N^+$-directed borosilicate frameworks upon ^{11}B incorporation. While distinct ^{11}B species are resolved and identified by 1D ^{11}B NMR, their exact locations and ^{11}B-induced structural modifications in both surfactant-directed borosilicate materials have still remained elusive.

Molecular interactions that involve ^{11}B species and their neighboring ^{1}H species were measured to provide insights about ^{11}B site distributions in both surfactant-directed borosilicate materials, because ^{11}B atoms inserted into Q^3 and Q^4 ^{29}Si sites, designated as Q^3 and Q^4 ^{11}B species, respectively, are expected to have different extents of influences of ^{1}H species. Q^3 ^{11}B sites would interact more strongly with ^{1}H species than Q^4 ^{11}B sites, due to the fact that Q^3 ^{11}B sites bonded to negatively-charged non-bridging oxygen atoms would be charge balanced by positively-charged headgroups of alkylammonium surfactants. Various spatial proximities between ^{1}H and ^{11}B species could be distinguished by measuring transverse ^{11}B dephasing times T_2' (*i.e.*, rate of signal loss during a spin echo) in presence or absence of heteronuclear ^{11}B-^{1}H decouplings.[77,78] The results are presented in Figure A2 and summarized in Table 2 for both surfactant-directed borosilicate materials. In the case of the $C_{16}H_{33}\mathbf{Me_3}N^+$-directed borosilicate, ^{11}B sites B1 and B2 show identical T_2' (*i.e.*, 24 ms) in the presence of heteronuclear ^{11}B-^{1}H decoupling. However, low ^{11}B signal sensitivity and

limited spectral resolution for ^{11}B site B3 prevent reliable T_2' measurements. In contrast, ^{11}B sites B1 and B2 exhibit significantly different T_2' times, 7.0 and 16 ms, respectively, in the absence of ^{1}H decoupling, indicating that magic-angle-spinning alone is insufficient to remove all the heteronuclear ^{11}B dipole-^{1}H dipole interactions. Residual ^{1}H-^{11}B dipolar couplings consequently affect T_2' times of the ^{11}B sites B1 and B2. Such large differences of T_2' times between the ^{11}B sites B1 and B2 reveal that ^{11}B site B1 is under greater influences than ^{11}B site B2. As such, the ^{11}B site B1 can be attributed to ^{11}B atoms incorporated into Q^3 ^{29}Si sites, and ^{11}B site B2 refers to ^{11}B atoms substituted into Q^4 ^{29}Si sites. The similar ^{11}B shifts of the ^{11}B sites B2 and B3 suggest that ^{11}B site B3 seems to stem from ^{11}B atoms incorporated into Q^4 ^{29}Si site. Similarly, in the case of the $C_{16}H_{33}$**Me$_2$Et**N^+-directed borosilicates, the ^{11}B signal shows very different T_2' times that are 35 and 4.0 ms measured in the presence and absence of ^{11}B-^{1}H decoupling, establishing that the associated four-coordinate ^{11}B sites result from the ^{11}B atoms incorporate into Q^3 ^{29}Si sites.

Table 2. Summary for transverse ^{11}B dephasing times (T_2') measured on $C_{16}H_{33}$**Me$_2$Et**N^+-(Si/B ~52) and $C_{16}H_{33}$**Me$_3$**N^+-directed layered borosilicates (Si/B ~142) in presence and absence of heteronuclear ^{1}H decoupling during ^{11}B signal acquisition.
[Courtesy: Dr. Mounesha Garaga]

Material	^{11}B signal (ppm)	T_2' (ms)		Local ^{11}B environments
		^{1}H Decoupling on	^{1}H decoupling off	
$C_{16}H_{33}Me_2EtN^+$ layered borosilicate	-0.4	35 ± 4	3.7 ± 0.2	Hydroxylated
$C_{16}H_{33}Me_3N^+$ layered borosilicate	-0.9	24 ± 1	6.7 ± 0.4	Hydroxylated
	-1.9	24 ± 7	16 ± 2	Fully condensed

In addition, 2D dipolar-mediated (through-space) ^{11}B{^{1}H} NMR analyses provide local information on ^{11}B sites that are molecularly proximate to their neighboring ^{1}H species (< 1 nm) in the $C_{16}H_{33}$**Me$_3$**N^+- and $C_{16}H_{33}$**Me$_2$Et**N^+-directed layered borosilicates, as shown in

Figure 3a and b, respectively. For example, both 2D $^{11}B\{^{1}H\}$ NMR spectra reveal correlated intensities among all ^{11}B signals and one ^{1}H signal (at *ca.* 3.5 ppm) that corresponds to ^{1}H species of surfactant headgroups (*i.e.*, N-C**H$_3$** and/or N-C**H$_2$**). Such strong intensity correlations show that the four-coordinate ^{11}B species are molecularly proximate to surfactant headgroups in the $C_{16}H_{33}$**Me$_3$**N^+- and $C_{16}H_{33}$**Me$_2$Et**N^+-directed layered borosilicates, as illustrated as insets in red in Figure 3a and b, respectively. The spatial proximities are characteristic of the strong electrostatic organic-inorganic interactions that govern the formation of surfactant-directed materials, previously observed on surfactant-directed silicates.[40] Interestingly, in the case of the $C_{16}H_{33}$**Me$_3$**N^+-directed borosilicate, the ^{11}B signal at -0.9 ppm (^{11}B site B1) exhibits correlation intensities with the relatively weak ^{1}H signal at 1.9 ppm associated with the second CH_2 group in the alkyl chain of $C_{16}H_{33}$**Me$_3$**N^+ surfactant molecules, as shown in blue in Figure 3a. By comparison, other ^{11}B signals at -1.9 and -2.5 ppm (^{11}B sites B2 and B3, respectively) do not reveal correlations with such a ^{1}H signal at 1.9 ppm. These differences demonstrate that ^{11}B site B1 interact more strongly with ^{1}H moieties than ^{11}B sites B2 and B3, consistent with the analyses of T_2' measurements. Similarly, the ^{11}B signal at -0.4 ppm (^{11}B site B1) is also correlated with the ^{1}H signal at 1.9 ppm, corresponding to the second CH_2 group in the alkyl chain of $C_{16}H_{33}$**Me$_2$Et**N^+ surfactant molecules in the case of the $C_{16}H_{33}$**Me$_2$Et**N^+-directed borosilicate highlighted in blue in Figure 3b. Furthermore, the ^{11}B signals at -0.9 and -0.4 ppm both show correlation intensities with the ^{1}H signal at *ca*. 1 ppm associated with B-OH or B-(OH)-Si moieties, highlighted in green in Figure 3a and b, respectively. These correlations indicate that these ^{1}H species appear to arise from the ^{11}B atoms incorporated in Q^3 ^{29}Si sites and consequently have a small fraction of the all ^{1}H moieties present in the

$C_{16}H_{33}$**Me$_3$**N^+- and $C_{16}H_{33}$**Me$_2$Et**N^+-directed layered borosilicates given the low ^{11}B contents (Si/B ratios of *ca.* 50 or more). 2D $^{11}B\{^1H\}$ NMR analyses provide such molecular-level insights about charge compensation of anionic ^{11}B sites in the borosilicate frameworks are essential to build models describing the plausibly distorted local structures around these ^{11}B sites.

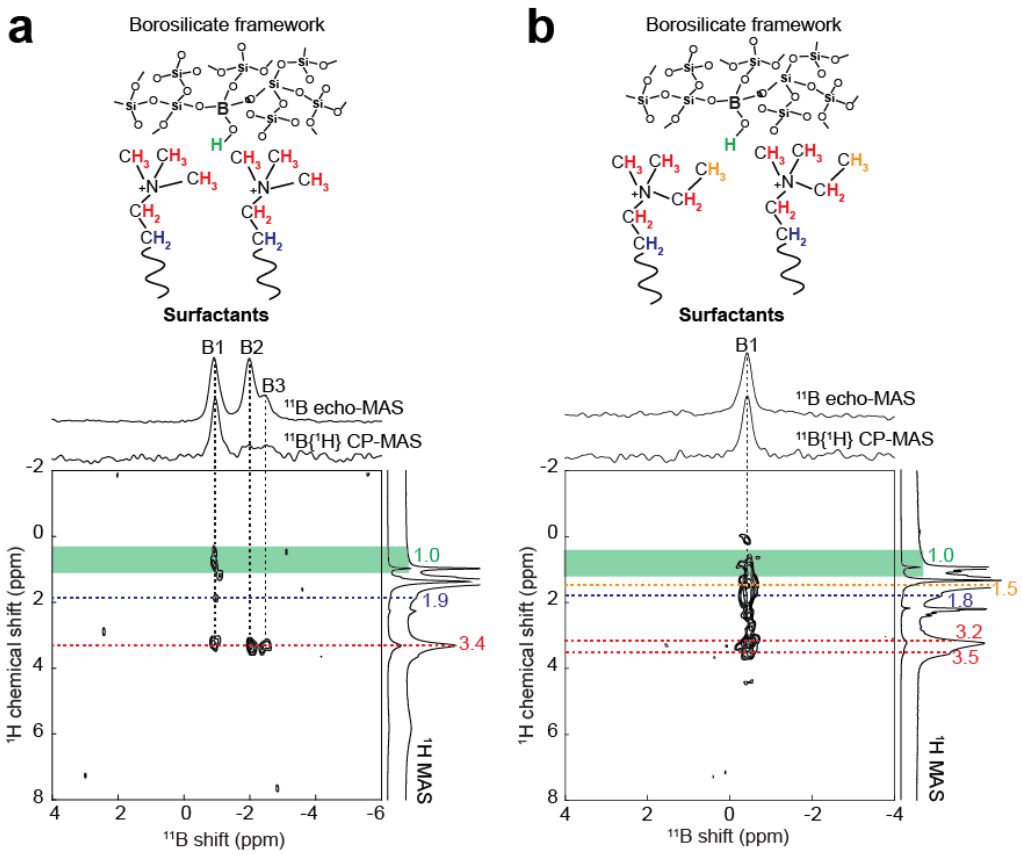

Figure 3. Solid-state 2D HETCOR $^{11}B\{^1H\}$ NMR spectra, acquired at 17.6 T and room temperature, of (a) $C_{16}H_{33}$**Me$_3$**N^+- (Si/B ~142) and (b) $C_{16}H_{33}$**Me$_2$Et**N^+-directed layered borosilicates (Si/B ~52), establishing spatial proximities between the four-coordinate ^{11}B and their nearby ^1H species. The corresponding 1D ^{11}B echo-MAS and $^{11}B\{^1H\}$ CP-MAS NMR spectra are shown along the top horizontal axis, and the 1D ^1H MAS spectrum is shown along the right vertical axis. The horizontal lines in different colors point to the various ^1H environments of the surfactants, as illustrated as insets. [Courtesy: Dr. Mounesha Garaga]

Molecular modeling can yield information about such short-range order and disorder near ^{11}B sites in the $C_{16}H_{33}\mathbf{Me_3}N^+$- and $C_{16}H_{33}\mathbf{Me_2Et}N^+$-directed layered borosilicates to support the NMR analyses. In particular, calculation of NMR parameters using density functional theory (DFT) is a powerful means to validate structural models. DFT calculations were conducted on representative models of both surfactant-directed borosilicates to examine and evaluate possible order and disorder near framework ^{11}B species in both surfactant-directed borosilicates, which can be described by (periodic) models that consist of a single 2D borosilicate sheet, because the presence of flexible and mobile surfactants in the inter-layer space of these layered materials results in a high degree of stacking disorder. Our $C_{16}H_{33}\mathbf{Me_3}N^+$-directed silicate models were based on the octosilicate structure[79] that possesses similar ^{29}Si-NMR signatures to the $C_{16}H_{33}\mathbf{Me_3}N^+$-directed silicate, due to their similar ^{29}Si-NMR signatures.[40,80] There are two distinct types of Q^4 and Q^3 ^{29}Si sites (labeled as T1 and T2) in the octosilicate corresponding to ^{29}Si sites Si2 and Si1 in the $C_{16}H_{33}\mathbf{Me_3}N^+$-directed layered silicates, respectively. On the other hand, advanced NMR-based structure determination protocols led to the identification of three equally valid candidate models of the $C_{16}H_{33}\mathbf{Me_2Et}N^+$-directed silicate,[45] all of which were considered in our calculations. This silicate framework also turns out to be identical to the individual layers of a highly crystalline material: the newly-discovered HUS-2 prepared with choline hydroxide ($C_5H_{15}NO_2$) as structure-directing agent (SDA) sepcies.[81]

Two different approaches were applied to model the alkylammonium surfactant molecules in the $C_{16}H_{33}\mathbf{Me_3}N^+$- and $C_{16}H_{33}\mathbf{Me_2Et}N^+$-directed layered borosilicates. First, surfactants with relatively short alkyl chains, such as CH_3-$(CH_2)_3$-$\mathbf{Me_3}N^+$ or CH_3-$(CH_2)_3$-$\mathbf{Me_2Et}N^+$ molecules, were included in the inter-layer space of all candidate structure models

to mimic charge-compensating surfactant molecules and streamline computations. The small molecules are expected to exhibit otherwise identical interactions with the borosilicate frameworks. A series of geometry optimizations were then conducted on model structures, in which one of the ^{29}Si sites was manually replaced by one ^{11}B atom. This thereby breaks the symmetry of the silicate structures before ^{11}B incorporation. The negative charge was balanced by adding a proton either directly on the non-bridging oxygen atom to form a B-O-H moiety if ^{11}B atoms are inserted into Q^3 ^{29}Si sites or on a non-bridging oxygen atom of ^{11}B neighboring Q^3 ^{29}Si sites if ^{11}B atoms occupy Q^4 ^{29}Si sites. Examples of ^{11}B atoms in Q^3 ^{29}Si sites in the $C_4H_9\mathbf{Me_3}N^+$ and $C_4H_9\mathbf{Me_2Et}N^+$-directed borosilicates are shown in Figure A3 (a, b) and (c, d), respectively. While these model structures were expected to describe the local ^{29}Si structures near framework ^{11}B species, calculated ^{29}Si and ^{11}B NMR chemical shifts reveal very limited relevance to the NMR analyses of $C_{16}H_{33}\mathbf{Me_3}N^+$- and $C_{16}H_{33}\mathbf{Me_2Et}N^+$-directed layered borosilicate materials. This may be because the frozen state of the surfactant-mimicking molecules in this approach results in broad distributions of calculated ^{29}Si chemical shifts in Figure A4 that are not well correlated with experimental results. Although the ^{11}B chemical shifts calculated via this approach turn out to be less affected by this problem (see Table A4) than ^{29}Si chemical shifts, a different modeling strategy was adopted for these systems.

In an alternative approach to model the complicated organic-inorganic interactions and their influence on the ^{29}Si and ^{11}B NMR signatures, the surfactant molecules were omitted and replaced by positive charges homogenously distributed across the entire unit cell. Such a strong approximation is expected to overcome problems caused by the frozen configurations of $C_4H_9\mathbf{Me_3}N^+$ and $C_4H_9\mathbf{Me_2Et}N^+$ surfactant headgroups, which were

previously observed.[82] This approach was first validated for the siliceous systems, as illustrated in Figure A5. Best results were obtained with calculations conducted on supercells that contain one ^{1}H atom per pair of non-bridging oxygen atoms, corresponding to each supercell to 2 ^{1}H atoms and 2 negative charges for 8 ^{29}Si atoms in the case of the $C_{16}H_{33}\mathbf{Me_3}N^{+}$-directed silicates, and 2 ^{1}H atoms and 2 negative charges for 10 ^{29}Si atoms in the case of the $C_{16}H_{33}\mathbf{Me_2Et}N^{+}$-directed silicates. Such configurations would lead to borosilicates with 0.5 charge-compensating surfactant molecule per Q^3 unit, which is reasonably close to the elemental analyses of both surfactant-directed borosilicates (see Table 1). This modeling strategy appears to substantially improve the agreement between experimental and calculated NMR parameters in the case of $C_{16}H_{33}\mathbf{Me_2Et}N^{+}$-directed silicates, as compared to the previously used approximation,[45] where all non-bridging oxygen atoms were protonated to form silanol groups. Importantly, these calculations further validate the three "equally-valid framework structural models" that were previously established,[45] two of which (structural models 2 and 4) appear to converge to a single structure when only two of their non-bridging oxygen atoms are protonated. Structural models 2 and 3, obtained after optimization with 2 ^{1}H atoms per supercell, were consequently considered reference systems to construct a second series of models of the $C_{16}H_{33}\mathbf{Me_2Et}N^{+}$-directed borosilicates. Similarly, our $C_{16}H_{33}\mathbf{Me_3}N^{+}$-directed borosilicate models were constructed from a pure-silicate model obtained from a single layer of the RUB-18 structure, with 2 ^{1}H per supercell (for 8 ^{29}Si atoms) and 2 positive charges distributed across the entire unit cell. In both series, ^{11}B atoms were introduced by replacing one ^{29}Si atom in a 2x2x1 supercell, corresponding to models of compositions $(BSi_{39}O_{88}H_8)^{9-}$ for the $C_{16}H_{33}\mathbf{Me_2Et}N^{+}$-directed borosilicates, and $(BSi_{31}O_{72}H_8)^{9-}$ for the $C_{16}H_{33}\mathbf{Me_3}N^{+}$-

directed borosilicates, as reported in Table 3, and in the first two rows of Table A5, respectively.

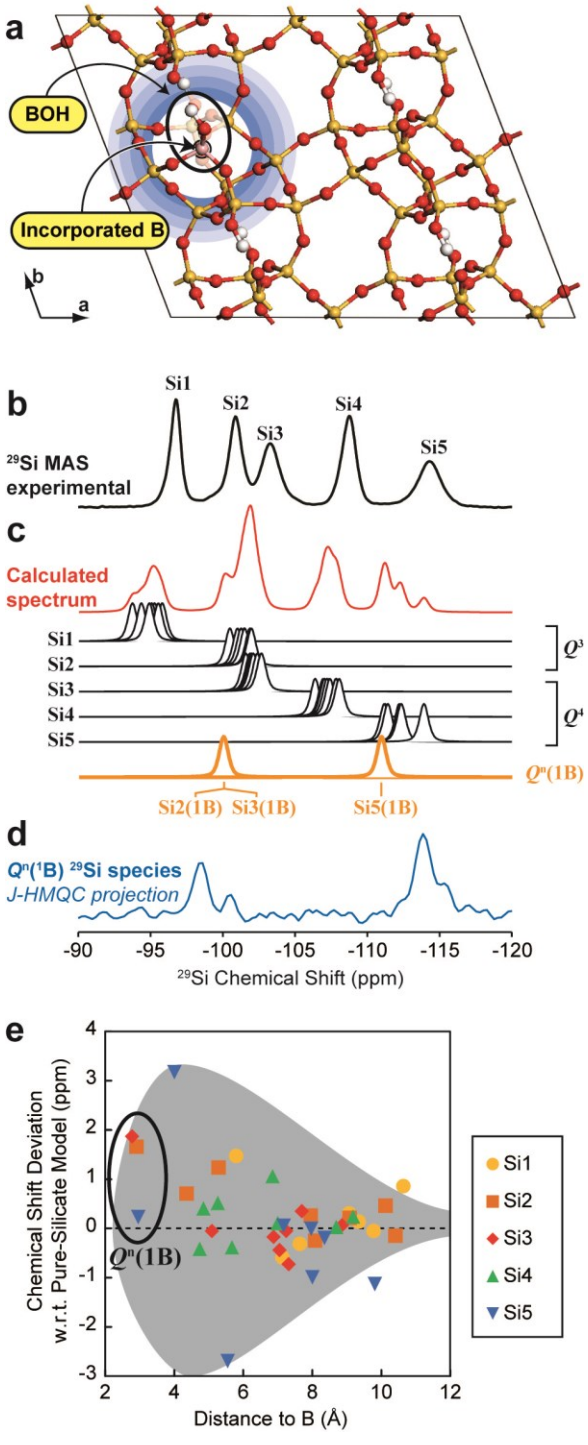

Figure 4. (a) DFT-optimized structural model of C_4H_9**Me$_2$Et**N^+-directed layered borosilicates with one ^{11}B atom inserted into one ^{29}Si site 1 (Q^3 ^{29}Si), which was constructed using a 2x2x1 supercell and has 8 ^1H atoms as well as homogenously distributed positive charges for charge compensation. (b) The 1D ^{29}Si NMR MAS spectrum of $C_{16}H_{33}$**Me$_2$Et**N^+-directed layered borosilicates (Si/B ~52) is comparison with (c) the calculated ^{29}Si NMR spectrum (in red) via DFT calculation that includes ^{29}Si signals corresponding to distinct types of Q^n (in black) and Q^n(1B) ^{29}Si species (in orange). (d) The 1D ^{29}Si projection extracted from 2D *J*-mediated HMQC $^{11}B\{^{29}Si\}$ NMR spectrum shows ^{29}Si signals associated with Q^n(1B) ^{29}Si sites. (e) A summary plot manifests differences of calculated ^{29}Si chemical shifts between the borosilicate model and the silicate model (*i.e.*, no ^{11}B incorporation) as a function of relative distances of various ^{29}Si sites with respect to the nearest ^{11}B atoms. The influences of ^{11}B atoms on borosilicate frameworks are depicted in grey for visual illustrations. [Courtesy: Dr. Sylvian Cadars]

Table 3. Comparisons between the experimental and the computational ^{11}B chemical shift values via DFT using the $C_{16}H_{33}$**Me$_2$Et**N^+-directed layered borosilicates based on the siliceous counterparts (frameworks no.2 and 3), where surfactants are replaced by homogeneously-distributed positive charges for charge compensation.

[Courtesy: Dr. Zalfa Nour]

Model composition and charge	B/Si substitution site	Calculated δ_{iso}(^{11}B) (ppm)		Experimental ^{11}B shift (ppm)
		Framework no. 2	Framework no. 3	
$(BSi_{39}O_{88}H_8)^{9-}$	Si1(Q^3)	0.3	0.9	-0.4
	Si2(Q^3)	-0.8	0.5	
	Si3(Q^4)	-2.8	-2.8	
	Si4(Q^4)	-3.8	-3.2	
	Si5(Q^4)	-3.9	-4.1	

Calculated NMR parameters obtained from the second modeling approach appear to be more reliable than the first approach. Figure 4a shows a representative structural model of the $C_{16}H_{33}$**Me$_2$Et**N^+-directed borosilicate (viewed from c-axis) after DFT geometry optimization. This model was built from the reference silicate framework structure no. 2 (Figure A5) in a 2x2x1 supercell, where one ^{29}Si site Si1 was replaced by one ^{11}B atom to form a B-OH unit. The resulting calculated ^{11}B chemical shifts, including the ones with ^{11}B atoms incorporate into one of the five distinct ^{29}Si sites in candidate framework structures 2 and 3, are summarized in Table 3. Interestingly, these calculations match well-separated ranges of ^{11}B chemical shifts for ^{11}B atoms located in Q^3 (-0.8 to 0.9 ppm) or Q^4 sites (-2.8 to -4.1 ppm). More importantly, the range of calculated ^{11}B NMR signals for Q^3 ^{11}B sites corresponds well to the experimental ^{11}B signal at -0.4 ppm attributed to a BOH moiety formed by substitution of a Q^3 ^{29}Si site in the $C_{16}H_{33}$**Me$_2$Et**N^+-borosilicates (Figure 2d).

This modeling approach, where surfactants are omitted, also considerably improves the reliability of ^{29}Si NMR calculations as compared to the models with occluded surfactant-mimicking molecules. The calculated ^{29}Si chemical shifts for Q^n ^{29}Si sites and for Q^n(1B) ^{29}Si sites Si2, Si3, and S5, shown in black and yellow in Figure 4c, respectively, and are all in good agreement with the experimental results (Figure 4b). Interestingly, the ^{29}Si sites neighboring the ^{11}B atoms seem to be strongly influenced by the structural rearrangements induced by ^{11}B incorporation, as illustrated in Figure 4e, which shows differences of the ^{29}Si chemical shifts between corresponding ^{29}Si sites calculated in the borosilicate and siliceous framework model. The qualitative influences of an isolated ^{11}B site on its nearby ^{29}Si sites in terms of proximities are highlighted in grey in Figure 4e. For the site directly replaced by ^{11}B atoms, there appears to be a compensation between the effect due to the difference of

electronegativity between Si and B (expected to systematically move the ^{29}Si shifts of connected neighbors to higher frequencies) and the geometrical rearrangements caused by the smaller size of the ^{11}B atom (typically an opening of the B-O-Si bonds as compared to Si-O-Si bonds). Similar conclusions may be drawn for the other models with ^{11}B atoms incorporated in ^{29}Si site Si2 and/or using candidate structure no. 3 as the reference pure-silicate framework structure, as shown in Figure A6. In summary, in the $C_{16}H_{33}$**Me$_2$Et**N^+-directed layered borosilicate case, the structural models with ^{11}B atoms incorporated in one specific Q^3 ^{29}Si site appear to match with all the experimental data discussed.

In contrast, ^{11}B incorporation into the $C_{16}H_{33}$**Me$_3$**N^+-directed layered silicate frameworks induces substantial structural modifications of ^{29}Si sites near ^{11}B atoms. This is also evidenced by the three ^{11}B NMR signals (Figure 2b) that over specify the number of distinct ^{29}Si sites (only two in this case). To understand the local order and disorder near ^{11}B species in the $C_{16}H_{33}$**Me$_3$**N^+-directed borosilicate materials, the same approach using homogeneously distributed positive charges instead of surfactant molecules was applied to calculate the ^{29}Si and ^{11}B NMR chemical shifts. Figure 5 shows two DFT-optimized models with the chemical composition $(BSi_{31}O_{72}H_8)^{9-}$ that were obtained by substituting one ^{11}B atom in Q^3 ^{29}Si site Si1 (Figure 5a) or in Q^4 ^{29}Si site Si2 (Figure 5d) in a 2x2x1 supercell. The main characteristics of these models are summarized in Table A5. The calculated NMR parameters based on these models are shown as vertical bars in the plots of Figure 5b, c, e, and f. Calculated ^{29}Si chemical shifts are in reasonable agreement with the experimental data (black spectrum on top of Figure 5b, e) for both Q^3 and Q^4 ^{29}Si sites (black lines). Interesting, the calculated ^{29}Si chemical shifts for Q^n(1B) ^{29}Si environments (blue lines in Figure 5b, e) exhibit small and non-systematic shift differences between Q^3(0B) and Q^3(1B)

^{29}Si or between Q^4(0B) and Q^4(1B) ^{29}Si sites. These DFT analyses suggest that such Q^n(1B) ^{29}Si sites could be very hard to distinguish experimentally from Q^n ^{29}Si sites. As for ^{11}B chemical shifts, calculated values are significantly different for ^{11}B species inserted into Q^3 or a Q^4 ^{29}Si site, as shown in Figure 5c and f, respectively, suggesting that ^{11}B site B1 (at -0.9 ppm) is very likely to correspond to the ^{11}B species incorporated in the Q^3 ^{29}Si site Si1 as a BOH moiety (Figure 5f). By comparison, ^{11}B signals at -1.9 and -2.5 ppm (labeled as ^{11}B sites B2 and B3, respectively) should be associated with the ^{11}B atoms incorporated in the Q^4 ^{29}Si site Si2 (Figure 5c). Nevertheless, these results do not explicitly explain the presence of two distinct four-coordinate ^{11}B sites B2 and B3, both of which are attributed to the ^{11}B atoms at Q^4 environments in the $C_{16}H_{33}\mathbf{Me_3}N^+$-directed borosilicate.

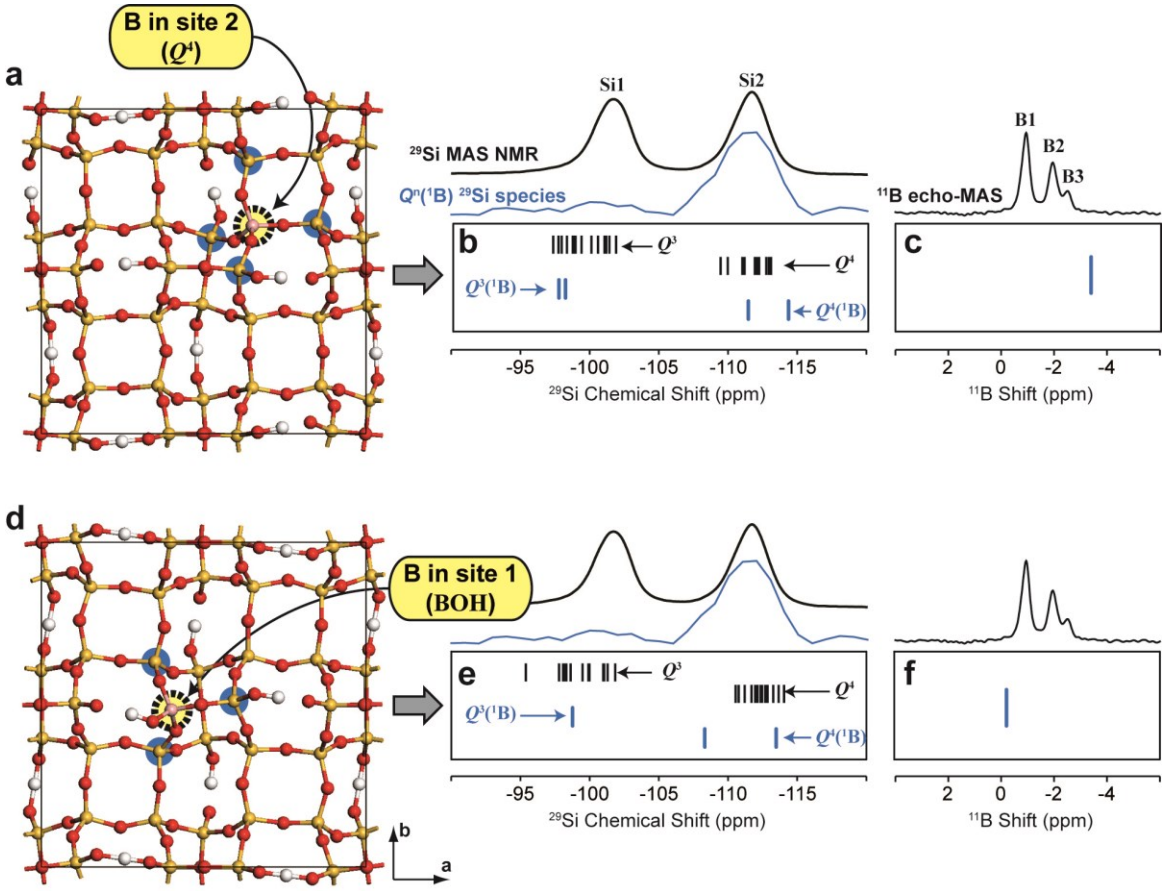

Figure 5. DFT-optimized structural models of $C_{16}H_{33}\mathbf{Me_3}N^+$-directed layered borosilicates viewed from the c-axis, where ^{11}B atoms are manually inserted into ^{29}Si site (a) Si 2 or (d) Si1. For each structural model, 8 ^{1}H atoms per unit cell and other homogeneously distributed positive charges are included for charge compensation. Calculated isotropic chemical shifts for distinct ^{29}Si and ^{11}B species in the models (a) and (b) are shown in plots (b, c) and (e, f), respectively, where the ^{29}Si chemical shifts in blue reveal the ^{29}Si species connected to one ^{11}B atom only. Experimental ^{29}Si and ^{11}B MAS NMR spectra are shown along the top axis accordingly for reference. [Courtesy: Dr. Sylvian Cadars]

The challenges of understanding such complicated short-range order and disorder near ^{11}B species in borosilicate frameworks were overcome by newly modified 2D *J*-mediated ^{11}B{^{29}Si} NMR techniques, which enable determination of distinct ^{11}B-O-^{29}Si site connectivities based on corresponding $^{2}J(^{11}\text{B-O-}^{29}\text{Si})$ couplings. Figure 6a shows a 2D $^{2}J(^{11}\text{B-O-}^{29}\text{Si})$-mediated Heteronuclear Multiple-Quantum Correlation (HMQC) ^{11}B{^{29}Si} NMR spectrum of *ca.* 99% ^{29}Si-enriched $C_{16}H_{33}\mathbf{Me_3}N^{+}$-directed layered borosilicate materials, where the 1D ^{29}Si and ^{11}B NMR spectra shown in black on right vertical and top horizontal axis of the 2D spectrum, respectively. Various correlated intensities in the 2D ^{11}B{^{29}Si} NMR spectrum reveal different ^{29}Si sites covalently bonded to ^{11}B atoms via bridging oxygen atoms in the borosilicate framework. The ^{29}Si projection shown in red on the right vertical axis of the 2D ^{11}B{^{29}Si} spectrum (Figure 6a) selectively reflects a fraction of Q^n(1B) ^{29}Si environments that are not possible to identify via 1D ^{29}Si NMR analyses, because the ^{29}Si signals associated with Q^n(1B) ^{29}Si sites are obscure by a substantial fraction of ^{29}Si signals contributed by Q^n ^{29}Si environments. This ^{29}Si projection was included (in blue) in Figure 5b, e for direct comparison with calculated ^{29}Si chemical shifts corresponding to Q^n(1B) ^{29}Si environments, which reveal well agreements between the calculated and experimental results. Both experimental and theoretical NMR analyses indicate that framework ^{11}B species seem to have limited influences on their nearby (likely next-nearest-neighboring) ^{29}Si sites.

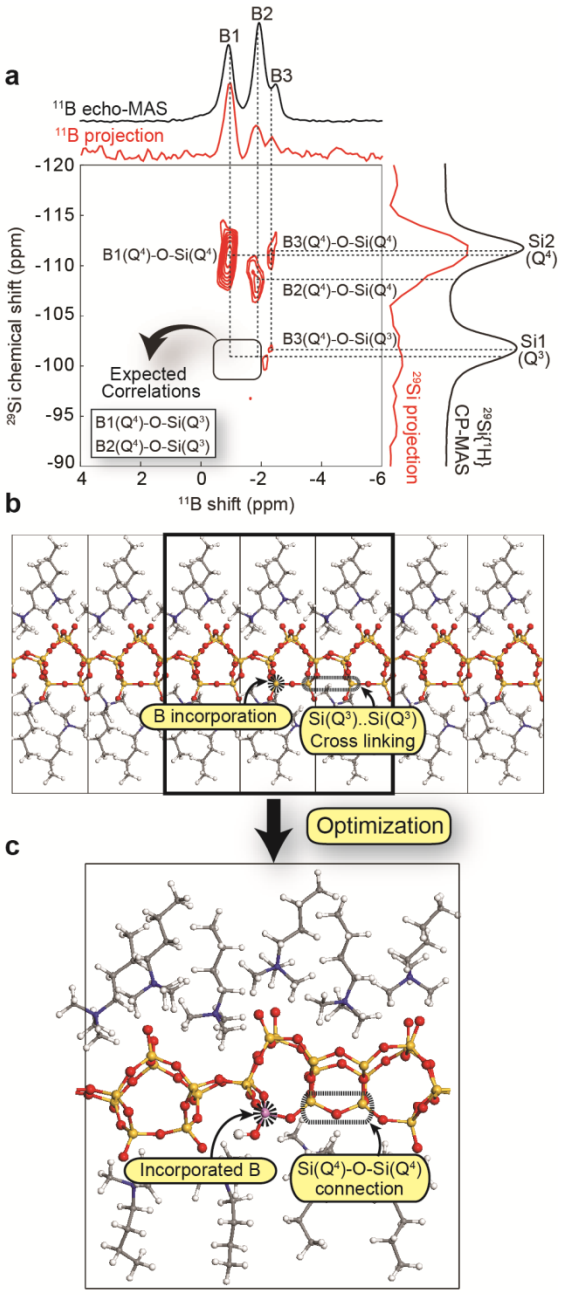

Figure 6. (a) Solid-state 2D *J*-mediated HMQC ^{11}B{^{29}Si} NMR spectrum, acquired at 9.4T and room temperature, of ^{29}Si-enriched $C_{16}H_{33}\mathbf{Me_3}N^+$-directed layered borosilicates (Si/B ~142 expected), establishing ^{29}Si-O-^{11}B site connectivities between the ^{11}B species and their next-nearest-neighboring ^{29}Si sites through bridging oxygen atoms. The 1D ^{11}B echo-MAS NMR spectrum (in black) and the ^{11}B projection (in red) are shown along the top horizontal axis. The 1D ^{29}Si{^{1}H} CP-MAS spectrum (in black) and the ^{29}Si projection (in red) are shown along the right vertical axis. (b) The structural model of $C_{16}H_{33}\mathbf{Me_3}N^+$-directed borosilicates for DFT optimization was constructed using multiple unit cells. (c) An example is selected to illustrate local structural changes in the DFT-optimized model of $C_{16}H_{33}\mathbf{Me_3}N^+$-directed borosilicates per supercell, where one ^{11}B atom is inserted into a Q^3

site, inducing framework condensations between next-nearest-neighboring Q^3 ^{29}Si sites. [Courtesy: Dr. Sylvian Cadars]

Specifically, the ^{11}B signal at -2.5 ppm associated with ^{11}B site B3 exhibits correlated intensities with the ^{29}Si signals at -111 and -101 ppm, corresponding to Q^4 and Q^3 ^{29}Si sites, respectively, establishing that the ^{11}B site B3 is bonded to the Q^3 and Q^4 ^{29}Si sites through bridging oxygen atoms. This is in agreement with the assignment of the ^{11}B site B3 inserted into Q^4 framework sites, because every Q^4 ^{29}Si site is connected to two Q^3 and two Q^4 ^{29}Si sites, as described using the DFT-optimized model shown in Figure 5a. On the contrary, ^{11}B signals at -0.9 and -1.9 ppm, designated as ^{11}B sites B1 and B2, are assigned to the ^{11}B atoms incorporated into Q^3 and Q^4 ^{29}Si environments, both of which show correlation intensities with the ^{29}Si signals corresponding to Q^4 ^{29}Si sites. However, both ^{11}B signals at -0.9 and -1.9 ppm are not correlated with any ^{29}Si signals corresponding to Q^3 ^{29}Si species, which is inconsistent with site connectivities of either Q^3 or Q^4 ^{29}Si sites established from $C_{16}H_{33}$**Me$_3$**N^+-directed silicate framework. For example, ^{11}B atoms incorporated into Q^3 or Q^4 ^{29}Si sites would expect to be bonded to one or two Q^3 ^{29}Si atoms, respectively,[79] which would lead to correlation intensities in the Q^3 ^{29}Si region (highlighted in Figure 6a). This analysis establishes that the local ^{29}Si structure around ^{11}B sites B1 and B2 is modified to have these ^{11}B sites connected with Q^4 ^{29}Si sites exclusively, reflecting an increased degree of framework condensation for the ^{11}B sites B1 and B2 with respect to the siliceous counterparts.

Such local structural rearrangements near ^{11}B atoms in the $C_{16}H_{33}$**Me$_3$**N^+-directed borosilicate material are supported via DFT calculations. For example, Figure 6b,c illustrates how a DFT-optimized borosilicate model (Figure 6c) was built using a supercell

made of 1x3x1 cells of the reference pure-silicate structure (Figure 6b), where one Q^3 ^{29}Si site was manually substituted by one ^{11}B atom with the addition of a ^{1}H to form a B-OH environment for charge compensation. The Q^3 ^{29}Si atom bonded to the ^{11}B site was manually connected with its next-nearest-neighbor Q^3 ^{29}Si atom by replacing the two non-bridging oxygen atoms of these two ^{29}Si atoms by a single bridging oxygen atom placed at their center of mass. In the example model shown here, the decreased framework charge caused by replacing two oxygen atoms with one oxygen atom was compensated by removal of two surfactant-mimicking $C_4H_9\mathbf{Me_3}N^+$ molecules, leading to a chemical composition $(BSi_{23}O_{53}H)^{10-} \cdot 10(C_4H_9\mathbf{Me_3}N^+)$. Interestingly, this model appears to deform during the geometry optimization (Figure 6c) to accommodate the additional cross-linking silicate units. This is a consequence of the local structural rearrangements necessary for SiO_4 and BO_4 units to retrieve appropriate tetrahedral geometries. The configurations of the ^{11}B atoms inserted into Q^3 sites and their connected ^{29}Si neighbors (Q^4(1B) only) in this model are well consistent with all the experimental NMR data of the ^{11}B site B1. The ^{11}B chemical shift calculated via this model (Table A5) is 0.1 ppm, which is in reasonable agreement with the experimental ^{11}B shift of ^{11}B site B1 (-0.9 ppm). Similar results were obtained for other models describing the same situation yet with different supercell sizes or strategies for the compensation of framework negative charges, as summarized in Table A5 and in Figure A7. Collectively, they all yielded calculated ^{11}B shifts between 0.1 and -0.4 ppm, in similarly good agreement with the experimental ^{11}B peak at -0.9 ppm.

Similar conclusions can be drawn with the alternative approach, where homogeneously distributed positive charges rather than surfactant molecules were applied for charge compensation in the surfactant-directed borosilicates. For example, the DFT-optimized

model with the chemical composition $(BSi_{31}O_{71}H_7)^{8-}$ (Figure 7a) depicts a similar BOH environment in a 2x2x1 supercell with one ^{1}H atom per pair of non-bridging oxygen atoms. With this model, the calculated ^{11}B shift (0.2 ppm, see Figure 7c or Table A5) is very close to the calculated value using the surfactant-occluded models and in reasonable agreement with the ^{11}B signal associated with ^{11}B site B1. Calculations of ^{29}Si chemical shifts conducted under such conditions (Figure 7b) predict $Q^4(1B)$ ^{29}Si signatures close to the region of the ^{29}Si spectrum correlated with the B1 frequency (Figure 6a), which is obscure by the dominant Q^4 ^{29}Si signal. In summary, all models that describe one ^{11}B atom inserted into Q^3 ^{29}Si site Si1 to form a B-OH and to induce a new Si-O-Si connectivity of its $Q^3(1B)$ neighbor are compatible with the ^{11}B shift of ^{11}B site B1.

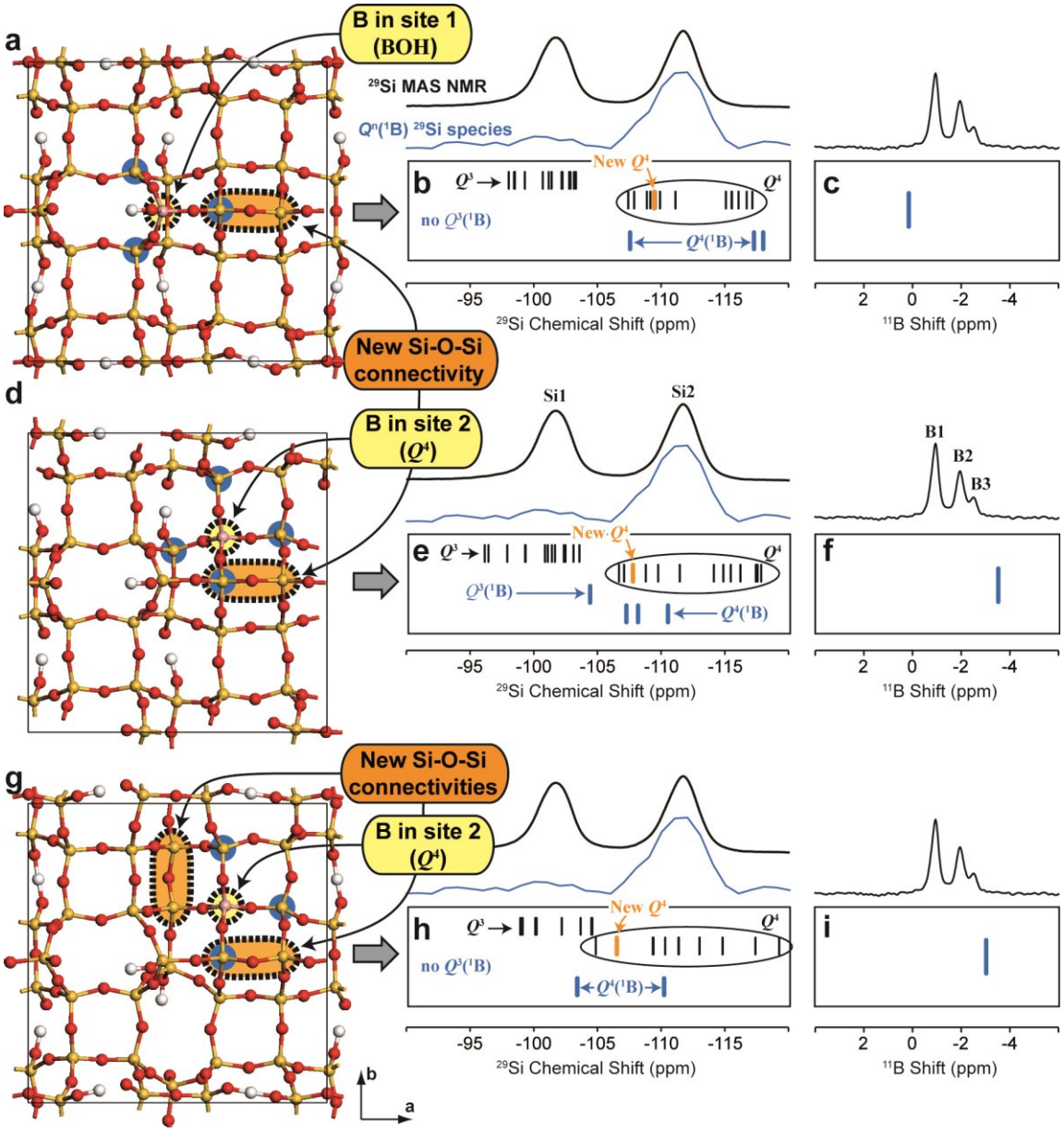

Figure 7. DFT-optimized structural models of $C_{16}H_{33}\mathbf{Me_3}N^+$-directed layered borosilicates viewed from the c-axis, where ^{11}B atoms are manually inserted into ^{29}Si site (a) Si 1 or (d, g) Si2. For each structural model, 8 ^{1}H atoms per unit cell and other homogeneously distributed positive charges are included for charge compensation. Specifically, ^{11}B incorporation induces framework condensations between nearby Q^3 ^{29}Si sites to form (a, d) one or (g) two new ^{29}Si-O-^{29}Si site connectivities. Calculated isotropic chemical shifts for distinct ^{29}Si and ^{11}B species in the models (a), (d), and (g) are shown in plots (b, e, h) and (c, f, i), respectively, where the ^{29}Si chemical shifts in blue reveal the ^{29}Si species connected to one ^{11}B atom only. The calculated ^{29}Si chemical shifts in orange refer to newly formed Q^4 ^{29}Si species via framework condensations. Experimental ^{29}Si and ^{11}B MAS NMR spectra are shown along the top horizontal axis accordingly for reference. [Courtesy: Dr. Sylvian Cadars]

Similar calculations were conducted on various models that describe local structures of the ^{11}B site B2 (*i.e.* one ^{11}B atom incorporates into one Q^4 ^{29}Si site), as well as its connectivities with other Q^4 ^{29}Si sites. Such local ^{29}Si and ^{11}B environments may be obtained by generating two additional framework condensations that involve the two Q^3 ^{29}Si sites adjacent to the ^{11}B atom (or the ^{11}B atom and an adjacent Q^3 ^{29}Si atom if the ^{11}B is incorporated in a Q^3 ^{29}Si site, thereby changed to a Q^4 ^{29}Si), which become Q^4(1B) ^{29}Si sites in the optimized structure. This procedure is illustrated in Figure A8 for the model of chemical composition $(BSi_{31}O_{70}H_6)^{7-}$ (Figure 7g). This and other models that describe the same type of ^{29}Si and ^{11}B environments but with different initial locations of ^{11}B atoms and charge-balance strategies (see Table A5) lead to ^{11}B chemical shifts between -3 and -4 ppm, which is not unreasonably far from the experimental ^{11}B shift of ^{11}B site B2 (-1.9 ppm). As a result, these calculations seem to confirm that the framework structure rearranges locally upon ^{11}B incorporation into the $C_{16}H_{33}$**Me$_3$**N^+-directed layered borosilicate material during the framework crystallization. Such ^{11}B incorporation appears to promote or to be facilitated by the condensation of originally incompletely-condensed ^{29}Si atoms around the incorporated ^{11}B site.

The situation is remarkably different in the case of $C_{16}H_{33}$**Me$_2$Et**N^+-directed borosilicates, where ^{11}B atoms seem to be preferentially incorporated into only one type of the five distinct tetrahedral ^{29}Si sites in the framework, most likely as a hydroxylated Q^3 ^{11}B moiety. This was manifested by the 1D ^{11}B NMR spectrum (Figure 2d) that shows only one type of four-coordinate ^{11}B environment, which could be confirmed by probing the connectivities and proximities between ^{11}B and ^{29}Si moieties. ^{11}B-O-^{29}Si site connectivities were probed on $C_{16}H_{33}$**Me$_2$Et**N^+-directed layered borosilicates with *ca.* 99% ^{29}Si

enrichment using the 2D $^{2}J(^{11}B\text{-}O\text{-}^{29}Si)$-mediated HMQC $^{11}B\{^{29}Si\}$ NMR spectroscopy (shown in red, Figure 8a). The 1D ^{11}B echo-MAS and $^{29}Si\{^{1}H\}$ CP-MAS spectra of this ^{29}Si-enriched material are shown along the top horizontal and the right vertical axis of the 2D $^{11}B\{^{29}Si\}$ spectra, both of which are similar to the corresponding $C_{16}H_{33}\mathbf{Me_2Et}N^{+}$-directed layered borosilicates with natural abundance of ^{29}Si (Figure 2c,d), except for the presence of an impurity (marked with a star in the 1D ^{11}B echo-MAS spectrum). The 2D *J*-mediated $^{11}B\{^{29}Si\}$ NMR spectrum shows that three ^{29}Si signals at -98.4, -100.5 and -113.8 ppm are correlated with one ^{11}B signal at -0.4 ppm. As mentioned above, the small broadening of this ^{11}B signal suggests highly uniform ^{11}B environments. Consequently, the three types of $^{29}Si\text{-}O\text{-}^{11}B$ correlations indicate that every incorporated ^{11}B atom is connected to three distinct ^{29}Si atoms (Q^3(1B) or Q^4(1B)) via bridging oxygen atoms. Specifically, two of the three Q^n(1B) ^{29}Si sites revealed in the *J*-mediated $^{11}B\{^{29}Si\}$ correlation NMR spectrum fall within a region of the ^{29}Si spectrum that is compatible with Q^3(1B) signatures, consistent with the connectivities established from the siliceous counterpart, where each Q^3 ^{29}Si site is connected to another Q^3 ^{29}Si site. Such information allows us to confirm that the ^{11}B signal at -0.4 ppm can be attributed to ^{11}B atoms incorporated into one of the two types of Q^3 ^{29}Si sites. Additionally, in stark contrast with the case of the $C_{16}H_{33}\mathbf{Me_3}N^{+}$-directed borosilicate material, the local ^{29}Si structure near ^{11}B sites in the $C_{16}H_{33}\mathbf{Me_2Et}N^{+}$-directed borosilicate does not appear to rearrange during framework crystallization.

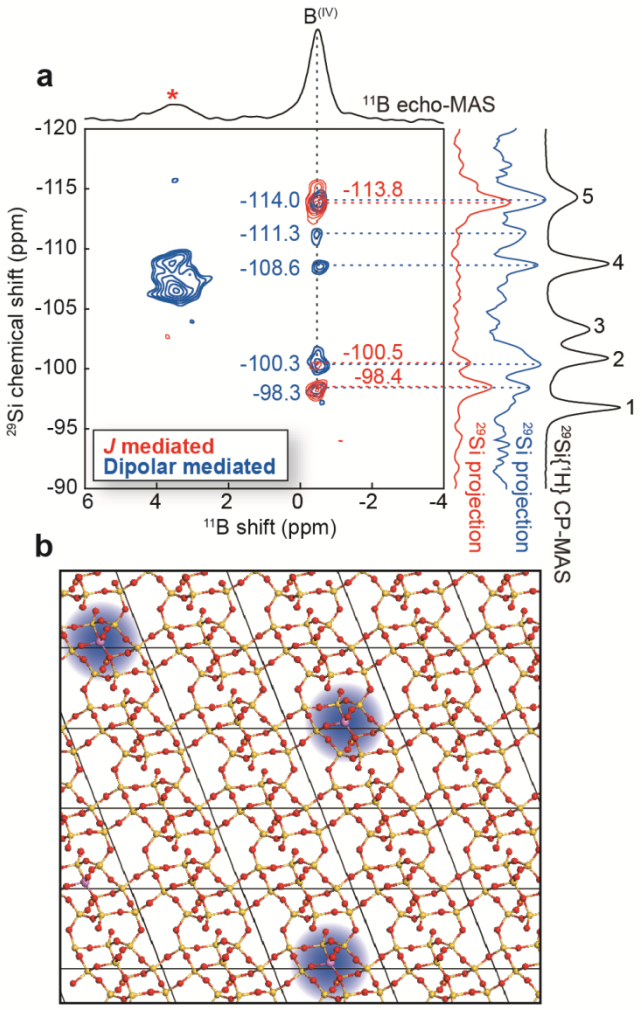

Figure 8. (a) Solid-state 2D dipolar- (in blue) and *J*-mediated (in red) HMQC $^{11}B\{^{29}Si\}$ NMR spectra, acquired at 9.4 T and room temperature, of ^{29}Si-enriched $C_{16}H_{33}$**Me$_2$Et**N^+-directed layered borosilicates (Si/B ~52 expected), which establish spatial proximities and site connectivities between ^{29}Si and ^{11}B species, respectively. The 1D ^{11}B echo-MAS spectrum is shown along the top horizontal axis. The $^{29}Si\{^1H\}$ CP-MAS spectrum (in black) and the ^{29}Si projections, extracted from 2D dipolar- (in blue) and *J*-mediated (in red) $^{11}B\{^{29}Si\}$ NMR spectra that focus on the regions associated with $C_{16}H_{33}$**Me$_2$Et**N^+-directed layered borosilicates (*i.e.*, from 1.0 to -2.0 ppm in the ^{11}B dimension), are all shown along with the right vertical axis. (b) A schematic representation illustrates the ^{11}B atom distributions in $C_{16}H_{33}$**Me$_2$Et**N^+-directed layered borosilicates, where the influences of ^{11}B sites on borosilicate frameworks are highlighted in blue. [Courtesy: Dr. Mounesha Garaga]

While the 2D *J*-mediated (through-bond) $^{11}B\{^{29}Si\}$ NMR analyses provide specific information on the ^{11}B sites that are covalently bonded to the next-nearest-neighbor ^{29}Si sites, ^{29}Si sites in the first coordination shells may be spatially close to ^{11}B sites in the $C_{16}H_{33}\mathbf{Me_2Et}N^+$-directed layered borosilicate framework, which can be revealed via 2D dipolar-mediated $^{11}B\{^{29}Si\}$ NMR experiments. Figure 8a shows a 2D dipolar-mediated HQMC $^{11}B\{^{29}Si\}$ NMR spectrum (in blue) of the *ca.* 99% ^{29}Si-enriched $C_{16}H_{33}\mathbf{Me_2Et}N^+$-directed layered borosilicate. Intensity correlations that involve the impurity, identified by the ^{11}B signal at *ca.* 4 ppm in the 1D ^{11}B NMR spectrum, are resolved with this 2D dipolar-mediated $^{11}B\{^{29}Si\}$ NMR technique, but they are distinguishable from the NMR signature of the layered borosilicate. The ^{11}B signal at *ca.* -0.4 ppm exhibits intensity correlations with the ^{29}Si signals at -98.4, -100.5 and -113.8 ppm in the 2D dipolar-mediated $^{11}B\{^{29}Si\}$ NMR spectrum (in blue, Figure 8a), consistent with the 2D *J*-mediated $^{11}B\{^{29}Si\}$ NMR spectrum (in red, Figure 8a), because of the short distances (*ca*. 3 Å) between the ^{29}Si-O-^{11}B site pairs. More importantly, additional correlated intensities are shown between the ^{11}B signal at -0.4 ppm and the ^{29}Si signals at -111.3 and -108.6 ppm, as well as a shoulder at *ca.* -101.0 ppm, all of which correspond to ^{29}Si sites that are molecularly proximate to (*ca*. 5 Å or less) yet not connected with the ^{11}B sites. Interestingly, the ^{29}Si signals at -108.6 and -101.0 ppm are very close to the ^{29}Si signals at -108.7 and -100.7 ppm, associated with ^{29}Si sites Si4 and Si2, respectively. Both ^{29}Si sites Si4 and Si2 in the $C_{16}H_{33}\mathbf{Me_2Et}N^+$-directed layered borosilicate exhibit similar ^{29}Si signals to the ^{29}Si sites Si4 and Si2 (-109.1 and -101.0 ppm) in the closely related $C_{16}H_{33}\mathbf{Me_2Et}N^+$-directed siliceous framework,[41] suggesting that the presence of ^{11}B atoms subtly modify their nearby ^{29}Si environments. Similarly, another correlation that involves the ^{29}Si signal at -111.3 ppm could be attributed

to ^{29}Si site 5, whose ^{29}Si chemical shift is slightly displaced with respect to the main one at -114.7 ppm due to its proximity to the ^{11}B sites. These 2D NMR analyses indicate that the ^{11}B incorporation would induce subtle influences on the ^{29}Si sites neighboring ^{11}B atoms, which are primarily restricted to the first coordination shell.

A direct consequence of such minor framework distortions is a high degree of local molecular order near the ^{11}B sites, as revealed by the narrow linewidths in both ^{11}B and ^{29}Si dimensions of the 2D ^{11}B{^{29}Si} NMR spectra of the $C_{16}H_{33}$**Me$_2$Et**N^+-directed borosilicates (Figure 8a). Specifically, the narrow linewidths of the ^{11}B signals (FWHM: 0.3 ppm) and the ^{29}Si signals (FWHM: 1.0 ~ 1.6 ppm) all reveal well-defined local ^{11}B and ^{29}Si environments, respectively, rather than distributions of local bonding geometries. By comparison, typical linewidths of ^{11}B and ^{29}Si signals observed in borosilicate glasses are of the order of 4 ppm for four-coordinate ^{11}B species and 10 ppm for Q^3 or Q^4 ^{29}Si environments.[83] The relatively narrow linewidths, as well as 2D ^{11}B{^{29}Si} NMR analyses clearly indicate that all ^{11}B atoms are preferentially inserted into one type of Q^3 ^{29}Si sites (*i.e.*, Si1 or Si2) in the $C_{16}H_{33}$**Me$_2$Et**N^+-directed borosilicate material. Furthermore, ^{11}B atoms appear to incorporate into one specific ^{29}Si site only, which leads to very similar and localized influences on their local ^{29}Si environments in this material. Additionally, these ^{11}B sites can be considered to be well isolated from each other, due to the Si/B molar ratio on the order of 50. Therefore, a substantial fraction of framework sites remain occupied by ^{29}Si atoms, which suggests that ^{11}B atoms appear to be distributed in a random manner rather than periodically (*e.g.*, every unit cell) in the $C_{16}H_{33}$**Me$_2$Et**N^+-directed borosilicate framework. The ^{11}B site distributions are illustrated in Figure 8b using the hypothetical

structure, where incorporated ^{11}B atoms exhibit poor long-range order and subtle influences on borosilicate frameworks.

The case of the $C_{16}H_{33}$**Me$_2$Et**N^+-directed borosilicate is significantly different from the case of borosilicate zeolite MCM-70 (crystal code MVY[84]) that contains four distinct crystallographic tetrahedral ^{29}Si sites, three of which are exclusively occupied by ^{29}Si atoms, whereas the fourth is only occupied by ^{11}B atoms, as established by X-ray diffraction analyses.[27] To our knowledge, there is no evidence that a siliceous MCM-70 structure can be formed, where this crystallographic site would be occupied (even partially) by ^{29}Si atoms in the average long-range structure. The situation is completely different here, because the $C_{16}H_{33}$**Me$_2$Et**N^+-directed borosilicate lacks the 3D (and even long-range 2D) periodicity, while possessing molecularly ordered. This is also because the ^{11}B loadings are small enough so that ^{11}B sites can be considered to be independent of each other. Based on the understanding of local order and disorder near ^{11}B sites in the $C_{16}H_{33}$**Me$_2$Et**N^+-directed borosilicate, we anticipate that corresponding physico-chemical properties of these ^{11}B sites should be the same.

The understanding on the ^{11}B incorporation into one specific type of Q^3 ^{29}Si sites in the $C_{16}H_{33}$**Me$_2$Et**N^+-directed borosilicate framework is of crucial importance for rational zeolite synthesis with controlled heteroatom siting, which has received considerable attention for many years. Such preferential ^{11}B incorporation is supported the DFT analyses, as summarized in Figure A6a that shows comparison of experimental and calculated NMR data, where Q^n(1B) ^{29}Si sites are represented with red squares. Figure A6c shows the same comparison between for a similar model, with ^{11}B also incorporated in Q^3 ^{29}Si site Si1, but obtained with structure # 3 (instead of 2, see ref [45]) as the reference silicate framework.

Again, the agreement between experimental and calculated shifts for Q^n(1B) ^{29}Si sites is reasonably good. By comparison, the agreement between experiment and calculations is considerably worse (especially for ^{29}Si sites Si1 and Si4) for the models where the ^{11}B is in substitution of Q^3 ^{29}Si site Si2, as shown in Figure A6b,d. These results thus seem to establish that the preferential substitution site of the ^{11}B atoms in the $C_{16}H_{33}$**Me$_2$Et**N^+-directed layered borosilicate is Q^3 ^{29}Si site Si1.

When ^{11}B atoms are incorporated into the two surfactant-directed silicate frameworks with very similar lamellar morphologies, prepared under identical synthesis conditions with very similar structure-directing alkylammonium molecules, profound differences appear between them. The presence of ^{11}B atoms is expected to create certain amount of stress in the silicate framework, due to its different size as compared with ^{29}Si atoms, which must relax (through variations in the bonding geometry) to attain a stable conformation. This mechanism particularly depends on the availability of sufficient degrees of freedom, and the subtle differences between the molecular structures of the layered frameworks in the corresponding reference materials are important in this respect. For example, the $C_{16}H_{33}$**Me$_2$Et**N^+-directed silicates are slightly more condensed than the $C_{16}H_{33}$**Me$_3$**N^+-directed silicates, with 2/5 of Q^3 ^{29}Si sites as compared to 1/2 for the other. This difference somehow contributes to imposing that the ^{11}B atoms are located in a single T site that can accommodate such structural distortions more easily than others. The slightly more condensed $C_{16}H_{33}$**Me$_2$Et**N^+-directed frameworks, in particular, do not seem to allow for (or to necessitate) the additional cross-linking that occurs in some cases for the other borosilicate material. Another possible reason for such differences, which may also have impacts on the available degrees of freedom of the frameworks, is the different ways, in

which the linear chains formed by the Q^3 sites and their mutually H-bonded non-bridging oxygen atoms are arranged in the two different framework structures. These chains are aligned in the same direction above and below the plane in the $C_{16}H_{33}$**Me$_2$Et**N^+-directed materials, whereas the chains of Q^3 sites, located on the top of a given layer, are perpendicular to the ones located at the bottom in the $C_{16}H_{33}$**Me$_3$**N^+-directed materials. Possibly as a result of this difference, the lamellar structure of the $C_{16}H_{33}$**Me$_2$Et**N^+-directed material is unlikely to deform such as to accommodate for new ^{29}Si-O-^{29}Si connectivities which appear to facilitate the incorporation of ^{11}B atoms into the framework of the $C_{16}H_{33}$**Me$_3$**N^+-directed materials.

It should be possible to relate these considerations to the differences in the amount of ^{11}B that can be incorporated in the two materials in identical synthesis conditions. All of our syntheses lead to a final amount of ^{11}B (Si/B ~ *ca.* 50 to 150) that is considerably lower than used for the synthesis (Si/B = 2.5). And yet this final amount of ^{11}B is generally higher for the $C_{16}H_{33}$**Me$_2$Et**N^+-directed materials, where the Si/B substitution can take place in a Q^3 ^{29}Si site (a situation seemingly more favorable than in a Q^4 ^{29}Si site) without profound rearrangements of the framework. For the $C_{16}H_{33}$**Me$_3$**N^+-directed materials, one among the three distinct types of ^{11}B sites that could be distinguished is still a Q^3 ^{29}Si site, but we showed that its local ^{29}Si environment is profoundly modified as compared to the Q^3 ^{29}Si sites without covalently bonded to ^{11}B atoms. The structural rearrangements that promote (or are driven by) the B/Si substitution probably represent a relatively high energy barrier that makes this situation kinetically unfavorable.

Concerning the astounding selectivity of ^{11}B incorporation into a single type of Q^3 ^{29}Si sites in the $C_{16}H_{33}$**Me$_2$Et**N^+-directed borosilicates, one can think of reasons related to

differences in the local structure around these sites. In particular, if we make the hypothesis that ^{11}B-connected ^{29}Si sites stay more or less at the same position as the ones in siliceous frameworks, the smaller size of ^{11}B atoms then has to be compensated by more open ^{29}Si-O-^{11}B angles as compared to the corresponding ^{29}Si-O-^{29}Si angles in the original structure. It is reasonable to believe in this context that ^{29}Si sites associated with smaller ^{29}Si-O-^{29}Si angles could be more easily substituted with by ^{11}B atoms without imposing major constraints on the structure. The strong limitations, which appear to exist in the amount of ^{11}B that can be incorporated into the $C_{16}H_{33}$**Me$_2$Et**N^+-directed silicates, indicate a high energy barrier during the synthesis (kinetically-limited process) and/or unfavorable energetics of the corresponding local environment (thermodynamically-limited process). In either case, conditions just slightly less favorable, due to a slightly higher energetic barrier or a slightly lower stability, might easily lead to a change from small amounts of ^{11}B incorporation into one type of ^{29}Si site to no ^{11}B incorporation at all on another. In the $C_{16}H_{33}$**Me$_2$Et**N^+-directed borosilicates, ^{29}Si site Si1 turns out to be the only ^{11}B incorporation site under the conditions used here only because (i) of a very small difference in energetics that are below the level of confidence of DFT calculations (differences of the order of 0.1 eV between equivalent models with ^{11}B in ^{29}Si site Si1 or Si2), or (ii) of a slight difference in the accessibility between the two ^{29}Si sites (although there is no obvious reason for this).

2.5 Conclusions

We have established the ^{11}B site distributions in the two chemically and structurally related $C_{16}H_{33}$**Me$_3$**N^+- and $C_{16}H_{33}$**Me$_2$Et**N^+-directed layered borosilicates using advanced

solid-state NMR techniques in conjunction with DFT calculations. The results and analyses reveal that ^{11}B atoms are incorporated into all types of framework sites in the $C_{16}H_{33}\mathbf{Me_3}N^+$-directed borosilicates, and they simultaneously induce structural rearrangements of ^{29}Si sites nearby ^{11}B species. In stark contract with the case of $C_{16}H_{33}\mathbf{Me_3}N^+$-directed borosilicates, ^{11}B atoms are shown to be selectively inserted into one type of Q^3 ^{29}Si sites in $C_{16}H_{33}\mathbf{Me_2Et}N^+$-directed borosilicates. Furthermore, we establish that the distorted ^{29}Si environments nearby ^{11}B sites in $C_{16}H_{33}\mathbf{Me_2Et}N^+$-directed borosilicates appear identical throughout the whole framework, resulting into a degree of molecular order that may be comparable to crystalline structures yet lacks long-range periodicity. Consequently, physicochemical properties (reactivities in particular) of such ^{11}B sites in $C_{16}H_{33}\mathbf{Me_2Et}N^+$-directed borosilicates are hypothesized to demonstrate a high degree of similarly. More importantly, the molecular-level insights into ^{11}B site distributions learned from the two surfactant-directed borosilicates are expected to guide rational synthesis of borosilicate zeolite catalysts with control ^{11}B site distributions.

2.6 References

1. Tanabe, K. & Holderich, W. F. Industrial application of solid acid–base catalysts. *Appl. Catal. A Gen.* **181,** 399–434 (1999).

2. Boria, M. & Dutta, P. K. Storgae of light energy by photoelectron transfer across a sensitized zeolite-solution interface. *Nature* **362,** 43–45 (1993).

3. Iwamoto, M. *et al.* Removal of Nitrogen Monoxide through a Novel Catalytk Process. 2. Infrared Study on Surface Reaction of Nltrogen Monoxide Adsorbed on Copper Ion-Exchanged ZSM-5. *J. Phys. Chem.* **96,** 9360–9366 (1992).

4. Barthomeuf, D. Basic Zeolites: Characterization and Uses in Adsorption and Catalysis. *Catal. Rev. - Sci. Eng.* **38,** 521–612 (1996).

5. Kuznicki, S. M. *et al.* A titanosilicate molecular sieve with adjustable pores for size-selective adsorption of molecules. *Nature* **412,** 720–4 (2001).

6. Joo, S. H. *et al.* Ordered nanoporous arrays of carbon supporting high dispersions of platinum nanoparticles. *Nature* **412,** 169–72 (2001).

7. Choi, J. *et al.* Grain boundary defect elimination in a zeolite membrane by rapid thermal processing. *Science (80-.).* **325,** 590–593 (2009).

8. Varoon, K. *et al.* Dispersible Exfoliated Zeolite Nanosheets and Their Application as a Selective Membrane. *Science (80-.).* **334,** 72–75 (2011).

9. Bermejo-Deval, R. *et al.* Metalloenzyme-like catalyzed isomerizations of sugars by Lewis acid zeolites. *Proc. Natl. Acad. Sci. U. S. A.* **109,** 9727–32 (2012).

10. Jae, J. *et al.* Investigation into the shape selectivity of zeolite catalysts for biomass conversion. *J. Catal.* **279,** 257–268 (2011).

11. Willhammar, T. *et al.* Structure and catalytic properties of the most complex intergrown zeolite ITQ-39 determined by electron crystallography. *Nat. Chem.* **4,** 188–94 (2012).

12. Dědeček, J., Sobalík, Z. & Wichterlová, B. Siting and Distribution of Framework Aluminium Atoms in Silicon-Rich Zeolites and Impact on Catalysis. *Catal. Rev. - Sci. Eng.* **54,** 135–223 (2012).

13. Román-Leshkov, Y., Moliner, M. & Davis, M. E. Impact of Controlling the Site Distribution of Al Atoms on Catalytic Properties in Ferrierite-Type Zeolites †. *J. Phys. Chem. C* **115,** 1096–1102 (2011).

14. Pinar, A. B., Márquez-Álvarez, C., Grande-Casas, M. & Pérez-Pariente, J. Template-controlled acidity and catalytic activity of ferrierite crystals. *J. Catal.* **263,** 258–265 (2009).

15. Hijar, C. A. *et al.* The Siting of Ti in TS-1 Is Non-Random. Powder Neutron Diffraction Studies and Theoretical Calculations of TS-1 and FeS-1. *J. Phys. Chem. B* **104,** 12157–12164 (2000).

16. Lamberti, C. *et al.* Ti location in the MFI framework of Ti-Silicalite-1: a neutron powder diffraction study. *J. Am. Chem. Soc.* **123,** 2204–2212 (2001).

17. Henry, P. F., Weller, M. T. & Wilson, C. C. Structural Investigation of TS-1: Determination of the True Nonrandom Titanium Framework Substitution and Silicon Vacancy Distribution from Powder Neutron Diffraction Studies Using Isotopes. *J. Phys. Chem. B* **105,** 7452–7458 (2001).

18. Milanesio, M. *et al.* Iron Location in Fe-Silicalites by Synchrotron Radiation Single Crystal X-ray Diffraction. *J. Phys. Chem. B* **104,** 9951–9953 (2000).

19. Palin, L. *et al.* Single-Crystal Synchrotron Radiation X-ray Diffraction Study of B and Ga Silicalites Compared to a Purely Siliceous MFI : A Discussion of the Heteroatom Distribution. *J. Phys. Chem. B* **107,** 4034–4042 (2003).

20. Van Bokhoven, J. A. *et al.* Determining the aluminium occupancy on the active T-sites in zeolites using X-ray standing waves. *Nat. Mater.* **7,** 551–555 (2008).

21. Fyfe, C. a, Bretherton, J. L. & Lam, L. Y. Solid-state NMR detection, characterization, and quantification of the multiple aluminum environments in US-Y catalysts by (27)Al MAS and MQMAS experiments at very high field. *J. Am. Chem. Soc.* **123,** 5285–5291 (2001).

22. Sklenak, S. *et al.* Aluminum siting in silicon-rich zeolite frameworks: A combined high-resolution Al-27 NMR spectroscopy and quantum mechanics/molecular mechanics study of ZSM-5. *Angew. Chem. Int. Ed. Engl.* **46,** 7286–9 (2007).

23. Han, O. H., Kim, C.-S. & Hong, S. B. Direct evidence for the nonrandom nature of Al substitution in zeolite ZSM-5: an investigation by (27)Al MAS and MQ MAS NMR. *Angew. Chem. Int. Ed. Engl.* **41,** 469–72 (2002).

24. Dědeček, J., Čapek, L., Sazama, P., Sobalík, Z. & Wichterlová, B. Control of metal ion species in zeolites by distribution of aluminium in the framework: From structural analysis to performance under real conditions of SCR-NOx and NO, N2O decomposition. *Appl. Catal. A Gen.* **391,** 244–253 (2011).

25. Dedecek, J., Balgova, V., Pashkova, V., Klein, P. & Wichterlová, B. Synthesis of ZSM-5 Zeolites with Defined Distribution of Al Atoms in the Framework and Multinuclear MAS NMR Analysis of the Control of Al Distribution. *Chem. Mater.* **24,** 3231–3239 (2012).

26. Sazama, P. *et al.* Effect of aluminium distribution in the framework of ZSM-5 on hydrocarbon transformation. Cracking of 1-butene. *J. Catal.* **254,** 180–189 (2008).

27. Xie, D. *et al.* Optimized Synthesis and Structural Characterization of the Borosilicate MCM-70. *J. Phys. Chem. C* **113,** 9845–9850 (2009).

28. Mackenzie, K. J. D. & Smith, M. E. *Multinuclear Solid-State Nuclear Magnetic Resonance of Inorganic Materials*. (Elsevier, 2002).

29. Engelhardt, G. & Michel, D. *High-Resolution Solid-State NMR of Silicates and Zeolites*. (Wiley, 1987).

30. Baerlocher, C. *et al.* Ordered silicon vacancies in the framework structure of the zeolite catalyst SSZ-74. *Nat. Mater.* **7,** 631–635 (2008).

31. Jeong, H.-K., Nair, S., Vogt, T., Dickinson, L. C. & Tsapatsis, M. A highly crystalline layered silicate with three-dimensionally microporous layers. *Nat. Mater.* **2,** 53–8 (2003).

32. Ikeda, T., Akiyama, Y., Oumi, Y., Kawai, A. & Mizukami, F. The topotactic conversion of a novel layered silicate into a new framework zeolite. *Angew. Chem. Int. Ed. Engl.* **43,** 4892–6 (2004).

33. Ikeda, T., Kayamori, S. & Mizukami, F. Synthesis and crystal structure of layered silicate PLS-3 and PLS-4 as a topotactic zeolite precursor. *J. Mater. Chem.* **19,** 5518 (2009).

34. Palin, L., Croce, G., Viterbo, D. & Milanesio, M. Monitoring the Formation of H-MCM-22 by a Combined XRPD and Computational Study of the Decomposition of the Structure Directing Agent. *Chem. Mater.* **23,** 4900–4909 (2011).

35. Yilmaz, B. *et al.* Al-RUB-41: a shape-selective zeolite catalyst from a layered silicate. *Chem. Commun.* **47,** 1812–1814 (2011).

36. Li, Z., Marler, B. & Gies, H. A New Layered Silicate with Structural Motives of Silicate Zeolites : Synthesis , Crystals Structure , and Properties. *Chem. Mater.* **20,** 1896–1901 (2008).

37. Mochizuki, D., Shimojima, A., Imagawa, T. & Kuroda, K. Molecular manipulation of two- and three-dimensional silica nanostructures by alkoxysilylation of a layered silicate octosilicate and subsequent hydrolysis of alkoxy groups. *J. Am. Chem. Soc.* **127,** 7183–91 (2005).

38. Moteki, T., Chaikittisilp, W., Shimojima, A. & Okubo, T. Silica sodalite without occluded organic matters by topotactic conversion of lamellar precursor. *J. Am. Chem. Soc.* **130,** 15780–1 (2008).

39. Marler, B. & Gies, H. Hydrous layer silicates as precursors for zeolites obtained through topotactic condensation: a review. *Eur. J. Mineral.* **24,** 405–428 (2012).

40. Christiansen, S. C. *et al.* Molecularly ordered inorganic frameworks in layered silicate surfactant mesophases. *J. Am. Chem. Soc.* **123,** 4519–4529 (2001).

41. Hedin, N. *et al.* Structure of a surfactant-templated silicate framework in the absence of 3d crystallinity. *J. Am. Chem. Soc.* **126,** 9425–32 (2004).

42. Choi, M. *et al.* Stable single-unit-cell nanosheets of zeolite MFI as active and long-lived catalysts. *Nature* **461,** 246–9 (2009).

43. Na, K. *et al.* Directing zeolite structures into hierarchically nanoporous architectures. *Science* **333,** 328–32 (2011).

44. Zhang, X. *et al.* Synthesis of self-pillared zeolite nanosheets by repetitive branching. *Science (80-.).* **336,** 1684–1687 (2012).

45. Brouwer, D. H. *et al.* A general protocol for determining the structures of molecularly ordered but noncrystalline silicate frameworks. *J. Am. Chem. Soc.* **135,** 5641–5655 (2013).

46. Xia, Y. & Mokaya, R. Molecularly ordered layered aluminosilicate-surfactant mesophases and their conversion to hydrothermally stable mesoporous aluminosilicates. *Microporous Mesoporous Mater.* **94,** 295–303 (2006).

47. Xia, Y. & Mokaya, R. Crystalline-like molecularly ordered mesoporous aluminosilicates derived from aluminosilica-surfactant mesophases via benign template removal. *J. Phys. Chem. B* **110,** 9122–31 (2006).

48. Millini, R., Perego, G. & Bellussi, G. Synthesis and characterization of boron-containing molecular sieves. **9,** 13–34 (1999).

49. Coudurier, G. *et al.* Properties of boron-substituted ZSM-5 and ZSM-11 zeolites. *J. Catal.* **108,** 1–14 (1987).

50. Burton, A. & Elomari, S. SSZ-60: a new large-pore zeolite related to ZSM-23. *Chem. Commun. (Camb).* 2618–9 (2004). doi:10.1039/b410010g

51. Burton, A. *et al.* SSZ-53 and SSZ-59: two novel extra-large pore zeolites. *Chemistry* **9,** 5737–5748 (2003).

52. Burton, A. *et al.* The synthesis, characterization, and structure solution of SSZ-58: a novel two-dimensional 10-ring pore zeolite with previously unseen double 5-ring subunits. *J. Am. Chem. Soc.* **125,** 1633–1642 (2003).

53. Elomari, S., Burton, A., Medrud, R. C. & Grosse-Kunstleve, R. The synthesis, characterization, and structure solution of SSZ-56: An extreme example of isomer specificity in the structure direction of zeolites. *Microporous Mesoporous Mater.* **118,** 325–333 (2009).

54. Elomari, S., Burton, A. W., Ong, K., Pradhan, A. R. & Chan, I. Y. Synthesis and Structure Solution of Zeolite SSZ-65. *Chem. Mater.* **19,** 5485–5492 (2007).

55. Li, Y. & Zou, X. SU-16: a three-dimensional open-framework borogermanate with a novel zeolite topology. *Angew. Chem. Int. Ed. Engl.* **44,** 2012–2015 (2005).

56. Wagner, P. *et al.* Electron Diffraction Structure Solution of a Nanocrystalline Zeolite at Atomic Resolution. *J. Phys. Chem. B* **103,** 8245–8250 (1999).

57. Vortmann, S., Marler, B., Gies, H. & Daniels, P. Synthesis and crystal structure of the new borosilicate zeolite RUB-13. *Microporous Mater.* **4,** 111–121 (1995).

58. Lobo, R. F. & Davis, M. E. CIT-1: A New Molecular Sieve with Intersecting Pores Bounded by 10- and 12-Rings. *J. Am. Chem. Soc.* **117,** 3766–3779 (1995).

59. Van Nordstrand, R. A., Santilli, D. S. & Zones, S. I. *Synthesis of Microporous Materials, Vol 1*. 932 (Springer-Verlag New York, LLC, 1992).

60. Chen, C. Y. & Zones, S. I. From Borosilicate to Gallo- and Aluminosilicate Zeolites : New Methods for Lattice Substitution via Post-Synthetic Treatment. *Stud. Surf. Sci. Catal.* **135,** 211 (2001).

61. *Zeolites and Catalysis: Synthesis Reactions and Applications*. (Wiley-VCH, 2010). doi:10.1002/9783527630295

62. Chen, C.-Y. & Zones, S. I. Method for heteroatom lattice substitution in large and extra-large pore borosilicate zeolites. (2002).

63. Zones, S. I. *et al.* Studies of Aluminum Reinsertion into Borosilicate Zeolites with Intersecting Channels of 10- and 12-Ring Channel Systems. *J. Am. Chem. Soc.* **57,** 1462−1471 (2014).

64. Iuga, D. & Kentgens, A. P. . Influencing the satellite transitions of half-integer quadrupolar nuclei for the enhancement of magic angle spinning spectra. *J. Magn. Reson.* **158,** 65–72 (2002).

65. Fung, B. M., Khitrin, a K. & Ermolaev, K. An improved broadband decoupling sequence for liquid crystals and solids. *J. Magn. Reson.* **142,** 97–101 (2000).

66. Hediger, S., Meier, B. H., Kurur, N. D., Bodenhausen, G. & Ernst, R. R. NMR cross polarization by adiabatic passage through the. *Chem. Phys. Lett.* **223,** 283–288 (1994).

67. Carravetta, M., Eden, M., Zhao, X., Brinkmann, A. & Levitt, M. H. Symmetry principles for the design of radiofrequency pulse sequences in the nuclear magnetic resonance of rotating solids. *Chem. Phys. Lett.* **321,** 205–215 (2000).

68. Brinkmann, A. & Levitt, M. H. Symmetry principles in the nuclear magnetic resonance of spinning solids: Heteronuclear recoupling by generalized Hartmann–Hahn sequences. *J. Chem. Phys.* **115,** 357 (2001).

69. Brinkmann, A. & Kentgens, A. P. M. Proton-Selective 17O-1H Distance Measurements in Fast Magic-Angle-Spinning Solid-State NMR Spectroscopy for the

Determination of Hydrogen Bond Lengths. *J. Am. Chem. Soc.* **128,** 14758–14759 (2006).

70. Hu, B., Trébosc, J. & Amoureux, J. P. Comparison of several hetero-nuclear dipolar recoupling NMR methods to be used in MAS HMQC/HSQC. *J. Magn. Reson.* **192,** 112–22 (2008).

71. Lesage, A., Sakellariou, D., Steuernagel, S. & Emsley, L. Carbon - Proton Chemical Shift Correlation in Solid-State NMR by Through-Bond Multiple-Quantum Spectroscopy. *J. Am. Chem. Soc.* **120,** 13194–13201 (1998).

72. Clark, S. J. *et al.* First Principles Methods using CASTEP. *ZEITSCHRIFT FUR Krist.* **220,** 567–570 (2005).

73. Perdew, J. P., Burke, K. & Ernzerhof, M. Generalized Gradient Approximation Made Simple. *Phys. Rev. Lett.* **77,** 3865–3868 (1996).

74. Vanderbilt, D. SOFT SELF-CONSISTENT PSEUDOPOTENTIALS IN A GENERALIZED EIGENVALUE FORMALISM. *Phys. Rev. B* **41,** 7892–7895 (1990).

75. Monkhorst, H. J. & Pack, J. D. SPECIAL POINTS FOR BRILLOUIN-ZONE INTEGRATIONS. *Phys. Rev. B* **13,** 5188–5192 (1976).

76. Pickard, C. & Mauri, F. All-electron magnetic response with pseudopotentials: NMR chemical shifts. *Phys. Rev. B* **63,** 245101 (2001).

77. De Paëpe, G. *et al.* Transverse dephasing optimized solid-state NMR spectroscopy. *J. Am. Chem. Soc.* **125,** 13938–9 (2003).

78. De Paëpe, G., Lesage, A., Steuernagel, S. & Emsley, L. Transverse dephasing optimised NMR spectroscopy in solids: natural-abundance 13C correlation spectra. *Chemphyschem* **5,** 869–75 (2004).

79. Vortmann, S., Rius, J., Siegmann, S. & Gies, H. Ab Initio Structure Solution from X-ray Powder Data at Moderate Resolution : Crystal Structure of a Microporous Layer Silicate. *J. Phys. Chem. A* **101,** 1292–1297 (1997).

80. Wolf, I., Gies, H. & Fyfe, C. A. Ordering of Silicate Layers by Hydrogen-Bonding Networks: Solid State NMR Investigation of the Perfect Three-Dimensional Registration in the Layer Silicate RUB-18. *J. Phys. Chem. B* **103,** 5933–5938 (1999).

81. Tsunoji, N., Ikeda, T., Ide, Y., Sadakane, M. & Sano, T. Synthesis and characteristics of novel layered silicates HUS-2 and HUS-3 derived from a SiO2–choline hydroxide–NaOH–H2O system. *J. Mater. Chem.* **22,** 13682 (2012).

82. Cadars, S. *et al.* Dynamics and Disorder in Surfactant-Templated Silicate Layers Studied by Solid-State NMR Dephasing Times and Correlated Line Shapes. *J. Phys. Chem. C* **112,** 9145–9154 (2008).

83. Du, L.-S. & Stebbins, J. F. Solid-state NMR study of metastable immiscibility in alkali borosilicate glasses. *J. Non. Cryst. Solids* **315,** 239–255 (2003).

84. http://www.iza-structure.org/databases/.

Chapter 3: Aluminum Heteroatom Distributions in Surfactant-Directed Aluminosilicates

3.1 Abstract

Aluminum site distributions are shown to be very similar in two closely related aluminosilicate frameworks synthesized using subtly different alkylammonium surfactant species. Multi-dimensional solid-state ^{1}H, ^{27}Al, and ^{29}Si nuclear magnetic resonance (NMR) spectroscopy identifies molecular interactions involving proton moieties of surfactants, as well as aluminum and silicon sites in surfactant-directed aluminosilicate frameworks. Notably, two-dimensional (2D) *J*-mediated (through-bond) $^{27}Al\{^{29}Si\}$ NMR analyses yield insights into aluminum sites that are covalently bonded to silicon sites through bridging oxygen atoms. The identified ^{27}Al-O-^{29}Si site pairs together with framework structures permit determination of aluminum site distributions in the aluminosilicate frameworks synthesized by $C_{16}H_{33}N^{+}Me_3$ and $C_{16}H_{33}N^{+}Me_2Et$ structure-directing surfactant molecules. While subtle differences of $C_{16}H_{33}N^{+}Me_2Et$ and $C_{16}H_{33}N^{+}Me_3$ surfactants lead to distinct framework structures, they do not appear to significantly influence the locations of aluminum atoms that are shown to be non-selective distributed among all types of sites in both aluminosilicate materials. In addition, 2D *J*-mediated $^{29}Si\{^{29}Si\}$ NMR analyses reveal that presence of aluminum atoms induces cross-linking of their nearby silicon sites. Such experimental observations of non-selective aluminum site distributions and aluminum-induced structural rearrangements are supported by density functional theory (DFT) calculations, which show substantial influences of aluminum atoms on aluminosilicate

frameworks. This combination of NMR spectroscopy and DFT calculations provides molecular insights into order and disorder near aluminum atoms in aluminosilicates, which are expected to aid the fundamental understanding of relationships between framework structures and associated catalytic and adsorption properties of aluminosilicate catalysts.

3.2 Introduction

Zeolites are currently used in chemical reactions,[1–4] ion exchange treatments,[5,6] gas separation membranes,[7–11] and other industrial processes,[12] all of which are governed by pore structures and, more importantly, active sites in relevant zeolite materials. Active sites typically refer to Brønsted acid sites that result from exchangeable protons present to balance negative framework charges near heteroatoms (*e.g.*, aluminum, ^{27}Al) in zeolite structures. Interestingly, various types of heteroatoms indeed impart catalytic activities, hydrophilicity, and other properties to zeolites .[13–16] Consequently, locating or even ideally controlling heteroatom distributions in zeolite frameworks is expected to optimize catalytic performances in zeolite catalysts, because several reports have shown the substantial influences of acid site density and distributions in zeolites on activities and selectivities of zeolite-catalyzed reactions.[17–22] However, precisely altering locations of acid sites in zeolites has still remained elusive. This could be partly attributed to complex chemistry during zeolite crystallization, where many synthesis parameters, such as structure-directing agents (SDAs), inorganic composition, and temperature, contribute together to desired zeolite products in a delicate way.[14,15,23,24] Recently, the distributions of ^{27}Al atoms in zeolites Ferrierite[25–27] and ITQ-7[28] were shown to be altered by SDA species. Similarly, various synthesis factors can influence the ^{27}Al site distributions in zeolites ZSM-5, BEA,

and FER.[17] Despite these investigations of relationships between ^{27}Al heteroatom siting and synthesis compositions, to the best of our knowledge, a generic synthesis protocol to control has not been proposed yet.

In addition , characterization of ^{27}Al site distributions in zeolite frameworks is very challenging, same as other heteroatoms (*e.g.*, boron (B) or ion (Fe)). Diffraction techniques, commonly used to determine long-range order, are unable to distinguish ^{29}Si from ^{27}Al atoms, due to their very similar scattering factors.[29] While substitution of ^{29}Si for ^{27}Al would change local bond lengths and angles, associated differences are generally very subtle, which can be attributed to the fact that bond lengths and angles of a given tetrahedral (T) site are correlated with relative numbers of ^{29}Si and ^{27}Al occupancies. It should be noted that in general, ^{27}Al-incorporated T sites are not exclusively occupied by ^{27}Al atoms only. Few exceptions were reported in ^{27}Al-containing scolecite[30] and ^{11}B-containing MCM-70.[31] These facts increase difficulty for diffraction techniques to approach such challenging questions, some of which were overcome by Dedecek and coworkers. They recently developed analytical methods of identifying Al-O-(Si-O)$_n$-Al sequences in several zeolites (*e.g.*, ZSM-5 and BEA) via UV-vis spectroscopy.[17] In stark contrast with the above characterization techniques, solid-state nuclear magnetic resonance (NMR) spectroscopy is able to probe short-range order of specific NMR-active nuclei, such as ^{29}Si and ^{27}Al.[32–34] It is therefore considered a promising tool that could possibly shed light on heteroatom site distributions in zeolites. For instance, ^{29}Si NMR spectroscopy could distinguish various similar yet subtly distinct four-coordinate ^{29}Si sites, because of slightly different bond lengths (*i.e.*, Si-O) and angles (*i.e.*, Si-O-Si). In addition, ^{29}Si NMR resonances could be influenced by heteroatoms present in the next nearest neighbors of associated ^{29}Si sites.

While the extent of such influences has been observed to depend on types of heteroatoms, their contents, and their relative distances with respect to given ^{29}Si sites, molecular-level analyses regarding heteroatom site distributions in zeolites are often complicated by overlapping ^{29}Si NMR resonances. Despite the recent advances in solid-state NMR spectroscopy, locating heteroatom sites in zeolites still remains a very difficult task.

By comparison, to determine heteroatom site distributions in zeolites could begin with layered zeolite precursors (often referred to as two-dimensional (2D) zeolites), which possess molecularly ordered frameworks similar to zeolites.[35–38] In such layered zeolite precursors, there are generally two types of ^{29}Si environments (Q^3 and Q^4 ^{29}Si), where Q^n ^{29}Si notation refers to a four-coordinate ^{29}Si site covalently bonded with *n* next-nearest ^{29}Si sites through bridging oxygen atoms (*n* is an integer from 0 to 4). Differences between Q^3 and Q^4 ^{29}Si sites are manifested not only by their respective ^{29}Si NMR resonances (*i.e.*, Q^3 ^{29}Si: *ca.* -90 ~ -102 ppm and Q^4 ^{29}Si: *ca.* -102 ~ -120 ppm), but also by their distinct molecular environments.[32,33,39] Specifically, Q^4 ^{29}Si species are fully condensed ^{29}Si sites, whereas Q^3 ^{29}Si moieties are incompletely condensed with a non-bridging oxygen atom. Such Q^3 ^{29}Si species are often considered as structural defects or surface sites in zeolites.[33] In the case of layered silicates, Q^3 ^{29}Si species are part of structures and molecularly ordered,[36,40,41] which may be good candidates for heteroatom incorporation, due to their less degree of framework condensation compared to Q^4 ^{29}Si sites.

Previous structural study by Galve *et al.* suggests that Q^3 ^{29}Si sites are preferred for ^{27}Al incorporation in the case of layered zeolite Nu-6(1).[42] In addition to distinct Q^3 and Q^4 ^{29}Si environments, layered zeolite precursors provide opportunities for post-synthesis treatments to utilize their lamellar structures, which have attracted great interest over a decade. Well-

known examples are zeolite MCM-22 and its precursor MCM-22(P),[35,43] in which stacking MCM-22(P) can be modified post-synthetically to yield different expanded layer structures with more accessible active sites for reactions involving bulky molecules,[44,45] such as delaminated ITQ-2,[46,47] MCM-56,[48–50] and MCM-36.[51,52] Similar concept was implemented into other layered zeolites, such as zeolites SSZ-70 and ERB-1.[53–56] Interestingly, certain types of layered silicates were shown to form three-dimensional (3D) zeolites via topotatic condensation (vice versa).[57–62] Such a synthesis aspect, in conjunction with the results, where ^{27}Al atoms prefer to occupy Q^3 ^{29}Si sites than Q^4 ones in layered zeolite Nu-6(1) that can be post-synthetically converted into Nu-6(2),[42] demonstrates a promising possibility of directing acid sites in zeolites from their layered precursors. Overall, synthesis aspects, ^{29}Si NMR signatures, and catalytic applications of layered silicates highlight their importance in materials science and suggest that they are good candidates for investigating ^{27}Al site distributions.

In this perspective, $C_{16}H_{33}N^+$**Me$_3$**- and $C_{16}H_{33}N^+$**Me$_2$Et**-directed layered silicates were chosen to examine whether determination of ^{27}Al site distributions in ordered silicate frameworks could be achieved via a combination of advanced NMR and theoretical methods. This is due to relatively simpler ^{29}Si NMR signatures of surfactant-directed silicates as compared to zeolites, where $C_{16}H_{33}N^+$**Me$_3$**- and $C_{16}H_{33}N^+$**Me$_2$Et**-directed silicates contain two and five distinct ^{29}Si sites, respectively.[40] Furthermore, the structure of $C_{16}H_{33}N^+$**Me$_2$Et**-directed silicates was recently established while it lacks long-range 3D crystallanity.[63,64] Such surfactant-directed silicates with a high degree of short- (molecular) and long-range (mesoscopic) order are particularly interesting in terms of novel zeolite synthesis, because they exhibit chemical and structural relevance to mesostructured zeolites

developed by Ryoo and coworkers.[65–69] Additionally, the molecular structure of $C_{16}H_{33}N^{+}$**Me$_2$Et**-directed silicates was found to be nearly identical to the intermediate during formation of mesostructured MFI nanosheets.[70] In this regard, molecular insights learned from ^{27}Al site distributions in $C_{16}H_{33}N^{+}$**Me$_2$Et**-directed frameworks may enable control of ^{27}Al atoms in MFI frameworks.

Here, we establish and compare ^{27}Al site distributions in two closely related $C_{16}H_{33}N^{+}$**Me$_3$**- and $C_{16}H_{33}N^{+}$**Me$_2$Et**-directed aluminosilicates via solid-state NMR techniques and density functional theory (DFT) calculation. With such combined methods, molecular-level understanding of ^{29}Si structural order and disorder nearby framework ^{27}Al atoms in aluminosilicates is obtained. Specifically, advanced solid-state 2D NMR techniques allow locations of four-coordinate ^{27}Al species in the two surfactant-directed aluminosilicates to be determined by identifying molecular interactions involving ^{27}Al species, ^{1}H moieties of SDA molecules, and framework ^{29}Si sites. Importantly, ^{27}Al atoms are shown to be non-selectively distributed among different crystallographic sites in both aluminosilicates that were synthesized under otherwise conditions and compositions, expect for the SDA species. Interestingly, the ^{29}Si sites nearby ^{27}Al species are found to be greatly influenced due to the presence of ^{27}Al atoms by exhibiting an increased degree of framework condensation. The molecular-level insights presented here are expected to allow determination of ^{27}Al site distributions in aluminosilicate zeolite catalysts.

3.3 Experimental

3.3.1 Materials.

Cetyltrimethylammonium bromide ($C_{16}H_{33}$**Me$_3$**NBr, ≥96.0%, Sigma-Aldrich), cetyldimethylethylammonium bromide ($C_{16}H_{33}$**Me$_2$Et**NBr, ≥98%, Sigma-Aldrich), tetramethylammonium hydroxide (TMAOH, 25 wt% in water, Sigma-Aldrich), sodium aluminate ($NaAlO_2$, anhydrous, Sigma-Aldrich), hydrofluoric acid (HF, 48 wt% in water, Sigma-Aldrich), nitric acid (HNO_3, ACS reagent and 70%), amorphous silica (SiO_2, CAB-O-SIL M5 scintillation grade, ACROS ORGANICS) and methanol (ACS grade, VWR®) were purchased and directly used as received. 99% ^{29}Si-enriched SiO_2 ($^{29}SiO_2$) was purchased from CortecNet (France). Surfactant-directed aluminosilicates were synthesized using the following molar compositions: 1.0 SiO_2: *x* $NaAlO_2$: 0.7 TMAOH: 113.4 H_2O: 9.9 CH_3OH: 0.7 $C_{16}H_{33}$**Me$_3$**NBr, where x can be 0.1, 0.04, and 0.02; 1.0 SiO_2: *y* $NaAlO_2$: 0.7 TMAOH: 113.4 H_2O: 9.9 CH_3OH: 0.7 $C_{16}H_{33}$**Me$_2$Et**NBr, where *y* can be 0.025 and 0.01. In a typical synthesis, $C_{16}H_{33}$**Me$_3$**NBr or $C_{16}H_{33}$**Me$_2$Et**NBr surfactants were first dissolved in deionized water, after which TMAOH and CH_3OH were added. Then the solution was stirred for 30 min. The silica precursors (either Cabosil or $^{29}SiO_2$) were sequentially added and the reaction media stirred at room temperature for 7 and 21 days in the case of Cabosil and $^{29}SiO_2$, respectively. $NaAlO_2$ were subsequently added and the solution was stirred for another 2 h, which was transferred into a Teflon-lined Parr™ 4745 stainless-steel reactor, well-sealed, and heated at 135 °C under static conditions for 7 and 11 days for $C_{16}H_{33}N^+$**Me$_3$**- and $C_{16}H_{33}N^+$**Me$_2$Et**-directed aluminosilicates, respectively. After the hydrothermal treatment, the as-synthesized surfactant-directed aluminosilicates were

collected by vacuum filtration, washed using excess deionized water, and dried in the oven at 90 °C overnight.

3.3.2 Characterization.

X-ray diffraction. As-synthesized $C_{16}H_{33}N^+$**Me$_3$**- and $C_{16}H_{33}N^+$**Me$_2$Et**-directed aluminosilicates were characterized by powder X-ray diffraction and solid-state NMR spectroscopy. Wide-angle powder XRD patterns were acquired on a Philips XPERT powder diffractometer using Cu Kα radiation with a wavelength of 1.5405 Å generated at 45 kV and 40 mA. The samples were scanned at 4°/min between 2θ angles of 5-45°. Small-angle powder XRD patterns were collected on a Riguku SMART lab diffractometer using Cu Kα radiation with a wavelength of 1.5405 Å generated at 44 kV and 40 mA, in which the samples were scanned at 0.5°/min between 2θ angles of 0.5-10°.

Elemental analyses. Bulk Al content (*i.e.*, Si/Al ratios) was measured using inductively coupled plasma (ICP) analysis (Thermo iCAP 6300 model). Prior to ICP measurements, the as-synthesized materials were calcined in air at 550 °C (heating rate of 1 °C/min) for 12 h, and the resulting calcined materials were dissolved using 2 wt% HF and 3 wt% HNO_3 acid solution under vigorous stirring for several days. The CHN results were provided by the analytical lab in the Marine Science Institute (MSI), UCSB using the CEC440HA model from Exeter Analytical, Inc.

Solid-state one- (1D) and two-dimensional (2D) NMR measurements were conducted under magic-angle-spinning (MAS) conditions to characterize molecular compositions and structures of as-synthesized $C_{16}H_{33}N^+$**Me$_3$**- and $C_{16}H_{33}N^+$**Me$_2$Et**-directed aluminosilicates. Solid-state 1D $^{29}Si\{^1H\}$ cross-polarization (CP) and quantitative 1D ^{29}Si single-pulse MAS spectra of as-synthesized $C_{16}H_{33}N^+$**Me$_3$**-directed aluminosilicates were acquired on a Bruker

ACANCE-III NMR spectrometer (9.4 T, 25 °C) operating at frequencies of 400.1 MHz for ^{1}H and 79.6 MHz for ^{29}Si under the MAS conditions of 10 kHz using a Bruker 4 mm probehead. A CP contact time of 8.0 ms and over 2048 transients were employed in all 1D ^{29}Si{^{1}H} CP-MAS measurements with a recycle delay of 2 s, whereas over 144 transients and a recycle delay of 500 s were used in all 1D quantitative ^{29}Si single-pulse MAS experiments, both of which heteronuclear ^{1}H decoupling small-phase-incremental-alternation-with-64-steps (SPINAL64)[71] was applied at a ^{1}H nutation frequency of 50 kHz during ^{29}Si signal acquisition. Solid-state 1D ^{27}Al echo-MAS NMR experiments of as-synthesized $C_{16}H_{33}N^{+}$**Me$_3$**-directed aluminosilicates were performed on a Bruker ACANCE-III NMR spectrometer (20 T, 25 °C) operating at frequencies of 850.26 MHz for ^{1}H and 221.57 MHz for ^{27}Al under MAS of 18 kHz using a Bruker 3.2 mm probehead with 1024 transients and a recycle delay of 1 s. Double frequency sweep (DFS) pulses[72] at 1.0 ms were used to enhance ^{27}Al signal sensitivity prior to ^{27}Al excitation. High power heteronuclear ^{1}H decoupling (SPINAL64) was also applied during ^{27}Al signal acquisition. ^{1}H and ^{29}Si chemical shifts were referenced to tetra-methyl silane (TMS) and ^{27}Al shifts were referenced to an aqueous solution of 1 M aluminum nitrate [$Al(NO_3)_3$].

Solid-state 2D ^{27}Al{^{1}H} HETeronuclear CORrelation (HETCOR) NMR spectra of as-synthesized $C_{16}H_{33}N^{+}$**Me$_3$**-directed aluminosilicates were collected on a Bruker ACANCE-III NMR spectrometer (20 T, 25 °C) at 18 kHz MAS using a Bruker 3.2 mm probehead with 200 t_1 increments, 32 transients, and a recycle delay of 2 s. The magnetization was transferred from ^{1}H to ^{27}Al nuclei using adiabatic passage satisfying Hartmann-Hahn condition[73], during which CP contact time of 6.0 ms was used. Heteronuclear ^{1}H decoupling (SPINAL64) was applied during ^{27}Al signal acquisition, corresponding to a ^{1}H nutation

frequency at 60 kHz. The 2D ^{27}Al{^{1}H} HETCOR NMR spectrum of as-synthesized ^{29}Si-enriched $C_{16}H_{33}N^{+}$**Me$_3$**-directed aluminosilicates was obtained on the same NMR spectrometer (20 T, 25 °C) at 10 kHz MAS with 218 t_1 increments, 416 transients, a recycle delay of 1.5 s, CP contact time of 0.2 ms, and 60 kHz heteronuclear ^{1}H decoupling (SPINAL64) during ^{27}Al signal acquisition. The 2D ^{27}Al{^{1}H} HETCOR NMR spectra of as-synthesized $C_{16}H_{33}N^{+}$**Me$_2$Et**-directed aluminosilicates were acquired on the same NMR spectrometer (20 T, 25 °C) at 18 kHz MAS, a recycle delay of 2 s, 40 kHz heteronuclear ^{1}H decoupling (SPINAL64) during ^{27}Al signal acquisition with over 200 t_1 increments for CP contact times: 0.5, 6, and 10 ms (240 t_1 increments for CP contact time: 2 ms), 192 transients for CP contact times: 0.5 and 6 ms (128 transients for 2 and 10 ms). For the 2D ^{27}Al{^{1}H} NMR experiments of $C_{16}H_{33}N^{+}$**Me$_2$Et**-directed aluminosilicates, the magnetization was transferred from ^{1}H to ^{27}Al nuclei using RAMP 155 satisfying Hartmann-Hahn condition.

Solid-state 2D ^{29}Si{^{29}Si} dipolar-mediated double-quantum (DQ) NMR experiments of as-synthesized ^{29}Si-enriched $C_{16}H_{33}N^{+}$**Me$_3$**- and $C_{16}H_{33}N^{+}$**Me$_2$Et**-directed aluminosilicates were collected on a Bruker ACANCE-I NMR spectrometer at 7.0 T, 25 °C, 4.6 kHz MAS, ^{29}Si-^{29}Si dipolar recoupling time of 3.5 ms, and 60 kHz SPINAL64 ^{1}H decoupling during ^{29}Si signal acquisition. All measurements were conducted using the symmetry-based $SR26_4^{11}$ homonuclear dipolar recoupling sequence.[74–76] The ^{29}Si nutation frequency during ^{29}Si-^{29}Si dipolar recoupling period was set to 30 kHz (~ 6.5 × 4.6 kHz). 90 kHz continuous-wave (CW) ^{1}H decoupling was applied during the ^{29}Si DQ excitation and reconversion periods. The 2D ^{29}Si{^{29}Si} DQ NMR spectrum of as-synthesized ^{29}Si-enriched

$C_{16}H_{33}N^{+}$**Me$_3$**- and $C_{16}H_{33}N^{+}$**Me$_2$Et**-directed aluminosilicates was acquired with 80 and 224 t_1 increments, 32 and 64 transients, and a recycle delay of 2 and 3 s, respectively.

Solid-state 2D ^{27}Al{^{29}Si} and ^{29}Si{^{27}Al} *J*-mediated Heteronuclear Multiple Quantum Coherence (HMQC) NMR spectra of as-synthesized ^{29}Si-enriched $C_{16}H_{33}N^{+}$**Me$_3$**-directed aluminosilicates were collected on a Bruker ACANCE-III NMR spectrometer (20 T, 25 °C) at 14 kHz MAS using a Bruker 3.2 mm H-X-Y triple-resonance probehead (^{27}Al-^{29}Si insert). The half-echo delay before and after the evolution period in the ^{27}Al{^{29}Si} and ^{29}Si{^{27}Al} *J*-mediated HMQC[77] were experimentally optimized to 5 ms. The indirect dimensions for the 2D ^{27}Al{^{29}Si} and ^{29}Si{^{27}Al} NMR measurements were acquired using 48 and 30 increments, 384 and 2624 transients, and a recycle delay of 2.0 and 2.0 s, respectively, both of which 60 kHz SPINAL64 ^{1}H decoupling was applied during the whole sequence. Magnetization was transferred from ^{1}H to ^{29}Si via adiabatic passage (CP contact time: 7.0 ms) before the HMQC sequence in 2D ^{29}Si{^{27}Al} NMR experiments. DFS pulses at 1.0 ms were used prior to ^{27}Al excitation in 2D ^{27}Al{^{29}Si} NMR measurements.

Solid-state 2D ^{27}Al{^{29}Si} and 1D ^{29}Si{^{27}Al} dipolar-mediated HMQC NMR spectrum of as-synthesized $C_{16}H_{33}N^{+}$**Me$_3$**-directed aluminosilicates with ^{29}Si natural abundance were collected on a Bruker ACANCE-III NMR spectrometer (17.6 T, 25 °C) at 7 kHz MAS using a 4.0 mm H-X-Y triple-resonance probehead (^{27}Al-^{29}Si insert). The heteronuclear ^{27}Al-^{29}Si dipole-dipole couplings were reintroduced using a $R4^2_1$ symmetry-based dipolar recoupling[78–81] scheme at a ^{29}Si nutation frequency of 14 kHz (2 × 7 kHz), and the recoupling durations were set to 5.1 ms (6 symmetry cycles of 6 rotor periods each) before and after the evolution period. The second ^{29}Si dimension was collected with 32 increments,

4480 transients, and a recycle delay of 1.5 s. 50 kHz CW and SPINAL64 ^{1}H decoupling were applied during the dipolar recoupling and acquisition period, respectively.

DFT calculations. All DFT calculations were conducted by French Researchers and Scientists at CNRS Orleans in France, primarily using CASTEP.

3.4 Results and Discussion

$C_{16}N^{+}Me_3$-directed aluminosilicates. Heteroatom site distributions in zeolite frameworks are known to strongly influence the resulting acidity, catalytic, and adsorption performances of heteroatom-containing zeolite catalysts,[20–22,82,83] which has been very difficult to characterize via different methodologies, such as diffraction, microscopy, and modeling. To overcome such challenging problems, new applications of recently developed NMR techniques are demonstrated here to probe molecular through-space and -bond interactions of ^{27}Al and ^{29}Si species, aiming for establishing ^{27}Al siting in aluminosilicates. First, $C_{16}H_{33}N^{+}Me_3$-directed silicates were chosen for ^{27}Al atom incorporation, mainly due to their much simpler ^{29}Si NMR signatures that result from two distinct ^{29}Si sites. The ^{27}Al insertion is expect to alter the $C_{16}H_{33}N^{+}Me_3$-directed aluminosilicate frameworks, as compared to siliceous ones, because of different bond lengths between Si-O (*ca.* 1.58 ~ 1.64 Å)[84] and Al-O (*ca.* 1.70 ~ 1.73 Å).[85,86] Figure 1 shows power X-ray diffraction (XRD) patterns of $C_{16}H_{33}N^{+}Me_3$-directed aluminosilicates as a function of ^{27}Al loadings, where several structural features are observed in the three materials. For instance, the reflections at *ca.* 21.0 and 25.5 degree 2θ, associated with *d*-spacing of 0.42 and 0.35 nm, respectively, appear to retain while Al loadings increase, which are identical to the $C_{16}H_{33}N^{+}Me_3$-directed

silicates.[40] In addition, the different Al loadings do not seem to interfere with the lamellar mesophase of $C_{16}H_{33}N^{+}Me_3$-directed aluminosilicates very much, as evidenced by two main reflections at *ca.* 2.5 and 5.0 degree 2θ (see Figure B1). Despite these similarities, differences caused by ^{27}Al incorporation are manifested by the reflections at *ca.* 22.8 and 24.2 degree 2θ. These two reflections are hypothesized to result from subtle structural changes due to the inserted ^{27}Al atoms. Further understanding as to how the incorporated ^{27}Al atoms modify the frameworks is severely hindered by the limited resolution of the powder XRD patterns. Nevertheless, these XRD results clearly reveal that the $C_{16}H_{33}N^{+}Me_3$-directed aluminosilicates with different Al contents possess not only lamellar but also long-range order.

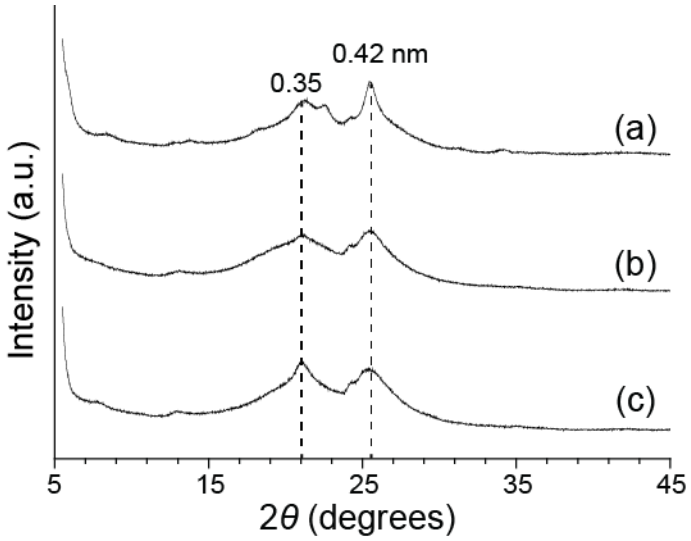

Figure 1. Powder X-ray diffraction (XRD) patterns of as-synthesized $C_{16}H_{33}N^{+}Me_3$-directed aluminosilicates as a function of Al loadings: Si/Al ~ (a) 11.1, (b) 25.3, and (c) 42.6.

While $C_{16}H_{33}N^{+}Me_3$-directed aluminosilicates exhibit lamellar and long-range order, their detailed structures cannot be established unambiguously, from which ^{27}Al site distributions may be obtained. Consequently, solid-state NMR spectroscopy, highly sensitive to short-range order, was employed to characterize local ^{29}Si and ^{27}Al

environments of $C_{16}H_{33}N^{+}Me_3$-directed aluminosilicates. Figure 2a-c shows the 1D $^{29}Si\{^{1}H\}$ CP MAS NMR spectra of $C_{16}H_{33}N^{+}Me_3$-directed aluminosilicates as a function of ^{27}Al contents, where four distinct ^{29}Si signals are observed at -97, -102, -107, and -112 ppm. The two ^{29}Si signals at -102 and -112 ppm correspond to the Q^3(0Al) and Q^4(0Al) ^{29}Si species, respectively, consistent with the ^{29}Si assignments of $C_{16}H_{33}N^{+}Me_3$-directed silicates[40] and aluminosilicates[87] (see Figure B2). Another two ^{29}Si signals at -97 and -107 ppm were respectively assigned to Q^3(1Al) and Q^4(1Al) ^{29}Si species, based on the hypothesis of ^{27}Al atoms inserted into one neighboring ^{29}Si site of Q^3(0Al) and Q^4(0Al) ^{29}Si species. Such downfield displacement (*ca.* 5 ppm) in the ^{29}Si chemical shift dimension has been observed in alumina-silica and zeolites.[32,33,39] Furthermore, the quantitative ^{29}Si MAS NMR analyses show that when the ^{27}Al contents increase, the relative population of Q^3(1Al) ^{29}Si species changes from 4.1 to 11.2%, similar to the Q^4(1Al) ^{29}Si species (from 3.9 to 34.0%), whereas the fractions of Q^3(0Al) and Q^4(0Al) ^{29}Si species decrease (see Figure B2). The detailed information is summarized in Table 1. This trend suggests that ^{27}Al atom incorporation helps increase the relative populations of Q^3(1Al) and Q^4(1Al) ^{29}Si sites at the expense of the Q^3(0Al) and Q^4(0Al) ^{29}Si species, respectively. The framework ^{27}Al species can be manifested not only by the presence of Q^3(1Al) and Q^4(1Al) ^{29}Si species but also by bonding configurations of ^{27}Al moieties. Figure 2d-f shows 1D ^{27}Al echo MAS NMR spectra of $C_{16}H_{33}N^{+}Me_3$-directed aluminosilicates as a function of ^{27}Al loadings. Only two ^{27}Al signals at 54 and 59.5 ppm are observed (in blue), associated with four-coordinate ^{27}Al moieties, and no ^{27}Al signals at *ca.* 0 ppm are detected at (in yellow), typically corresponding to six-coordinate ^{27}Al moieties.[33,39,88,89] The two ^{27}Al NMR signatures support the hypothesis that $C_{16}H_{33}N^{+}Me_3$-directed aluminosilicates contain in-framework

rather than extra-framework ^{27}Al species. These ^{29}Si and ^{27}Al NMR analyses indicate that a fraction of $C_{16}H_{33}N^{+}Me_3$-directed aluminosilicate structures could remain undisturbed even after ^{27}Al incorporation, and suggest that ^{27}Al atoms have been readily inserted into frameworks.

Table 1. Summary of ^{29}Si NMR quantitative analyses of $C_{16}H_{33}N^{+}Me_3$-directed aluminosilicates as a function of Al loadings

Synthesis Si/Al ratio	Relative Population (%)					Measured Si/Al ratios			
						NMR[(a)]			
	Q^3(1Al)	Q^3	Q^4(1Al)	Q^4	ICP	^{27}Al in Q^4 or Q^3 ^{29}Si[(b)]	^{27}Al in Q^3 ^{29}Si[(c)]	^{27}Al in Q^4 or Q^3 ^{29}Si[(d)]	^{27}Al in Q^4 ^{29}Si[(e)]
∞	0	50	0	50	∞	∞	∞	∞	∞
50	4.1	40.5	3.9	51.4	42.6	49.2	37.4	49	49
25	5	32.8	14.9	47.3	25.3	20.1	15.1	19.1	19.1
10	11.2	16.6	34	38.2	11.1	8.9	6.6	7.9	7.9

[(a)] n(Si) / n(Al) = a*(n[Q^n(1Al)]+ n[Q^n]) / (n[Q^n(1Al)]) with $3 \le a \le 4$ and $3 \le n \le 4$.

[(b)] Assumption: framework ^{27}Al atoms have four next-nearest-neighboring ^{29}Si sites, where ^{27}Al atoms could be inserted into either Q^3 or Q^4 ^{29}Si sites. That is, in the case of ^{27}Al incorporation into Q^3 ^{29}Si sites, the nearby Q^3 ^{29}Si species would condense to form Q^4(1Al) ^{29}Si species.

[(c)] Assumption: framework ^{27}Al atoms have three next-nearest-neighboring ^{29}Si sites.

[(d)] All ^{27}Al atoms inserted into either Q^3 or Q^4 ^{29}Si sites induce one framework condensation between Q^3 ^{29}Si species (Figure 6b,c).

[(e)] All ^{27}Al atoms inserted into Q^4 ^{29}Si sites induce two framework condensations between Q^3 ^{29}Si species (Figure 6d).

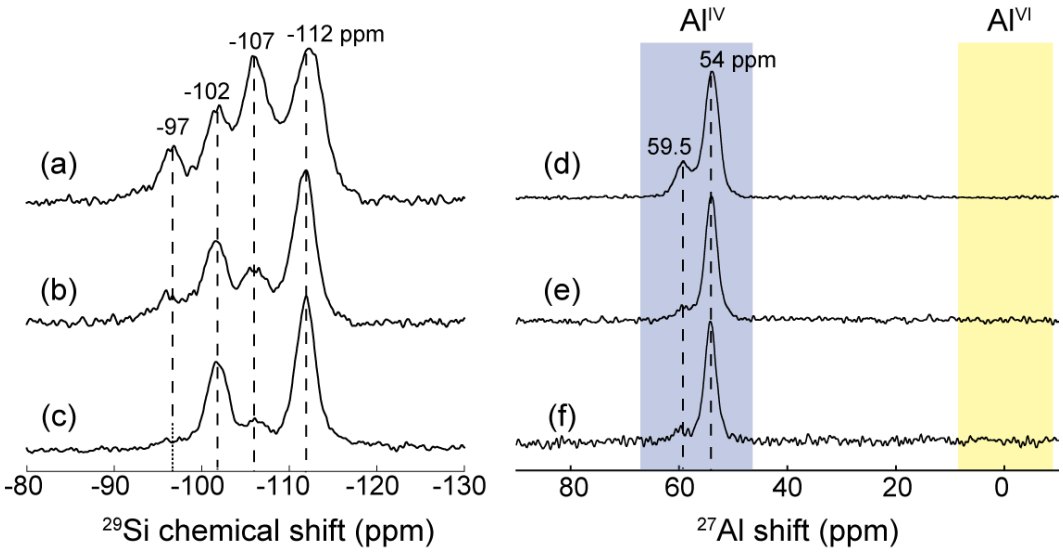

Figure 2. Solid-state 1D $^{29}Si\{^{1}H\}$ CP and ^{27}Al echo MAS NMR spectra, which were acquired at 9.4 T, 25 °C, 10 kHz MAS and 20.0 T, 25 °C, 18 kHz MAS, respectively, of as-synthesized $C_{16}H_{33}N^{+}Me_3$-directed aluminosilicates as a function of Al loadings (Si/Al ~ (a, d) 11.1, (b, e) 25.3, and (c, f) 42.6)

Although the different types of local ^{29}Si and ^{27}Al structures in the as-synthesized $C_{16}H_{33}N^{+}Me_3$-directed aluminosilicates were determined using 1D MAS NMR measurements, multidimensional and/or double-resonance NMR techniques can provide insights into molecular interactions between homo- and heteronuclear moieties of $C_{16}H_{33}N^{+}Me_3$-directed aluminosilicates. For instance, through-bond $^{2}J(^{29}Si\text{-}O\text{-}^{29}Si)$ and $^{2}J(^{29}Si\text{-}O\text{-}^{27}Al)$ couplings can be used to establish site connectivities among the ^{27}Al and ^{29}Si species (ideally ^{27}Al site distributions can be derived), whereas through-space dipolar interactions can probe molecularly proximate species (< 1 nm). In particular, molecular interactions, involving ^{1}H species of $C_{16}H_{33}N^{+}Me_3$ molecules and four-coordinate ^{27}Al moieties (Al^{IV}) in as-synthesized $C_{16}H_{33}N^{+}Me_3$-directed aluminosilicates, are unambiguously identified by 2D $^{27}Al\{^{1}H\}$ HETCOR NMR experiments. The 2D $^{27}Al\{^{1}H\}$ NMR measurements would correlate the ^{27}Al and ^{1}H chemical shifts of corresponding ^{27}Al-

^{1}H dipole-dipole interacting species (Figure 3). Specifically, intensity correlations are observed between two ^{1}H signals (at 1.4 and 3.3 ppm in the ^{1}H dimension), associated with the I and II of the $C_{16}H_{33}N^{+}Me_3$ molecules, and one ^{27}Al signal (at 54 ppm in the ^{27}Al dimension) from four-coordinate ^{27}Al sites. The observations are very similar to the previously observed ones in the $C_{16}H_{33}N^{+}Me_3$-directed silicates.[40] Interestingly, no ^{1}H signals that possibly result from Si-OH, Al-OH, Al-OH-Si (Brønsted acid sites), and water have correlated intensities with the two ^{27}Al signals at 59.5 and 54 ppm. Such observation indicates that the negative charges near framework ^{27}Al atoms must be balanced by the cationic head groups of $C_{16}H_{33}N^{+}Me_3$ molecules. This is also confirmed by another 2D ^{27}Al{^{1}H} HETCOR NMR experiment with a much shorter CP contact time (200 μs), revealing one strong correlation between the ^{27}Al signal at 54 ppm and the ^{1}H signal at 3.4 ppm, associated with the ^{1}H species II of $C_{16}H_{33}N^{+}Me_3$ molecules (see Figure B3). The above 2D ^{27}Al{^{1}H} NMR results demonstrate that four-coordinate ^{27}Al sites are molecularly proximate to the cationic $C_{16}H_{33}N^{+}Me_3$ surfactant head groups, and they suggest that the ^{27}Al atoms are readily incorporated into the $C_{16}H_{33}N^{+}Me_3$-directed structures, based on the very similar inorganic silicate frameworks-organic $C_{16}H_{33}N^{+}Me_3$ molecules interactions.[40]

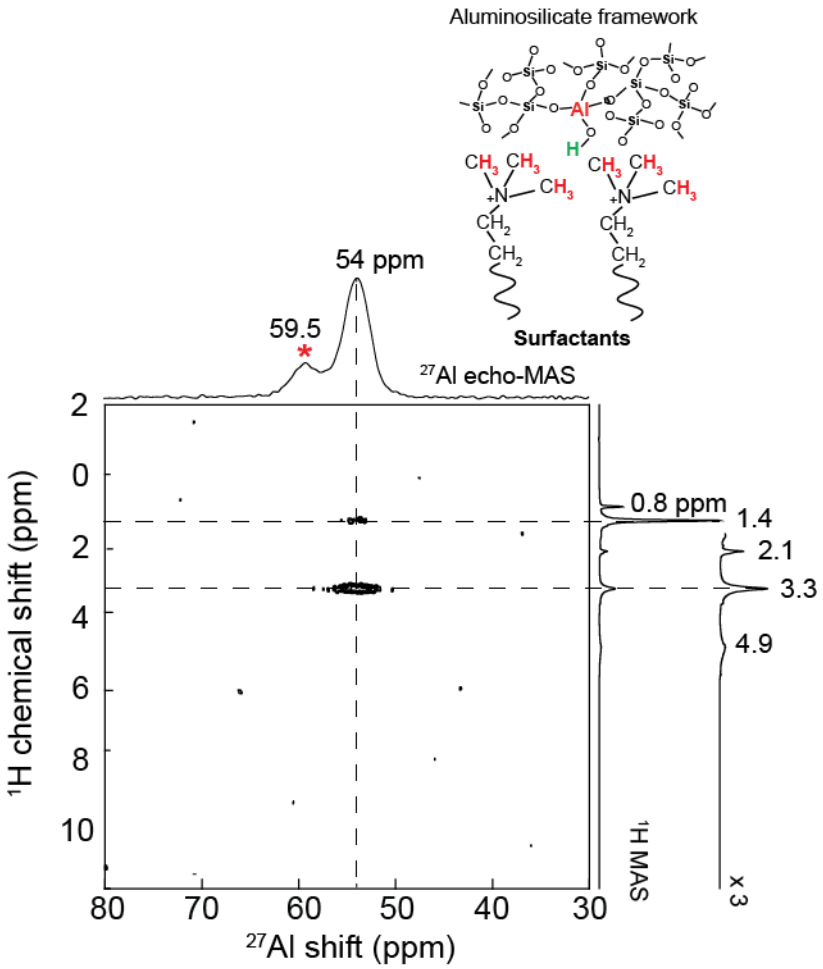

Figure 3. Solid-state 2D dipolar-mediate heteronuclear correlation (HETCOR) ^{27}Al{^{1}H} NMR spectrum of as-synthesized $C_{16}H_{33}N^{+}Me_3$-directed aluminosilicates, which was collected at 20.0 T, 25 °C, and 18 kHz MAS. Solid-state 1D ^{27}Al echo and ^{1}H MAS are shown along the top horizontal and right vertical axis, respectively. Schematic representation of $C_{16}H_{33}N^{+}Me_3$ molecules spatially adjacent to four-coordinate ^{27}Al sites is included as an inset. [Courtesy: Dr. Mounesha Garaga]

In addition, the presence of ^{27}Al atoms in $C_{16}H_{33}N^{+}Me_3$-directed silicate frameworks can be revealed by probing ^{29}Si site connectivities and proximities. This is because ^{27}Al atoms would alter their nearby local ^{29}Si environments, leading to changes of ^{29}Si signals in ^{29}Si NMR spectra. As discussed above, such changes are clearly manifested in 1D ^{29}Si MAS NMR measurements (Figures 2a-c and B2b-d), where ^{29}Si signals at -97 and -107 ppm, assigned to the Q^3(1Al) and Q^4(1Al) ^{29}Si species, respectively, increase their relative

populations as ^{27}Al contents increase. Further details regarding ^{29}Si site connectivities and proximities of the four ^{29}Si species can be exploited respectively using solid-state 2D ^{29}Si{^{29}Si} *J*- and dipolar-mediated MAS NMR techniques. Prior to ^{27}Al atom incorporation, the $C_{16}H_{33}N^{+}Me_3$-directed silicate is composed of two distinct ^{29}Si sites (Figure B2a), whose connectivities have been established, showing that the Q^3(0Al) and Q^4(0Al) ^{29}Si species are interconnected and bonded to other Q^3(0Al) and Q^4(0Al) ^{29}Si species, respectively.[40,90] The specific connectivities are substantially influenced by ^{27}Al insertion, creating new ^{29}Si site connectivities simultaneously. This is supported by the solid-state 2D ^{29}Si{^{29}Si} *J*-mediated NMR spectrum (Figure 4a), where covalently bonded ^{29}Si sites would share the same NMR resonance frequency in the double-quantum (DQ) dimension, due to their ^2J(^{29}Si-O-^{29}Si) couplings. While two ^{29}Si site connectivities of $C_{16}H_{33}N^{+}Me_3$-directed aluminosilicates are the same as the siliceous framework, such as the Q^3(0Al)-Q^4(0Al) (-214 ppm, DQ) and Q^4(0Al)-Q^4(0Al) ^{29}Si pairs (-224 ppm, DQ),[40,90] several new structural features appear after ^{27}Al incorporation. Specifically, the ^{29}Si signal at -107 ppm (Q^4(1Al) ^{29}Si species) exhibits correlations at -209 and -219 ppm in the DQ dimension, showing that Q^4(1Al) are respectively connected to Q^3(0Al) and Q^4(0Al) ^{29}Si moieties. Similarly, the ^{29}Si signal at -97 ppm (Q^3(1Al) ^{29}Si species) has correlated DQ intensities at -209 ppm, which establishes its site connectivity with Q^4(0Al) ^{29}Si sites (-112 ppm). It should be noticed that Q^3(0Al)-Q^3(0Al) ^{29}Si site connectivity, found in $C_{16}H_{33}N^{+}Me_3$-directed siliceous frameworks, is not clearly revealed in aluminosilicates. This suggests that ^{29}Si structural transformation occurs, due to ^{27}Al incorporation. Additionally, it is observed that once one ^{27}Al atom is inserted into the first coordination shell of a given ^{29}Si site (either Q^3(0Al) or Q^4(0Al)), the resulting Q^3(1Al) or Q^4(1Al) ^{29}Si site does not appear to have connectivities

with Q^3(0Al) ^{29}Si species. This provides direct evidence of ^{29}Si structural rearrangements near framework ^{27}Al species.

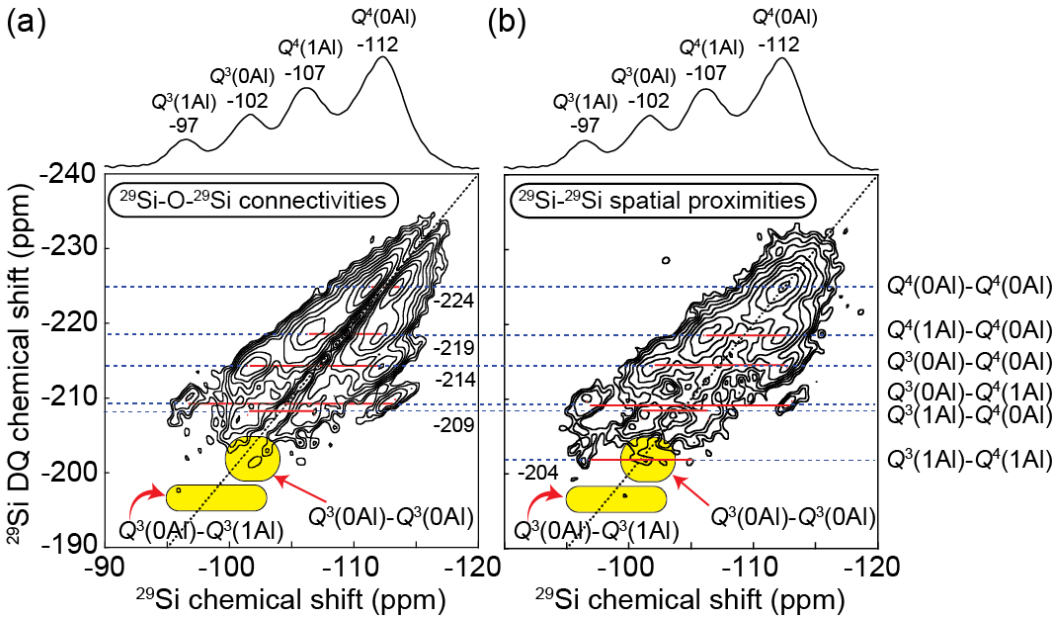

Figure 4. Solid-state 2D (a) *J*- and (b) dipolar-mediated ^{29}Si{^{29}Si} NMR spectra, both of which were acquired at 7.0 T, 25 °C, and 4.6 kHz MAS, of as-synthesized $C_{16}H_{33}N^+Me_3$-directed aluminosilicates with *ca.* 99 % ^{29}Si enrichment (Si/Al = 10 in reactant). Solid-state 1D ^{29}Si{^{1}H} CP MAS NMR spectra are shown in the top horizontal axis of both 2D NMR spectra. [Courtesy: Dr. Mounesha Garaga]

By considering the cancellation effects of *J*-couplings between two chemically identical ^{29}Si sites during 2D *J*-mediated NMR experiements, a solid-state 2D ^{29}Si{^{29}Si} dipolar-mediated measurement was conducted to probe molecularly proximate ^{29}Si moieties. This dipolar-mediate experiment could reveal correlated signal intensities between chemically identical ^{29}Si sites (Figure 4b), complementary to the *J*-mediated NMR techniques. Similar to the 2D ^{29}Si{^{29}Si}*J*-mediated NMR spectrum, molecularly proximate ^{29}Si species would share the same NMR resonance frequency in the DQ dimension, due to their ^{29}Si-^{29}Si dipole-dipole couplings. Given that a relatively short recoupling time (3.5 ms) was applied, detected ^{29}Si site proximities here are considered to be within their first shell

coordination. Therefore, most ^{29}Si-^{29}Si site proximities are exactly the same as the corresponding ^{29}Si site connectivities, such as Q^4(1Al)-Q^4(0Al) (-219 ppm, DQ), Q^3(0Al)-Q^4(0Al) (-214 ppm, DQ), Q^3(1Al)-Q^4(0Al) (-209 ppm, DQ), Q^3(0Al)-Q^4(1Al) (-209 ppm, DQ) ^{29}Si site connectivities. It is worth mentioning that the ^{29}Si signal at -112 ppm (associated with Q^4(0Al) ^{29}Si species) is strongly correlated to the DQ signal at -224 ppm, which suggests Q^4(0Al)-Q^4(0Al) ^{29}Si site connectivity. Furthermore, the Q^3(1Al)-Q^4(1Al) ^{29}Si species are found to be molecularly proximate, as revealed by the DQ signal at -204 ppm. Interestingly, very similar to the 2D ^{29}Si{^{29}Si}*J*-mediated NMR spectrum (Figure 4a), there are no Q^3(0Al) ^{29}Si species molecularly proximate to Q^3(1Al) and/or Q^4(1Al) ^{29}Si sites. Together with the Q^3(1Al)-Q^4(1Al) ^{29}Si spatial proximities, such observation suggests the high possibility of ^{29}Si structural transformation around the framework ^{27}Al atoms regardless of Q^3(0Al) or Q^4(0Al) ^{29}Si sites, based on the site connectivities established in $C_{16}H_{33}N^+Me_3$-directed siliceous frameworks. According to the 2D ^{29}Si{^{29}Si}*J*- and dipolar-mediated NMR analyses, it can be concluded that the local ^{29}Si environments are significantly influenced by ^{27}Al incorporation, which appears to induce ^{29}Si structural transformation near the inserted ^{27}Al sites.

The ^{27}Al siting of $C_{16}H_{33}N^+Me_3$-directed aluminosilicates, however, could not be confirmed only based on the above NMR analyses, such as 1D ^{27}Al, ^{29}Si MAS, 2D ^{27}Al{^{1}H}, and ^{29}Si{^{29}Si} NMR correlations. They all suggest that ^{27}Al atoms are readily present in the framework, but are unable to provide "direct" evidence to support this hypothesis. Such challenging problem can be overcame by solid-state 2D ^{27}Al{^{29}Si} and ^{29}Si{^{27}Al} dipolar-/*J*-meditated heteronuclear multiple quantum coherence (HMQC) NMR experiments. The 2D ^{27}Al{^{29}Si} and ^{29}Si{^{27}Al} NMR techniques are designed to probe ^{27}Al-

^{29}Si site connectivities and proximities, which together with crystallography can allow the determination of ^{27}Al site distributions in aluminosilicates. Similar to the previous 2D ^{27}Al{^{1}H} and ^{29}Si{^{29}Si} NMR spectra, correlated signal intensities will be observed between spatial proximate (< 1 nm) and covalently bonded ^{27}Al and ^{29}Si moieties in 2D ^{27}Al{^{29}Si} dipolar- and *J*-mediated NMR results, respectively. Figure 5a shows a 2D ^{27}Al{^{29}Si} dipolar-mediated NMR spectrum of $C_{16}H_{33}N^{+}Me_3$-directed aluminosilicates, where two main intensity correlations are clearly exhibited among various ^{29}Si and ^{27}Al signals. Specifically, the ^{27}Al signal at 52 ppm (associated with the four-coordinate ^{27}Al species) is correlated with the ^{29}Si signals at -97, -102, -107, and -112 ppm in the ^{29}Si dimension, corresponding to Q^3(1Al), Q^3(0Al), Q^4(1Al), and Q^4(0Al) ^{29}Si sites, respectively. These correlations establish that ^{27}Al atoms are molecularly proximate to all types of ^{29}Si moieties in $C_{16}H_{33}N^{+}Me_3$-directed aluminosilicates. Furthermore, a substantial fraction of the four-coordinate ^{27}Al species appears to be more surrounded by Q^4(1Al) than Q^3(1Al), Q^3(0Al), and Q^4(0Al) ^{29}Si sites, as evidenced by their relatively stronger 2D intensities compared to others.

Given the ^{27}Al-^{29}Si recoupling time (5.1 ms) employed during the measurement, the four-coordinate ^{27}Al species are considered to be within first and/or second coordination shell of ^{29}Si sites, supporting the hypothesis regarding the presence of ^{27}Al atoms in the framework. Such hypothesis is further confirmed by the 2D ^{27}Al{^{29}Si} *J*-mediated NMR spectra (Figure 5b and c), where correlation intensities only exist between covalently bonded ^{27}Al and ^{29}Si sites. Specifically, the ^{27}Al signal at 52 ppm possesses a strong correlation with the ^{29}Si signal at -107 ppm, establishing that the corresponding four-coordinate ^{27}Al sites are covalently bonded with Q^4(1Al) ^{29}Si sites through bridging oxygen

atoms. This is consistent with the same correlation (yet broader) in the 2D ^{27}Al{^{29}Si} dipolar-mediated NMR spectrum (Figure 5a). Interestingly, not many of the same type ^{27}Al sites are bonded with Q^3(1Al) ^{29}Si species, as indicated by a weak correlation between the ^{27}Al (52 ppm in the ^{27}Al dimension) and ^{29}Si signal (-97 ppm in the ^{29}Si dimension). Furthermore, no correlations are visible between ^{27}Al (52 ppm) and ^{29}Si signals (-102 and -112 ppm), demonstrating that none of the same ^{27}Al sites are connected with Q^3(0Al) and Q^4(0Al) ^{29}Si moieties. It should be noticed that an additional correlation (in red) is observed between ^{27}Al (51 ppm, four-coordinate ^{27}Al sites) and ^{29}Si signal (-110 ppm, Q^4(1Al) ^{29}Si species), both of which are displaced with respect to the main ^{27}Al (52 ppm) and ^{29}Si resonance (-107 ppm). Such additional correlation manifests subtle changes in local structures around Q^4(1Al) ^{29}Si sites. This interesting feature could be due to the small portion of newly created connectivities among the ^{27}Al and ^{29}Si sites after ^{27}Al atom incorporation, which will be discussed via theoretical calculation below.

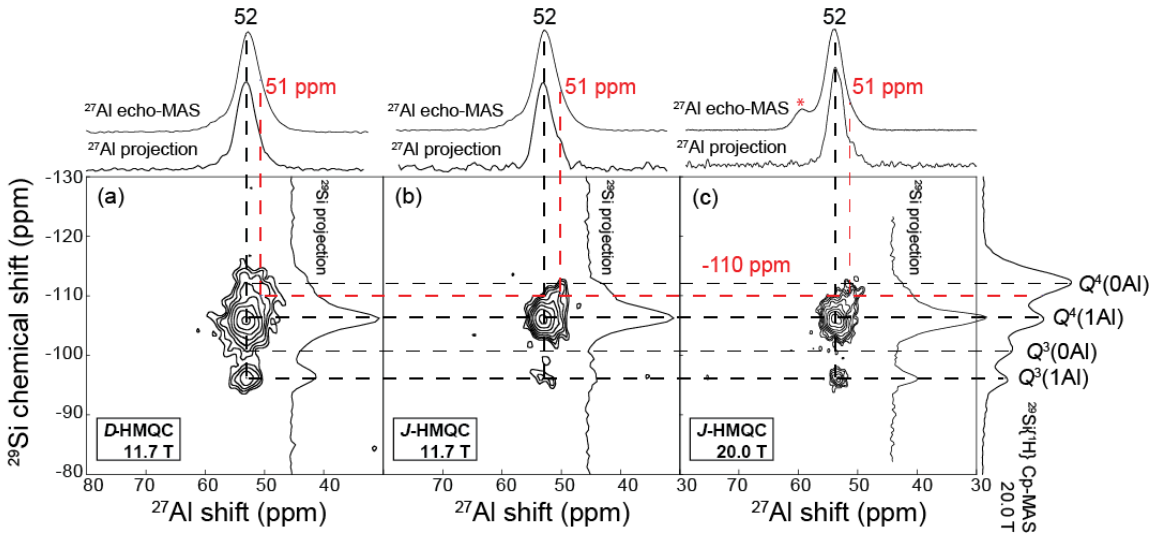

Figure 5. Solid-state 2D (a) dipolar- and (b, c) *J*-mediated heteronuclear multiple-quantum correlation (HMQC) ^{27}Al{^{29}Si} NMR spectra, the first two of which were acquired at 11.7 T, 25 °C, and 8 kHz MAS and the last of which was collected at 20.0 T, 25 °C, and 14 kHz MAS, of as-synthesized $C_{16}H_{33}N^+Me_3$-directed aluminosilicates with *ca.* 99 % ^{29}Si enrichment (Si/Al = 10 in reactant). Solid-state 1D ^{27}Al echo-MAS NMR spectra and ^{27}Al projections are shown along the top horizontal axis, whereas a solid-state 1D ^{29}Si{^{1}H} CP-MAS NMR spectrum and ^{29}Si projections are demonstrated along the right vertical axis. [Courtesy: Dr. Mounesha Garaga]

The various pairs of ^{27}Al-^{29}Si site connectivities in $C_{16}H_{33}N^+Me_3$-directed aluminosilicates are determined for the first time by the 2D ^{27}Al{^{29}Si} dipolar- and *J*-mediated HMQC NMR spectra (Figure 5a and b). These ^{27}Al-^{29}Si site connectivities are confirmed again by the 2D ^{27}Al{^{29}Si} and ^{29}Si{^{27}Al} *J*-mediated HMQC NMR measurements at higher magnetic field (20.0 T), aiming at excluding ambiguity that might result from the quadrupolar moment of ^{27}Al nuclei. Figure 5c shows a 2D ^{27}Al{^{29}Si} *J*-mediated NMR spectrum acquired at 20.0 T, where the identical correlation intensities are revealed with improved spectral resolution, such as the correlations between ^{27}Al (at 52 ppm) and ^{29}Si signals (at -97 and -107 ppm). More importantly, the weaker intensity correlation (in red) is observed as well, consistent with the 2D ^{27}Al{^{29}Si} dipolar- and *J*-mediated NMR

spectra collected at 11.7 T (Figure 5a and b, respectively), which determines the presence of such distinct local ^{27}Al and ^{29}Si structures. Similarly, the same ^{27}Al-^{29}Si site connectivities are shown by the 2D ^{29}Si{^{27}Al} *J*-mediated NMR spectrum (Figure B4), which utilizes the same theoretical principles yet detects ^{29}Si in the direct dimension instead of ^{27}Al nuclei. Based on the 2D ^{27}Al{^{29}Si} and ^{29}Si{^{27}Al} NMR results, it can be concluded that the four-coordinate ^{27}Al sites are covalently bonded with Q^3(1Al) and Q^4(1Al) ^{29}Si species, whereas such framework ^{27}Al atoms are not connected with Q^3(0Al) and Q^4(0Al) ^{29}Si sites. Furthermore, a small portion of ^{27}Al bonded Q^4(1Al) ^{29}Si sites (-110 ppm) are molecularly distinct from the main Q^4(1Al) ^{29}Si species (-107 ppm). The ^{27}Al signal at 60 ppm (also associated with four-coordinate ^{27}Al sites) possibly belongs to a small quantity of impurity, because it does not have no intensity correlations with ^{29}Si signals. The ^{29}Si structural modification around the framework ^{27}Al sites is investigated using first principle calculations below.

Plane-wave based DFT calculations were used to understand local ^{29}Si structural rearrangement in the $C_{16}H_{33}N^+Me_3$-directed aluminosilicates. The $C_{16}H_{33}N^+Me_3$-directed silicate structure used in DFT calculations employed the reported octosilicate, composed of 32 tetrahedral ^{29}Si sites per unit cell with a 16-fold symmetry, where two distinct T sites exist (denoted as T_1 and T_2). T_1 and T_2 correspond to Q^4 and Q^3 ^{29}Si sites, respectively.[90] Our models were constructed by a single octosilicate layer per unit cell with an inter-layer space along the *c* axis adjusted to accommodate charge-compensating alkylammonium molecules between octosilicate layers, where $C_4H_9N^+Me_3$ molecules were utilized for all models instead of the $C_{16}H_{33}N^+Me_3$ molecules in the $C_{16}H_{33}N^+Me_3$-directed aluminosilicates. An example model is shown in Figure 6. A series of geometry

optimizations were then conducted on all models, based on the same initial structure, where one ^{29}Si atom was replaced by one ^{27}Al atom at each time. For all models, $C_4H_9N^+Me_3$ species were included to balance the negative charges near framework ^{27}Al sites, while such negative charges are generally compensated by protons in aluminosilicates as Brønsted acid sites. These structural manipulations are based on no correlations between ^{27}Al sites and proton species from Brønsted acid sites in the solid-state 2D ^{27}Al{^{1}H} HETCOR NMR spectra (Figures 3 and B3). Furthermore, solid-state ^{29}Si NMR measurements suggest that local ^{29}Si framework condensation occurs around the inserted ^{27}Al sites, motivating us to manually connect incompletely condensed framework ^{29}Si or ^{27}Al sites by replacing the two non-bridging oxygen atoms with one bridging oxygen atom located midway between the two four-coordinate sites. We applied such manipulation in all models before geometry optimization if necessary, as illustrated in Figure 7. Because two negative framework charges are removed from the above manual treatment, one surfactant molecule is excluded to maintain the whole structure charge neutral. Table B1 summarizes the computational details for each model, such as the supercell size and Si/Al ratio.

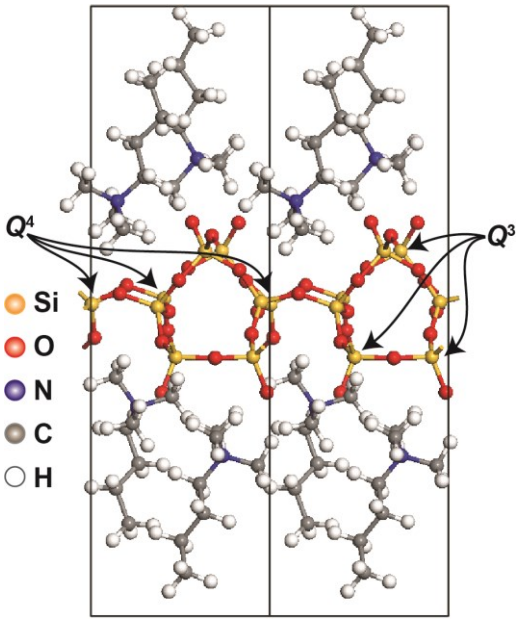

Figure 6. An example of DFT optimized models for the $C_{16}H_{33}N^{+}$**Me$_3$**-directed silicates, where there are 8 T-sites per unit cell. The negative charges are balanced by $C_4H_9N^{+}$**Me$_3$** molecules used to mimic $C_{16}H_{33}N^{+}$**Me$_3$**- surfactants and to reduce calculation time. [Courtesy: Dr. Zalfa Nour]

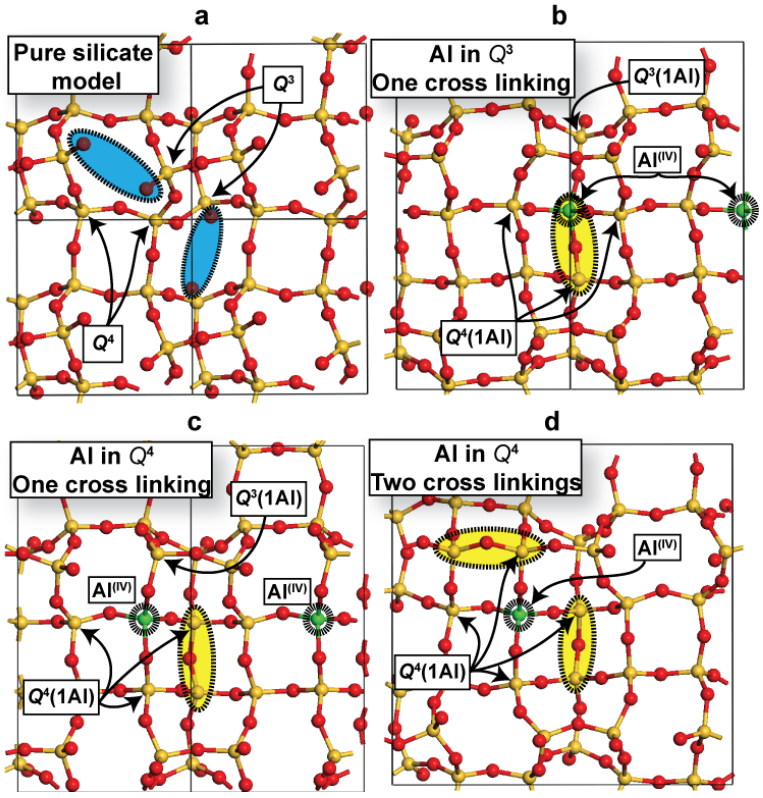

Figure 7. Optimized $C_4H_9N^+Me_3$-directed aluminosilicate models used to calculate NMR parameters under various situations. (a) $C_4H_9N^+Me_3$-directed silicate model without ^{27}Al incorporation was included as reference. (b) $C_4H_9N^+Me_3$-directed aluminosilicate model was implemented by inserting ^{27}Al atoms into $Q^3(0Al)$ ^{29}Si sites, which induces one framework condensation of the next-nearest-neighboring $Q^3(0Al)$ ^{29}Si sites. (c) $C_4H_9N^+Me_3$-directed aluminosilicate model was used by incorporating ^{27}Al atoms into $Q^4(0Al)$ ^{29}Si sites, which initiates one framework condensation between $Q^3(0Al)$ and $Q^3(1Al)$ ^{29}Si site to form $Q^4(1Al)$ ^{29}Si species. (d) $C_4H_9N^+Me_3$-directed aluminosilicate model was employed by considering that ^{27}Al atoms are inserted into $Q^4(0Al)$ ^{29}Si sites, and both next-nearest-neighboring $Q^3(1Al)$ become $Q^4(1Al)$ ^{29}Si sites via framework condensations that involve neighboring $Q^3(0Al)$ ^{29}Si sites. All the structural models shown here are viewed along c-axis, where surfactant molecules are obmitted for clarity. Solid lines delimitate the supercell used for each model. [Courtesy: Dr. Sylvian Cadars]

Three scenarios are described as for ^{29}Si structural rearrangements around the in-framework ^{27}Al sites. Figure 7a shows the highlighted Q^3 ^{29}Si sites in the $C_4H_9N^+Me_3$-directed silicate model (in blue), which would be cross-linked upon ^{27}Al incorporation. First, ^{27}Al atoms are hypothesized to insert into Q^3(0Al) ^{29}Si sites (in green), causing the ^{29}Si framework condensation between the ^{27}Al atoms and their nearest-neighbor Q^3(0Al) ^{29}Si sites (Figure 7b). Second, ^{27}Al atoms are incorporated into Q^4(0Al) ^{29}Si sites (in green), resulting into the formation of covalent bonds between the neighboring Q^3(1Al) and Q^3(0Al) ^{29}Si sites (Figure 7c). Lastly, ^{27}Al atoms substitute Q^4(0Al) ^{29}Si sites (in green), and the inserted ^{27}Al atoms lead to two framework condensations among two pairs of surrounding Q^3(1Al) and Q^3(0Al) ^{29}Si sites (Figure 7d). For the models with one cross linking, one surfactant per supercell was eliminated as compared to the siliceous structure model, whereas three surfactants per supercell must be removed to balance the negative framework charges for the case with two cross linkings. The models shown in Figure 7 were all obtained after geometry optimizations, where no Si-O-Si or Al-O-Si bond breaking is observed. This suggests that the models have reached their local energy minima, which also supports our hypotheses of local framework condensation near the incorporated ^{27}Al atoms.

In addition to the solid-state ^{29}Si CPMAS NMR results and DFT calculations, the quantitative analyses of single-pulse ^{29}Si MAS NMR spectra suggest that local polymerizations occur around framework ^{27}Al. As discussed above, the numbers of distinct ^{29}Si species were shown to be greatly influenced by the ^{27}Al loadings, which could be estimated in quantitative ^{29}Si MAS experiments. Specifically, the relative populations of various ^{29}Si species can be theoretically calculated by considering whether ^{27}Al atoms are inserted into Q^3(0Al) or Q^4(0Al) ^{29}Si sites and whether or not cross-linking takes place

between Q^3(0Al) and Q^3(1Al) ^{29}Si near framework ^{27}Al sites. Therefore, different scenarios (Figure 7) can be validated by comparing the experimental and theoretical populations of ^{29}Si moieties, both of which are plotted in percentage against the number of framework ^{27}Al atoms per 100 ^{29}Si atoms (Figure 8). It should be noticed that the Si/Al ratios used in calculations were estimated from the quantitative single-pulse ^{29}Si MAS NMR spectra, based on the total populations of Q^n(1Al) and Q^n(0Al) ^{29}Si species (where n could be 3 or 4), all of which are well resolved in the 1D ^{29}Si NMR spectra (Figure B2) and the corresponding ^{29}Si assignments are unambiguously confirmed by the 2D J-mediated ^{29}Si-^{27}Al correlation experiments (Figures 5 and B4). We believe that the NMR analyses provide the ^{27}Al contents of interest within the $C_{16}H_{33}N^+Me_3$-directed aluminosilicates, while the main uncertainty could be attributed to the relative populations of Q^n(1Al) ^{29}Si species and ^{27}Al atoms (the ratio could be between 3 and 4), depending on the locations of ^{27}Al atoms that may have 3 or 4 ^{29}Si neighbors. The corresponding results are summarized in Table 1, where one can see that the significant effects of ^{27}Al loadings on the relative populations of ^{29}Si species. Interestingly, the amount of Q^3(1Al) and Q^4(1Al) ^{29}Si sites increases as the ^{27}Al contents increase, whereas the number of Q^3(0Al) and Q^4(0Al) ^{29}Si sites decreases simultaneously. While quantitative NMR analysis shows the close correlations of ^{27}Al loadings with the distributions of ^{29}Si species, the NMR-derived Si/Al ratios do not match well with the Si/Al ratios obtained from the elemental analysis. We attribute such a discrepancy to subtle experimental errors. Also, the discrepancy might come from the assumptions used in the quantitative NMR analysis, which may not represent the complicated structural rearrangement in the real $C_{16}H_{33}N^+Me_3$-directed aluminosilicates.

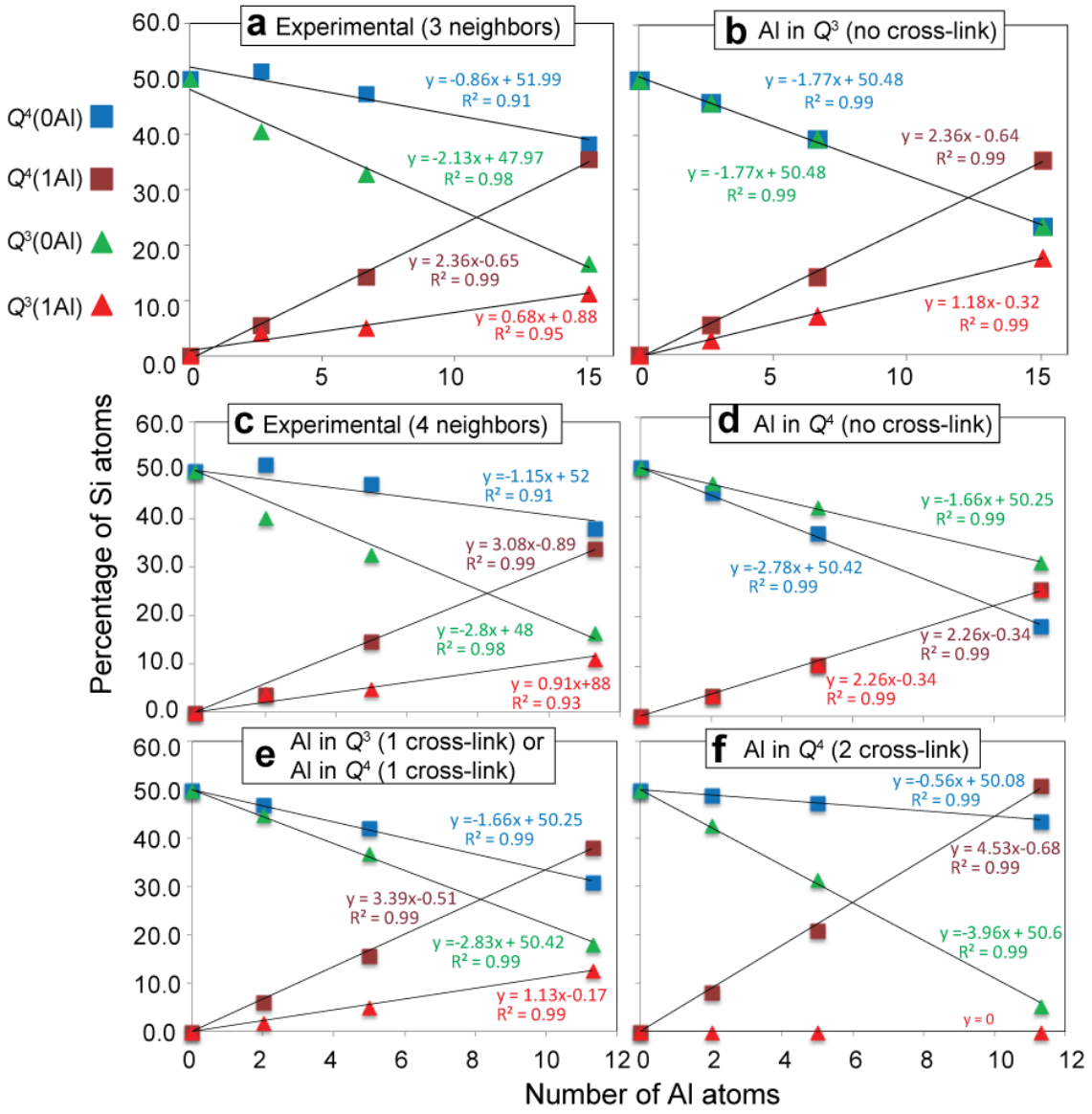

Figure 8. Structural rearrangements nearby ^{27}Al atoms in $C_{16}H_{33}N^{+}Me_3$-directed aluminosilicates are probed by correlating the ^{27}Al contents with the relative popluations of different ^{29}Si spcies from quantitative ^{29}Si NMR spectra (Figure B2) under various situations. Plots (a) and (c) show the cases of framework ^{27}Al atoms surrounded by 3 ^{29}Si neighbors and 4 ^{29}Si neighbors, respectively. Plots (b) and (d) indicate the situations, where theoretical values were calculated by considering ^{27}Al atoms incorporated into Q^3 and Q^4 ^{29}Si sites with no framework condensations nearby, respectively. Plot (e) represents the cases of ^{27}Al atoms inserted into either Q^3 or Q^4 ^{29}Si sites, which induce one framework condensation of next-nearest-neighboring Q^3 ^{29}Si sites. In both cases, three Q^4(1Al) and one Q^3(1Al) ^{29}Si species are formed at the expense of two Q^4 and three Q^3 ^{29}Si sites per incorporated ^{27}Al atom. Plot (f) demonstrates the case of ^{27}Al atoms incorporated into Q^4 ^{29}Si sites, inducing two framework condensations of next-nearest-neighboring Q^3 ^{29}Si sites. Such condensations lead to four Q^4(1Al) ^{29}Si species at the expense of one Q^4 and four Q^3

^{29}Si sites. Symbols with various colors represent different types of T-sites (see inset for details). [Courtesy: Dr. Sylvian Cadars]

Several possible ^{27}Al siting is based on the quantitative ^{29}Si NMR analyses in terms of the ^{27}Al locations in structure and the degree of polymerization between their nearby Q^3(0Al) ^{29}Si sites. The relative populations of distinct ^{29}Si sites as a function of ^{27}Al loadings are plotted in Figure 8a and c, obtained from the ^{29}Si quantitative MAS NMR spectra (Figure B2). Plots in Figure 8a and c assume that the inserted ^{27}Al atoms are surrounded by 3 and 4 ^{29}Si sites, respectively, and they both reveal similar trends, in which the number of Q^3(1Al) and Q^4(1Al) ^{29}Si sites grows as the ^{27}Al loadings increase at the expense of Q^3(0Al) and Q^4(0Al) ^{29}Si sites. However, subtle differences exist between these two situations, as revealed by their different dependence of ^{29}Si species on the ^{27}Al loadings. For instance, when the number of ^{27}Al atoms increases to 10, the fraction of Q^3(0Al) ^{29}Si sites decreases to *ca.* 26.7 and 20.0% for 3 and 4 ^{29}Si sites near framework ^{27}Al atoms, respectively. All framework ^{27}Al atoms were first considered to be inserted into either Q^3(0Al) or Q^4(0Al) ^{29}Si sites without any structural rearrangement (Figure 8b and d). In these two cases, the numbers of Q^3(1Al) and Q^3(0Al) ^{29}Si sites are both overestimated, whereas the amounts of Q^4(1Al) and Q^4(0Al) ^{29}Si sites are underestimated, indicating the presence of more locally polymerized aluminosilicate than siliceous framework. As such, the possibility of cross-linking Q^3(1Al) and/or Q^3(0Al) ^{29}Si sites has be taken into account.

Next, ^{27}Al atoms are incorporated into either Q^3(0Al) or Q^4(0Al) ^{29}Si sites, the former of which one framework ^{27}Al site condenses with its neighboring Q^3(0Al) ^{29}Si site (Figure 7b). In the latter case, the cross-linking occurs between a Q^3(1Al) ^{29}Si site and a its neighboring Q^3(0Al) ^{29}Si site (Figure 7c). Given the relative populations of ^{29}Si species,

both cases are identical, because three Q^4(1Al) and one Q^3(1Al) ^{29}Si sites would be created by consuming two Q^4(0Al) and three Q^3(0Al) ^{29}Si sites, and the incorporated ^{27}Al species are four-coordinated. The dependences of the ^{27}Al contents on ^{29}Si species are demonstrated in Figure 8e, which shows an improved agreement with the experimental values (Figure 8c). Also, it supports that local ^{29}Si framework condensation appears to occur around most of the framework ^{27}Al sites. Lastly, the third situation was proposed by incorporating ^{27}Al atoms into Q^4(0Al) ^{29}Si sites, forming two new connectivities of their nearby Q^3(1Al) and Q^3(0Al) ^{29}Si sites (Figure 7d). The corresponding dependence between ^{27}Al loadings and ^{29}Si species is shown in Figure 8f, suggesting that the third situation might not represent the realistic phenomenon in $C_{16}H_{33}N^+Me_3$-directed aluminosilicates, mainly due to its disagreement with the experimental values (Figure 8 a and c) for all ^{29}Si species, especially for the Q^3(1Al) ^{29}Si one (triangle in red).

The ^{27}Al and ^{29}Si chemical shifts calculated using all these optimized models (Figure 7) were unfortunately unable to agree with the experimental values perfectly. This could be because the calculations were conducted at 0 K on a static configuration, in which each framework ^{29}Si site "experiences" one of many possible orientations and positions of nearby $C_{16}H_{33}N^+Me_3$ molecules. The much less mobile surfactants would yield large ^{29}Si chemical shift distributions for each type of ^{29}Si site in the framework.[91] However, the $C_{16}H_{33}N^+Me_3$ molecules are highly mobile at room temperature to dynamically average the distributions of ^{29}Si chemicl shifts, leading to one relatively sharp ^{29}Si NMR signal for each ^{29}Si site. Also, the ^{27}Al chemical shifts were calculated to be between 61 and 66 ppm, as compared to an experimental shift of 54 ppm (at 20.0 T). This could also be explained by the fact that thes^{27}Al chemical shifts were calculated using static models at 0 K, aiming at simulating a

very dynamic system at 25 °C (298 K). Nevertheless, the ^{29}Si structural modification upon ^{27}Al incorporation in the aluminosilicate framework is strongly supported by the convergence of aluminosilicate models after geometrical optimization (Figure 7b-d).

Although synthesized under very similar chemical compositions as $C_{16}H_{33}N^{+}Me_3$-directed silicates except for SDA species, $C_{16}H_{33}N^{+}Me_2Et$-directed silicates consists of five distinct ^{29}Si sites.[40] Such $C_{16}H_{33}N^{+}Me_2Et$-directed silicates were chosen as another model system for investigating ^{27}Al incorporation, due to their five different ^{29}Si sites (two incompletely condensed, Q^3; three completely condensed, Q^4) that could be possibly inserted by ^{27}Al atoms, as compared to $C_{16}H_{33}N^{+}Me_3$-directed silicates (one Q^3 and one Q^4 ^{29}Si sites). In addition, it would be very interesting to understand ^{27}Al siting in this $C_{16}H_{33}N^{+}Me_2Et$-directed silicate framework, because the resulting insights are expected to be useful for zeolites that contain four- (4-MR) and six-member-rings (6-MR) as secondary building units, similar to $C_{16}H_{33}N^{+}Me_2Et$-directed silicates.[40] More importantly, the structural features of $C_{16}H_{33}N^{+}Me_2Et$-directed silicates were recently discovered to be the same as the intermediate material during the crystallization toward zeolite MFI nanosheets,[70] a technologically significant zeolite of various applications.[2,4,92,93]

Similar to $C_{16}H_{33}N^{+}Me_3$-directed aluminosilicates, powder XRD, 1D ^{29}Si, and ^{27}Al MAS NMR were conducted to characterize long-range order, local ^{29}Si, and ^{27}Al structures of $C_{16}H_{33}N^{+}Me_2Et$-directed aluminosilicates, respectively. XRD patterns (Figure 9) show several reflections associated with long-range order of $C_{16}H_{33}N^{+}Me_2Et$-directed aluminosilicates with various ^{27}Al loadings, very similar to previously reported $C_{16}H_{33}N^{+}Me_2Et$-directed silicates.[40,41] For example, the two reflections at 10.8 and 12.0 degree 2θ correspond to *d*-spacing of 0.82 and 0.74 nm, respectively. Other reflections (*e.g.*,

ca. 27 and 31 degree 2θ) are also very similar to the siliceous framework, suggesting that part of $C_{16}H_{33}N^{+}Me_2Et$-directed structures retains even after ^{27}Al incorporation.

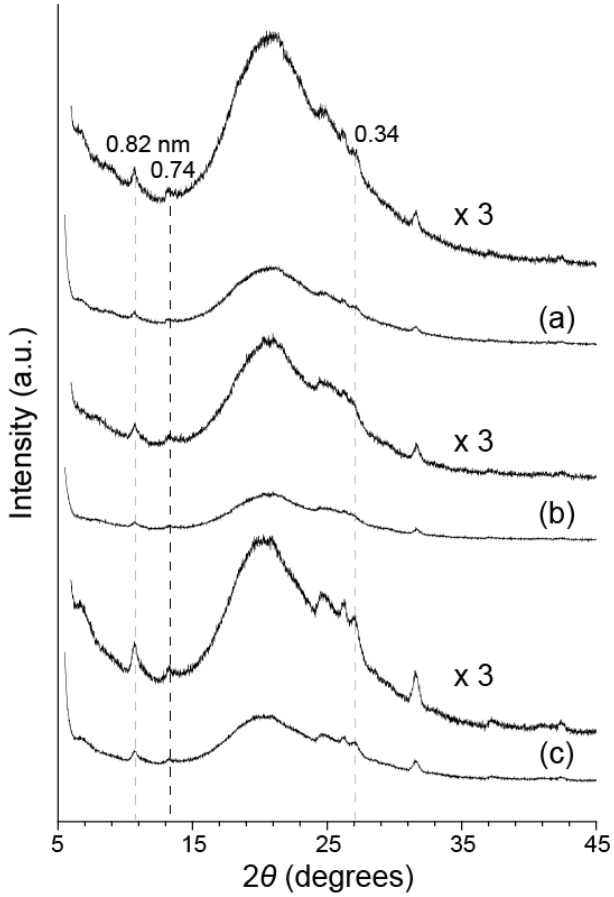

Figure 9. Wide-angle powder X-ray diffraction (XRD) patterns of as-synthesized $C_{16}H_{33}N^{+}Me_2Et$-directed aluminosilicates as a function of Al loadings: Si/Al ~ (a) 38.2, (b) 60.3, and (c) 170.

Nevertheless, limited resolution of the powder XRD patterns prevents detailed structural analysis of $C_{16}H_{33}N^{+}Me_2Et$-directed aluminosilicates, from which the ^{27}Al site distribution may be established. In contrast, 1D $^{29}Si\{^{1}H\}$ CPMAS NMR spectrum of $C_{16}H_{33}N^{+}Me_2Et$-directed aluminosilicates (Figure 10a) reveals five well resolved ^{29}Si signals at -96.8, -100.7, -103.4, -108.8, and -114.5 ppm, designated as ^{29}Si sites 1, 2, 3, 4, and 5, respectively. The ^{29}Si sites 1 and 2 are incompletely condensed $Q^3(0Al)$ ^{29}Si species,

whereas the ^{29}Si site 3, 4, and 5 belong to completely condensed Q^4(0Al) ^{29}Si species. It should be noticed that the spectral line widths (FWHM) and ^{29}Si chemical shifts of the five ^{29}Si peaks are nearly identical to the $C_{16}H_{33}N^+Me_2Et$-directed silicates,[40] suggesting a fraction of aluminosilicate structures retains after ^{27}Al incorporation (consistent with the XRD patterns). In addition to the five ^{29}Si signals, a broad ^{29}Si signal from *ca.* -90 to -120 ppm is also revealed, indicating that some local ^{29}Si environments are strongly influenced by their neighboring ^{27}Al sites, as commonly observed in zeolites.[32,33,39] Based on the XRD and 1D NMR results, it can be concluded that the $C_{16}H_{33}N^+Me_2Et$-directed aluminosilicates appear to have ^{27}Al-disturbed and -undisturbed regions in the frameworks.

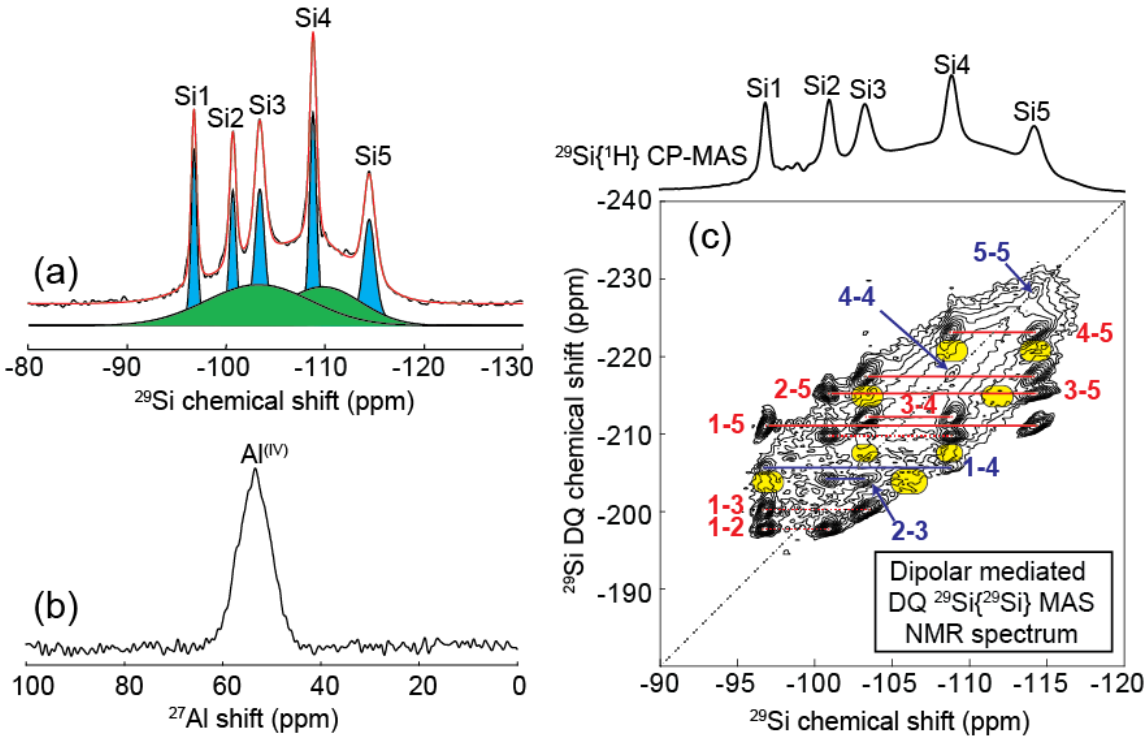

Figure 10. Solid-state (a) 1D ^{29}Si{^{1}H} CP-MAS (in black) and (b) 1D ^{27}Al echo-MAS NMR spectra, collected at 9.4 T and 17.6 T, respectively, of $C_{16}H_{33}N^+Me_2Et$-directed aluminosilicates (Si/Al ~38.2). The simulated ^{29}Si MAS spectrum modeled by Dmfit program[94] is shown in red, which includes the ^{29}Si signals of local ^{29}Si environments that are (in green) and are not under the influences of framework ^{27}Al atoms (in blue), respectively. (c) 2D dipolar-mediated ^{29}Si{^{29}Si} NMR specturm, collected at 7.0 T, 25 °C, and 4.6 kHz MAS, of ^{29}Si-enriched $C_{16}H_{33}N^+Me_2Et$-directed aluminosilicates (Si/Al ~38.2

expected), where correlation intensities (in yellow) identify ^{29}Si-O-^{29}Si connectivities that are and are not under the influences of ^{27}Al atoms. [Courtesy: Dr. Mounesha Garaga]

Local ^{27}Al surroundings of $C_{16}H_{33}N^{+}Me_2Et$-directed aluminosilicates were directly probed via 1D ^{27}Al echo-MAS measurements. The 1D ^{27}Al MAS NMR spectrum (Figure 10b) shows a broad ^{27}Al signal centered at *ca.* 53.4 ppm (FWHM, *ca.* 10 ppm), associated with four-coordinate ^{27}Al species. Interestingly, no ^{27}Al signals are observed between 0 to 30 ppm, where six-coordinate ^{27}Al species are expected to appear.[33,39,89] The only presence of four-coordinate ^{27}Al species suggests that they correspond to in-framework ^{27}Al sites. Such relatively broad ^{27}Al signal was hypothesized to result from a distribution of isotropic ^{27}Al chemical shifts and/or second-order quadrupolar couplings of ^{27}Al nuclei. To test this hypothesis, another 1D ^{27}Al MAS NMR experiment was conducted at a lower magnetic field (11.7 T), because the second-order quadrupolar interactions are proportional to the inverse of magnetic fields, which exhibits a similar ^{27}Al signal (FWHM, *ca.* 10 ppm) centered at 53.2 ppm (not shown). The 1D ^{27}Al NMR results indicate that the relatively broad linewidth of ^{27}Al signals is due to different isotropic ^{27}Al chemical shifts rather than the influences of second-order quadrupolar interactions, suggesting that ^{27}Al atoms appear to be incorporated into several ^{29}Si sites instead of one specific ^{29}Si site.

The complicated local ^{29}Si structures that may be viewed as ^{27}Al-disturbed and -undisturbed regions were further investigated using 2D ^{29}Si{^{29}Si} dipolar-mediated correlation experiments to establish molecularly proximate ^{29}Si sites, resulting from their ^{29}Si-^{29}Si dipole-dipole interactions. The 2D ^{29}Si{^{29}Si} dipolar-mediated NMR spectrum (Figure 10c) shows intensity correlations among various ^{29}Si species, manifesting various ^{29}Si site-^{29}Si site proximities. Because of the short dipolar recoupling time (3.5 ms) applied

during ^{29}Si singal acquistion, the identified proximities can be viewed as ^{29}Si site connectivities (*ca.* 3 to 4 Å from each other). Contributions from ^{29}Si site pairs of longer distances (*e.g.*, 5 Å or more) would be signicantly reduced, caused by the attenuation of dipolar truncation over such long-range contacts, especially true for isopotically ^{29}Si enriched materials. Consistent with the XRD and 1D NMR results, some local ^{29}Si environments in $C_{16}H_{33}N^{+}Me_2Et$-directed aluminosilicates are identical to the siliceous counterpart,[40,41] as revealed by several intensity correlations (in red) between ^{29}Si sites 4 ↔ 5, ^{29}Si sites 3 ↔ 5, ^{29}Si sites 2 ↔ 5, ^{29}Si sites 1 ↔ 3, and other ^{29}Si- ^{29}Si site pairs. Notice that the above ^{29}Si site pairs (in red) are in fact connected with each other. Meanwhile, relatively weaker correlations (in blue) are observed between non-boned ^{29}Si sites, such as ^{29}Si sites 1 ↔ 4, ^{29}Si sites 2 ↔ 3, and ^{29}Si sites 4 ↔ 4. Furthermore, a large broad correlation (not highlighted in colors) is shown from *ca.* -95 to -118 ppm in the ^{29}Si chemical shift dimension, consistent with the 1D ^{29}Si{^{1}H} CPMAS spectrum (Figure 10a). It suggests that part of the $C_{16}H_{33}N^{+}Me_2Et$-directed aluminosilicate structures exhibit molecularly disordered when ^{29}Si sites neighbor the framework ^{27}Al atoms, and that ^{27}Al atoms appear to be incorporated into several rather than one specific ^{29}Si site. Interestingly, the ordered ^{29}Si sites (^{27}Al-unaffected region) are molecularly proximate to the disordered ^{29}Si sites (^{27}Al-affected region), as evidenced by several correlations in yellow in the 2D ^{29}Si{^{29}Si} NMR spectrum (Figure 10c). Similarly, other intensity correlations are observed among ordered and disordered ^{29}Si sites. Nevertheless, it is very challenging to determine their proximities (or connectivities), mainly due to the severely overlapping ^{29}Si signals. According to the analyses of XRD patterns, 1D ^{29}Si and ^{27}Al NMR, and 2D ^{29}Si{^{29}Si} NMR

correlation spectra, it can be concluded that ^{27}Al incorporation causes the molecular disorder in its nearby ^{29}Si sites within $C_{16}H_{33}N^{+}Me_2Et$-directed aluminosilicates.

The presence of ^{27}Al atoms in the $C_{16}H_{33}N^{+}Me_2Et$-directed frameworks could be investigated by probing spatial interactions between the four-coordinate ^{27}Al sites and their neighboring ^{1}H moieties via solid-state 2D $^{27}Al\{^{1}H\}$ HETCOR NMR experiments. This is because the ^{27}Al incorporation would induce negative charges that are hypothesized to be balanced by cationic headgroups of $C_{16}H_{33}N^{+}Me_2Et$ molecules. Figure 11 a-d shows 2D $^{27}Al\{^{1}H\}$ HETCOR NMR spectra of $C_{16}H_{33}N^{+}Me_2Et$-directed aluminosilicates collected with different CP contact times from 0.5 to 10 ms. Relatively long CP contact times were employed to understand interactions between the four-coordinate ^{27}Al sites and the ^{1}H moieties of surfactants in particular, whereas short contact times are expected to determine strongly dipole-dipole coupled ^{27}Al and ^{1}H pairs, such as Al-OH and Al-OH-Si species. All the 2D $^{27}Al\{^{1}H\}$ NMR spectra (Figure 11a-d) exhibit a strong correlaiton involving the ^{27}Al signal (54 ppm, four-coordinate ^{27}Al sites) and one ^{1}H signal (3.4 ppm), corresponding to the protons of surfactant headgroups. These result establish strong through-space dipolar interactions between the ^{27}Al sites and surfactant headgroups. Such strong interactions with surfactant headgroups are very similar to the previous observations in the siliceouse counterpart,[40] providing a strong evidence of considering the four-coordinate ^{27}Al species framework ^{27}Al sites. In addition, a much weaker correlation is visible at a ^{1}H signal (1.4 ppm), associated with the α-CH_2 group of alkyl-ammonium surfactant chain, with respect to the same ^{27}Al signal (54 ppm) when the CP contact time (6 ms) was used (see Figure 11c). More importantly, the same ^{27}Al signal (54 ppm) does not exhibit correlated intensities with ^{1}H signals associated with other ^{1}H species, such as Al-OH, Si-OH, and Al-OH-Si. This fact

indicates that the negative charges near framework ^{27}Al sites are balanced by the cationic surfactant headgroups ($C_{16}H_{33}N^{+}$**Me$_2$Et**).

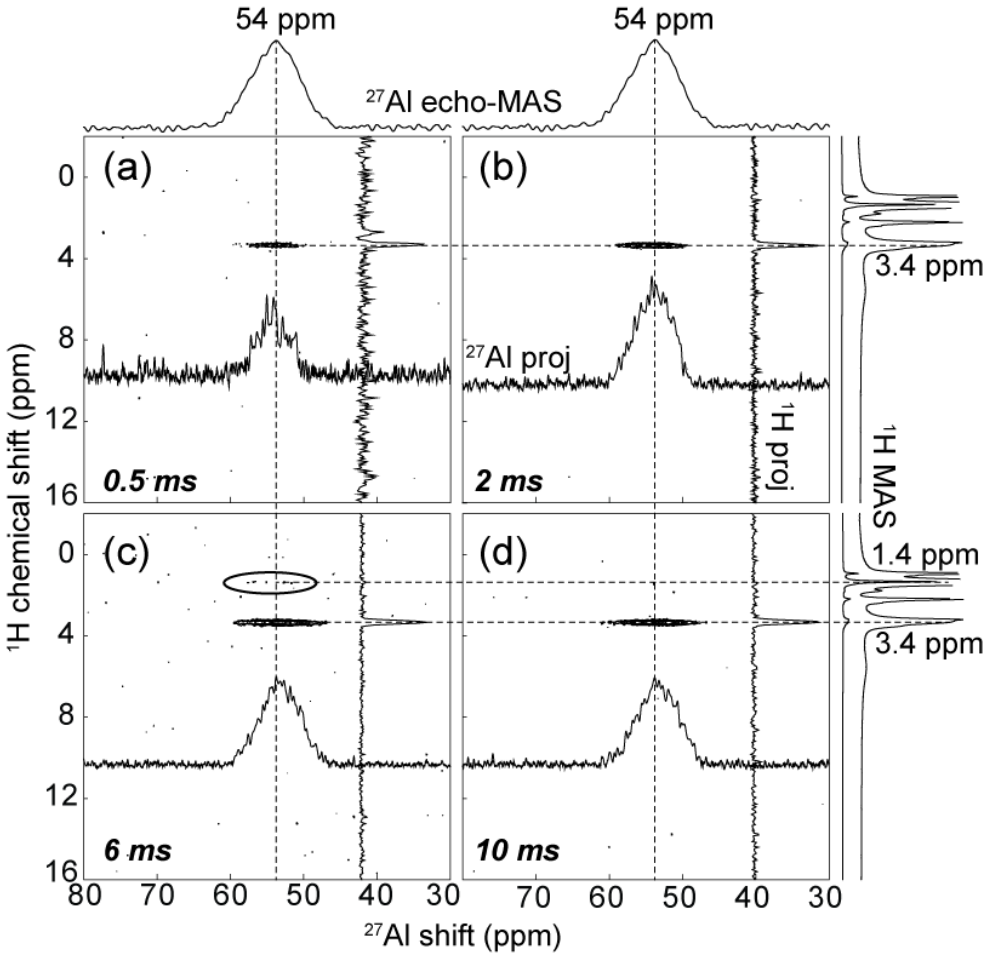

Figure 11. Solid-state 2D ^{27}Al{^{1}H} HETCOR NMR spectra of as-synthesized $C_{16}H_{33}N^{+}Me_2Et$-directed aluminosilicates (Si/Al ~38.2), collected at 20.0 T, 25 °C, and 18 kHz MAS with CP contact time of (a) 0.5, (b) 2, (c) 6, and (d) 10 ms, respectively. Solid-state 1D ^{27}Al echo and 1D ^{1}H MAS NMR spectra are shown along the top horizontal and the right vertical axis, respectively. [Courtesy: Dr. Mounesha Garaga]

Similar to the $C_{16}H_{33}N^{+}Me_3$-directed aluminosilicates, direct information regarding ^{27}Al siting in the $C_{16}H_{33}N^{+}Me_2Et$-directed aluminosilicates could be obtained using solid-state 2D ^{27}Al{^{29}Si} *J*- (through-bond) and dipolar-mediated (through-space) NMR measurements, which would detect connected and proximate ^{27}Al-^{29}Si pairs, respectively.

Here, a 2D $^{27}Al\{^{29}Si\}$ dipolar-mediated HMQC NMR spectrum was successfully acquired on $C_{16}H_{33}N^{+}Me_2Et$-directed aluminosilicates with natural abundance of ^{29}Si (*ca.* 4.7%) to demonstrate the applicability of this through-space experiment, despite the low Al contents (Si/Al ~ 60) and limited ^{29}Si NMR signal sensitivity (Figure 12). This opens the possibilties to exploit ^{27}Al siting within ^{27}Al heteroatom-containing zeolites (or other related materials) at a molecular level. A broad correlation is observed between the ^{27}Al signal (centered at *ca.* 54 ppm) and various ^{29}Si signals (from -98 to -114 ppm), indicating that the four-coordinate ^{27}Al sites are molecularly surrounded by these different corresponding ^{29}Si sites. Given the employed $^{27}Al\{^{29}Si\}$ recoupling duration (5.2 ms), most of the ^{27}Al-^{29}Si pairs are expected to be within their first and second coordination shell structure. Nevertheless, it is extremely difficult to precisely determine the ^{27}Al siting of $C_{16}H_{33}N^{+}Me_2Et$-directed aluminosilicate structures, only based on this 2D $^{27}Al\{^{29}Si\}$ NMR spectrum (Figure 12). The broad correlation suggests that ^{27}Al atoms appear to be non-preferentially distributed among different ^{29}Si sites. Similar signal broadening is found in the 1D $^{29}Si\{^{27}Al\}$ dipolar-mediated CP-HMQC spectrum (shown in red and the horizontal dimension, Figure 12), which directly detects the ^{29}Si signal to understand spatially coupled ^{29}Si-^{27}Al pairs. This fact reveals that the ^{27}Al neighboring ^{29}Si sites are molecularly disordered. Furthermore, this 1D $^{29}Si\{^{27}Al\}$ CP-HMQC NMR signal is centered *ca.* -106 ppm (that genetrally corresponds to Q^4(1Al) ^{29}Si species) with little or no signal intensity at -95 ppm (Q^3(1Al) ^{29}Si species). The absence of ^{29}Si signals associated with Q^3(1Al) ^{29}Si species suggests that local ^{29}Si structural modification occurs upon ^{27}Al incorporation, because one or two neighboring Q^3(0Al) are expected to become Q^3(1Al) ^{29}Si sites if ^{27}Al atoms are inserted into one of the five ^{29}Si site.[40,41]

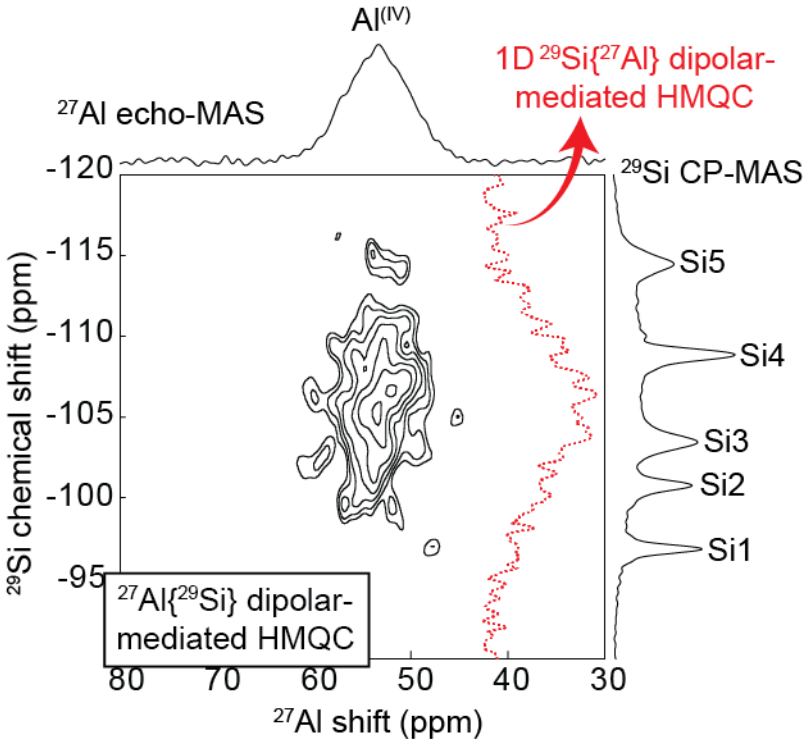

Figure 12. Solid-state 2D dipolar-mediated HMQC $^{27}Al\{^{29}Si\}$ NMR spectrum, collected at 17.6 T, 25° C, and 7.5 kHz MAS, of as-synthesized $C_{16}H_{33}N^{+}Me_2Et$-directed aluminosilicates (Si/Al ~38.2). The ^{29}Si CP and ^{27}Al MAS NMR spectra are showed along the right vertical and the top horizontal axis, respectively. 1D $^{29}Si\{^{27}Al\}$ dipolar-mediated CP-HMQC spectrum collected at 17.6 T is displayed horizontally (in red). [Courtesy: Dr. Mounesha Garaga]

Due to the low ^{29}Si natural abundance (4.7%), $C_{16}H_{33}N^{+}Me_2Et$-directed aluminosilicate was synthesized with ^{29}Si enrichment to greatly improve ^{29}Si NMR signal sensitivity, aiming at resolving detailed ^{27}Al-^{29}Si site connectivities and proximities that are difficult to observe on $C_{16}H_{33}N^{+}Me_2Et$-directed aluminosilicates of ^{29}Si natural abundance. The 1D ^{27}Al echo-MAS and $^{29}Si\{^{1}H\}$ CP-MAS NMR spectra of ^{29}Si-enriched $C_{16}H_{33}N^{+}Me_2Et$-directed aluminosilicates (Figure 13) are almost identical to those of aluminosilicates with ^{29}Si in natural abundance (Figure 10 a-b), indicating the similar local ^{27}Al and ^{29}Si environments regardless of ^{29}Si enrichment. A relatively shorter ^{27}Al-^{29}Si dipolar recoupling

time (2.25 instead of 5.20 ms) was applied in the 2D ^{27}Al{^{29}Si} dipolar-mediated HMQC NMR measurement (Figure 13). Therefore, the visible correlations are expected to reveal the ^{27}Al-O-^{29}Si site connectivities exclusively. Nevertheless, contributions from non-bonded ^{27}Al and ^{29}Si species cannot be ruled out entirely. Similar to the previously discussed 2D ^{27}Al{^{29}Si} dipolar-mediated NMR spectrum (Figure 12), a broad correlation is observed between the ^{27}Al singal (centered at 52 ppm, four-coordinate ^{27}Al sites) and several ^{29}Si signals from -98 to -112 ppm (Figure 13), whereas no ^{29}Si signals corresponding to Q^3(1Al) ^{29}Si species are found to correlate with any ^{27}Al signals. Again, such broad correlations suggest that ^{27}Al atoms are non-preferentially distributed among several rather than one specific ^{29}Si sites in the $C_{16}H_{33}N^{+}Me_2Et$-directed frameworks. However, based on the broad ^{27}Al{^{29}Si} correlations here, it is very challenging to perform reliable deconvolution analyses of ^{27}Al site distributions.

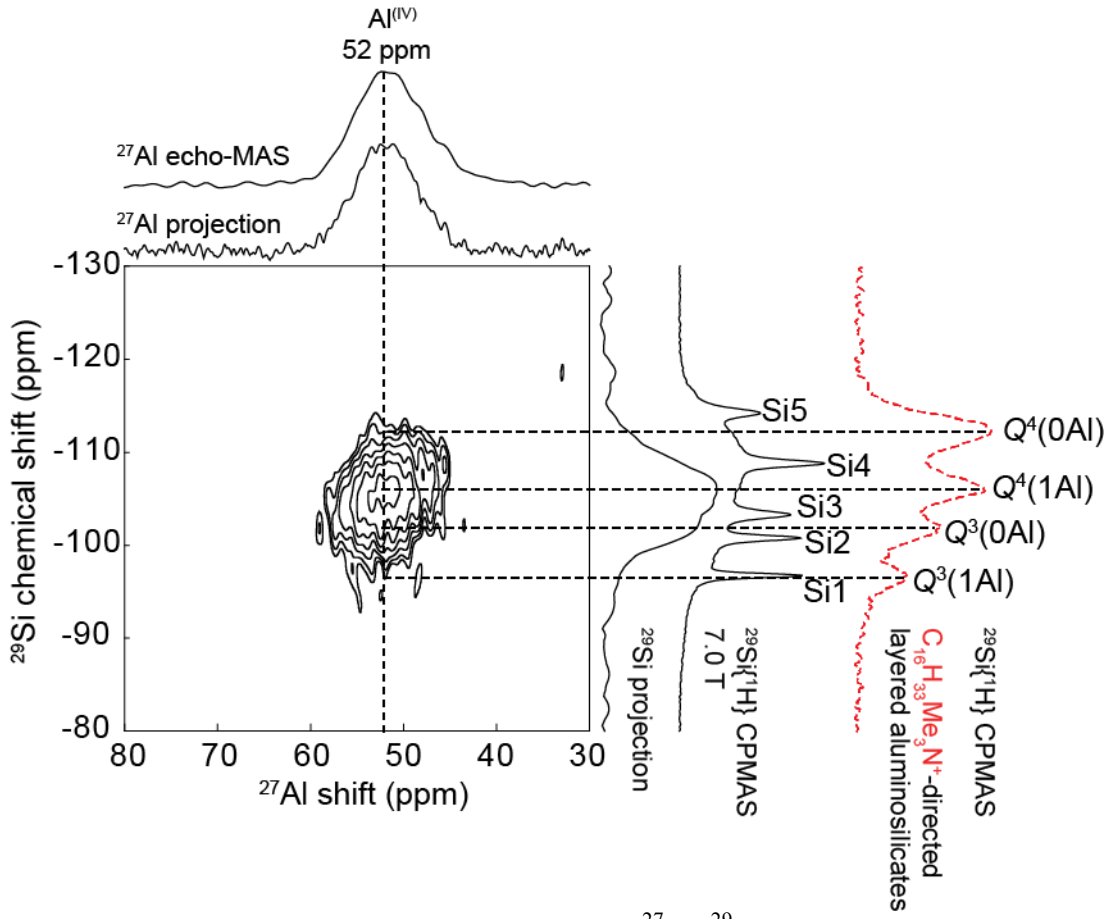

Figure 13. Solid-state 2D dipolar-mediated HMQC ^{27}Al{^{29}Si} NMR spectrum, collected at 11.7 T, 25 C and 8 kHz MAS, of ^{29}Si-enriched as-synthesized $C_{16}H_{33}N^{+}Me_2Et$-directed aluminosilicates (Si/Al ~38.2 expected). The 1D ^{27}Al echo-MAS and ^{29}Si{^{1}H} CP-MAS NMR spectra and the corresponding projections are shown along the top horizontal and the right vertical axis, respectively. 1D ^{29}Si{^{1}H} CP-MAS NMR spectrum of $C_{16}H_{33}N^{+}Me_3$-directed aluminosilicates is shown (in red) horizontally as reference.

The absence of Q^3(1Al) ^{29}Si species in the $C_{16}H_{33}N^{+}Me_2Et$-directed aluminosilicates is different from the $C_{16}H_{33}N^{+}Me_3$-directed aluminosilicates by comparing their 1D ^{29}Si{^{1}H} CP-MAS NMR spectra (Figure 13). Local ^{29}Si environments are found to be strongly influenced by their nearby ^{27}Al atoms, which would typically displace corresponding ^{29}Si NMR resonances by *ca.* 5 ppm per ^{27}Al neighbor to higher frequencies in the ^{29}Si dimension.[33,39,95] It should be noticed that this may not be a general trend and depends on Si-O-Al bond angles and lengths in aluminosilicate materials. In other words, displacement

of ^{29}Si chemical shift might not be the exact 5 ppm per ^{27}Al neighbor. According to ^{29}Si NMR spectra of zeolites, ^{29}Si chemical shifts of Q^4(0Al), Q^4(1Al), Q^3(0Al), and Q^3(1Al) ^{29}Si species are expected to be centered around -110, -105 -100 and -95 ppm, respectively.[33,39,95] These expected ^{29}Si signals are nicely illustrated by the 1D ^{29}Si{^{1}H} CP-MAS NMR spectrum of $C_{16}H_{33}N^+Me_3$-directed aluminosilicates (shown in red, Figure 13). The absence of ^{29}Si signals at *ca.* -95 ppm (Q^3(1Al) ^{29}Si species) for $C_{16}H_{33}N^+Me_2Et$-directed aluminosilicates suggests the local ^{29}Si structural modification occurs upon ^{27}Al incorporation. The fact points out that the framework ^{27}Al species are only bonded to Q^4(1Al) ^{29}Si sites, similar to the case of $C_{16}H_{33}N^+Me_3$-directed aluminosilicates. The hypothesis of local ^{29}Si structural modification is also supported by the previously established ^{29}Si-^{29}Si site connectivities of $C_{16}H_{33}N^+Me_2Et$-directed silicates,[41,74] from which at least one Q^3(1Al) ^{29}Si site is expected to connect with ^{27}Al sites whatever Q^3(0Al) and/or Q^4(0Al) ^{29}Si species are substituted by ^{27}Al atoms. Several possible ^{29}Si sites replaced by ^{27}Al atoms and the resulting ^{29}Si framework condensation are further explored using theoretical calculation below.

The NMR parameters of $C_{16}H_{33}N^+Me_2Et$-directed aluminosilicates were computed by first principle calculations to compare simulated with the experimental results. Agreement between the experimental and calculated NMR results allows different structural constraints to be evaluated. Three models (from the possible structures of $C_{16}H_{33}N^+Me_2Et$-directed silicates denoted as 2, 3, and 4[74]) were employed in our calculations with one ^{27}Al atom successively substituting one of possible crystallographic ^{29}Si sites. For each model, the silicate framework is composed of a unit cell with 10 ^{29}Si sites (related two by two by symmetry). Similar to the $C_{16}H_{33}N^+Me_3$-directed aluminosilicates, $C_4H_9N^+Me_2Et$ surfactant

molecules with shorter alkyl chains were included in the interlayer space for all models to mimic the charge-compensating surfactant molecules ($C_{16}H_{33}N^{+}Me_2Et$) and to save computational time. Geometry optimizations were conducted on these model structures to calculate NMR parameters after one of the 10 ^{29}Si sites in $C_4H_9N^{+}Me_2Et$-directed aluminosilicate model was manually replaced by one ^{27}Al atom. The calculations were then performed separately for all the three candidate structures by successively incorporating one ^{27}Al atom into each ^{29}Si site (*i.e.*, Si1, Si2, Si3, Si4 and Si5). The negative charges near framework ^{27}Al atoms are compensated by adding protons (1) to the non-bridging oxygen atoms connected to the ^{27}Al sites if they are incompletely condensed or (2) to the non-bridging oxygen atoms of ^{27}Al-connected Q^3(1Al) ^{29}Si sites if ^{27}Al sites are completely condensed. This is because the unit cell is not large enough to accommodate an additional surfactant molecule ($C_4H_9N^{+}Me_2Et$) for charge compensation, while the 2D ^{27}Al{^{1}H} HETCOR NMR spectra (Figure 11) do not show the presence of such hydroxyl groups. An example of the $C_4H_9N^{+}Me_2Et$-directed aluminosilicate model is shown in Figure B5, where ^{27}Al atoms are inserted into ^{29}Si site Si1 and protons are added directly to ^{27}Al sites via bridging oxygen atoms (*i.e.*, Al-O-H).

The framework ^{27}Al sites have substantial influences on their nearby ^{29}Si sites, as reflected by downfield shifts with respect to the original ^{29}Si chemical shifts,[95] including $C_{16}H_{33}N^{+}Me_2Et$-directed aluminosilicates here. To assign the possible ^{27}Al site locations in $C_{16}H_{33}N^{+}Me_2Et$-directed aluminosilicates, various situations were simulated by considering ^{27}Al atoms incorporated into different ^{29}Si sites. For example, suppose that ^{27}Al atom is inserted into ^{29}Si site 1, the calculated ^{29}Si chemical shifts are plotted against the experimental values (Figure 14a), where distinct crystallographic ^{29}Si sites are colored

differently, and the open triangle and circle symbols refer to ^{29}Si(1Al) and ^{29}Si(0Al) species, respectively. Specifically, calculated ^{29}Si chemical shifts exhibit a large distribution (from *ca.* 5 to 13 ppm) for each distinct ^{29}Si site, independent of whether or not they are connected to ^{27}Al atoms. This could be attributed to the static models used in all DFT calculations, which only allows each ^{29}Si site to experience one of many possible positions and orientations of alkyl-ammonium surfactant head groups ($C_4H_9N^+$**Me_2Et**). In contrast, the motions of surfactant head groups at ambient temperature are so rapid, compared to the ^{29}Si NMR experimental timescale (*i.e.*, 10^{-8} s), to dynamically average these possible positions and orientations of head groups, as previously established for the siliceous counterpart.[91] Consequently, distributed ^{29}Si chemical shifts for each ^{29}Si site are averaged to yield a single ^{29}Si NMR frequency. As temperature decreases to 0 °C or lower, the ^{29}Si NMR spectral linewidths of these five ^{29}Si signals start to broaden considerably (even to largely overlap) due to the slow motions of head groups. Such slow motions lead to distributions of ^{29}Si chemical shifts for each ^{29}Si site. Similar scenario occurs in the theoretical ^{29}Si chemical shift computation, making the absolute values from calculations less reliable, because the results depend a lot on the local energy minimization with nearby surfactant molecules. Nevertheless, the computed ^{29}Si chemical shifts at least verify the influences of framework ^{27}Al sites on their neighboring ^{29}Si environments, as revealed by downfield shifts of ^{29}Si chemical shifts.

Similar calculations were conducted by substituting ^{27}Al atoms into one of the five distinct ^{29}Si sites each time for three possible $C_{16}H_{33}N^+Me_2Et$-directed silicate structures. The results are summarized in Figure 14b by plotting the average calculated ^{29}Si chemical shifts, obtained from incorporating ^{27}Al atoms into one specific ^{29}Si site in the three

candidate structures, against the experimental values. Interestingly, the average calculated ^{29}Si chemical shift of ^{29}Si(1Al) is 5.9 ppm higher than that of the ^{29}Si(0Al) species for these five distinct ^{29}Si sites. Such displaced ^{29}Si chemical shifts to higher frequencies strongly support the influences of ^{27}Al atoms on their nearby ^{29}Si sites in the first coordination shell. This suggests that the DFT calculations are robust to exploit the extent of chemical interactions between neighboring ^{29}Si and ^{27}Al environment. A notable point is that the large distributions of ^{29}Si chemical shifts, calculated using static models, are less reliable and should be considered with much caution. On the basis of the above NMR experimental and theoretical results, we conclude that ^{27}Al atoms are non-selectively incorporated into different crystallographic ^{29}Si sites in $C_{16}H_{33}N^{+}Me_2Et$-directed frameworks.

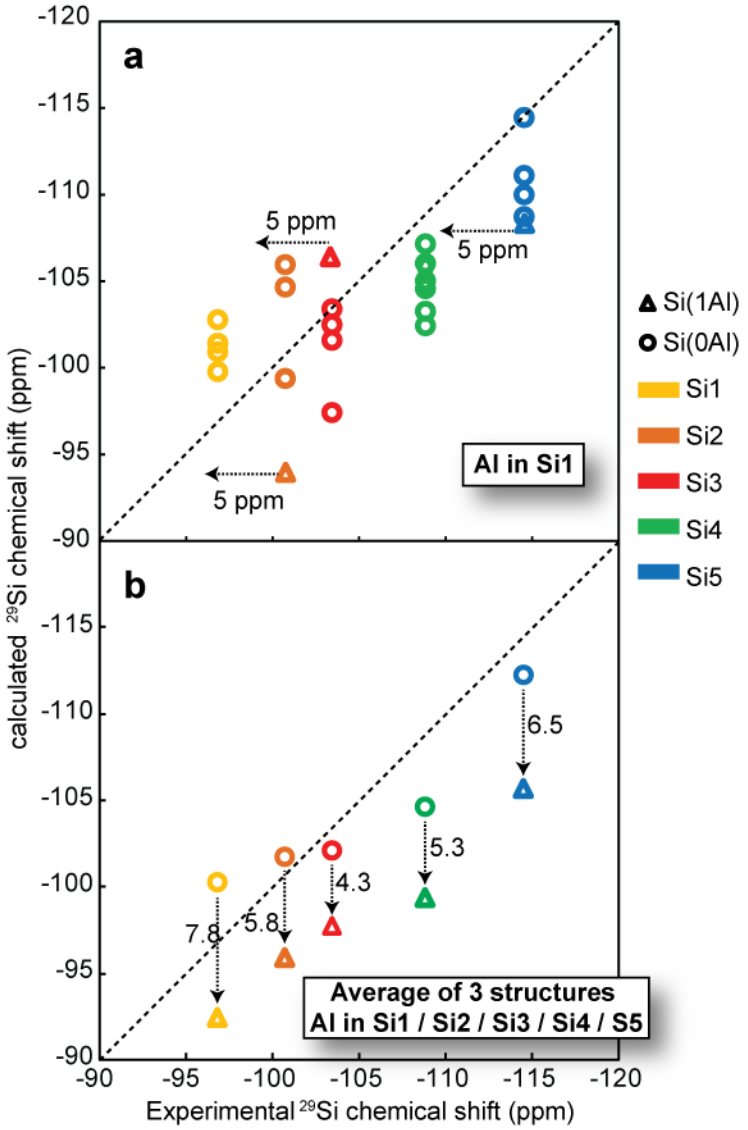

Figure 14. Calculated ^{29}Si chemical shifts are compared with experimental results in the case of $C_{16}H_{33}N^{+}$**Me$_2$Et**-directed aluminosilicates, where the DFT calculations were conducted using three plane-wave optimized structural models. (a) A specific example is shown in the case of ^{27}Al atoms inserted into ^{29}Si site Si1. (b) A summary plot shows the average ^{29}Si chemical shifts obtained from the three structural models by considering ^{27}Al atoms incorporated into distinct crystallographic sites. The color of symbols triangle (Si(0Al)) and circle (Si(1Al)) represents different types of crystallographic sites: Si1 (yellow), Si2 (orange), Si3 (red), Si4 (green), and Si5 (blue). [Courtesy: Dr. Zalfa Nour]

The non-selective ^{27}Al atom distributions in the $C_{16}H_{33}N^{+}Me_3$- and $C_{16}H_{33}N^{+}Me_2Et$-directed aluminosilicates may be explained by the role of ^{27}Al species in the crystallization, where ^{29}Si and ^{27}Al sources interact strongly with surfactant SDA molecules under alkaline conditions to form the two surfactant-directed aluminosilicates. It was hypothesized that ^{27}Al species start to react with ^{29}Si reagents in the early stage of crystallization, and such complicated reactions between ^{27}Al and ^{29}Si species have continued over the course of crystallization, resulting into the observations of non-selective ^{27}Al atom distributions in both aluminosilicates. In contrast with the case of aluminosilicates, ^{11}B atoms were shown to be preferentially inserted into certain framework sites in the associated borosilicate counterparts. These results suggest that ^{11}B and ^{27}Al species participate differently during crystallization. Our hypothesis is very similar to the reported observations in boro- and aluminosilicate zeolite synthesis.[96,97]

3.5 Conclusions

The molecular interactions involving ^{1}H moieties of SDA molecules as well as ^{29}Si and ^{27}Al sites in $C_{16}H_{33}N^{+}Me_3$- and $C_{16}H_{33}N^{+}Me_2Et$-directed aluminosilicate frameworks are shown to be similar, as identified by solid-state multidimensional NMR spectroscopy. Specifically, solid-state 2D dipolar- (through-space) and *J*-mediated (through-bond) NMR measurements yield insights into molecular proximities and site connectivities of ^{29}Si-O-^{29}Si as well as ^{27}Al-O-^{29}Si site pairs, respectively, including short-range interactions between ^{27}Al sites and the SDA molecules. For example, the head groups of $C_{16}H_{33}N^{+}Me_3$ and $C_{16}H_{33}N^{+}Me_2Et$ surfactant molecules were determined to be molecularly proximate to four-coordinate ^{27}Al species in $C_{16}H_{33}N^{+}Me_3$- and $C_{16}H_{33}N^{+}Me_2Et$-directed aluminosilicates,

respectively via 2D dipolar-mediated $^{27}Al\{^{1}H\}$ NMR techniques. Notably, 2D *J*-mediated $^{27}Al\{^{29}Si\}$ NMR spectra unambiguously confirm the presence of framework ^{27}Al sites in $C_{16}H_{33}N^{+}Me_3$- and $C_{16}H_{33}N^{+}Me_2Et$-directed aluminosilicates, based on through-bond couplings of ^{27}Al and ^{29}Si sites. Interestingly, ^{27}Al atoms are found to be non-selectively distributed among distinct sites in both aluminosilicates, where ^{27}Al incorporation appears to induce the local ^{29}Si structural rearrangements nearby framework ^{27}Al sites. The influences of ^{27}Al species on their next-nearest-neighbor ^{29}Si sites were further modeled using DFT calculations, yielding that the extent of such influence can be revealed by displacements of ^{29}Si signals to high frequencies. Overall, this report demonstrates applications of newly modified 2D NMR techniques and their beautiful combinations with theoretical calculations in the characterization of ^{27}Al site distributions in aluminosilicates at the molecular-level. More importantly, such molecular understanding of ^{27}Al site distributions are expected to aid rational synthesis of aluminosilicate zeolite catalysts, aiming to enable correlation of bulk catalytic and adsorption properties with relevant active sites in zeolitic materials.

3.6 References

1. Corma, A. From Microporous to Mesoporous Molecular Sieve Materials and Their Use in Catalysis. *Chem. Rev.* **97,** 2373–2419 (1997).

2. Degnan, T. F. The implications of the fundamentals of shape selectivity for the development of catalysts for the petroleum and petrochemical industries. *J. Catal.* **216,** 32–46 (2003).

3. Chang, C. D. & Silvestri, A. J. The Conversion of Methanol and Other O-Compounds to Hydrocarbons over Zeolite Catalysts. *J. Catal.* **47,** 249–259 (1977).

4. Busca, G. Acid catalysts in industrial hydrocarbon chemistry. *Chem. Rev.* **107,** 5366–5410 (2007).

5. Boria, M. & Dutta, P. K. Storgae of light energy by photoelectron transfer across a sensitized zeolite-solution interface. *Nature* **362,** 43–45 (1993).

6. García, H. & Roth, H. D. Generation and reactions of organic radical cations in zeolites. *Chem. Rev.* **102,** 3947–4007 (2002).

7. Varoon, K. *et al.* Dispersible Exfoliated Zeolite Nanosheets and Their Application as a Selective Membrane. *Science (80-.).* **334,** 72–75 (2011).

8. Tsapatsis, M. Materials science. Toward high-throughput zeolite membranes. *Science* **334,** 767–768 (2011).

9. Zhang, X. *et al.* Synthesis of self-pillared zeolite nanosheets by repetitive branching. *Science (80-.).* **336,** 1684–1687 (2012).

10. Lin, L.-C. *et al.* In silico screening of carbon-capture materials. *Nat. Mater.* **11,** 633–641 (2012).

11. Kim, J., Abouelnasr, M., Lin, L.-C. & Smit, B. Large-scale screening of zeolite structures for CO2 membrane separations. *J. Am. Chem. Soc.* **135,** 7545–7552 (2013).

12. Martínez, C. & Corma, A. Inorganic molecular sieves: Preparation, modification and industrial application in catalytic processes. *Coord. Chem. Rev.* **255,** 1558–1580 (2011).

13. *Zeolites and Catalysis: Synthesis Reactions and Applications*. (Wiley-VCH, 2010). doi:10.1002/9783527630295

14. Cundy, C. S. & Cox, P. A. The hydrothermal synthesis of zeolites: history and development from the earliest days to the present time. *Chem. Rev.* **103,** 663–702 (2003).

15. Cundy, C. S. & Cox, P. A. The hydrothermal synthesis of zeolites: Precursors, intermediates and reaction mechanism. *Microporous Mesoporous Mater.* **82,** 1–78 (2005).

16. Davis, M. E. Ordered porous materials for emerging applications. *Nature* **417,** 813–821 (2002).

17. Dědeček, J., Sobalík, Z. & Wichterlová, B. Siting and Distribution of Framework Aluminium Atoms in Silicon-Rich Zeolites and Impact on Catalysis. *Catal. Rev. - Sci. Eng.* **54,** 135–223 (2012).

18. Dedecek, J., Balgova, V., Pashkova, V., Klein, P. & Wichterlová, B. Synthesis of ZSM-5 Zeolites with Defined Distribution of Al Atoms in the Framework and Multinuclear MAS NMR Analysis of the Control of Al Distribution. *Chem. Mater.* **24,** 3231–3239 (2012).

19. Gounder, R. & Iglesia, E. Effects of partial confinement on the specificity of monomolecular alkane reactions for acid sites in side pockets of mordenite. *Angew. Chem. Int. Ed. Engl.* **49,** 808–11 (2010).

20. Gounder, R. & Iglesia, E. Catalytic consequences of spatial constraints and acid site location for monomolecular alkane activation on zeolites. *J. Am. Chem. Soc.* **131,** 1958–71 (2009).

21. Janda, A. & Bell, A. T. Effects of Si/Al Ratio on the Distribution of Framework Al and on the Rates of Alkane Monomolecular Cracking and Dehydrogenation in H-MFI. *J. Am. Chem. Soc.* **135,** 19193–19207 (2013).

22. Jones, A. J., Carr, R. T., Zones, S. I. & Iglesia, E. Acid strength and solvation in catalysis by MFI zeolites and effects of the identity, concentration and location of framework heteroatoms. *J. Catal.* **312,** 58–68 (2014).

23. Lobo, R. F., Zones, S. I. & Davis, M. E. Structure-Direction in Zeolite Synthesis. *J. Incl. Phenom. Mol. Recognit. Chem.* **21,** 47–78 (1995).

24. Davis, M. E. & Lobo, R. F. Zeolite and Molecular Sieve Synthesis. *Chem. Mater.* **4,** 756–768 (1992).

25. Pinar, A. B., Márquez-Álvarez, C., Grande-Casas, M. & Pérez-Pariente, J. Template-controlled acidity and catalytic activity of ferrierite crystals. *J. Catal.* **263,** 258–265 (2009).

26. Román-Leshkov, Y., Moliner, M. & Davis, M. E. Impact of Controlling the Site Distribution of Al Atoms on Catalytic Properties in Ferrierite-Type Zeolites †. *J. Phys. Chem. C* **115,** 1096–1102 (2011).

27. Márquez-Alvarez, C., Pinar, A. B., García, R., Grande-Casas, M. & Pérez-Pariente, J. Influence of Al Distribution and Defects Concentration of Ferrierite Catalysts Synthesized From Na-Free Gels in the Skeletal Isomerization of n-Butene. *Top. Catal.* **52,** 1281–1291 (2009).

28. Sastre, G., Fornes, V. & Corma, A. On the Preferential Location of Al and Proton Siting in Zeolites: A Computational and Infrared Study. *J. Phys. Chem. B* **106,** 701–708 (2002).

29. Cromer, D. T. & Liberman, D. Relativistic Calculation of Anomalous Scattering Factors for X Rays. *J. Phys. Chem.* **53,** 1891–1898 (1970).

30. Van Bokhoven, J. A. *et al.* Determining the aluminium occupancy on the active T-sites in zeolites using X-ray standing waves. *Nat. Mater.* **7,** 551–555 (2008).

31. Xie, D. *et al.* Optimized Synthesis and Structural Characterization of the Borosilicate MCM-70. *J. Phys. Chem. C* **113,** 9845–9850 (2009).

32. Fyfe, C. A., Feng, Y., Grondey, H., Kokotailo, G. T. & Gies, H. One- and Two-Dimensional High-Resolution Solid-State NMR Studies of Zeolite Lattice Structures. *Chem. Rev.* **91,** 1525–1543 (1991).

33. Koller, H. & Weiß, M. Solid state NMR of porous materials : zeolites and related materials. *Top. Curr. Chem.* **306,** 189–227 (2012).

34. Zhang, W., Xu, S., Han, X. & Bao, X. In situ solid-state NMR for heterogeneous catalysis: a joint experimental and theoretical approach. *Chem. Soc. Rev.* **41,** 192–210 (2012).

35. Roth, W. J. & Čejka, J. Two-dimensional zeolites: dream or reality? *Catal. Sci. Technol.* **1,** 43–53 (2011).

36. Marler, B. & Gies, H. Hydrous layer silicates as precursors for zeolites obtained through topotactic condensation: a review. *Eur. J. Mineral.* **24,** 405–428 (2012).

37. Ramos, F. S. O., Pietre, M. K. De & Pastore, H. O. Lamellar zeolites: an oxymoron? *RSC Adv.* **3,** 2084–2111 (2013).

38. Roth, W. J., Nachtigall, P., Morris, R. E. & Cejka, J. Two-Dimensional Zeolites: Current Status and Perspectives. *Chem. Rev.* **114,** 4807–4837 (2014).

39. Engelhardt, G. & Michel, D. *High-Resolution Solid-State NMR of Silicates and Zeolites*. (Wiley, 1987).

40. Christiansen, S. C. *et al.* Molecularly ordered inorganic frameworks in layered silicate surfactant mesophases. *J. Am. Chem. Soc.* **123,** 4519–4529 (2001).

41. Hedin, N. *et al.* Structure of a surfactant-templated silicate framework in the absence of 3d crystallinity. *J. Am. Chem. Soc.* **126,** 9425–32 (2004).

42. Galve, A. *et al.* Structural study on the Al distribution in zeolites Nu-6(1) and Nu-6(2). *Microporous Mesoporous Mater.* **145,** 211–216 (2011).

43. Roth, W. J., Gil, B. & Marszalek, B. Comprehensive system integrating 3D and 2D zeolite structures with recent new types of layered geometries. *Catal. Today* (2013). doi:10.1016/j.cattod.2013.09.032

44. Chlubna, P. *et al.* 3D to 2D Routes to Ultrathin and Expanded Zeolitic Materials. *Chem. Mater.* **25,** 542–547 (2013).

45. Corma, A., Fornes, V., Martinez-Triguero, J. & Pergher, S. B. Delaminated Zeolites : Combining the Benefits of Zeolites and Mesoporous Materials for Catalytic Uses. *J. Catal.* **63,** 57–63 (1999).

46. Corma, A. *et al.* Preparation , characterisation and catalytic activity of ITQ-2 , a delaminated zeolite. *Microporous Mesoporous Mater.* **38,** 301–309 (2000).

47. Corma, A., Fornes, V., Pergher, S. B., Maesen, T. L. M. & Buglass, J. G. Delaminated zeolite precursors as selective acidic catalysts. *Nature* **396,** 353–356 (1998).

48. Juttu, G. G. & Lobo, R. F. Characterization and catalytic properties of MCM-56 and MCM-22 zeolites. *Microporous Mesoporous Mater.* **40,** 9–23 (2000).

49. Wang, L. *et al.* Post-transformation of MWW-type lamellar precursors into MCM-56 analogues. *Microporous Mesoporous Mater.* **113,** 435–444 (2008).

50. Roth, W. J., Chlubná, P., Kubů, M. & Vitvarová, D. Swelling of MCM-56 and MCM-22P with a new medium — surfactant–tetramethylammonium hydroxide mixtures. *Catal. Today* **204,** 8–14 (2013).

51. Chlubná, P., Roth, W. J., Zukal, A., Kubů, M. & Pavlatová, J. Pillared MWW zeolites MCM-36 prepared by swelling MCM-22P in concentrated surfactant solutions. *Catal. Today* **179,** 35–42 (2012).

52. Roth, W. J. & Dorset, D. L. Expanded view of zeolite structures and their variability based on layered nature of 3-D frameworks. *Microporous Mesoporous Mater.* **142,** 32–36 (2011).

53. Eilertsen, E. A. *et al.* Nonaqueous Fluoride/Chloride Anion-Promoted Delamination of Layered Zeolite Precursors: Synthesis and Characterization of UCB-2. *Chem. Mater.* **23,** 5404–5408 (2011).

54. Ogino, I. *et al.* Heteroatom-Tolerant Delamination of Layered Zeolite Precursor Materials. *Chem. Mater.* **25,** 1502–1509 (2013).

55. Ogino, I. *et al.* Delamination of Layered Zeolite Precursors under Mild Conditions: Synthesis of UCB-1 via Fluoride/Chloride Anion-Promoted Exfoliation. *J. Am. Chem. Soc.* **133,** 3288–3291 (2011).

56. Ouyang, X. *et al.* Single-Step Delamination of a MWW Borosilicate Layered Zeolite Precursor under Mild Conditions without Surfactant and Sonication. *J. Am. Chem. Soc.* **57,** 1449−1461 (2014).

57. Kubů, M. *et al.* A New Family of Two-Dimensional Zeolites Prepared from the Intermediate Layered Precursor IPC-3P Obtained during the Synthesis of TUN Zeolite. *Chem. - A Eur. J.* **19,** 13937–1945 (2013).

58. Roth, W. J. *et al.* prepared using a top-down method. *Nat. Chem.* **5,** 628–633 (2013).

59. Verheyen, E. *et al.* Design of zeolite by inverse sigma transformation. *Nat. Mater.* **11,** 1059–1064 (2012).

60. Yilmaz, B. *et al.* Al-RUB-41: a shape-selective zeolite catalyst from a layered silicate. *Chem. Commun.* **47,** 1812–1814 (2011).

61. Ramos, F. S. O., Munsignatti, E. C. O. & Pastore, H. O. 2D–3D structures: The hydrothermal transformation of a layered sodium silicate, Na-RUB-18, into mordenite zeolite. *Microporous Mesoporous Mater.* **177,** 143–150 (2013).

62. Wang, Y. X., Gies, H. & Lin, J. H. Crystal Structure of the New Layer Silicate RUB-39 and Its Topotactic Condensation to a Microporous Zeolite with Framework Type RRO. *Chem. Mater.* **19,** 4181–4188 (2007).

63. Brouwer, D. H. Structure solution of network materials by solid-state NMR without knowledge of the crystallographic space group. *Solid State Nucl. Magn. Reson.* **51-52,** 37–45 (2013).

64. Kiba, S., Itagaki, T., Nakato, T. & Kuroda, K. Interlayer modification of a layered H-octosilicate (H-RUB-18) with methanol: formation of a highly ordered organosilicate nanohybrid. *J. Mater. Chem.* **20,** 3202–3210 (2010).

65. Choi, M. *et al.* Stable single-unit-cell nanosheets of zeolite MFI as active and long-lived catalysts. *Nature* **461,** 246–9 (2009).

66. Na, K. *et al.* Directing zeolite structures into hierarchically nanoporous architectures. *Science* **333,** 328–32 (2011).

67. Na, K., Choi, M. & Ryoo, R. Recent advances in the synthesis of hierarchically nanoporous zeolites. *Microporous Mesoporous Mater.* **166,** 3–19 (2013).

68. Seo, Y., Lee, S., Jo, C. & Ryoo, R. Microporous aluminophosphate nanosheets and their nanomorphic zeolite analogues tailored by hierarchical structure-directing amines. *J. Am. Chem. Soc.* **135,** 8806–9 (2013).

69. Jo, C., Jung, J., Shin, H. S., Kim, J. & Ryoo, R. Capping with Multivalent Surfactants for Zeolite Nanocrystal Synthesis. *Angew. Chem. Int. Ed. Engl.* 1–5 (2013). doi:10.1002/anie.201303088

70. Messinger, R. J., Na, K., Seo, Y., Ryoo, R. & Chmelka, B. F. Co-development of Crystalline and Mesoscopic Order in Mesostructured Zeolite MFI Nanosheets. *In preparation*

71. Fung, B. M., Khitrin, a K. & Ermolaev, K. An improved broadband decoupling sequence for liquid crystals and solids. *J. Magn. Reson.* **142,** 97–101 (2000).

72. Iuga, D. & Kentgens, A. P. . Influencing the satellite transitions of half-integer quadrupolar nuclei for the enhancement of magic angle spinning spectra. *J. Magn. Reson.* **158,** 65–72 (2002).

73. Hediger, S., Meier, B. H., Kurur, N. D., Bodenhausen, G. & Ernst, R. R. NMR cross polarization by adiabatic passage through the. *Chem. Phys. Lett.* **223,** 283–288 (1994).

74. Brouwer, D. H. *et al.* A general protocol for determining the structures of molecularly ordered but noncrystalline silicate frameworks. *J. Am. Chem. Soc.* **135,** 5641–5655 (2013).

75. Brouwer, D. H., Darton, R. J., Morris, R. E. & Levitt, M. H. A solid-state NMR method for solution of zeolite crystal structures. *J. Am. Chem. Soc.* **127,** 10365–70 (2005).

76. Brouwer, D. H. An efficient peak assignment algorithm for two-dimensional NMR correlation spectra of framework structures. *J. Magn. Reson.* **164,** 10–18 (2003).

77. Lesage, A., Sakellariou, D., Steuernagel, S. & Emsley, L. Carbon - Proton Chemical Shift Correlation in Solid-State NMR by Through-Bond Multiple-Quantum Spectroscopy. *J. Am. Chem. Soc.* **120,** 13194–13201 (1998).

78. Carravetta, M., Eden, M., Zhao, X., Brinkmann, A. & Levitt, M. H. Symmetry principles for the design of radiofrequency pulse sequences in the nuclear magnetic resonance of rotating solids. *Chem. Phys. Lett.* **321,** 205–215 (2000).

79. Brinkmann, A. & Levitt, M. H. Symmetry principles in the nuclear magnetic resonance of spinning solids: Heteronuclear recoupling by generalized Hartmann–Hahn sequences. *J. Chem. Phys.* **115,** 357 (2001).

80. Brinkmann, A. & Kentgens, A. P. M. Proton-Selective 17O-1H Distance Measurements in Fast Magic-Angle-Spinning Solid-State NMR Spectroscopy for the Determination of Hydrogen Bond Lengths. *J. Am. Chem. Soc.* **128,** 14758–14759 (2006).

81. Hu, B., Trébosc, J. & Amoureux, J. P. Comparison of several hetero-nuclear dipolar recoupling NMR methods to be used in MAS HMQC/HSQC. *J. Magn. Reson.* **192,** 112–22 (2008).

82. Pine, L. A., Maher, P. J. & Wachter, W. A. Prediction of cracking catalyst behavior by a zeolite unit cell size model. *J. Catal.* **476,** 466–476 (1984).

83. Mikovsky, R. J. & Marshall, J. F. Random aluminum-ion siting in the faujasite lattice. *J. Catal.* **44,** 170–173 (1976).

84. Hill, R. J. & Gibbs, G. V. Variation in d(T-O),d(T.T) and ∠TOT in silica and silicate minerals, phosphates and aluminates. *Acta Crystallogr. Sect. B Struct. Crystallogr. Cryst. Chem.* **35,** 25–30 (1979).

85. Qiu, S., Pang, W., Kessler, H. & Guth, J. L. Synthesis and structure of the [AlPO4]12 Pr4NF molecular sieve with AFI structure. *Zeolites* **9,** 440–444 (1989).

86. Pluth, J. J. & Smith, J. V. Accurate Redetermination of Crystal Structure of Dehydrated Zeolite A. Absence of Near Zero Coordination of Sodium. Refinement of Si, Al-Ordered Superstructure. *J. Am. Chem. Soc.* **102,** 4704–4708 (1980).

87. Xia, Y. & Mokaya, R. Crystalline-like molecularly ordered mesoporous aluminosilicates derived from aluminosilica-surfactant mesophases via benign template removal. *J. Phys. Chem. B* **110,** 9122–31 (2006).

88. Janicke, M. T. *et al.* Low Silica MCM-41 Composites and Mesoporous Solids. *Chem. Mater.* **11,** 1342–1351 (1999).

89. Janicke, M. T. *et al.* Aluminum Incorporation and Interfacial Structures in MCM-41 Mesoporous Molecular Sieves. *J. Am. Chem. Soc.* **120,** 6940–6951 (1998).

90. Vortmann, S., Rius, J., Siegmann, S. & Gies, H. Ab Initio Structure Solution from X-ray Powder Data at Moderate Resolution : Crystal Structure of a Microporous Layer Silicate. *J. Phys. Chem. A* **101,** 1292–1297 (1997).

91. Cadars, S. *et al.* Dynamics and Disorder in Surfactant-Templated Silicate Layers Studied by Solid-State NMR Dephasing Times and Correlated Line Shapes. *J. Phys. Chem. C* **112,** 9145–9154 (2008).

92. Corma, A. Inorganic Solid Acids and Their Use in Acid-Catalyzed Hydrocarbon Reactions. *Chem. Rev.* **95,** 559–614 (1995).

93. Corma, A. State of the art and future challenges of zeolites as catalysts. *J. Catal.* **216,** 298–312 (2003).

94. Massiot, D. *et al.* Modelling one- and two-dimensional solid-state NMR spectra. *Magn. Reson. Chem.* **40,** 70–76 (2002).

95. Mackenzie, K. J. D. & Smith, M. E. *Multinuclear Solid-State Nuclear Magnetic Resonance of Inorganic Materials*. (Elsevier, 2002).

96. Zones, S. I. & Hwang, S.-J. The inorganic chemistry of guest-mediated zeolite crystallization: a comparison of the use of boron and aluminum as lattice-substituting components in the presence of a single guest molecule during zeolite synthesis. *Microporous Mesoporous Mater.* **58,** 263–277 (2003).

97. Archer, R. H. *et al.* Physicochemical Properties and Catalytic Behavior of the Molecular Sieve SSZ-70. *Chem. Mater.* **22,** 2563–2572 (2010).

Chapter 4: Combined Solid-State NMR and Scattering Structural Analyses of the Layered Siliceous Zeolite SSZ-70

4.1 Abstract

Zeolite SSZ-70 is shown to possess a high degree of structural similarity to zeolite MCM-22 that is commercially used in industrial production of benzene derivatives. A combination of multi-dimensional solid-state nuclear magnetic resonance (NMR) spectroscopy, electron microscopy, and powder diffraction techniques was applied to elucidate the complicated crystal structure of SSZ-70. High-resolution transmission electron microscopy clearly indicates that while both SSZ-70 and MCM-22 have MWW cages with interconnected 10-membered ring channels, SSZ-70 appears to have silicate layers between MWW cages that are not present in MCM-22, consistent with one-dimensional solid-state ^{29}Si NMR analyses. Notably, two-dimensional *J*- (through-bond) and dipolar-mediated (through-space) ^{29}Si{^{29}Si} NMR analyses provide local information on connectivities and proximities of silicon sites that are covalently bonded to other silicon sites through bridging oxygen atoms in SSZ-70, respectively. The resolution and identification of various ^{29}Si-O-^{29}Si site pairs allows building a structural model of SSZ-70 that contains MWW cages and silicate layers. The presence of MWW cages in SSZ-70 is also supported by powder diffraction analyses performed on calcined SSZ-70, which suggest a high degree of stacking disorder of MWW cages. This combination of characterization methods provides

complementary short- and long-range order of the SSZ-70 structure and is expected to form the basis of a general protocol for solving unknown zeolite structures in the future.

4.2 Introduction

Zeolite SSZ-70 is a new molecular sieve that was first discovered by Chevron in its borosilicate form,[1] which exhibits relatively weak solid acidity. The framework compositions of SSZ-70 were later extended to siliceous and aluminosilicate forms,[2] the former of which is proving useful in determining its structure, while the latter exhibits stronger acidity that is attractive for potential applications. Although the syntheses of these novel zeolites have been well established, the topological and compositional structures of SSZ-70 have not been determined. Initial characterization results, from hydrocarbon adsorption and hydrocracking reaction testing, suggest that SSZ-70 has similar structural features to SSZ-25/MCM-22 (three-letter IZA code:[3] MWW).[4] Importantly, for zeolitic materials with complicated extents of structural order, a molecular-level understanding of their physicochemical properties and catalytic behaviors typically requires a detailed knowledge of their 3D framework structures. Furthermore, such structural information is important for exploring possible applications of new zeolite catalysts. Recently, solid-state nuclear magnetic resonance (NMR) spectroscopy has emerged as a powerful tool to aid in the determination of zeolite structures. Solid-state NMR is able to probe short-range (< 1nm) bonding environments among nuclei of interest (*e.g.*, ^{29}Si, ^{1}H, ^{19}F), which are sensitive to local framework structure. A combination of spectroscopic, diffraction, and microscopy

analyses can be used to reveal new molecular-level insights about the crystalline structure of zeolite SSZ-70.

Here, we show a series of 1D and 2D solid-state ^{29}Si NMR spectra for as-synthesized siliceous SSZ-70 with *ca.* 99% ^{29}Si-enrichment, which establish the types and relative populations of various ^{29}Si species, as well as the connectivities and proximities between distinct ^{29}Si sites. First, 1D solid-state ^{29}Si NMR experiments reveal that the short-range molecular order of zeolite SSZ-70 is comparable to that of ITQ-1 (*i.e.,* siliceous MCM-22) in their as-synthesized forms, with some important differences. Additional and complementary information about the local interactions among various ^{29}Si sites are provided by solid-state 2D ^{29}Si{^{29}Si} NMR methods, which probe the ^{29}Si site connectivities and proximities via through-bond scalar (*J*) and through-space dipolar interactions, respectively. A 2D ^{29}Si{^{29}Si} *J*-mediated NMR spectrum resolves correlated signal intensities from intramolecular ^{2}J(^{29}Si-O-^{29}Si) interactions between different pairs of covalently linked ^{29}Si nuclei, establishing connectivities among various ^{29}Si sites (an exception is that connectivities between identical sites are not able to be detected by *J*-mediated experiments). In contrast, a 2D ^{29}Si{^{29}Si} dipolar-mediated NMR spectrum exploits through-space dipolar interactions to yield complementary information on site proximities between structurally distinct *and* identical pairs of ^{29}Si sites, including next-nearest neighbor T-site atoms. Together, the insights provided by these two types of 2D ^{29}Si{^{29}Si} experiments establish the presence of MWW-like cages (10-ring structures) in the SSZ-70 framework, as well as partial connectivities of T-site atoms in the silicate layers between the MWW cages. Based on the current solid-state ^{29}Si NMR results, we propose a

candidate structure for SSZ-70 that is expected to aid diffraction, modeling, and electron micrograph investigations.

4.3 Experimental

4.3.1 Materials.

As-synthesized siliceous zeolite SSZ-70 with *ca.* 99% ^{29}Si enrichment was kindly provided by Dr. Stacey I. Zones at the Chevron Energy Technology Company.

4.3.2 Characterization.

High-resolution transmission electron microscopy image was acquired and kindly provided by Dr. Wei Wan and Prof. Xiaodong Zou at the Stockholm University.

Solid-state one-dimensional (1D) and two-dimensional (2D) NMR measurements were all acquired at room temperature (~25 °C) on a Bruker AVANCE II 500 spectrometer with a 11.7 T wide-bore superconducting magnet, operating at frequencies of 500.0 and 99.4 MHz corresponding to ^{1}H and ^{29}Si resonances, respectively. Quantitative solid-state 1D single-pulse ^{29}Si magic-angle-spinning (MAS) experiments were performed using a 90° pulse corresponding to a ^{29}Si nutation frequency of 40 kHz under the MAS conditions of 10 kHz with a recycle day of 700 s. High-power broadband ^{1}H decoupling using the pulse scheme small-phase-incremental-alternation-with-64-steps (SPINAL-64)[5] was applied during ^{29}Si signal acquisition.

Solid-state 2D *J*-mediated ^{29}Si{^{29}Si} DQ NMR correlation measurements were conducted under the MAS conditions of 10 kHz with a recycle day of 8 s using the

refocused Incredible Natural Abundance DoublE Quantum Transfer Experiment (INADEQUATE) technique[6,7] that was designed for probing ^{29}Si-O-^{29}Si spin pairs via their scalar (*J*) couplings (*i.e.*, $^{2}J(^{29}\text{Si-O-}^{29}\text{Si})$). The experiments were initiated with $^{1}\text{H} \rightarrow {}^{29}\text{Si}$ cross-polarization (CP) methods, where an 3.13 μs ^{1}H 90° pulse was first applied and followed by a 1.75 ms adiabatic CP shape to transfer magnetization to ^{29}Si nuclei. Subsequently, a rotor-synchronized echo period (τ-180°-τ) of total delay 2τ = 12 ms with a 8.34 μs ^{29}Si 180° pulse was used to generate anti-phase coherences under $^{2}J(^{29}\text{Si-O-}^{29}\text{Si})$ coupling evolution while chemical shift interactions were focused. The τ = 6.0 ms was optimized to yield maximum ^{29}Si signal intensity. The anti-phase magnetization was then converted into a mixture of zero- (ZQ) and double-quantum (DQ) coherences with a 4.17 μs ^{29}Si 90° pulse. The ZQ coherences were eliminated with phase-cycling, whereas the DQ coherences were indirectly measured from incrementing evolution period t_1. Then a following 4.17 μs ^{29}Si 90° pulse converted the remaining DQ coherences into anti-phase ones, which were further converted by a 8.34 μs ^{29}Si 180° into in-phase single-quantum (SQ) coherences. Such in-phase SQ coherences evolved again under $^{2}J(^{29}\text{Si-O-}^{29}\text{Si})$ interactions, forming a full echo period that next initiated the ^{29}Si signal detection period t_2. High-power broadband ^{1}H decoupling using SPINAL-64 was again applied during ^{29}Si signal acquisition.

Solid-state 2D dipolar-mediated $^{29}\text{Si}\{^{29}\text{Si}\}$ DQ NMR correlation experiments were conducted under MAS conditions of 4.6 kHz using the robust symmetry-based SR26_4^{11} homonuclear dipolar recoupling sequence.[8,9] All measurements were carried out with a recycle delay of 8 s, a contact time of 0.5 ms for $^{1}\text{H} \rightarrow {}^{29}\text{Si}$ CP via an adiabatic shape, and 90 kHz continuous-wave (CW) ^{1}H decoupling during ^{29}Si signal acquisition. The ^{29}Si nutation frequency during dipolar recoupling periods was manually set to 30 kHz (~6.5 ×

MAS rate), and the dipolar recoupling time was set to 5.2 ms. During the ^{29}Si DQ excitation and reconversion periods, CW ^{1}H decoupling was used, corresponding to the ^{1}H nutation frequency of 90 kHz.

4.4 Results and Discussion

Preliminary results from hydrocarbon adsorption and reaction testing (specifically cracking of a mixture of *n*-hexane/3-methylpentane) suggest that there are structural similarities between zeolites SSZ-70 and MCM-22/SSZ-25 (MWW).[4] These analyses are consistent with high-resolution transmission electron microscopy (HRTEM) images shown in Figure 1a,b for zeolites SSZ-70 and MCM-22, respectively, which reveal the presence of MWW cages (highlighted in orange) in both materials. The framework structure of MCM-22 is shown for reference in Figure 1c. Despite similarly having MWW cages, important structural differences exist between SSZ-70 and MCM-22/SSZ-25. First, the MWW cages appear to be separated by additional silicate layers (highlighted in pink) in SSZ-70, unlike in MCM-22. Furthermore, the upper row of MWW cages in SSZ-70 are displaced compared to the ones below, in contrast to MCM-22 (Figure 1b) in which the MWW cages are well aligned. The types of distinct ^{29}Si atoms, their site connectivities and proximities and corresponding bond angles to other framework ^{29}Si sites in SSZ-70 are, however, challenging to unambiguously establish via diffraction analyses alone in the absence of a well-defined single crystal. In this case, the structural analyses might be exceedingly difficult because of the stacking disorder. The associated diffraction and stimulated pattern

of calcined SSZ-70 is shown in Figure C1, manifesting high degree of similarity to the calcined MCM-22.

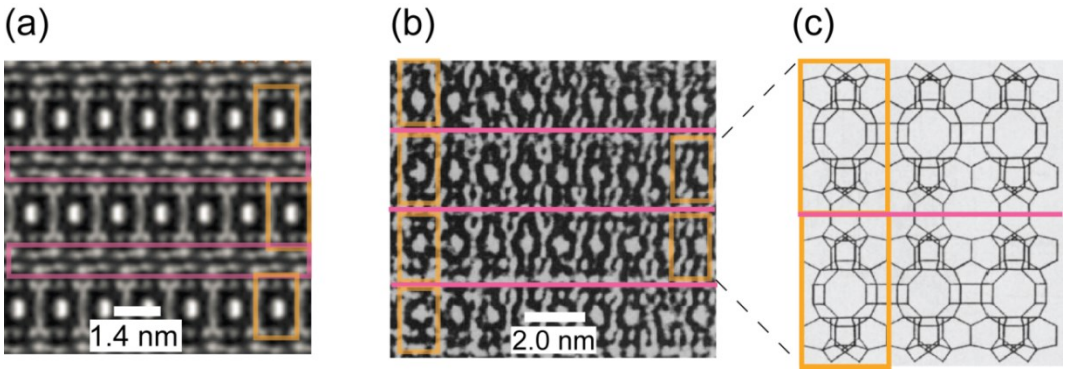

Figure 1. Representative HRTEM images of zeolite (a) SSZ-70 [Courtesy: Dr. Wei Wan and Prof. Xiaodong Zou] and (b) MCM-22,[10] accompanied by (c) the proposed model structure of MCM-22 with only T-atoms shown for clarity. The MWW cages of both zeolites are highlighted in orange, whereas the pink boxes indicate the different silicate layers in zeolite SSZ-70, not present in MCM-22.

The analyses of solid-state ^{29}Si NMR experiments, which are sensitive to local ^{29}Si environments, provide structural insights that are complementary to diffraction and microscopy results. For example, a quantitative 1D single-pulse ^{29}Si magic-angle-spinning (MAS) NMR measurements shown in Figure 2a,b establish that the overall populations of fully- (Q^4) and partially-condensed (Q^3) ^{29}Si species (80% and 20%, respectively) are approximately the same for both as-synthesized SSZ-70 and ITQ-1. A representative quantitative ^{29}Si NMR spectral analysis of as-synthesized SSZ-70 is shown in Figure C2. The relatively high fractions of Q^3 ^{29}Si species generally arise from structural defects in zeolites, especially for those synthesized under alkaline hydroxide conditions. This may apply for the siliceous SSZ-70 material studied here, because it was also prepared under hydroxide conditions. However, the same zeolite (siliceous SSZ-70) prepared using fluoride media indeed exhibits a substantial amount of Q^3 ^{29}Si species (*ca.* 5%).[4] Thus, it is hypothesized that these incompletely condensed Q^3 ^{29}Si species result from ordered,

structural features in as-synthesized SSZ-70. Alternatively, the high population of Q^3 ^{29}Si species could come as a result of charge balancing interactions between anionic SiO^- moieties and the cationic organic SDA molecules, which are present in as-synthesized mesostructured zeolites and layered silicates.[11–13]

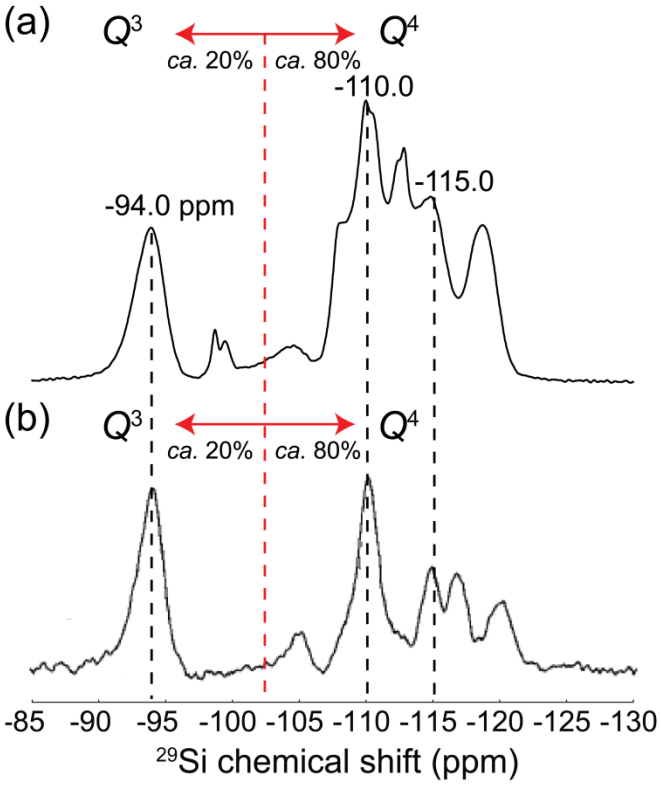

Figure 2. Solid-state 1D single-pulse ^{29}Si MAS NMR spectra of as-synthesized (a) siliceous SSZ-70 and (b) ITQ-1.[14] The dotted red line separates the ^{29}Si chemical shift ranges for Q^3 and Q^4 ^{29}Si species.

Additionally, the ^{29}Si MAS NMR spectra show several identical ^{29}Si NMR signals associated with Q^3 and Q^4 ^{29}Si species for both materials (Figure 2a, b) at -94.0, -110.0, and -115.0 ppm. Consistent with previous studies,[4] the results suggest that the frameworks of SSZ-70 and ITQ-1 have similar structures. Interestingly, these spectra also reveal important differences that indicate structural dissimilarities between these two zeolites. For example,

the observed differences in the relative intensities of the various Q^4 ^{29}Si signals indicate differences in relative populations of Q^4 ^{29}Si species in SSZ-70 and ITQ-1. This could arise because of the different types of organic structure-directing agents (SDAs) used in material preparation (see Figure C3a,b) and their respective effects on the local ^{29}Si T-site environments in the zeolites. The most significant differences between the two ^{29}Si NMR spectra are the ^{29}Si signals at *ca.* -98.8 and -99.5 ppm for SSZ-70, which are not present for ITQ-1. These two ^{29}Si signals correspond to Q^3 ^{29}Si species and are hypothesized to be associated with ^{29}Si sites in the silicate layer between the MWW cages in SSZ-70 (highlighted in pink in Figure 1a). This hypothesis is supported by 2D ^{29}Si{^{29}Si} NMR results, which will be discussed in detail below. Although different types of ^{29}Si species and their relative populations in as-synthesized SSZ-70 are clearly determined by 1D ^{29}Si NMR, more powerful 2D NMR methods are needed to establish the connectivities and proximities of the different ^{29}Si sites.

Advanced solid-state 2D ^{29}Si{^{29}Si} NMR correlation methods are applied here to probe ^{29}Si site connectivities and proximities in as-synthesized SSZ-70. For example, 2D *J*-mediated ^{29}Si{^{29}Si} double-quantum (DQ) correlation NMR measurements are sensitive to through-bond scalar (*J*) couplings between ^{29}Si sites through bridging oxygen atoms.[11,15–17] The 2D *J*-mediated ^{29}Si{^{29}Si} DQ NMR spectrum yields a frequency map with single- (SQ) and double-quantum (DQ) ^{29}Si dimensions shown on the horizontal and vertical axis, respectively. The ^{29}Si signals in the SQ dimension reveal isotropic chemical shifts (Ω_a , commonly observed in 1D ^{29}Si MAS NMR spectra), whereas ^{29}Si signals in the DQ dimension represent the sums of chemical shifts of a given *J*-coupled pair of ^{29}Si spins ($\Omega_a + \Omega_b$). Pairs of correlated intensities at (Ω_a , $\Omega_a + \Omega_b$) and (Ω_b , $\Omega_a + \Omega_b$) establish that ^{29}Si

species with corresponding isotropic chemical shifts (Ω_a , Ω_b) are covalently bonded through bridging oxygen atoms, from which ^{29}Si-O-^{29}Si site interconnectivities can be established in zeolite structures. Figure 3a shows a 2D *J*-mediated ^{29}Si{^{29}Si} DQ NMR spectrum of as-synthesized siliceous SSZ-70, which exhibits SQ and DQ correlated signal intensities among different Q^3 and Q^4 ^{29}Si species. Specifically, the SQ signal at -118.8 ppm, associated with ^{29}Si site *6*, is correlated with the signals at -229.0 and -234.0 ppm in the DQ dimension (Figure 3b,c). These results unambiguously establish that ^{29}Si site *6* is covalently bonded to ^{29}Si sites *3* and *7* (through bridging oxygen atoms), respectively. Similarly, the ^{29}Si signal at -110.2 ppm in the SQ dimension, associated with ^{29}Si site *3*, exhibits correlated intensities at -218.4 and -229.0 ppm in the DQ dimension (Figure 3e,c), corresponding to ^{29}Si-O-^{29}Si connectivities with ^{29}Si sites *2* and *6*, respectively. Additionally, the SQ signal attributed to ^{29}Si site *8* at -113.0 ppm is correlated with the DQ signal at -228.2 ppm (Figure 3d), establishing covalent bonds to ^{29}Si site *7*. Another 2D intensity correlation is observed between the SQ ^{29}Si signals at *ca.* -112 ppm from site *5* and at *ca.* -114 ppm, which we attribute to site *7*, as evidenced by the associated DQ signal intensity at *ca.* -226 ppm. The strong intensities of these correlated signals are also consistent with the previously established connectivities of ^{29}Si sites in the MWW cages, in which there are three covalently bonded ^{29}Si-O-^{29}Si site pairs *5*-*7*. Interestingly, the SQ ^{29}Si signal attributed to site *7* (*ca.* -114 ppm) is slightly displaced to higher frequency, compared to the position(s) of other correlated intensities associated with site *7* moieties (*ca.* -115 ppm) that are covalently bonded to ^{29}Si site *6* (-118.8 ppm) and site *8* (-113.0 ppm). This suggests that a substantial fraction of the ^{29}Si site-*7* atoms interact differently with the SDAs than

sites *5*, *6*, or *8*. Such influences of SDAs on the local environments of the ^{29}Si framework moieties will be discussed in more detail later in this chapter.

The systematic approach discussed above is used to determine the remaining ^{29}Si site interconnectivities among structurally distinct ^{29}Si sites in SSZ-70. Consistent with the 2D NMR analyses and previous work, a schematic structure of the MWW cages is shown in Figure 4, and the results are summarized in Table 1. However, there are a number of additional 2D intensity correlations that reflect ^{29}Si-O-^{29}Si site connectivities that have not been previously observed or accounted for in structure analyses of SSZ-70. These include ^{29}Si-O-^{29}Si site pairs *9-10* and *2-1'*, and overspecification of the connectivities of Q^4 ^{29}Si site *1*. These will be discussed in greater detail together with a 2D dipolar-mediated ^{29}Si{^{29}Si} DQ NMR spectrum in Figure 5a below.

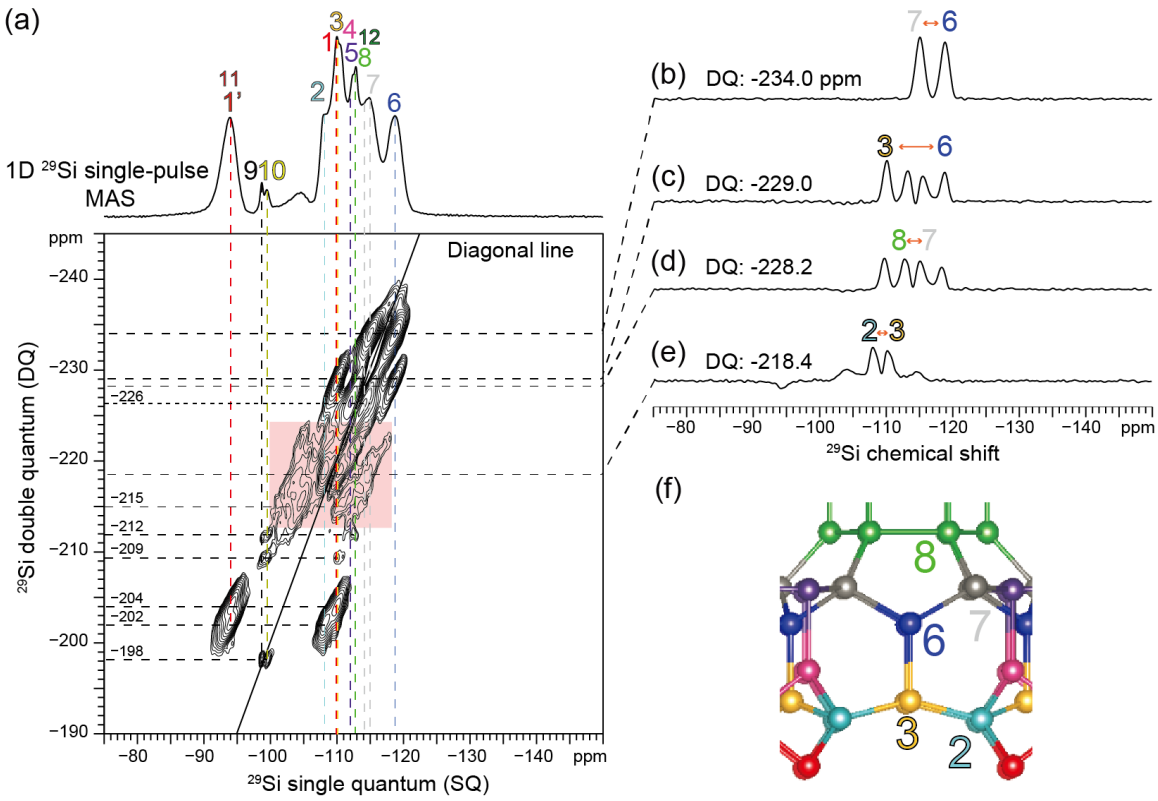

Figure 3. (a) Solid-state 2D *J*-mediated ^{29}Si{^{29}Si} DQ NMR spectrum of as-synthesized siliceous zeolite SSZ-70 acquired at 25 °C and 10 kHz MAS with a 1D single-pulse ^{29}Si MAS spectrum shown along the top horizontal axis. Contour slices, extracted at (b) -234.0 ppm, (c) -229.0 ppm, (d) -228.2 ppm, and (e) -218.4 ppm in the DQ dimension, are shown as examples to assign different ^{29}Si-O-^{29}Si site pairs that establish (f) the local connectivities of ^{29}Si site *6* within a MWW cage in SSZ-70.

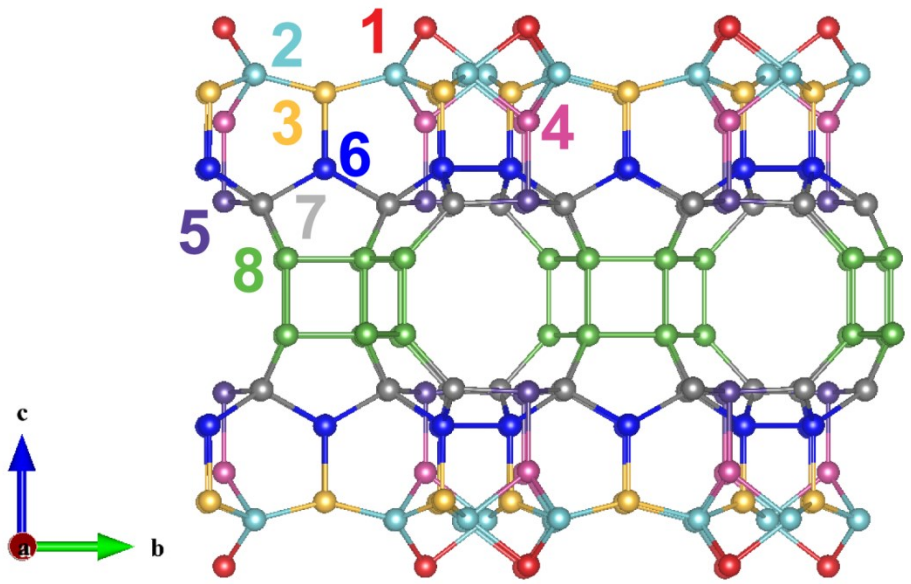

Figure 4. Schematic representation of MWW cages in zeolite SSZ-70, where distinct ^{29}Si site is colored accordingly. Oxygen atoms are omitted for simplicity. [Courtesy: Dr. Dan Xie]

Table 1. ^{29}Si NMR signal assignments to ^{29}Si sites in as-synthesized siliceous SSZ-70, based on the 2D *J*- and dipolar-mediated ^{29}Si{^{29}Si} DQ NMR results

^{29}Si chemical shift (ppm)	Type	Assignment	Connectivities[(a)]	Connectivities[(b)]
-94.0	Q^3	*1'*	*2* (x3)	*2* (x3)
-94.0	Q^3	*11*	*1* (x3)	*1* (x3)
-98.8	Q^3	*9*	*10* (x2), *12*	*10* (x2), *12*
-99.5	Q^3	*10*	*1*, *9* (x2)	*1*, *9* (x2)
-105	Q^4	*?*	?	?
-108.2	Q^4	*2*	*1*, *9* (x2)	*1*, *9* (x2)
-110.0	Q^4	*1*	*2* (x3), *9* or *10* or *11*	*2* (x3), *9* or *10* or *11*
-110.2	Q^4	*3*	*2* (x2), *6*	*2* (x2), *3*, *6*
-110.8	Q^4	*4*	*2* (x3), *5*	*2* (x3), *5*
-112.0	Q^4	*5*	*4*, *7* (x3)	*4*, *7* (x3)
-113.0	Q^4	*8*	*7*	*7*, *8* (x3)
-113.0	Q^4	*12*	*9* or *10* (x4)	*9* or *10* (x4)
-114 ~ -115	Q^4	*7*	*5*, 6 (x2), *8*	*5*, 6 (x2), *8*
-118.8	Q^4	*6*	*3*, *7* (x2)	*3*, *6*, *7* (x2)

(a) The ^{29}Si site pairs were derived based on correlated SQ and DQ signals in 2D *J*-mediated ^{29}Si{^{29}Si} NMR spectrum (Figure 3a).
(b) The ^{29}Si site pairs were derived based on correlated SQ and DQ signals in 2D dipolar-mediated ^{29}Si{^{29}Si} NMR spectrum (Figure 5a).

Although ^{29}Si-O-^{29}Si site connectivities can be determined by 2D *J*-mediated ^{29}Si{^{29}Si} DQ NMR, this type of NMR experiment cannot measure intensity correlations arising from ^{29}Si-O-^{29}Si connectivities between chemically identical ^{29}Si sites. To overcome this limitation, Brouwer *et al.* have applied a complementary technique that relies on through-space dipolar couplings instead of weaker through-bond *J*-couplings among ^{29}Si nuclei to acquire 2D dipolar-mediated ^{29}Si{^{29}Si} DQ NMR spectra,[8,18,19] which allow connectivities between structurally identical ^{29}Si sites to be established. Additionally, this method yields

higher signal sensitivity than for 2D *J*-mediated ^{29}Si{^{29}Si} DQ NMR, due to the much stronger ^{29}Si-^{29}Si dipolar interactions compared to *J*-interactions. For example, for a standard distance of approximately 3.2 Å between ^{29}Si-O-^{29}Si T-sites, ^{29}Si-^{29}Si dipolar interactions are expected to be *ca.* 150 Hz, compared to *ca.* 15 Hz for ^{2}J(^{29}Si-O-^{29}Si) interactions. These 2D dipolar-mediated ^{29}Si{^{29}Si} DQ NMR experiments are processed similar to their 2D *J*-mediated analogues, yielding SQ and DQ dimensions along the horizontal and vertical axes, respectively.

Analyses of 2D dipolar-mediated ^{29}Si{^{29}Si} DQ NMR spectra, together with the results from the similar *J*-mediated spectra, provide complementary insights about the local ^{29}Si environments in zeolite frameworks. For example, Figure 5a shows a 2D dipolar-mediated ^{29}Si{^{29}Si} DQ NMR spectrum of as-synthesized siliceous SSZ-70, which reveals correlated SQ and DQ signal intensities among nearly all of the ^{29}Si signals associated with the Q^3 and Q^4 ^{29}Si sites. Based on these intensity correlations, various pairs of ordered ^{29}Si-O-^{29}Si sites can be established, most of which are identical to those observed in the 2D *J*-mediated ^{29}Si{^{29}Si} DQ NMR spectrum (Figure 3a). For example, the SQ signal at -118.8 ppm, corresponding to ^{29}Si site *6*, is correlated with the DQ signals at -229.0 and -234.0 ppm (Figure 5c,d), which is consistent with ^{29}Si site *6* being covalently linked to ^{29}Si sites *3* and *7*, respectively. Furthermore, the signal at -113.0 ppm in the SQ dimension, associated with ^{29}Si site *8*, is correlated with the signal at – 228.2 ppm in the DQ dimension (Figure 5e), which is also consistent with the connectivity between ^{29}Si sites *7* and *8* (through a bridging oxygen atom). More interestingly, the 2D dipolar-mediated ^{29}Si{^{29}Si} NMR spectrum manifests additional correlated signal intensities that are not observed in the *J*-mediated

experiment (highlighted with a diagonal line in Figures 3a and 5a), from which new ^{29}Si-O-^{29}Si site pairs are determined.

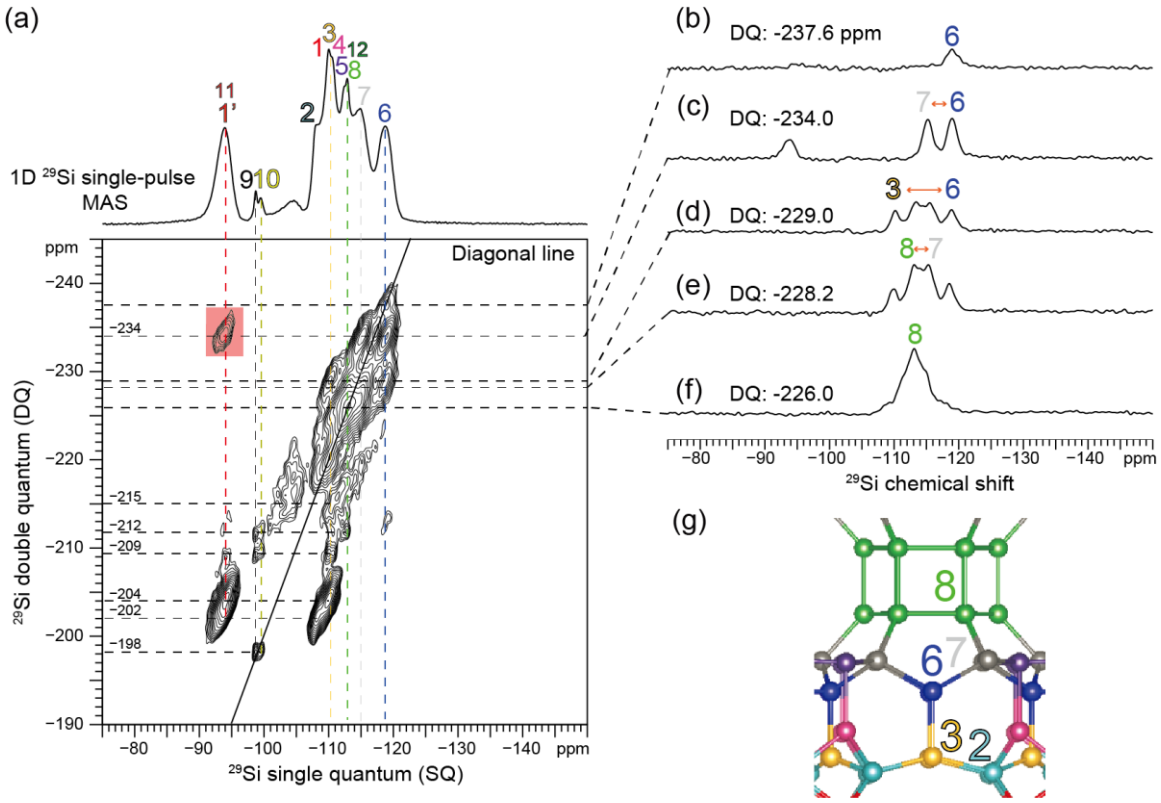

Figure 5. (a) Solid-state 2D dipolar-mediated ^{29}Si{^{29}Si} DQ NMR spectrum of as-synthesized siliceous zeolite SSZ-70 acquired at 25 °C and 4.6 kHz MAS with a 1D single-pulse ^{29}Si MAS spectrum (performed at 25 °C and 10 kHz MAS) shown along the top horizontal axis. Contour slices, extracted at (b) -237.6 ppm, (c) -234.0 ppm, (d) -229.0 ppm, (e) -228.2 ppm, and (f) -226.0 ppm in the DQ dimension, are shown as examples to assign different ^{29}Si site-O-^{29}Si site pairs that establish (g) the local connectivities of ^{29}Si sites *6* and *8* within a MWW cage in SSZ-70.

For example, the SQ signal at -118.8 ppm corresponding to ^{29}Si site *6* is correlated with the signal at -237.6 ppm in the DQ dimension (Figure 5b), indicating that two ^{29}Si site-*6* atoms are covalently bonded to each other (through a bridging oxygen atom). Similarly, 2D signal intensity is observed for the signal at -113.0 ppm in the SQ dimension associated with ^{29}Si site *8* and the signal at -226.0 ppm in the DQ dimension (Figure 5f), revealing the presence of ^{29}Si-O-^{29}Si connectivities between two ^{29}Si site *8* atoms. The ^{29}Si site

assignments and their corresponding connectivities are summarized in Table 1. Together with previous diffraction and microscopy analyses, these NMR results confirm that the SSZ-70 structure consists of MWW-like cages. Furthermore, most of the ^{29}Si site connectivities of these MWW-like cages are identical to those previously reported for ITQ-1 (Table 2), with the exception of ^{29}Si site *1* (the site on the edge of MWW cages). These structural conclusions provided by solid-state NMR are supported by direct correlation with complementary XRD data, as discussed below.

Table 2. Established ^{29}Si site connectivities in zeolite ITQ-1[3,14]

^{29}Si site	connectivities
1	*1, 2, 2, 2*
2	*1, 3, 3, 4*
3	*2, 2, 3, 6*
4	*2, 2, 2, 5*
5	*4, 7, 7, 7*
6	*3, 6, 7, 7*
7	*5, 6, 6, 8*
8	*7, 8, 8, 8*

Given the inherent sensitivity of solid-state ^{29}Si NMR spectroscopy to ^{29}Si molecular environments, the local bonding configurations of ^{29}Si sites are expected to correlate with their resulting ^{29}Si isotropic chemical shifts. Engelhardt *et al.* investigated the relationship between ^{29}Si chemical shifts (δ_{Si}) and corresponding Si-O-Si bond angles (designated as α) obtained from XRD data using the relation: $\langle \rho_T \rangle = \langle \frac{\cos \alpha}{(\cos \alpha - 1)} \rangle$,[20,21,19] where $<\rho_T>$ represents the average value of the cosine terms for the four Si-O-Si angles about a central ^{29}Si site. While the regression analysis of the δ_{Si} and ρ_T data yields an approximately linear

relationship between them, this regression approach has been improved by also considering Si-O bond distances.[22] Here, we used this modified regression analysis, taking into account both bond parameters, first on surfactant-directed layered silicates, whose molecular structure was recently determined.[18] As shown in Figure 6a, the modified expression reveals a clear linear relationship (squared correlation coefficient, R^2 = 0.927) between the ^{29}Si isotropic chemical shifts (δ_{Si}) and the product average of Si-O bond distances (expressed as d(Si-O)) and Si-O-Si bond angles, $\langle d(\text{Si-O}) \times \rho_T \rangle$. We subsequently applied the same regression approach to zeolite SSZ-70, based on ^{29}Si signal assignments from our NMR analyses discussed above. As clearly shown in Figure 6b, there is also a strong linear correlation (R^2 = 0.938) between the ^{29}Si isotropic chemical shifts and the local bonding configurations.

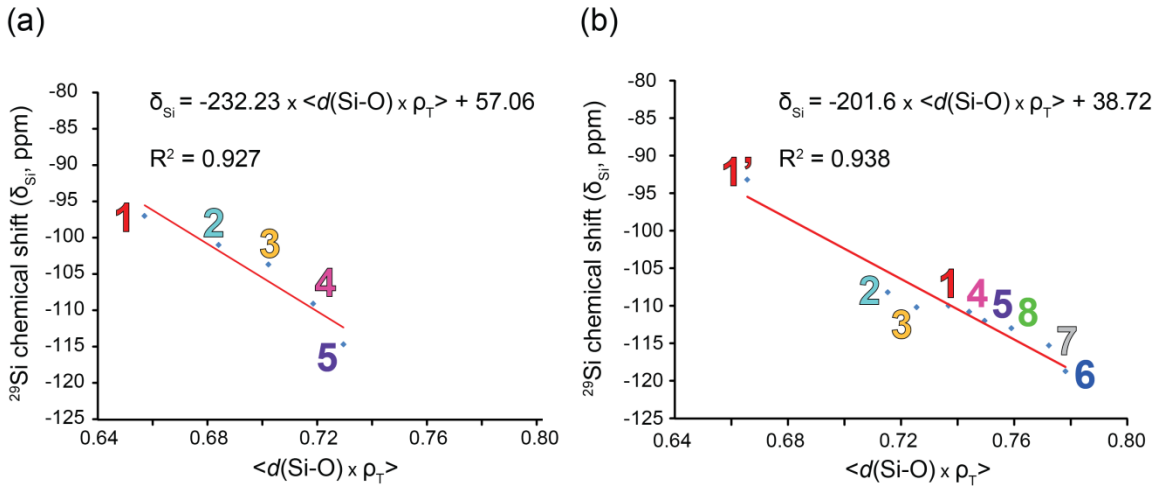

Figure 6. Correlation of ^{29}Si chemical shifts (δ_{Si}) and the corresponding local structures ($\langle d(\text{Si-O}) \times \rho_T \rangle$) for ^{29}Si sites in (a) surfactant-directed layered silicates and (b) zeolite SSZ-70, where d(Si-O) stands for bond distances between Si and O atoms. Equations derived from the regression analyses are included (insets).

Note that the bond angles and distances for each ^{29}Si site in the MWW cage were adapted from the structure previously reported for MCM-22 (MWW),[3] and the ^{29}Si assignments are similar to those previously reported for ITQ-1 (listed in Table 3).[14] Consequently, the connection between solid-state ^{29}Si NMR spectroscopy and X-ray diffraction analyses is expected to provide significant new constraints and insights to aid the structural determination of the SSZ-70 framework.

Table 3. Reported ^{29}Si signal assignments to ^{29}Si sites in zeolite ITQ-1[14]

As-synthesized		Calcined		
^{29}Si chemical shift (ppm)	Type	^{29}Si chemical shift (ppm)	Type	^{29}Si site
-92.6	Q^3			
-94.1	Q^3			
-103.7	Q^3			
-105.0	Q^4	-105.9	Q^4	2
-108.3	Q^4	-111.2	Q^4	3
-110.1	Q^4	-111.8	Q^4	
-112.4	Q^4	-112.6	Q^4	
-114.7	Q^4	-113.9	Q^4	8
-116.7	Q^4	-116.5	Q^4	7
-119.8	Q^4	-120.3	Q^4	6

Whereas the 1D ^{29}Si MAS NMR reveal the presence of additional Q^3 ^{29}Si species in SSZ-70 compared to ITQ-1, the 2D ^{29}Si{^{29}Si} correlation NMR spectra provide detailed structural insights on the local bonding configurations of ^{29}Si atoms in the silicate layer and their associations with the MWW cages. Specifically, the two well-resolved ^{29}Si signals at -98.8 and -99.5 ppm are assigned as ^{29}Si sites *9* and *10*, respectively, and are hypothesized to arise from within the silicate layers between the MWW cages in SSZ-70 (pink line, Figure

1a). Based on analyses of the 2D *J*-mediated NMR spectra, ^{29}Si sites *9* and *10* are covalently bonded to each other (through bridging oxygen atoms), as established by the correlated SQ signals at -98.8 and -99.5 ppm with the DQ signal at -198.3 ppm (Figures 3a and 5a). Interestingly, the same SQ signals (-98.8 and -99.5 ppm) are weakly correlated with the DQ signals at *ca.* -209.2 and -212 ppm, which correspond to isotropic ^{29}Si (SQ) chemical shifts of *ca.* -110 and -113 ppm, respectively. The SQ signal at *ca.* -110 ppm is hypothesized to be from a distinct Q^4 ^{29}Si site within the silicate layers, which is covalently bonded to ^{29}Si site *10* (through bridging oxygen atoms). This ^{29}Si site (designated as site 1_b) is also connected with ^{29}Si site *11*, as evidenced by the DQ signal at -204 ppm, from which the corresponding isotropic ^{29}Si SQ chemical shift for site *11* is calculated to be -94 ppm. The SQ signal at *ca.* -113 ppm is also hypothesized to be associated with a Q^4 ^{29}Si site in the silicate layers, and is assigned as ^{29}Si site *12*. Additionally, its correlation with the SQ signal at -99 ppm (*ca.* -212 in the DQ dimension) suggests that ^{29}Si site *12* is only bonded to site *9*. These results are summarized in Table 4, and a schematic diagram depicting the bonding configuration is shown in Figure 7a, which will be discussed in great detail below. This configuration is similar to the model proposed by Prof. Bärlocher and Prof. McCusker (Figure 7b), although in their model the T9 (in blue) and T10 (in green) ^{29}Si sites are Q^4 moieties, whereas in ours they are Q^3 sites.

In addition, correlated intensities in the 2D NMR spectra (Figures 3a and 5a) indicate incompletely condensed ^{29}Si sites between the MWW cages and the additional silicate layers in SSZ-70. For example, the ^{29}Si SQ signal at -94.0 ppm in the Q^3 ^{29}Si region (designated as ^{29}Si site *1'*) exhibits a strong correlated intensity with the SQ signal at -108 ppm (-202 ppm in the DQ dimension in Figures 3a and 5a), establishing that ^{29}Si site *1'* is

connected to ^{29}Si site-*2* atoms of the MWW cage, and consistent with bonding to three separated site-*2* atoms. This reveals that those ^{29}Si site-*1* atoms that are not covalently bonded to the additional silicate layers are incompletely-condensed Q^3 ^{29}Si species (site *1'*). These results are consistent with the HRTEM image (Figure 1a) and the structural model proposed by Dr. Xie (Figure 7c), and they suggest that SSZ-70 has ordered Q^3 moieties similar to SSZ-74.[23]

The bonding configuration in Figure 7a is constructed from the 2D NMR analyses by considering the connectivities among ^{29}Si sites between MWW cages and the additional silicate layers in SSZ-70, from which the respective degree of condensation for each ^{29}Si site is satisfied. For example, ^{29}Si sites *9*, *10*, *11*, and *1'* are incompletely condensed Q^3 ^{29}Si sites, whereas ^{29}Si sites 1_a, 1_b, and *12* have four ^{29}Si nearest T-site neighbors and are Q^4 ^{29}Si moieties. The ^{29}Si site 1_a is bonded to three ^{29}Si site-*2* atoms, as well as a Q^3 ^{29}Si site-*11* atom in the additional silicate layer, whereas the ^{29}Si site 1_b is bonded to two ^{29}Si site-*10* and two ^{29}Si site-*11* atoms. Although ^{29}Si sites 1_a and 1_b have different site connectivities, they appear to have very similar ^{29}Si isotropic chemical shifts (*ca.* -110 ppm). Additionally, ^{29}Si site 1_a is alternately bonded to ^{29}Si site-*11* atoms on opposite edges of the MWW cages, where the non-bonded species result in Q^3 ^{29}Si moieties (^{29}Si site *1'*). This is consistent with the HRTEM image (Figure 1a) and associated model (Figure 7c). Based on the stoichiometry of the configuration in Figure 7a, ^{29}Si sites *9*, *10*, and *11* are expected to have similar relative populations, though the relative intensity of the ^{29}Si signal from site *11* is obscured by its overlap with that of site *1'* (*ca.* -94 ppm) in the 1D single-pulse ^{29}Si MAS NMR spectrum (Figure 2a). Therefore, based on quantitative analyses of the ^{29}Si MAS NMR spectrum, we estimate that a substantial fraction of the ^{29}Si signal at *ca.* -94 ppm

corresponds to ^{29}Si site *1'* (*ca.* 95%), compared to ^{29}Si site *11* (*ca.* 5%). This hypothesis indicates that only a small fraction of MWW cages are connected to additional silicate layers, which suggest the possibility of a distribution of local structural environments for the silicate layers.

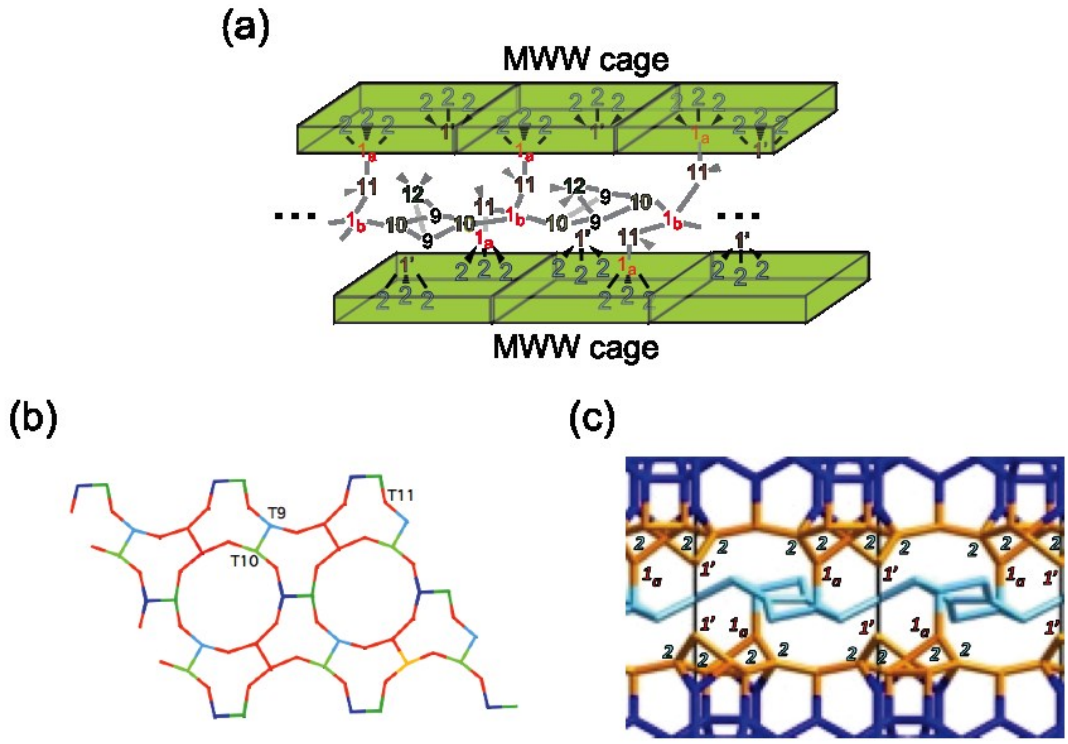

Figure 7. A candidate bonding configuration (a) that is consistent with the 2D ^{29}Si{^{29}Si} NMR results along with models of layered silicates proposed by (b) Profs. Bärlocher and McCusker, (c) Dr. Xie for zeolite SSZ-70.

The broad ^{29}Si signal intensity at *ca.* -105 ppm in the 1D and 2D ^{29}Si NMR spectra (Figures 1a, 3a, and 5a) suggest that there are other Q^4 ^{29}Si moieties present in SSZ-70. Specifically, the 2D *J*-mediated ^{29}Si{^{29}Si} spectrum (Figure 8a, red shaded region) reveals correlated intensities between the SQ signal at *ca.* -105 ppm and the SQ signals at *ca.* -110, -113, and -115 ppm (consistent with their appearances at *ca.* -215, -218, and -220 ppm in

the DQ dimension). Additionally, the SQ signals at *ca.* -102 and -103 ppm are correlated with the SQ signals at *ca.* -112 and -113 ppm the (DQ signals at *ca.* -214 and -216 ppm), respectively. In Figure 8a, the colored dots correspond to the assignments of ^{29}Si sites (*1* in red, *3* in orange, *5* in purple, *6* in blue, *7* in gray, and *8* in green) in the MWW cages and indicate regions of correlated intensity associated with the ^{29}Si signal(s) around -105 ppm.

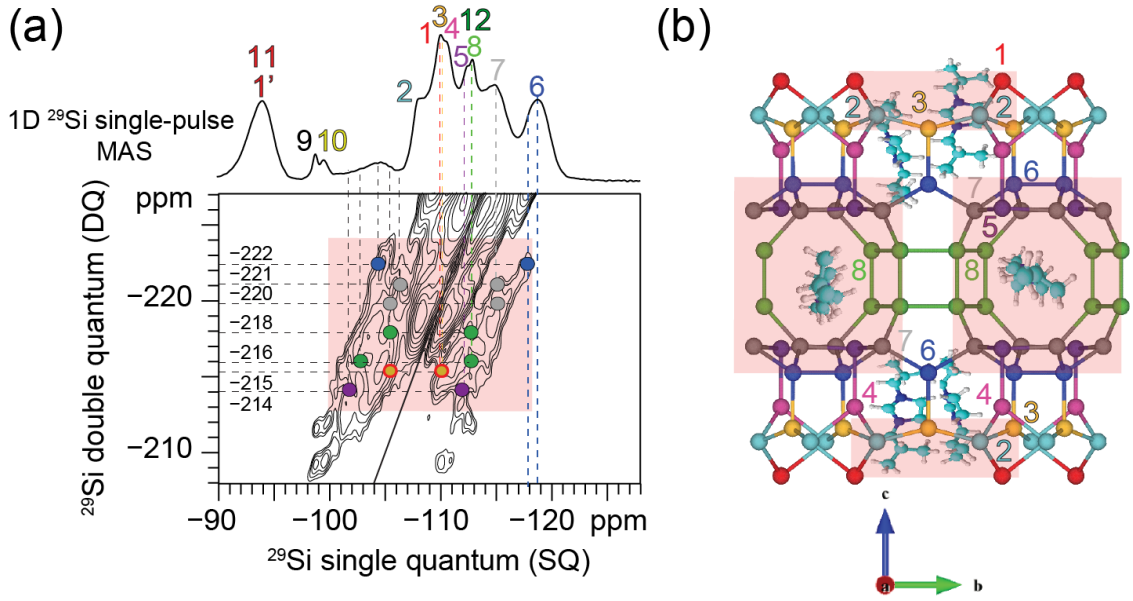

Figure 8. (a) Enlargement of a portion of the solid-state 2D *J*-mediated ^{29}Si{^{29}Si} DQ NMR spectrum shown in Figure 3a for as-synthesized siliceous zeolite SSZ-70. (b) Schematic representation of the MWW cages in SSZ-70, along with 1,3-dicyclohexyl imidazolium SDA molecules, where red shaded regions represent portions of the framework whose associated ^{29}Si sites are expected to strongly interact with the SDAs.

We hypothesize that the ^{29}Si signal(s) at *ca.* -105 ppm and their respective 2D intensity correlations arise due to a distribution of interactions between various Q^4 ^{29}Si sites of the MWW cages and the imidazolium SDAs, whose cationic charges and/or π electrons are expected to influence the local environments of the molecularly proximate ^{29}Si sites. This hypothesis is consistent with the relatively broad linewidths of these ^{29}Si signal(s) compared to other ^{29}Si signals in the ^{29}Si NMR spectra, which reflects a broader distribution of Q^4 ^{29}Si environments. This is similar to the influences of similar imidazolium SDAs observed by Shayib *et al.*[15] in other siliceous zeolite systems. Correspondingly, specific regions of the MWW cages in SSZ-70 are shaded in Figure 8b, where the SDAs (shown in teal) are likely to interact with nearby Q^4 ^{29}Si sites, consistent with the 2D correlated intensities in Figure 8a (red shaded region). For example, ^{29}Si sites *5*, *7*, and *8* associated with the purple, gray, and green dots in Figure 8a are part of the 10-member ring channels of the MWW cages (as shaded accordingly in Figure 8b). Additionally, correlated intensity is also observed between the broad SQ ^{29}Si signals at *ca.* -104 ppm and at *ca.* -118 ppm, the latter of which we attribute to a relatively small fraction of ^{29}Si site-*6* atoms that are displaced to higher frequency (from -118.8 ppm), possibly also due to interactions with the SDAs. Interestingly, broad 1D ^{29}Si signals at *ca.* -105 ppm were similarly observed for as-synthesized ITQ-1 (Figure 2b), which may also be explained by interactions between various ^{29}Si sites of the MWW cages and the SDA molecules. Overall, the analyses of the 2D ^{29}Si{^{29}Si} NMR spectra provide detailed and highly specific insights on complicated site connectivities between MWW-like cages and the additional silicate layers in SSZ-70.

Table 4. ^{29}Si NMR signal assignments of distinct four-coordinate ^{29}Si sites within the silicate layers and at the edges of MWW cages in as-synthesized siliceous SSZ-70. The assignments are based on the 2D *J*- and dipolar-mediated ^{29}Si{^{29}Si} DQ NMR analyses and are consistent with the structural model depicted in Figure 7a.

^{29}Si chemical shift (ppm)	Type	Assignment	Connectivities
-94.0	Q^3	*1'*	*2, 2, 2*
-94.0	Q^3	*11*	1_a, 1_b (x*2*)
-98.8	Q^3	*9*	*10* (x*2*), *12*
-99.5	Q^3	*10*	1_b, *9* (x*2*)
-108.2	Q^4	*2*	1_a or *1'*, *3* (x*2*), *4*
-110.0	Q^4	1_a	*2* (x*3*), *11*
-110.0	Q^4	1_b	*10* (x*2*), *11* (x*2*)
-113	Q^4	*12*	*9* (x*4*)

Although many ^{29}Si site connectivities in zeolite SSZ-70 are established by the 2D ^{29}Si{^{29}Si} NMR analyses, several intensity correlations involve broad and/or overlapping ^{29}Si signals that have been difficult to assign to specific structural features. For example, the ^{29}Si signal at -94 ppm associated with Q^3 ^{29}Si species exhibits correlation intensity at *ca.* -234 ppm in the ^{29}Si DQ dimension (Figure 5a, red shaded region), which should be paired with a ^{29}Si SQ signal at *ca.* -140 ppm, though which is not observed. The causes for such DQ ^{29}Si signal at *ca.* -234 ppm are currently under investigation.

Additional structural features regarding the origins and bonding configurations of the Q^3 ^{29}Si sites at the edges and between the MWW cages also remain to be unambiguously determined. Previously, it was hypothesized by Camblor *et al.* [9] that the ^{29}Si signal(s) at *ca.* -94 ppm for ITQ-1 corresponded to Q^3 ^{29}Si "defect sites" that formed upon the breaking of covalent bonds between ^{29}Si sites *2* and *3*, as shown schematically in Figure 9. If a similar resulting structural feature were present in SSZ-70, one of the Q^3 ^{29}Si sites would be expected to be bonded to ^{29}Si site *6*, manifesting 2D correlated intensities in the SQ

dimension at -94.0 and -118.8 ppm with the signal at -212.8 ppm in the DQ dimension. However, such correlations are not observed in either the 2D *J*- or dipolar-mediated ^{29}Si{^{29}Si} NMR spectra (Figures 3a and 5a, respectively), suggesting a different origin for the Q^3 ^{29}Si species in SSZ-70.

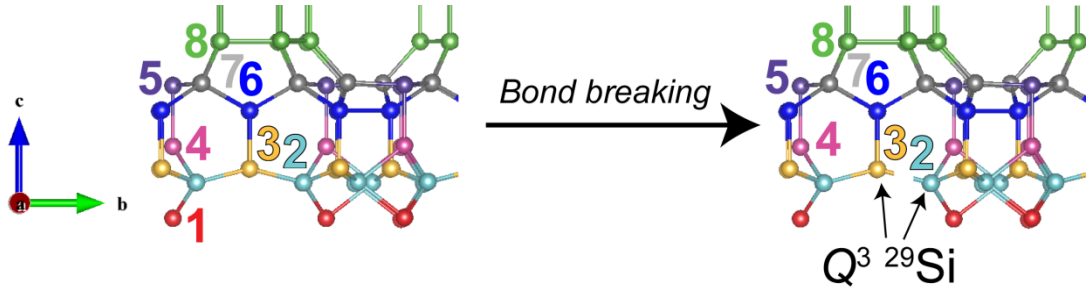

Figure 9. Schematic representation of the hypothesis regarding covalent bond breaking between ^{29}Si sites *2* and *3* in MWW cages, manifesting ^{29}Si signals at *ca.* -93 and -94 ppm.[9]

4.5 Conclusions

A combination of solid-state 1D and 2D ^{29}Si NMR measurements, along with complementary diffraction and electron micrograph analyses, provide important molecular-level insights towards the structure elucidation of zeolite SSZ-70, including the presence of MWW cages and their partial connectivities with the additional silicate layers. Furthermore, the assignment of ^{29}Si NMR signals to various ^{29}Si sites is supported by the clear linear correlation between the ^{29}Si isotropic chemical shifts and the product averages of the Si-O-Si bond angles and Si-O distances associated with the corresponding ^{29}Si sites (Figure 6b). Consistent with the diffraction and electron micrograph measurements, the NMR results also indicate the presence of additional silicate layers between the MWW cages in SSZ-70, as evidenced by connectivities involving Q^4 ^{29}Si sites in the MWW cages and incompletely condensed Q^3 ^{29}Si sites. Based on these NMR analyses, a structural model is proposed

(Figure 7a), where only two of the four Q^4 ^{29}Si site-*1* atoms per MWW cage are bonded to two Q^3 ^{29}Si sites of the additional silicate layers. Specifically, Q^4 ^{29}Si site-1_a atoms on opposite edges of an MWW cage are connected to Q^3 ^{29}Si site-*11* atoms. The other two remaining ^{29}Si site-*1* atoms are incompletely condensed Q^3 ^{29}Si species (labeled ^{29}Si site *1'*), consistent with the ^{29}Si signal intensity at -94.0 ppm. These Q^3 ^{29}Si site-*1'* atoms within the SSZ-70 framework constitute a substantial fraction of the total Q^3 ^{29}Si species present. These observations and proposed structural features are consistent with the HRTEM image for SSZ-70 in Figure 1a. Furthermore, we hypothesize that interactions between the imidazolium SDAs and various Q^4 ^{29}Si sites of the MWW cages manifest broad ^{29}Si signal intensity around -105 ppm in the 1D and 2D ^{29}Si NMR spectra (Figure 8a,b).

While the characterization of the MWW-like cages are now clearly established, including their connectivities to the additional silicate layers, the exact structure of the incompletely condensed silicate layers remains under some discussion. Quantitative analyses of the 1D and 2D ^{29}Si NMR spectra are currently in progress that will take into account the proposed assignments above. We anticipate that these analyses will be helpful for establishing the interconnectivities among ^{29}Si sites in the silicate layers, especially for ^{29}Si sites 1_b, *9*, *10*, *11*, and *12*. Overall, the above 1D and 2D NMR analyses provide detailed insights on the structure of zeolite SSZ-70, notably specific T-site connectivities within and between the MWW cages and additional silicate layers.

4.6 References

1. Zones, S. I. & Burton, A. W. Molecular Sieve SSZ-70 Composition of Matter and Synthesis Thereof. (2006).

2. Archer, R. H., Zones, S. I. & Davis, M. E. Imidazolium structure directing agents in zeolite synthesis: Exploring guest/host relationships in the synthesis of SSZ-70. *Microporous Mesoporous Mater.* **130,** 255–265 (2010).

3. http://www.iza-structure.org/databases/.

4. Archer, R. H. *et al.* Physicochemical Properties and Catalytic Behavior of the Molecular Sieve SSZ-70. *Chem. Mater.* **22,** 2563–2572 (2010).

5. Fung, B. M., Khitrin, a K. & Ermolaev, K. An improved broadband decoupling sequence for liquid crystals and solids. *J. Magn. Reson.* **142,** 97–101 (2000).

6. Lesage, A., Bardet, M. & Emsley, L. Through-Bond Carbon - Carbon Connectivities in Disordered Solids by NMR. 10987–10993 (1999).

7. Cadars, S. *et al.* The refocused INADEQUATE MAS NMR experiment in multiple spin-systems: interpreting observed correlation peaks and optimising lineshapes. *J. Magn. Reson.* **188,** 24–34 (2007).

8. Brouwer, D. H., Kristiansen, P. E., Fyfe, C. a & Levitt, M. H. Symmetry-based 29Si dipolar recoupling magic angle spinning NMR spectroscopy: a new method for investigating three-dimensional structures of zeolite frameworks. *J. Am. Chem. Soc.* **127,** 542–3 (2005).

9. Brouwer, D. H., Darton, R. J., Morris, R. E. & Levitt, M. H. A Solid-state NMR Method for Structure Solution of Zeolite Crystal Structures. 1–34

10. Leonowicz, M. E., Lawton, J. A., Lawton, S. L. & Rubin, M. K. MCM-22: A molecular sieve with two independent multidimensional channel systems. *Science (80-.).* **264,** 1910–1913 (1994).

11. Christiansen, S. C. *et al.* Molecularly ordered inorganic frameworks in layered silicate surfactant mesophases. *J. Am. Chem. Soc.* **123,** 4519–4529 (2001).

12. Hedin, N. *et al.* Structure of a surfactant-templated silicate framework in the absence of 3d crystallinity. *J. Am. Chem. Soc.* **126,** 9425–32 (2004).

13. Na, K. *et al.* Directing zeolite structures into hierarchically nanoporous architectures. *Science* **333,** 328–32 (2011).

14. Camblor, M. A., Corma, A., Diaz-Cabanas, M. J. & Baerlocher, C. Synthesis and Structural Characterization of MWW Type Zeolite ITQ-1 , the Pure Silica Analog of MCM-22 and SSZ-25. *J. Phys. Chem. B* **102,** 44–51 (1998).

15. Shayib, R. M. *et al.* Structure-directing roles and interactions of fluoride and organocations with siliceous zeolite frameworks. *J. Am. Chem. Soc.* **133,** 18728–18741 (2011).

16. Cadars, S., Brouwer, D. H. & Chmelka, B. F. Probing local structures of siliceous zeolite frameworks by solid-state NMR and first-principles calculations of 29Si-O-29Si scalar couplings. *Phys. Chem. Chem. Phys.* **11,** 1825–37 (2009).

17. Fyfe, C. A., Feng, Y., Grondey, H., Kokotailo, G. T. & Gies, H. One- and Two-Dimensional High-Resolution Solid-State NMR Studies of Zeolite Lattice Structures. *Chem. Rev.* **91,** 1525–1543 (1991).

18. Brouwer, D. H. *et al.* A general protocol for determining the structures of molecularly ordered but noncrystalline silicate frameworks. *J. Am. Chem. Soc.* **135,** 5641–5655 (2013).

19. Brouwer, D. H., Darton, R. J., Morris, R. E. & Levitt, M. H. A solid-state NMR method for solution of zeolite crystal structures. *J. Am. Chem. Soc.* **127,** 10365–70 (2005).

20. Thomas, J. M., Klinowski, J., Ramdas, S., Hunter, B. K. & Tennakoon, D. T. B. The evaluation of non-equivalent tetrahedral sites from 29Si NMR chemical shifts in zeolites and related aluminosilicates. *Chem. Phys. Lett.* **102,** 158–162 (1983).

21. Engelhardt, G. & Michel, D. *High-Resolution Solid-State NMR of Silicates and Zeolites*. (Wiley, 1987).

22. Lewis, J. E., Freyhardt, C. C. & Davis, M. E. Location of Pyridine Guest Molecules in an Electroneutral {3∞}[SiO4/2] Host Framework: Single-Crystal Structures of the As-Synthesized and Calcined Forms of High-Silica Ferrierite. *J. Phys. Chem.* **100,** 5039–5049 (1996).

23. Baerlocher, C. *et al.* Ordered silicon vacancies in the framework structure of the zeolite catalyst SSZ-74. *Nat. Mater.* **7,** 631–635 (2008).

Chapter 5: Influences of Structure-Directing Species on Boron Site Distributions in Borosilicate Zeolite SSZ-70 Catalysts

5.1 Abstract

Boron atoms are shown to be inserted into specific types of crystallographic sites in borosilicate zeolite SSZ-70 (B-SSZ-70), and such preferential boron site distributions appear to depend subtly on the chemical moieties of structure-directing agents (SDAs). Multi-dimensional solid-state ^{11}B and ^{29}Si nuclear magnetic resonance (NMR) spectroscopy identifies subtle differences in local ^{11}B and ^{29}Si environments in B-SSZ-70 materials synthesized by using 1,3-diisobutyl- (DiBI) and 1,3-dicyclohexyl-imidazolium (DiC_6I) molecules under otherwise identical synthesis compositions and conditions. Two-dimensional (2D) solid-state dipolar-mediated (through-space) $^{11}B\{^1H\}$ NMR analyses provide molecular proximities between proton moieties of SDAs and boron sites in B-SSZ-70, suggesting that SDAs could potentially alter boron site distributions in borosilicate zeolites. More importantly, 2D *J*-mediated (through-bond) $^{11}B\{^{29}Si\}$ NMR analyses determine connectivities of boron and silicon sites through bridging oxygen atoms in B-SSZ-70. Such molecular information on the identified ^{11}B-O-^{29}Si site connectivities, together with the structure of zeolite SSZ-70, allows us to understand influences of SDAs on boron atom distributions in B-SSZ-70. Specifically, while boron atoms are shown to be similarly distributed among framework sites that are accessible through 10- and 12-

membered rings in B-SSZ-70 synthesized with DiBI and DiC_6I molecules, the degree of hydrophilicity of the SDA species (DiBI > DiC_6I) has a significant influence on the extents of boron atom incorporation. DiBI-directed B-SSZ-70 is shown to have greater boron contents in the final product (Si/B ~22) than DiC_6I-directed B-SSZ-70 (Si/B ~32) even under otherwise synthesis compositions and conditions, suggesting that more hydrophilic SDAs will allow more boron incorporation in B-SSZ-70. This hypothesis is further supported by the study of 1,3-diisopropyl imidazolium (DiPI)-directed B-SSZ-70 that contains more boron contents (Si/B ~14) than DiBI-directed B-SSZ-70, which is attributed to the greater hydrophilicity of DiPI. The molecular-level understanding of the relationships between SDA hydrophilicity and boron site distributions in B-SSZ-70 is expected to aid rational syntheses of borosilicate zeolites with controlled boron siting.

5.2 Introduction

Zeolite catalysts have been extensively used in a wide range of industrial processes, because of their outstanding shape selectivities and strong acidity, as well as high thermal and chemical stabilities.[1,2] Shape selectivities and strong acidity are shown to strongly depend on framework topologies and locations of acid sites.[1,3–6] Therefore, synthesis of targeted zeolite structures with controlled acid site distributions has been an ultimate goal to achieve, aiming for tailoring zeolite catalysts to specific applications. Nevertheless, to the best of our knowledge, this objective has not been fully accomplished yet.[7–15] This might be in part due to exceedingly complicated chemistry during zeolite crystallization, although certain understanding of synthesis conditions on resulting zeolite topologies has been reported.[16–19] This might be also because of conventional characterization methods that have

limited capacity of unambiguously establishing acid site distributions, which are thus poorly understood and considered as formidable tasks to accomplish. Such a challenging characterization question was recently overcome by newly developed nuclear magnetic resonance (NMR) techniques, which can provide *direct* evidence of heteroatom site distributions (*i.e.*, locations of acid sites) in zeolite frameworks.[20,21]

To date, investigations of heteroatom distributions in zeolites mostly focus on ^{27}Al site distributions, where locations of aluminum (^{27}Al) atoms in aluminosilicate zeolites were shown to depend on structure-directing agents (SDAs) and/or synthesis compositions.[7–10,14,22–25] In contrast with the case of ^{27}Al site distributions in aluminosilicate zeolites, very limited data are available for other types of heteroatoms in zeolites (*e.g.*, boron).[26] Very interestingly, Xie and coworkers previously showed that boron (^{11}B) atoms are exclusively inserted into one type of crystallographic sites in borosilicate zeolite MCM-70,[26] which is consistent with the case of surfactant-directed borosilicates.[20] Both studies suggest that preferential ^{11}B site distributions occur in borosilicate zeolites. Furthermore, ^{11}B species in borosilicate zeolites provide versatile opportunities to modify properties of zeolite catalysts.[27–31] These aspects motivate us to investigate ^{11}B site distributions in borosilicate zeolite frameworks using borosilicate zeolite SSZ-70 (B-SSZ-70) as the case study. While the structure of zeolite SSZ-70 has not been completely solved yet, we have demonstrated that tetrahedral site (T-site) connectivities in SSZ-70 must be very similar to zeolite MCM-22 (three letter code: MWW[32]), based on results and analyses of two-dimensional (2D) ^{29}Si{^{29}Si} NMR correlation spectra, electron microscopy, and diffraction patterns. This conclusion is consistent with the previous physicochemical characterization results of SSZ-70.[33] Importantly, catalytic tests clearly indicated that SSZ-70 exhibits a much slower

deactivation rate compared to SSZ-25.[33] In light of significant commercial applications (*e.g.*, alkylation of aromatics) of MWW-type zeolites,[1,34] determination of heteroatom siting in zeolite SSZ-70 is of great interest.

Different from ^{27}Al incorporation that is typically used to create acid sites in zeolite catalysts, ^{11}B incorporation is often applied in synthesizing new zeolite frameworks.[35–43] Additionally, framework ^{11}B species could be post-synthetically exchanged with other heteroatoms, such as Al or titanium (Ti), to impart new catalytic activity to zeolite catalysts.[27–31,44–47] More importantly, we have shown that ^{11}B atoms are preferentially incorporated into certain framework sites in layered borosilicates, significantly different from the results of the aluminosilicate counterpart (*i.e.*, ^{27}Al being everywhere).[20,21] Interestingly, Archer and coworkers previously demonstrated that B-SSZ-70 can be synthesized using various imidazolium derivatives.[48] With the understanding of B-SSZ-70 synthesis compositions and conditions, as well as advanced NMR characterization methods, we hypothesize that ^{11}B site distributions in B-SSZ-70 can be judiciously altered by different types of SDA species.

Here, molecular-level interactions between organic SDAs and inorganic borosilicate frameworks are identified and analyzed using solid-state multi-dimensional NMR techniques with the intention of establishing correlations of SDA species with associated ^{11}B site distributions in B-SSZ-70. In this regard, the chemistry of phase selectively in synthesis of B-SSZ-70 is first discussed by screening combinations of different imidazolium SDAs and inorganic chemical compositions. 1,3-dicyclohexyl imidazoliums (designated as DiC_6I) were shown to have outstanding selectivity toward B-SSZ-70 across a large range of ^{11}B contents (Si/B from 10 to 50 in gel), whereas 1,3-diisobutyl imidazoliums (referred to as

DiBI) could yield B-SSZ-70 only with high ^{11}B loading (Si/B from 10 to 15 in gel). Interestingly, while DiC_6I has superior phase selectivity to B-SSZ-70 than DiBI, its resulting B-SSZ-70 (designated as DiC_6I-synthesized B-SSZ-70) has less ^{11}B contents than DiBI-synthesized B-SSZ-70 under otherwise synthesis compositions and conditions. This observation is hypothesized to be due to the different hydrophobic properties between DiBI and DiC_6I species.

Second, the local ^{29}Si, ^{11}B, and ^{1}H environments of DiBI- and DiC_6I-synthesized B-SSZ-70 were established and compared via solid-state one-dimensional (1D) NMR spectroscopy measurements. 1D ^{29}Si NMR results manifest subtle differences of ^{29}Si signals between DiBI- and DiC_6I-synthesized B-SSZ-70, which are attributed to the subtly distinct local ^{29}Si structures caused by DiBI and DiC_6I SDAs, respectively. The chemical moieties of DiBI and DiC_6I SDAs are also hypothesized to cause very similar yet distinct ^{11}B environments in DiBI- and DiC_6I-synthesized B-SSZ-70, respectively, as revealed by ^{11}B NMR spectroscopy. Consequently, molecular interactions involving ^{29}Si, ^{11}B, and ^{1}H moieties in B-SSZ-70 are measured and elucidated using powerful two-dimensional (2D) NMR techniques. For example, analyses of 2D $^{11}B\{^{1}H\}$ heteronuclear correlation (HETCOR) measurements demonstrate short molecular proximities between ^{11}B and ^{1}H moieties in DiBI- and DiC_6I-synthesized B-SSZ-70. Specifically, in both cases, a major fraction of four-coordinate ^{11}B species are shown to be nearby ^{1}H moieties of either DiC_6I or DiBI SDA^+ molecules, supporting our hypothesis that organic SDAs can direct ^{11}B site distributions in borosilicate zeolite frameworks. Nevertheless, these 1D and 2D NMR results and analyses are insufficient to unambiguously determine ^{11}B site distributions in zeolite B-SSZ-70.

Such challenges of understanding ^{11}B site distributions in B-SSZ-70 were overcome with newly modified 2D NMR methods and zeolite crystallography, where distinct ^{11}B-O-^{29}Si site connectivities in B-SSZ-70 are identified via 2D $^{11}B\{^{29}Si\}$ *J*-mediated (through-bond) NMR experiments. Interestingly, the molecular-level analyses show that ^{11}B atoms are preferentially distributed among certain framework sites, accessible through internal 10-membered-ring (10-MR) and external 12-MR, in both DiBI- and DiC_6I-synthesized B-SSZ-70. These conclusions resonate with the above 2D $^{11}B\{^{1}H\}$ NMR results, where a majority of ^{11}B species are shown to be molecularly proximate to SDA^+ species that appear occluded in 10- and 12-MR in B-SSZ-70. More interestingly, we found that the degree of ^{11}B incorporation is correlated with the hydrophobic properties of SDA+ species as well as the relative population of surface ^{29}Si species, which are further supported by B-SSZ-70 zeolite synthesis using 1,3-diisopropyl imidazolium (DiPI) molecules that are more hydrophilic than DiBI. Overall, the molecular-level understanding of interactions between organic SDA^+ molecules and inorganic B-SSZ-70 frameworks, presented in this report, is expected to aid rational synthesis of borosilicate zeolite catalysts with controlled ^{11}B site distributions.

5.3 Experimental

5.3.1 Materials.

Organic 1,3-diisopropyl imidazolium (DiPI) and 1,3-diisobutyl imidazolium (DiBI) in the hydroxide (OH^-) form were kindly provided by Dr. Stacey Zones at the Chevron Energy Technology Company. Organic 1,3-dicyclohexyl imidazolium tetrafluoroborate (97 %, DiC_6I) was purchased from Sigma-Aldrich and dissolved in water, which was subsequently

ion-exchanged to the OH^- form using AGX-X8 resin (BioRad). The resulting alkaline solutions used in zeolite preparation typically have concentrations of 0.4 ~ 1.0 M.

All the zeolite reactions were performed in 23 mL of poly(tetrafluoroethylene) (PTFE)-lined stainless steel Parr™ autoclaves. Reagents for B-SSZ-70 with ^{29}Si natural abundance synthesis are Cab-O-Sil M5 (scintillation grade, ACROS ORGANICS), 1N sodium hydroxide solution (NaOH, Fisher Chemical), boric acid (Sigma-Aldrich), deionized water (DI H_2O), and SDA OH solutions (DiPI or DiBI or DiC_6I). Detailed gel compositions and conditions are summarized in Table 1. A general zeolite preparation will be described with detail below using DiBI SDA^+, 26 mmol Si basis, and Si/B = 10 as an example. First, the calculated amount of 1N NaOH (2.6 g), DI H_2O (1.74 g), and DiBI SDA^+ OH (10.8 g, 0.48 M) were well mixed, after which boric acid (160 mg) and small amount of as-synthesized B-SSZ-70 (40 mg, 2.5 wt % on the silica oxide basis) were added as ^{11}B sources and seed crystals, respectively. Then Cab-O-Sil M5 (1.56 g) was slowly added into the mixture under vigorous stirring. Once the whole reaction media had been well mixed, it was transferred into the 23 mL autoclaves, and the whole reaction was typically heated at 160 °C and tumbled at ~43 rpm for 5 days. After synthesis, zeolite products were filtered, washed using excess DI H_2O, and then air dried. The synthesis of B-SSZ-70 with ~99 % ^{29}Si enrichment followed the identical procedure described above, except for using ~99 % ^{29}Si-enriched SiO_2 (CortecNet) as ^{29}Si source.

5.3.2 Characterization.

Powder X-ray diffraction (PXRD) patterns were collected on either a Siemens D5000 diffractometer or a Bruker D8 Advance. Scanning electron microscopy (SEM) images were collected using a Hitachi S-570 instrument. Elemental analysis was either performed at

Galbraith Laboratories (Knoxville, TN) or conducted using Thermo jCAP 6300 model at University of California, Santa Barbara (UCSB). The CHN results were provided by the analytical lab in the Marine Science Institute (MSI) at UCSB using the CEC440HA model from Exeter Analytical, Inc. Thermogravimetric analysis (TGA) was performed using Mettler STARe ThermoGravimetric Analyzer (TGA/sDTA851e) under the 25 mL/min argon and 25 mL/min air at a heating rate 10 °C/min from 25 to 600 °C.

Solid-state 1D and 2D NMR spectroscopy measurements were performed to characterize the molecular compositions and structures of the as-synthesized B-SSZ-70 prepared by DiPI, DiBI, and DiC_6I SDA^+ molecules. All the solid-state magic-angle-spinning (MAS) NMR experiments were conducted at room temperature (~25 °C) on a Bruker AVANCE II 500 spectrometer with a 11.7 T wide-bore superconducting magnet, operating at frequencies of 500.0, 160.4 and 99.4 MHz corresponding to ^{1}H, ^{11}B, and ^{29}Si resonances, respectively. Solid-state 1D single-pulse ^{29}Si and spin-echo ^{11}B MAS NMR experiments were performed under MAS conditions of 8 kHz using a 4.0 mm variable-temperature H-X-Y triple-resonance MAS NMR probehead installed with an ^{11}B-^{29}Si insert, both of which high power ^{1}H heteronuclear decoupling was applied during ^{29}Si and ^{11}B signal acquisition using the pulse scheme small-phase-incremental-alternation-with-64-steps (SPINAL-64). Quantitative 1D single-pulse ^{29}Si NMR experiments were acquired using a 90° pulse, corresponding to a ^{29}Si nutation frequency of 16 kHz, and a recycle delay of 500 s. 1D spin-echo ^{11}B NMR spectra were acquired using a recycle delay of 2 s, weak excitation pulse power, and double frequency sweep (DFS) preparation sequence to increase ^{11}B signal sensitivities. 1D single-pulse ^{1}H, $^{29}Si\{^{1}H\}$ and $^{11}B\{^{1}H\}$ cross-polarization (CP) MAS NMR measurements were performed under MAS conditions of 12.5 kHz using a 4.0

mm H-X double-resonance MAS NMR probehead. Pulse power was set to satisfy the Hartmann-Hahn conditions via the adiabatic passage and high power ^{1}H heteronuclear decoupling (SPINAL-64) was applied in 1D ^{29}Si{^{1}H} and ^{11}B{^{1}H} CP MAS NMR measurements, where CP contact time of 6.0 and 0.5 ms and a recycle delay of 8 and 2 s were used for ^{1}H → ^{29}Si and ^{1}H → ^{11}B, respectively. Quantitative 1D single-pulse ^{1}H MAS NMR experiments were conducted using a 90° pulse (corresponding to a ^{1}H nutation frequency of 100 kHz) and a recycle delay of 2 and 8 s for DiBI- and DiC_6I-synthesized B-SSZ-70, respectively. ^{1}H and ^{29}Si NMR chemical shifts were referenced to tetrakis(trimethylsilyl)silane (TKS). ^{11}B NMR shifts were referenced to borontrifluoride diethyletherate (BF_3OEt_2).

2D ^{29}Si{^{1}H} and ^{11}B{^{1}H} heteronuclear correlation (HETCOR) NMR spectra of ^{29}Si-enriched DiBI- and DiC_6I-synthesized B-SSZ-70 were acquired at ~25 °C under MAS conditions of 12.5 kHz using a 4.0 mm H-X double-resonance MAS NMR probehead. All CP conditions of ^{1}H → ^{29}Si and ^{1}H → ^{11}B were the same as the ones in 1D ^{29}Si{^{1}H} and ^{11}B{^{1}H} NMR measurements, where CP contact time of 6.0 and 0.5 ms was used, respectively. STATES-TPPI mode was applied for the indirect dimension in all 2D ^{29}Si{^{1}H} and ^{11}B{^{1}H} NMR experiments. ^{1}H-^{1}H homonuclear decoupling was applied during the ^{1}H spin evolution time t_1 using a phase-modulated rf pulse (associated with a ^{1}H nutation frequency at 100 kHz) based on the eDUMBO-1_{22} (experimental decoupling using mind boggling optimization) pulse sequence. A magic-angle ^{1}H pre-pulse of 0.6 and 0.8 μs was used in 2D NMR measurements of ^{29}Si-enriched DiBI- and DiC_6I-synthesized B-SSZ-70, respectively. Scaling factors for the indirect ^{1}H dimension were calibrated using ^{13}C- and ^{15}N-enriched glycine.

2D $^{11}B\{^{29}Si\}$ *J*-mediated (through-bond) heteronuclear multiple quantum coherence (HMQC) NMR spectra were performed on ^{29}Si-enriched DiBI- and DiC_6I-synthesized B-SSZ-70 at room temperature (~25 °C) and 11.7 T under MAS conditions of 8 kHz. The half-echo delay before and after the evolution period was experimentally optimized to 11.3 ms for both DiBI- and DiC_6I-synthesized B-SSZ-70, during which a 90° ^{29}Si pulse (corresponding to a ^{29}Si nutation frequency of 16 kHz) was applied to refocus the ^{11}B NMR signals right after the first evolution period. STATES mode was applied for the indirect dimension in all 2D $^{11}B\{^{29}Si\}$ NMR experiments. ^{1}H heteronuclear decoupling (50 kHz) with the SPINAL-64 scheme was applied during the whole 2D $^{11}B\{^{29}Si\}$ *J*-mediated HMQC experiments. A recycle delay of 2.0 and 2.8 s was used for DiBI- and DiC_6-synthesized B-SSZ-70, respectively.

5.4 Results and Discussion

Understanding the influences of SDA^+ molecules on heteroatom siting in crystalline zeolite structures has been very challenging to achieve, because SDA^+ molecules and heteroatom species lack long-range order, very different from crystalline frameworks that exhibit high degrees of long-range order. In this regard, solid-state nuclear magnetic resonance (NMR) spectroscopy is considered a promising characterization tool to elucidate such complicated questions. Here, we will particularly discuss the phase selectivities of SDA^+ molecules toward B-SSZ-70 and the resulting ^{11}B siting under various synthesis compositions via combinations of diffraction and NMR techniques, because B-SSZ-70 potentially has significant industrial applications (*e.g.*, catalytic reforming) and contains

interesting structural features that would alleviate mass transport limitations of zeolite-based catalysts.[44] This is also because framework ^{11}B sites could be post-synthetically exchanged with other heteroatom to impart new catalytic activities to SSZ-70 zeolite catalysts.[27,44,47]

First, long-range order of as-synthesized B-SSZ-70, prepared with DiBI or DiC_6I SDA^+ molecules (designated as DiBI- or DiC_6I-synthesized B-SSZ-70, respectively) under different gel compositions, are compared to understand their effects on phase selectivities toward B-SSZ-70. Figure 1 shows powder X-ray diffraction (PXRD) patterns of materials made with DiBI SDA^+ species and varied ^{11}B content in reactant, where different zeolite phases are manifested. For example, PXRD patterns a and b indicate the presence of B-SSZ-70, because the reflections at *ca*. 3.3° and 6.6° 2θ correspond to *d*-spacing of *ca*. 26.7 and 13.4 Å, respectively, suggesting the lamellar structures of B-SSZ-70. Such lamellar features are also observed in the SEM image (Figure D1a). In addition, other indexable reflections, such as the ones at ~20° and 26° 2θ, exhibit distinct long-range order of B-SSZ-70 as well. All these reflections are consistent with the previous characterization results.[33,44] Interestingly, when ^{11}B content in synthesis gel decreases to certain extents (*i.e.*, Si/B = 20 ~ 50), a competing phase, B-ZSM-12 (MTW), appears together with B-SSZ-70 in final products, as shown by patterns c-e (Figure 1c-e). On the basis of the PXRD patterns, the DiBI SDA^+ species are shown to enable the formation of B-SSZ-70 only under high ^{11}B concentrations in synthesis gel (Si/B < ~15).

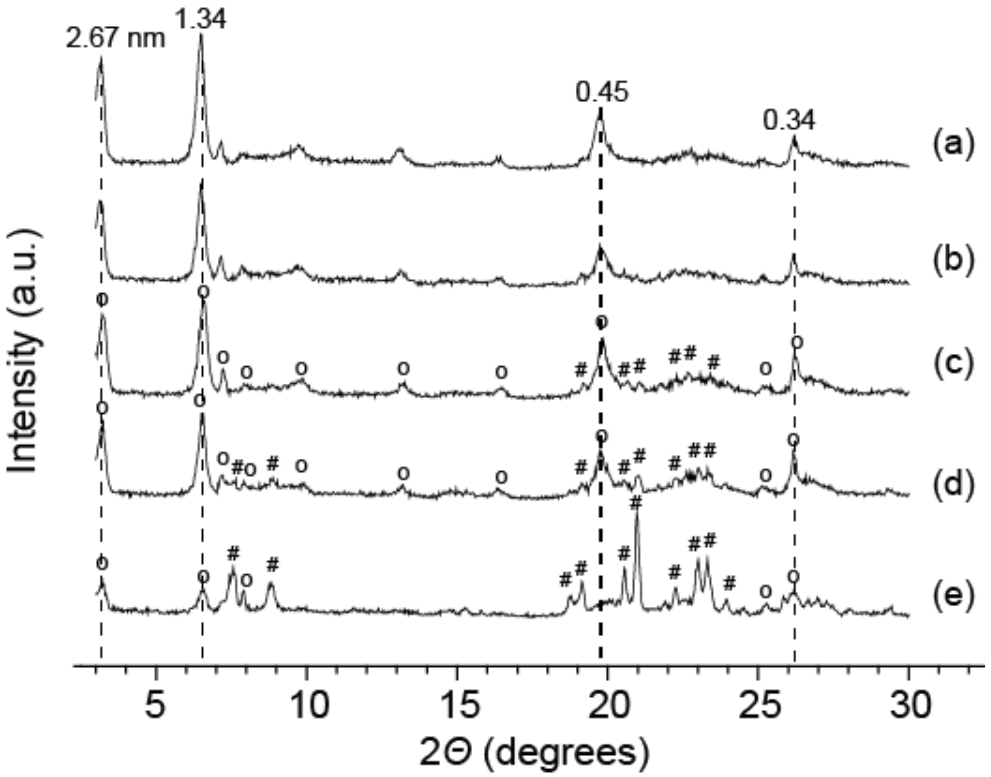

Figure 1. Powder X-ray diffraction (PXRD) patterns of as-synthesized B-SSZ-70 prepared with 1,3-diisobutyl imidazolium (DiBI) SDA^+ species and gel composition of Si/B = (a) 10, (b) 15, (c) 20, (d) 25, and (e) 50, where reflections belonging to B-SSZ-70 and B-ZSM-12 are marked with circle (o) and pound (#) symbols, respectively.

In addition to the DiBI, the DiC_6I can also be used to synthesize B-SSZ-70. While both SDA^+ molecules could yield the same type of zeolite, the DiC_6I shows superior phase selectivities toward B-SSZ-70, as compared to the DiBI. This is evidenced by the PXRD patterns shown in Figure 2a-e. Specifically, the use of DiC_6I is able to produce pure B-SSZ-70 phase under not only high B concentrations (Si/B = 10 and 15 in reactant) but also low B contents (Si/B = 20, 25, and 50 in reactant). All the DiC_6I-synthesized B-SSZ-70 products show very similar reflections (*e.g.*, the ones at *ca*. 3.3°, 6.6°, and 20° 2θ), as discussed above, consistent with the SEM image (Figure D1b). The synthesis compositions and their resulting zeolite phases are summarized in Table 1. Very interestingly, despite the fact that

the DiC_6I has better phase selectivities toward B-SSZ-70 than the DiBI, resulting DiC_6I-synthesized B-SSZ-70 contains less ^{11}B contents than DiBI-synthesized products. Figure 3 compares the Si/B ratios of synthesis gel as well as DiBI- and DiC_6I-synthesized B-SSZ-70. In general, the DiBI-synthesized B-SSZ-70 is shown to have higher ^{11}B contents than the DiC_6I-synthesized products, although the same Si/B ratios (*e.g.*, 10, 15, and 20) were used in synthesis gel. Such different degrees of ^{11}B incorporation are hypothesized to result from relatively distinct hydrophobicities between the DiBI and DiC_6I SDA^+ molecules. The more hydrophobic the SDAs are, the less ^{11}B contents the resulting B-SSZ-70 would possess. This could explain why the DiBI-synthesized B-SSZ-70 materials have higher ^{11}B contents than the DiC_6I-synthesized ones by considering that the DiBI is more hydrophilic than the DiC_6I SDA^+ molecules. Overall, the above PXRD and elemental analyses clearly indicate some differences (*e.g.*, ^{11}B contents and phase selectivities) of borosilicates prepared using DiBI and DiC_6I SDA^+ species. Nevertheless, due to the limited resolution of the PXRD patterns, it is very difficult to understand short-range order around ^{29}Si and ^{11}B sites in B-SSZ-70, which may be altered via different SDA^+ species.

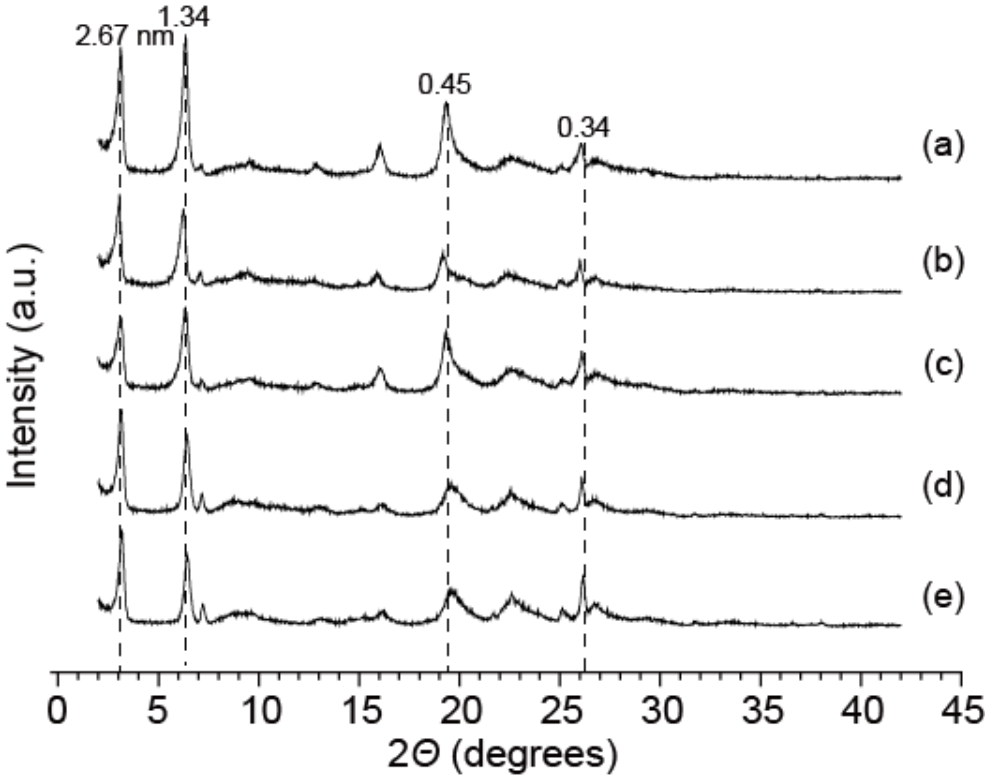

Figure 2. Powder X-ray diffraction (PXRD) patterns of as-synthesized B-SSZ-70 prepared with 1,3-dicyclohexyl imidazolium (DiC_6I) as SDA^+ species and gel composition of Si/B = (a) 10, (b) 15, (c) 20, (d) 25, and (e) 50.

Table 1. Phases obtained from borosilicate hydroxide conditions

SDA	Si/B	SDA^+/SiO_2	H_2O/SiO_2	$NaOH/SiO_2$	Temperature (ºC)	Product
DiBI	10	0.20	30	0.1	160, 43 rpm	B-SSZ-70
	15	0.20	30	0.1		B-SSZ-70
	20	0.20	30	0.1		B-SSZ-70 + B-ZSM-12
	25	0.20	30	0.1		B-SSZ-70 + B-ZSM-12
	50	0.20	30	0.1		B-SSZ-70 + B-ZSM-12
DiC_6I	10	0.20	30	0.1	160, 43 rpm	B-SSZ-70
	15	0.20	30	0.1		B-SSZ-70
	20	0.20	30	0.1		B-SSZ-70
	25	0.20	30	0.1		B-SSZ-70
	50	0.20	30	0.1		B-SSZ-70
DiPI	4	0.12	20	0.1	170, 43 rpm	B-SSZ-70
DiBI	4	0.20	30	0.1	160, 43 rpm	B-SSZ-70
DiC_6I	4	0.20	30	0.1	160, 43 rpm	B-SSZ-70

Note: all ratios in Table 1 refer to molar rations.

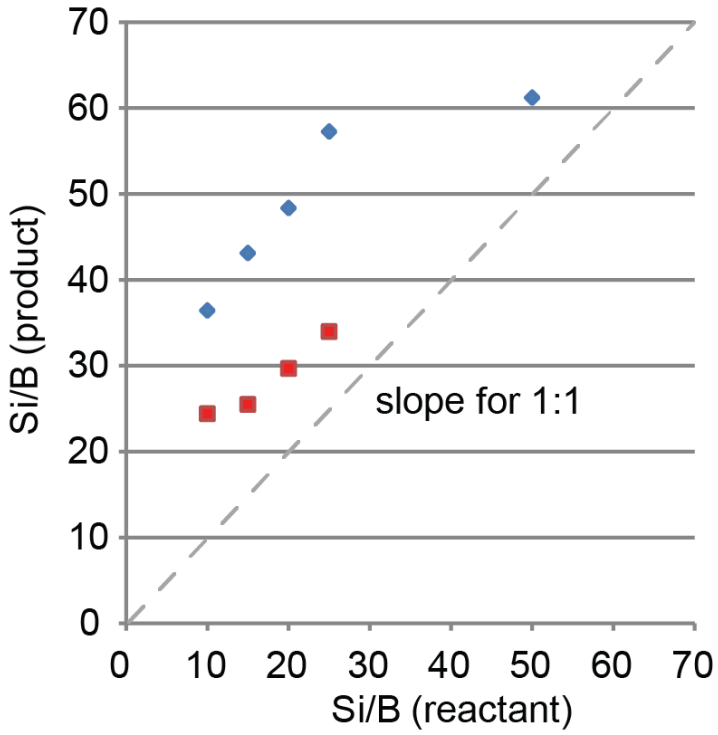

Figure 3. Comparisons of ^{11}B available in the synthesis of B-SSZ-70 and the efficiency of uptake in the product, where compositions associated with DiBI- and DiC_6I-synthesized B-SSZ-70 are shown in red and blue, respectively.

By comparison, solid-state NMR spectroscopy is highly sensitive to nuclear and electronic environments of NMR-active nuclei, and it was consequently applied to interrogate local ^{29}Si and ^{11}B environments of B-SSZ-70. Figure 4a-b shows two 1D single-pulse ^{29}Si MAS NMR spectra of DiBI- and DiC_6I-synthesized B-SSZ-70 with ~99 % ^{29}Si enrichment and Si/B = 10 in reactant, respectively. These two ^{29}Si MAS NMR results manifest various Q^3 and Q^4 ^{29}Si species in the two B-SSZ-70 materials, where Q^m ^{29}Si species correspond to a central ^{29}Si site connected with *m* next-nearest-neighbor (NNN) ^{29}Si sites through bridging oxygen atoms (*m* is an integer between 0 and 4). For example, both B-SSZ-70 products exhibit a ^{29}Si signal at *ca*. -94 ppm associated with Q^3 ^{29}Si species, attributed to the inherent structural features rather than defects of zeolite SSZ-70.

Furthermore, several ^{29}Si signals, such as the ones at *ca*. -110 and -119 ppm, are observed in both B-SSZ-70 (Figure 4a-b), both of which are associated with distinct Q^4 ^{29}Si sites. In addition to the similar ^{29}Si signals, some subtle differences exist in the local ^{29}Si environments within the two B-SSZ-70 materials. Specifically, the ^{29}Si signals (*e.g.*, the ones at *ca*. -103 to -104 ppm and at -113 ppm) reveal a distribution of various Q^4 ^{29}Si species, suggesting that these ^{29}Si sites may interact with SDAs differently. Unlike the ^{27}Al incorporation into silicate frameworks whose influence on ^{29}Si environments has been well recognized,[49–51] framework ^{11}B species do not appear to affect their neighboring ^{29}Si sites very much. Instead, the effects of ^{11}B incorporation are likely subject to its first NNN ^{29}Si species, as shown by our previous experimental and theoretical investigations of surfactant-directed layered borosilicates.[20]

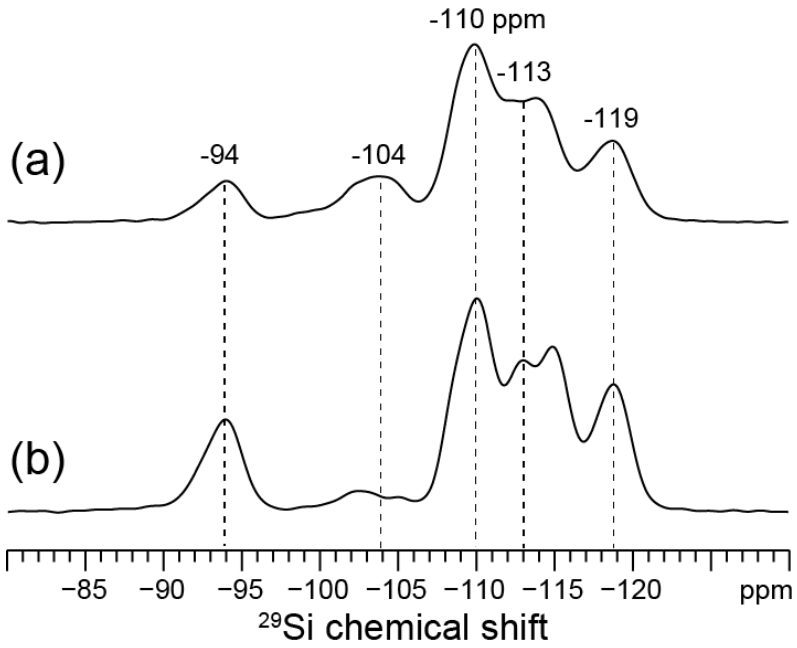

Figure 4. Solid-state 1D single-pulse ^{29}Si MAS NMR spectra of (a) DiBI- and (b) DiC_6I-synthesized zeolite B-SSZ-70 with *ca.* 99% ^{29}Si enrichment and Si/B = 10 in reactant, all of which were acquired at 25 °C under MAS conditions of 8 kHz.

The two DiBI and DiC_6I SDA^+ molecules appear to interact differently with nearby ^{29}Si sites in B-SSZ-70, as revealed by the 1D ^{29}Si NMR results (Figure 4a-b). Such subtle differences in organic-inorganic interactions are hypothesized to also occur between SDA^+ species and ^{11}B sites by considering that negative charges near framework ^{11}B species must be balanced by cationic SDA^+ molecules. Figure 5a and b shows 1D ^{11}B spin-echo MAS NMR spectra of DiBI- and DiC_6I-synthesized B-SSZ-70 with *ca*. 99 % ^{29}Si enrichment and Si/B = 10 in reactant, respectively, revealing several similar ^{11}B signals in both B-SSZ-70 materials. For example, the ^{11}B signals at *ca*. 1.6, -0.5, -2.0, -2.8, and -3.2 ppm in Figure 5a-b are all associated with four-coordinate ^{11}B species, designated as ^{11}B species *A* (*A'*), *B* (*B'*), *C* (*C'*), *D* (*D'*), and *E* (*E'*) in DiBI- (DiC_6I-) synthesized B-SSZ-70, respectively. The ^{11}B species *A*-*E* (*A'*-*E'*) could be reasonably considered as framework ^{11}B sites, because ^{11}B species must become four-coordinated when inserted into zeolite structures. Interestingly, some differences exist in the local ^{11}B environments within the DiBI- and DiC_6I-synthesized B-SSZ-70, as evidenced by the relative populations of ^{11}B species *B*-*E* and *B'*-*E'*. All these subtle changes in local ^{11}B environments are believed to result from the influences of organic DiBI- and DiC_6I SDA^+ species primarily because of their relatively different hydrophobicity, suggesting that the ^{11}B siting in the two B-SSZ-70 materials may be altered via the selection of SDA^+ molecules. Despite various ^{29}Si and ^{11}B species identified via 1D MAS NMR measurements, detailed understanding regarding the ^{11}B siting and how it may be altered via SDA^+ species has still remained elusive.

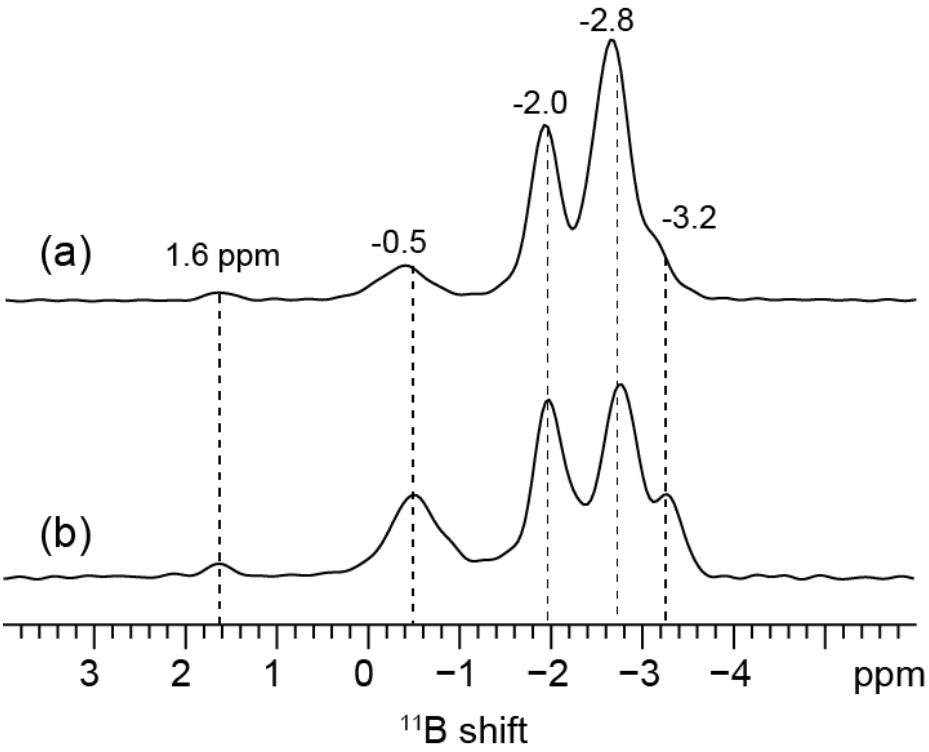

Figure 5. Solid-state 1D spin-echo ^{11}B MAS NMR spectra of (a) DiBI- and (b) DiC$_6$I-synthesized zeolite B-SSZ-70 with *ca*. 99 % ^{29}Si enrichment and Si/B = 10 in reactant, all of which were acquired at 25 °C under MAS conditions of 8 kHz.

In contrast, powerful two-dimensional (2D) NMR techniques are capable of yielding deep insights into molecular interactions among different ^{1}H, ^{29}Si, and ^{11}B species within as-synthesized B-SSZ-70 regardless of the SDA^{+} molecules used in preparation. In particular, 2D NMR methods based on through-space dipolar and through-bond *J* couplings can be employed to determine proximities and site connectivities of two NMR-active nuclei, respectively. These NMR active components include ^{1}H, ^{29}Si, and ^{11}B species within as-synthesized B-SSZ-70. For example, Figure 6 shows a 2D dipolar-mediated ^{29}Si{^{1}H} HETCOR NMR spectrum of ^{29}Si-enriched DiBI-synthesized B-SSZ-70 prepared with Si/B = 10 in reactant, where various intensity correlations are observed among different ^{1}H and ^{29}Si species, indicating the correlated ^{1}H and ^{29}Si species are molecularly proximate (< 1

nm). Specifically, the ^{1}H signal at *ca*. 0.9 ppm (associated with the ^{1}H species *I* of DiBI) exhibits correlated intensities with the ^{29}Si signals at *ca*. -94, -104, -110, -114, and -119 ppm, establishing that such ^{1}H moieties are in short proximities with respect to nearly all ^{29}Si sites within B-SSZ-70. Interestingly, other ^{1}H signals at around 2.2, 3.8, and 7.0 ppm (corresponding to the ^{1}H species *II*, *III*, and *IV* of DiBI SDA^{+} molecules, respectively) only show intensity correlations with the ^{29}Si signals associated with the ^{29}Si sites within the **MWW**-like cages, such as the ones at *ca*. -110 (^{29}Si site *3*), -114 (^{29}Si site *7*), and -119 ppm (^{29}Si site *6*). Detailed ^{29}Si signal assignments are given in Table 2, and the corresponding ^{29}Si sites and their connectivities are illustrated in Figure D2. These results suggest that most part of the DiBI SDA^{+} molecules interact preferentially with the ^{29}Si sites of the **MWW**-like cages in DiBI-synthesized B-SSZ-70. This may imply that ^{11}B species would be inserted into framework sites near these DiBI-proximate ^{29}Si sites within the **MWW**-like cages.

Table 2. ^{29}Si chemical shift assignments in as-synthesized siliceous SSZ-70

^{29}Si chemical shift (ppm)	Type	Assignment	Connectivities
-94.0	Q^3	*1'*	*2* (x3)
-94.0	Q^3	*11*	*1* (x3)
-98.8	Q^3	*9*	*10* (x2), *12*
-99.5	Q^3	*10*	*1*, *9* (x2)
-105	Q^4	*?*	?
-108.2	Q^4	*2*	*1*, *3* (x2), *4*
-110.0	Q^4	*1*	*2* (x3), *9* or *10* or *11*
-110.2	Q^4	*3*	*2* (x2), *3*, *6*
-110.8	Q^4	*4*	*2* (x3), *5*
-112.0	Q^4	*5*	*4*, *7* (x3)
-113.0	Q^4	*8*	*7*, *8* (x3)
-113.0	Q^4	*12*	*9* or *10* (x4)
-114 ~ -115	Q^4	*7*	*5*, *6* (x2), *8*
-118.8	Q^4	*6*	*3*, *6*, *7* (x2)

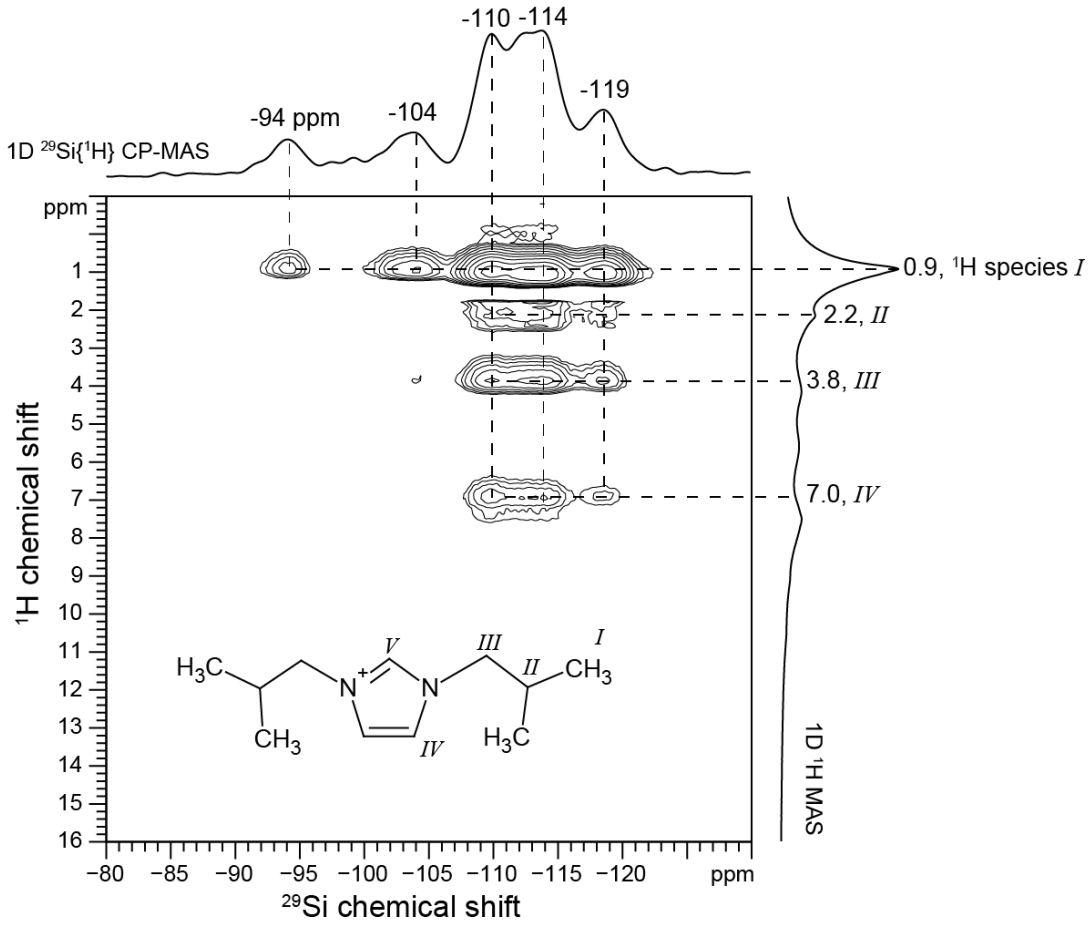

Figure 6. Solid-state 2D dipolar-mediate heteronuclear correlation (HETCOR) $^{29}Si\{^{1}H\}$ NMR spectrum of ^{29}Si-enriched DiBI-synthesized zeolite B-SSZ-70 (Si/B = 10 in reactant), where solid-state 1D ^{1}H and $^{29}Si\{^{1}H\}$ CP-MAS spectra are shown along the right vertical and the top horizontal axes, respectively. ^{1}H chemical shift assignments are shown in the inset for the 1,3-diisobutylimidazolium (DiBI) SDA^{+} molecules.

As compared to DiBI-synthesized B-SSZ-70, all ^{1}H components of the DiC_6I SDA^{+} molecules appear to interact with all ^{29}Si sites within DiC_6I-synthesized B-SSZ-70. For example, the ^{1}H species *I'-III'* (associated with protons of cyclohexyl groups) are shown to be molecularly proximate to nearly all ^{29}Si sites, as evidenced by the intensity correlations among ^{1}H signals at approximately 1.8 ~ 3.0 ppm and ^{29}Si signals at *ca*. -94, -110, -113, -115, and -119 ppm in the 2D dipolar-mediated $^{29}Si\{^{1}H\}$ HETCOR NMR spectrum (Figure 7). Furthermore, such Q^4 ^{29}Si signals in the range of *ca*. -110 to -119 ppm also exhibit

correlated intensities with the ^{1}H signals at *ca*. 5.0 and 8.0 ppm that correspond to the ^{1}H moieties *IV'* and *V'* of DiC_6I SDA^+ molecules, respectively, from which the pairs of ^{1}H-^{29}Si site proximities (< 1 nm) are determined. Interestingly, the Q^3 ^{29}Si signal at *ca*. -94 ppm is correlated not only with the ^{1}H signals at *ca*. 1.8 ~ 3.0 ppm (^{1}H species *I'-III'*) but also with the ^{1}H resonances at *ca*. 5.0 and 8.0 ppm (^{1}H species *IV'* and *V'*), different from the case of DiBI-synthesized B-SSZ-70, where the same Q^3 ^{29}Si signal exhibits correlations only with the ^{1}H signal associated with protons of diisobutyl groups (^{1}H species *I*) of DiBI SDA^+ molecules. Such differences in the 2D $^{29}Si\{^{1}H\}$ NMR spectra (Figures 6 and 7) suggest that the DiBI and DiC_6I SDA^+ molecules may fit differently within B-SSZ-70 frameworks, despite the fact that both SDA^+ molecules yielded B-SSZ-70 as final products.

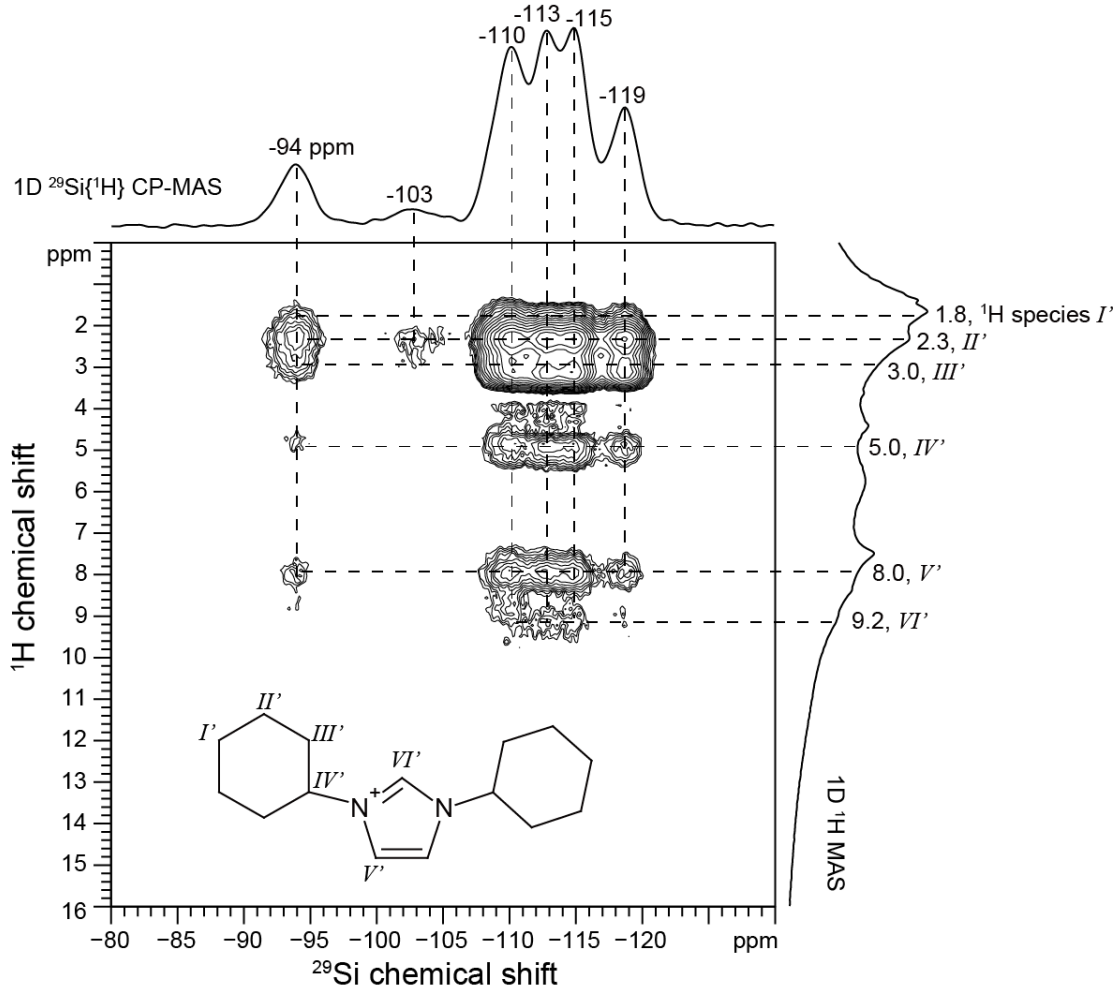

Figure 7. Solid-state 2D dipolar-mediated heteronuclear correlation (HETCOR) $^{29}Si\{^{1}H\}$ NMR spectrum of ^{29}Si-enriched DiC_6I-synthesized zeolite B-SSZ-70 (Si/B = 10 in reactant), where solid-state 1D ^{1}H and $^{29}Si\{^{1}H\}$ CP-MAS spectra are shown along the right vertical and the top horizontal axes, respectively. ^{1}H chemical shift assignments are shown in the inset for the 1,3-dicyclohexylimidazolium (DiC_6I) SDA^+ molecules.

In addition to the 2D $^{29}Si\{^{1}H\}$ NMR analyses, thermogravimetric analysis (TGA) was performed on DiBI- and DiC_6I-synthesized B-SSZ-70. Figure 8 compares TGA profiles of the two B-SSZ-70 products, where DiBI- and DiC_6I-synthesized B-SSZ-70 exhibit mass loss of 19.7% and 23.7% between 200 and 600 ºC, respectively. Such differences may be attributed to the molecular weights (MW) of DiBI (MW: 181.3) and DiC_6I (MW: 233.4) molecules, suppose that the amount of occluded SDA^+ molecules are the same. Interestingly,

the smaller DiBI reveals one major mass loss beginning with the temperature at *ca*. 250 °C, whereas two distinct mass loss regions are observed in the larger DiC_6I. Specifically, the first region starts at approximately 250 °C as well, similar to the case of DiBI, followed by the second mass loss region with an inflection point at around 440 °C. The TGA profiles of the DiBI- and DiC_6I-synthesized B-SSZ-70 (Figure 8) may indicate that the DiBI and DiC_6I are occluded differently within the B-SSZ-70 frameworks, leading to distinct organic/inorganic environments. These observations are consistent with the 2D $^{29}Si\{^1H\}$ NMR results (Figures 6 and 7). Based on the 2D $^{29}Si\{^1H\}$ NMR and TGA results, the DiC_6I SDA^+ molecules appear to fit within the B-SSZ-70 structure more tightly than the DiBI, which may result into higher thermal protection. Consequently, the DiC_6I SDA^+ molecules have to experience two stages of decompositions during thermal treatments. With the understanding of such organic-inorganic interactions, we hypothesize that framework ^{11}B sites would be greatly influenced by how organic SDA^+ molecules are occluded within B-SSZ-70, achieving altered ^{11}B siting via selection of SDA^+ molecules.

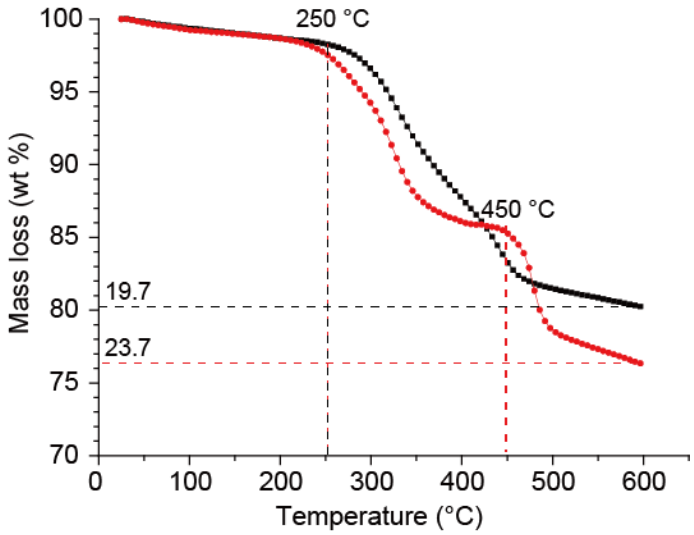

Figure 8. Thermogravimetric analysis (TGA) profiles of as-synthesized B-SSZ-70 prepared with DiBI (in black) and DiC_6I (in red) SDA^+ molecules.

The ^{11}B siting within B-SSZ-70 is believed to be strongly influenced by SDA^+ molecules, because the negative charges near framework ^{11}B species must be compensated with cationic groups of SDA^+ molecules. Such hypotheses can be examined by performing 2D dipolar-mediated $^{11}B\{^1H\}$ NMR measurements. Various correlated signal intensities are observed between different ^1H and ^{11}B species in a 2D dipolar-mediated $^{11}B\{^1H\}$ NMR spectrum of DiBI-synthesized B-SSZ-70 (Figure 9), which manifests distinct types of molecular ^{11}B-^1H proximities. For example, the ^{11}B signals at 1.6 and -0.5 ppm, corresponding to ^{11}B species *A* and *B*, are correlated only with the ^1H signals at 2.0 and 1.6 ppm, respectively, both of which are assigned to silanol groups from structural defects (*i.e.*, Si-O**H**). In contrast, the ^{11}B signals at *ca*. -2.0 and -2.8 ppm show intensity correlations with several ^1H signals instead of single one. Specifically, the ^{11}B signal (-2.0 ppm, ^{11}B species *C*) exhibits correlations with the ^1H signals at 1.6 and 4.5 ppm associated with structural defects (Si-O**H**) and water (H_2O), respectively. More importantly, the ^1H signals at 2.6, 3.8, 7.8, and 8,6 ppm, which correspond to the ^1H species *II*, *III*, *IV*, and *V* of the DiBI SDA^+ molecules, respectively. These observations establish that such ^{11}B species *C* are very close to the DiBI SDA^+ molecules (< *ca*. 0.2 ~ 0.3 nm) given the relatively short CP contact time (0.5 ms) applied during the NMR measurements. Interestingly, the same ^{11}B signal is also correlated with the ^1H signal at *ca*. 10.4 ppm, indicating that such ^{11}B species *C* neighbor hydrogen-bonding ^1H species. Finally, similar to the ^{11}B signal at *ca*. -2.0 ppm, the ^{11}B signal at *ca*. -2.8 ppm (^{11}B species *D*) also shows correlated intensities with the ^1H signals at 1.6, 2.8, 3.8, 4.5, 7.8, and 8.6 ppm, associated with protons of structural defects, ^1H species *II*, *III*, *IV*, H_2O, and *V* of the DiBI SDA^+ molecules, respectively. Furthermore, the correlated pairs of the ^{11}B signal at -2.8 ppm and the ^1H signal at 5.5 ppm reflect short

molecular proximities between ^{11}B species *D* and the Brønsted acid sites near hydrogen-bonding species within B-SSZ-70, similar to ^{11}B species *C*. Very interestingly, the ^{1}H signals at 10.4, 11.5, and 12.9 ppm, corresponding to various types of hydrogen-bonding ^{1}H species, are correlated with the same ^{11}B signal at -2.8 ppm. This suggests that a fraction of ^{11}B species *D* may be on the edge of **MWW**-like cages in B-SSZ-70, where there are more Q^3 ^{29}Si species (*e.g.*, $\equiv$Si-OH) relatively less condensed than any parts of structures, which would increase the probabilities of hydrogen-bonding protons nearby the ^{11}B species *D*. As compared to the ^{11}B signals at *ca*. 1.6 and -0.5 ppm, the complicated correlations between the ^{11}B signals at -2.0 and -2.7 ppm and different ^{1}H signals, most of which result from DiBI SDA$^+$ molecules, indicate that the ^{11}B species *C* and *D* should correspond to framework ^{11}B sites. In contrast, the ^{11}B species *A* and *B* appear to be associated with extra-framework ^{11}B species. On the basis of the 2D ^{11}B{^{1}H} NMR spectrum (Figure 9), it is concluded that the ^{11}B species *C* and *D* are shown to be molecularly proximate with respect to DiBI SDA$^+$ molecules, consistent with the hypothesis regarding charge compensation mechanism involving ^{11}B sites and DiBI SDA$^+$ molecules.

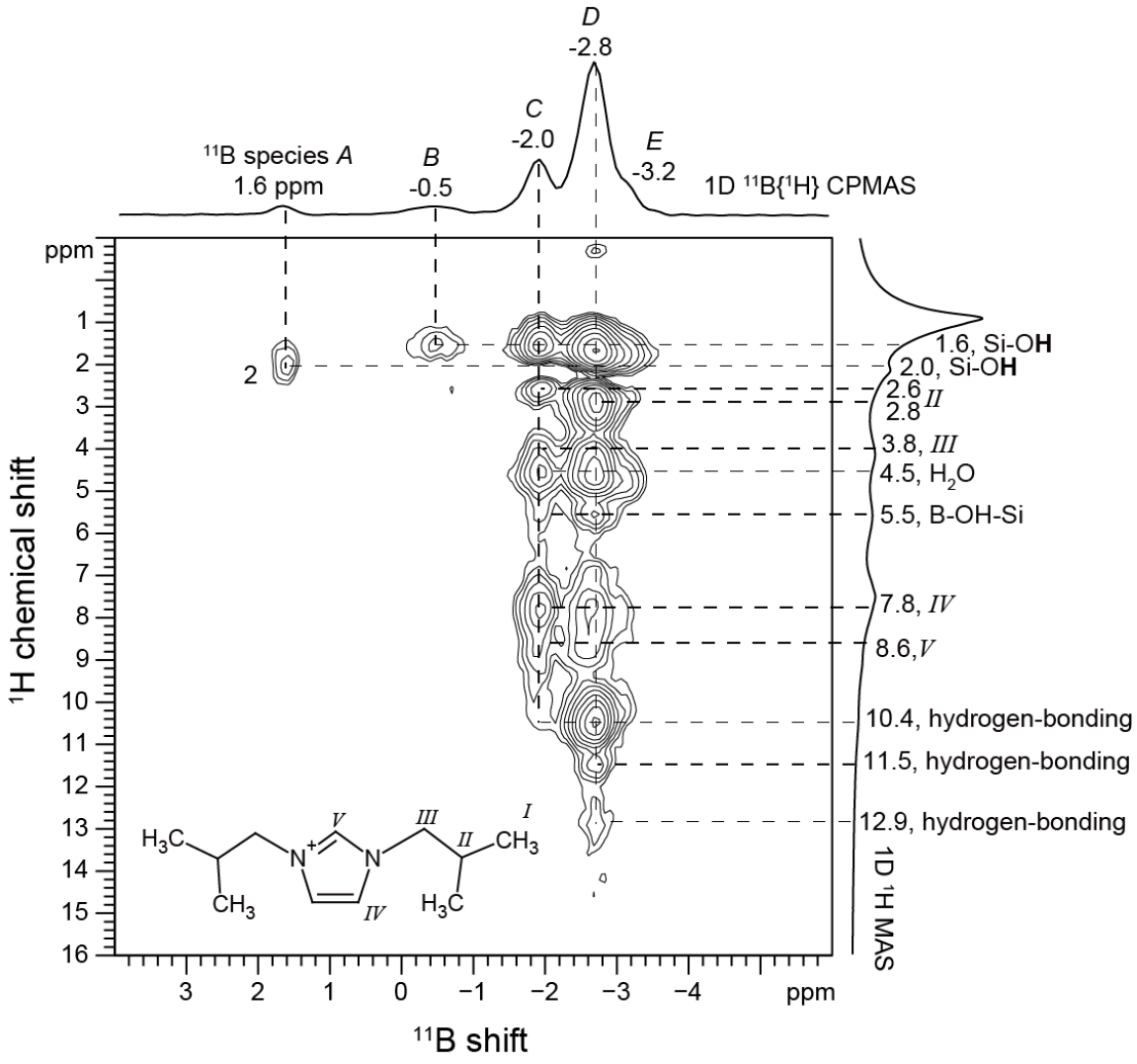

Figure 9. Solid-state 2D dipolar-mediated heteronuclear correlation (HETCOR) $^{11}B\{^{1}H\}$ NMR spectrum of ^{29}Si-enriched DiBI-synthesized zeolite B-SSZ-70 (Si/B = 10 in gel), where solid-state 1D ^{1}H and $^{11}B\{^{1}H\}$ CP-MAS spectra are shown along the right vertical and the top horizontal axes, respectively. ^{1}H chemical shift assignments are shown in the inset for the DiBI SDA^{+} molecules.

Similar to the DiBI-synthesized B-SSZ-70, each four-coordinate ^{11}B site (especially for ^{11}B species *C'*, *D'*, and *E'*) is affected by the presence of DiC_6I SDA^{+} molecules to different extents within DiC_6I-synthesized B-SSZ-70. Such pairs of ^{1}H-^{11}B molecular proximities are identified via 2D dipolar-mediated $^{11}B\{^{1}H\}$ NMR experiments, and the resulting 2D spectrum is shown in Figure 10. For example, the ^{11}B signal at *ca*. 1.6 ppm (^{11}B species *A'*)

is correlated with the ^{1}H signal at 1.2 ppm (assigned to structural defects, Si-O**H**), indicating the short distance between such ^{11}B species *A'* and Si-O**H**. Likewise, the ^{11}B signal at *ca*. -0.5 ppm (^{11}B species *B'*) exhibits correlated intensities with the ^{1}H signal at 1.2, 6.8, and 8.5 ppm, the first of which is attributed to Si-O**H**, whereas the latter two of which are associated with different Brønsted acid sites interacting with hydrogen bond. These observations establish that the ^{11}B species *B'* is proximate not only to structural defects but also to acid sites (close to hydrogen bonding configurations), slightly different from ^{11}B species *A'*. As compared to the ^{11}B species *A'* and *B'*, the ^{11}B species *C'*, *D'*, and *E'* appear to be strongly influenced by DiC_6I SDA^+ molecules, as evidenced by the correlated ^{11}B signals at *ca*. -2.0, -2.8, and -3.2 ppm with the ^{1}H signal, respectively. Specifically, the ^{11}B species *C'* is determined to neighbor the structural defects (Si-O**H**), adsorbed water, ^{1}H moieties *V'* of DiC_6I, and acid sites nearby hydrogen bonding, because its ^{11}B signal at *ca*. -2.0 ppm shows correlated intensities with the ^{1}H signals at *ca*. 1.6, 4.2, 7.2, and 8.8 ppm, respectively. The ^{11}B species *D'* is established to be molecularly proximate to structural defects (Si-O**H**), ^{1}H moieties *I'*, *II'*, and *III'* of DiC_6I, and water molecules, as manifested by the intensity correlations between the ^{11}B signal at *ca*. -2.8 ppm and the respective ^{1}H signals at *ca*. 1.2, 1.8, 2.3, 3.0, and 4.2 ppm. Furthermore, the ^{11}B species *D'* exhibit short proximities with respect to the ^{1}H moieties *V'* and *VI'* of DiC_6I, supported by the correlations involving the same ^{11}B signal at *ca*. -2.8 ppm and the ^{1}H signals at *ca*. 7.4 and 9.4, respectively. Lastly, the ^{11}B species *E'* appears to possess similar ^{11}B-^{1}H proximities as the ^{11}B species *D'* expect for the ^{1}H moieties *F'* of DiC_6I on the basis of the correlated intensities involving the ^{11}B signal at *ca*. -3.3 ppm and the ^{1}H signals at *ca*. 1.2, 1.8, 2.3, 3.0, 4.2, and 7.2 ppm. Again, similar to the case of DiBI-synthesized B-SSZ-70, the ^{11}B species *A'* and *B'* seem to be

extra-framework ^{11}B sites, whereas the ^{11}B species *C'*, *D'*, and *E'* should stand for framework ^{11}B sites by comparing their molecular proximities to DiC_6I SDA^+ molecules. Interestingly, the close proximities between the ^{11}B species *C'*, *D'*, and *E'* and DiC_6I SDA^+ molecules suggest that these framework ^{11}B sites would be strongly influenced by the presence of DiC_6I SDA^+ molecules. While the molecular interactions involving organic DiBI or DiC_6I SDA^+ molecules and inorganic ^{29}Si and ^{11}B sites within B-SSZ-70 can be nicely identified and compared via 2D NMR methods, the exact locations of such four-coordinate ^{11}B species in borosilicate frameworks are still very difficult to establish.

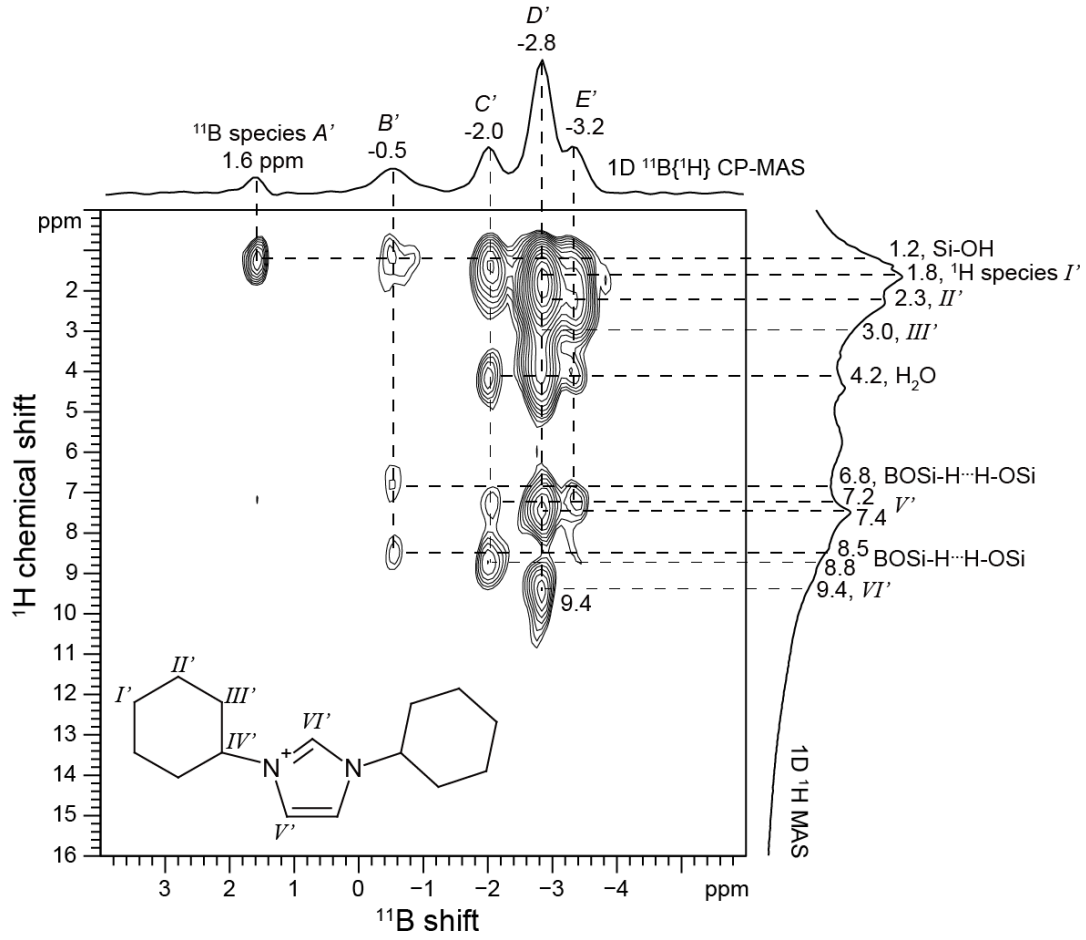

Figure 10. Solid-state 2D dipolar-mediated heteronuclear correlation (HETCOR) $^{11}B\{^{1}H\}$ NMR spectrum of ^{29}Si-enriched DiC_6I-synthesized zeolite B-SSZ-70 (Si/B = 10 in gel), where solid-state 1D ^{1}H and $^{11}B\{^{1}H\}$ CP-MAS spectra are shown along the right vertical and the top horizontal axes, respectively. ^{1}H chemical shift assignments are shown in the inset for the DiC_6I SDA^{+} molecules.

2D NMR techniques rely not only on through-space dipolar interactions that can be utilized to estimate molecular proximities of two NMR-active species, as extensively discussed above, but also on through-bond *J* couplings that can be essentially used to determine site connectivities of two NMR-active components. In particular, $^{2}J(^{29}Si\text{-}O\text{-}^{11}B)$ couplings can be detected in 2D *J*-mediated $^{11}B\{^{29}Si\}$ NMR experiments to identify various $^{29}Si\text{-}O\text{-}^{11}B$ site connectivities, from which, together with the zeolite crystallography, the ^{11}B siting in borosilicate frameworks would be established. Figure 11 shows a 2D *J*-mediated

$^{11}B\{^{29}Si\}$ NMR spectrum of ^{29}Si-enriched DiBI-synthesized B-SSZ-70, where correlated intensities are shared between a variety of ^{11}B and ^{29}Si signals, manifesting distinct ^{29}Si-O-^{11}B site connectivities. Specifically, the ^{11}B signal at 2.8 ppm corresponding to ^{11}B species *D* is correlated with the ^{29}Si signal at -113 ppm associated with ^{29}Si site *8*, indicating that ^{11}B species *D* is connected with ^{29}Si site *8* (through bridging oxygen atoms). The same ^{11}B signal (2.8 ppm, ^{11}B species *D*) also exhibits intensity correlations with the ^{29}Si signal at *ca*. -114 ~ -115 ppm (^{29}Si site *7*), revealing that ^{11}B species *D* is bonded to ^{29}Si site *7* (through bridging oxygen atoms) as well. The two sets of connectivities, in conjunction with the crystallographic understanding of B-SSZ-70, unambiguously show that a fraction of ^{11}B species *D* originate from the ^{11}B atoms inserted into ^{29}Si site *8* (designated as ^{11}B species *D-8*) in internal 10-MR within **MWW**-like cages. Similarly, other ^{11}B-O-^{29}Si site pairs could be identified from the 2D $^{11}B\{^{29}Si\}$ NMR spectrum (Figure 11). For example, the ^{11}B signal at *ca*. -2.5 ppm (previously assigned to ^{11}B species *D*, due to the limited resolution in the 1D ^{11}B MAS NMR spectrum, Figure 5a) has correlated intensities with the ^{29}Si signals at *ca*. -120 ppm (associated with ^{29}Si site *6*), and the ^{11}B signal at *ca*. -2.6 ppm (also referred to as ^{11}B species *D*) is correlated with the ^{29}Si signals at *ca*. -108 and -110 ppm, corresponding to ^{29}Si sites *2* and *3*, respectively. The site connectivities with ^{29}Si sites *2*, *3*, and *6* allow us to conclude that certain portion of ^{11}B species *D* are composed of the ^{11}B atoms incorporated into ^{29}Si site *3* (within external 12-MR of **MWW**-like cages, labeled as ^{11}B species *D-3*). The subtle displacement in ^{11}B signals of ^{11}B species *D-3* (-2.5 to -2.6 ppm) is attributed to the local deformation around ^{11}B species *D-3* caused by ^{11}B incorporation.

Interestingly, still a fraction of the ^{11}B species *D* are shown to result from the ^{29}Si site *1* (Q^4) substituted by ^{11}B atoms, as supported by the intensity correlations between the ^{11}B

signal at *ca*. -2.7 ppm and the ^{29}Si signals at *ca*. -101 and -108 ppm, associated with the ^{29}Si sites *10* and *2*, respectively. Such framework ^{11}B sites are referred to as ^{11}B species *D-1*. On the basis of detailed 2D ^{11}B{^{29}Si} NMR results and analyses, it can be realized that distinct ^{11}B sites may manifest very similar ^{11}B shifts in 1D ^{11}B MAS NMR spectra, increasing difficulty in distinguishing various types of framework ^{11}B species without applying 2D NMR methods. Similar observations take place in the ^{11}B signal at *ca*. -2.0 ppm (^{11}B species *C*), because it exhibits correlations with the ^{29}Si signals at *ca*. -95, -100, -108, -109, -110, and -110.5 ppm, which exceeds the maximum coordination number for a given ^{29}Si site (*i.e.*, 4). In other words, there are at least two distinct ^{11}B sites sharing the ^{11}B signal at -2.0 ppm. Specifically, on one hand, a portion of the ^{11}B signals at -2.0 ppm are contributed by the ^{11}B atoms incorporated into ^{29}Si site *1* (Q^4), designated as ^{11}B species *C-1*, as evidenced by the correlated ^{11}B signal at -2.0 ppm (^{11}B species *C*) with the ^{29}Si signals at -100 and -108 ppm, corresponding to the ^{29}Si sites *9* and *2*, respectively. On the other hand, another fraction of the ^{11}B species *C* can be considered as two types of ^{11}B sites caused by ^{11}B incorporation into ^{29}Si sites *2* (bonded to Q^4 ^{29}Si site 1) and *2'* (bonded to Q^3 ^{29}Si site 1), named as ^{11}B species *C-2* and *C-2'*, respectively. The assignment of ^{11}B species *C-2* is based on the correlated intensities among the ^{11}B signal at -2.0 ppm (^{11}B species *C*) and the ^{29}Si signals at approximately -109, -110, -110.5 ppm corresponding to the ^{29}Si sites *1* (Q^4), *3*, and *4*, respectively. In contrast, the correlated pairs of the same ^{11}B signal and the ^{29}Si signals at around -95, -110, -110.5 ppm, associated with the ^{29}Si sites *1* (Q^3), 3, and 4, respectively, indicate the presence of ^{11}B species *C-2'*. Lastly, the ^{11}B species *E* in fact represents the ^{11}B atoms inserted into ^{29}Si site *7* (designated as ^{11}B species *E-7*), because of the intensity correlations involving the ^{11}B signal at -3.2 ppm (^{11}B species *E*) and the ^{29}Si signals at

approximately -112 (^{29}Si site *5*), -113 (^{29}Si site *8*), and -119 ppm (^{29}Si site *5*). All the specific ^{11}B shift assignments are summarized in Table 3 and illustrated in Scheme 1. More importantly, the ^{11}B siting in DiBI-synthesized B-SSZ-70 is determined to be preferentially distributed among certain ^{29}Si sites (in the internal 10-MR and the external 12-MR of **MWW**-like cages). Additionally, the ^{11}B species *A* and *B* are shown to be extra-framework ^{11}B moieties due to the absence of correlated intensities between ^{11}B signals (1.6 and -0.5 ppm) and any ^{29}Si signals, consistent with the 2D ^{11}B{^{1}H} NMR result (Figure 9). Also, the ^{11}B site distributions within DiBI-synthesized B-SSZ-70 may suggest that DiBI SDA^{+} molecules are occluded within similar inorganic environments, due to the short molecular proximities of the ^{11}B species *C*, *D*, and *E* with respect to DiBI SDA^{+} molecules. Overall, the powerful 2D *J*-mediated ^{11}B{^{29}Si} NMR methods enable the determination of ^{11}B siting in B-SSZ-70, which spurs the interest in understanding the influence of organic SDA^{+} molecules on their resulting ^{11}B atom site distributions by comparing ^{11}B site distributions within DiBI- and DiC_6I-synthesized B-SSZ-70.

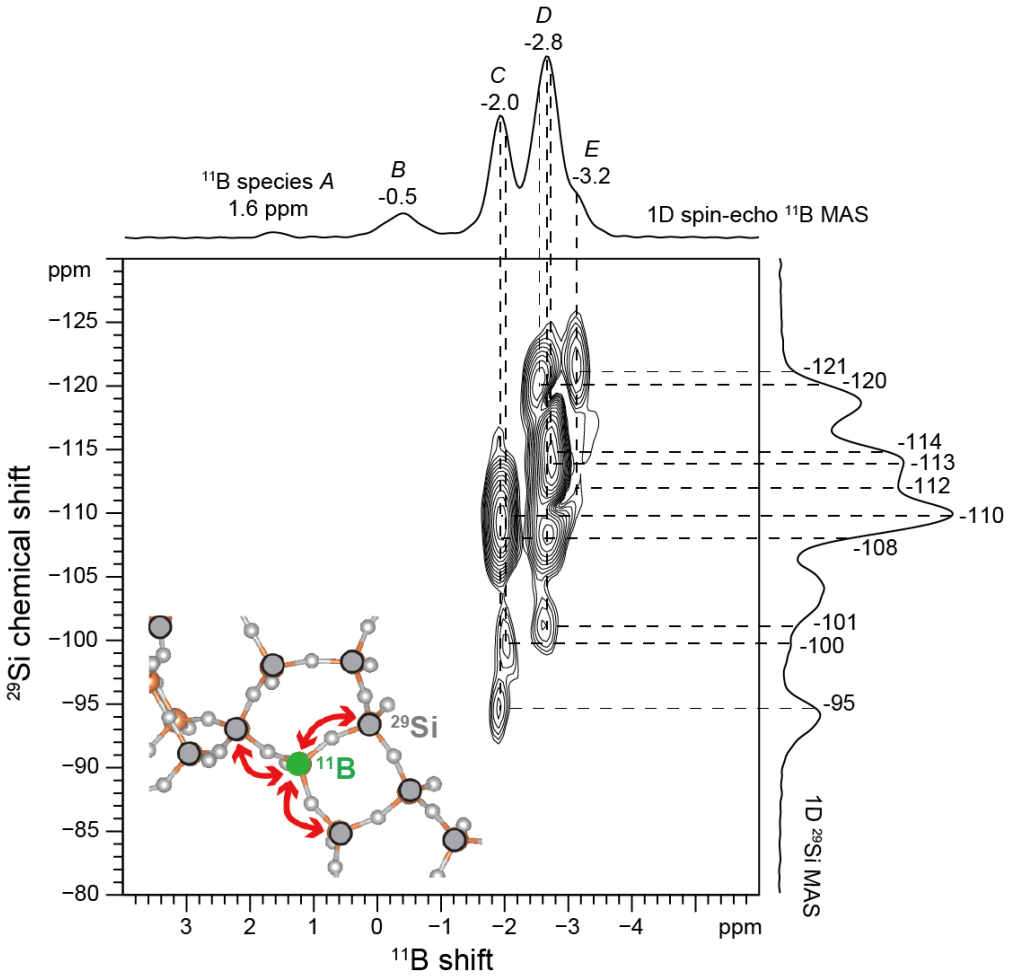

Figure 11. Solid-state 2D *J*-mediated heteronuclear multiple-quantum correlation (HMQC) ^{11}B{^{29}Si} NMR spectra of ^{29}Si-enriched DiBI-synthesized B-SSZ-70 prepared with Si/B = 10 in reactant, acquired at 25 °C under MAS conditions of 8 kHz. Solid-state 1D single-pulse ^{29}Si and spin-echo ^{11}B MAS spectra are shown along the right vertical and the top horizontal axes, respectively.

Table 3. Summary of ^{11}B shift assignments and their corresponding ^{11}B sites in DiBI-synthesized B-SSZ-70

^{11}B shift (ppm)	Coordination number	^{11}B species assignment	Location
1.6	4	Ex-ramework[a]	?
-0.5	4	Ex-framework	?
-2.0	4	*C-1*	*1* (bonded with ^{29}Si site *9*)
-2.0	4	*C-2*	*2* (bonded with Q^4 ^{29}Si site *1*)
-2.0	4	*C-2'*	*2* (bonded with Q^3 ^{29}Si site *1*)
-2.6	4	*D-3*	*3*
-2.7	4	*D-1*	*1* (bonded with ^{29}Si site *10*)
-2.8	4	*D-8*	*8*
-3.2	4	*E-7*	*7*

(a) "Ex-framework" means extra-framework species.

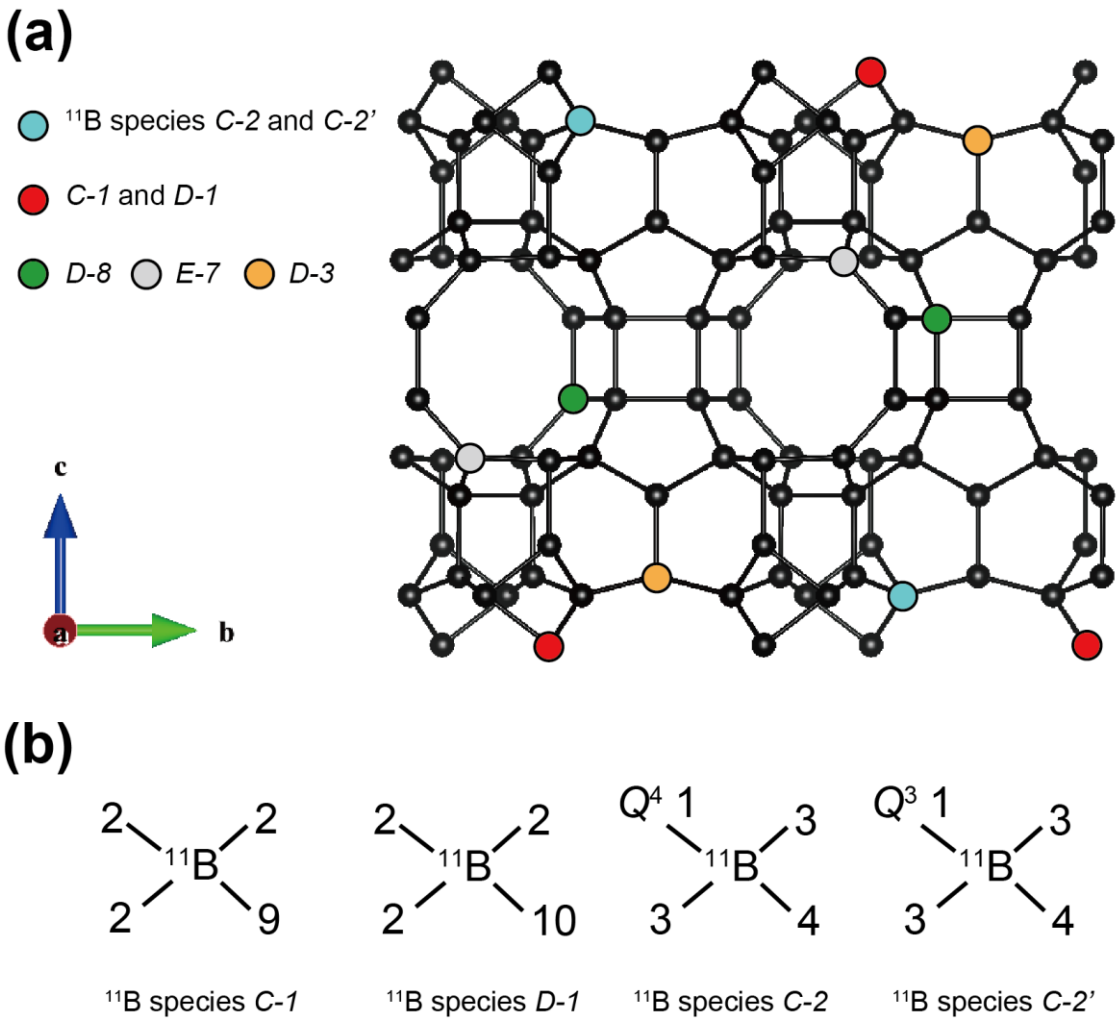

Scheme 1. (a) Schematic diagram of ^{11}B site distributions in DiBI-synthesized B-SSZ-70, where ^{29}Si sites are shown in black, various ^{11}B sites are colored differently (see the inset for details), and bridging oxygen atoms are omitted for simplicity. Note the ^{11}B siting presented in this scheme is only for demonstration and may not represent the real ^{11}B contents (Si/B ~26 in product). (b) Schematic illustrations of structural differences between ^{11}B species *C-1* and *D-1* as well as *C-2* and *C-2'*. The ^{29}Si-O-^{29}Si and ^{11}B-O-^{29}Si bond angles and lengths shown here may not be accurate.

The DiBI- and DiC_6I-synthesized B-SSZ-70 possess slightly different local ^{11}B environments, as identified via 1D ^{11}B NMR measurements (Figure 5), and the ^{11}B species within the DiBI- and DiC_6I-synthesized B-SSZ-70 are shown to be greatly influenced by the organic SDA^+ molecules based on the 2D $^{11}B\{^1H\}$ NMR results (Figures 9 and 10). These

observations motivate us to compare the ^{11}B siting within DiBI-synthesized B-SSZ-70 (the preferential ^{11}B site distribution) with the one in DiC_6I-synthesized B-SSZ-70, aiming for shedding light on controlling ^{11}B siting via selection of organic SDA^+ molecules. Figure 12 shows a 2D *J*-mediated $^{11}B\{^{29}Si\}$ HMQC NMR spectrum of ^{29}Si-enriched DiC_6I-synthesized B-SSZ-70, where correlated intensities are observed among various ^{11}B and ^{29}Si signals. Each paired ^{1}B-^{29}Si signal correlation represents one specific ^{11}B-O-^{29}Si site connectivity due to their distinct $^{2}J(^{11}B\text{-O-}^{29}Si)$ couplings. For example, the ^{11}B signal at *ca*. -2.8 ppm (^{11}B species *D'*) exhibits correlated intensities with the ^{29}Si signals at *ca*. -114 and -115 ppm corresponding to the ^{29}Si sites *8* and *7*, indicating that ^{11}B species *D'* are connected with the ^{29}Si sites *8* and *7*, respectively. Such observations further support that a fraction of ^{11}B species *D'* result from the ^{11}B atoms inserted into ^{29}Si site *8* (designated to ^{11}B species *D'-8*). Similarly, the ^{11}B species *E'* is identified to stem from the ^{11}B atoms incorporated into ^{29}Si site *7* (referred to as ^{11}B species *E'-7*), as evidenced by the intensity correlations between the ^{11}B signal at around -3.2 ppm (^{11}B species *E'*) and the ^{29}Si signals at *ca*. -112 (^{29}Si site *5*), -115 (^{29}Si site *8*), and -122 ppm (^{29}Si site *6*). The subtly displaced ^{29}Si signal associated with ^{29}Si site *8* is attributed to the local deformation around ^{11}B species *E'-7* caused by the ^{11}B atom incorporation.

Similar to the case of DiBI-synthesized B-SSZ-70, several distinct ^{11}B sites may share very similar ^{11}B signals, difficult to distinguish via 1D ^{11}B NMR experiments. For example, the ^{11}B signal at *ca*. -2.8 ppm in fact is correlated not only with the ^{29}Si signals at *ca*. -114 ~ -115 ppm but also with the ^{29}Si signals at *ca*. -103, -110, and -111 ppm, suggesting the presence of at least two distinct four-coordinate ^{11}B sites. Specifically, a portion of ^{11}B species *D'* are believed to come from the ^{29}Si site *5* substituted by ^{11}B atoms (named as ^{11}B

species *D'-5*) on the basis of correlations involving the ^{11}B signal at *ca*. -2.7 ppm (^{11}B species *D'*) and the ^{29}Si signals at around -111 (^{29}Si site *4*) and -115 ppm (^{29}Si site *7*). Furthermore, still a fraction of ^{11}B species *D'* are contributed by the ^{11}B atoms incorporated into ^{29}Si site *1* (Q^4) and designated as ^{11}B species *D'-1*, as manifested by the correlated intensities shared by the same ^{11}B signal (-2.7 ppm, ^{11}B species *D'*) and the ^{29}Si signals at around -103 (^{29}Si site *10*) and -110 ppm (^{29}Si site *2*). The shifted ^{29}Si signals of ^{29}Si sites *2* and *10* with respect to their corresponding ^{29}Si chemical shifts in the siliceous counterpart (see Table 2), are again attributed to the local ^{29}Si structural changes induced by ^{11}B atom incorporation.

Similar observations take place in the ^{11}B signal at *ca*. -2.0 ppm, showing correlated intensities with the ^{29}Si signals at *ca*. -96, -99, -109, -110, and -110.5 ppm. Such complicated correlations with the ^{11}B signal at *ca*. -2.0 ppm (^{11}B species *C'*) can be assigned to four distinct ^{11}B sites within DiC_6I-synthesized B-SSZ-70. The first one is hypothesized to come from the ^{29}Si sites *1* (Q^4) substituted by ^{11}B atoms, designated as ^{11}B species *C'-1*, which is based on the correlated pairs: ^{11}B (-2.0 ppm) ↔ ^{29}Si (-109 ppm, ^{29}Si site *2*) and ^{11}B (-2.0 ppm) ↔ ^{29}Si (-99 ppm, ^{29}Si site *9*). Interestingly, the same ^{11}B signal at -2.0 ppm appears to be contributed by another two ^{11}B sites resulting from the ^{11}B atoms inserted into ^{29}Si sites *2* (connected with Q^3 or Q^4 ^{29}Si site *1*), referred to as ^{11}B species *C'-2a* and *C'-2b*, respectively. The assignment of ^{11}B species *C'-2a* is based on the correlated pairs of ^{11}B (-2.0 ppm) ↔ ^{29}Si (-110 ppm, ^{29}Si site *3*) and ^{11}B (-2.0 ppm) ↔ ^{29}Si (-110.5 ppm, ^{29}Si site *4*). Such two correlated pairs, in conjunction with the intensity correlations between ^{11}B signal (-2.0 ppm) and ^{29}Si signal (-96 ppm, Q^3 ^{29}Si site *1*), indicate the presence of ^{11}B species *C'-2b*. Different from the ^{11}B species *C'*, *D'*, and *E'*, the ^{11}B species *A'* and *B'* are very likely

to be extra-framework ^{11}B sites, due to the absence of correlated intensities among the ^{11}B signals (1.6 ppm, ^{11}B species *A'*; -0.5 ppm, ^{11}B species *B'*) and any ^{29}Si signals in the 2D *J*-mediated ^{11}B{^{29}Si} HMQC NMR spectrum (Figure 12). This is similar to the ^{11}B species *A* and *B* within DiBI-synthesized B-SSZ-70. All the detailed ^{11}B signal assignments are summarized in Table 4, and the ^{11}B site distribution within DiC_6-synthesized B-SSZ-70 is illustrated in Scheme 2. More importantly, the ^{11}B atoms are shown to be preferentially distributed among certain ^{29}Si sites within B-SSZ-70.

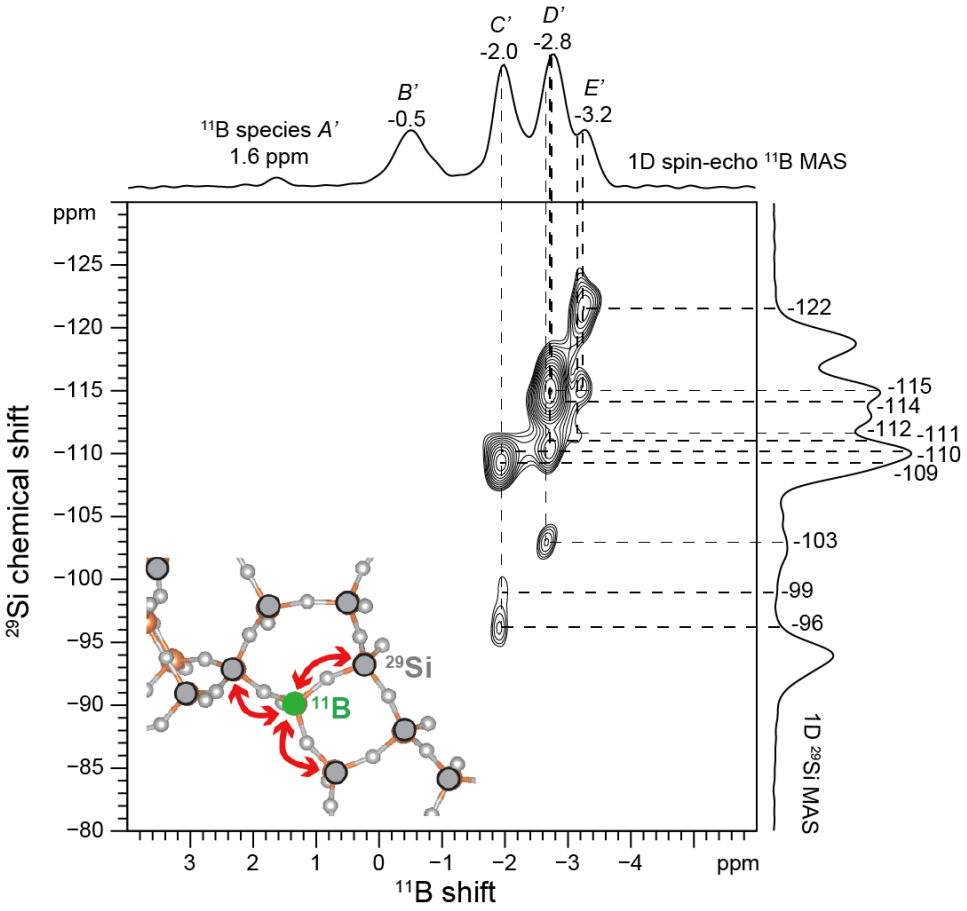

Figure 12. Solid-state 2D *J*-mediated heteronuclear multiple-quantum correlation (HMQC) ^{11}B{^{29}Si} NMR spectra of ^{29}Si-enriched DiC6I-synthesized B-SSZ-70 prepared with Si/B = 10 in reactant, acquired at 25 °C under MAS conditions of 8 kHz. Solid-state 1D single-pulse ^{29}Si and spin-echo ^{11}B MAS spectra are shown along the right vertical and the top horizontal axes, respectively.

Table 4. Summary of ^{11}B shift assignments and their corresponding ^{11}B sites in DiC_6I-synthesized B-SSZ-70

^{11}B shift (ppm)	Coordination number	^{11}B species assignment	Location
1.6	4	Ex-ramework[a]	?
-0.5	4	Ex-framework	?
-2.0	4	*C'-1*	*1* (bonded with ^{29}Si site *9*)
-2.0	4	*C'-2a*	*2* (bonded with Q^4 ^{29}Si site *1*)
-2.0	4	*C'-2b*	*2* (bonded with Q^3 ^{29}Si site *1*)
-2.7	4	*D'-5*	*5*
-2.8	4	*D'-1*	*1* (bonded with ^{29}Si site *10*)
-2.8	4	*D'-8*	*8*
-3.2	4	*E'-7*	*7*

(a) "Ex-framework" means extra-framework species.

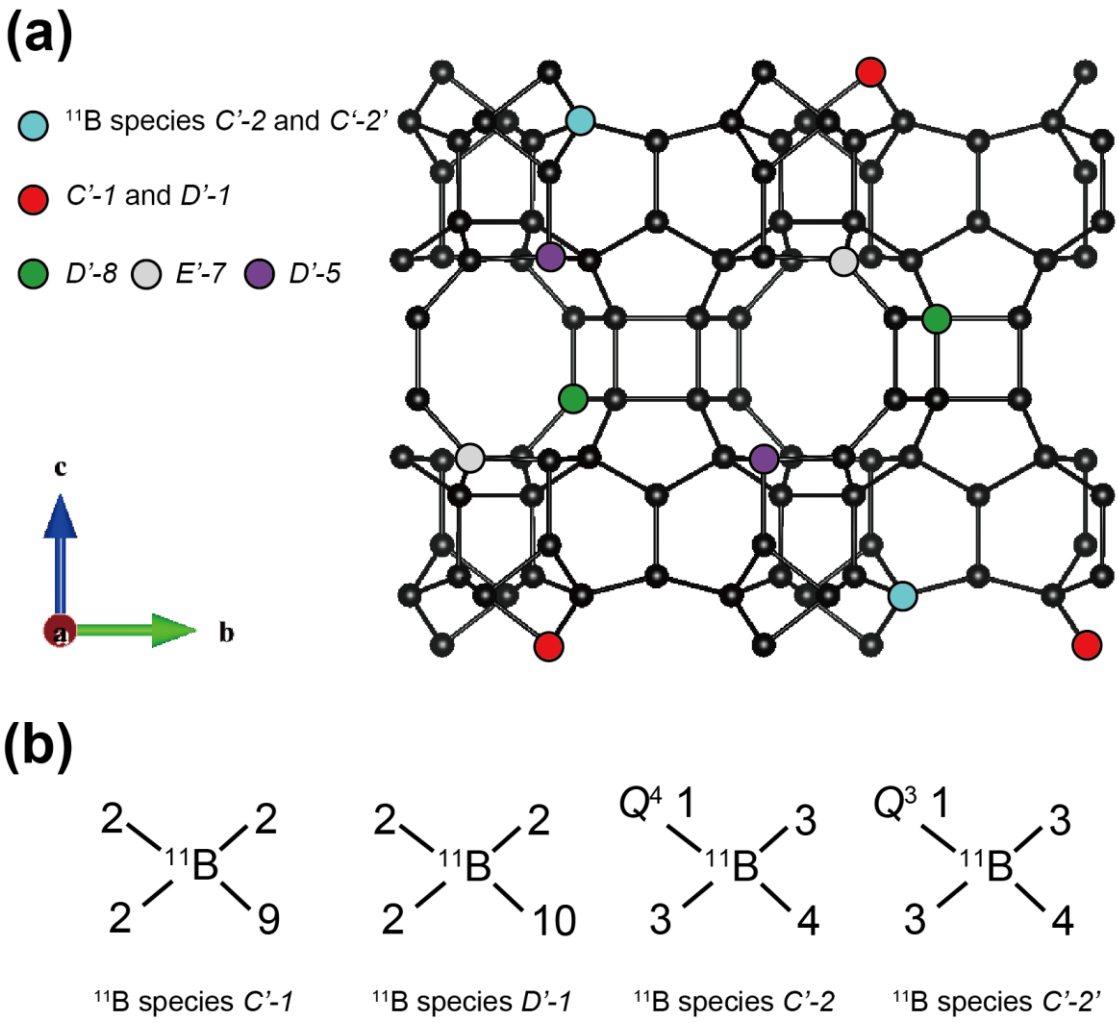

Scheme 2. (a) Schematic diagram of ^{11}B site distributions in DiC$_6$I-synthesized B-SSZ-70, where ^{29}Si sites are shown in black, various ^{11}B sites are colored differently (see the inset for details), and bridging oxygen atoms are omitted for simplicity. Note the ^{11}B siting presented in this scheme is only for demonstration and may not represent the real ^{11}B contents (Si/B ~ 37 in product). (b) Schematic illustrations of structural differences between ^{11}B species *C'-1* and *D'-1* as well as *C'-2* and *C'-2'*. The ^{29}Si-O-^{29}Si and ^{11}B-O-^{29}Si bond angles and lengths shown here may not be accurate.

On the basis of 2D *J*-mediated ^{11}B{^{29}Si} NMR spectra acquired on DiBI- (Figure 11) and DiC$_6$I-synthesized B-SSZ-70 (Figure 12), similar yet distinct ^{11}B site distributions are identified within the two B-SSZ-70 materials. For example, both B-SSZ-70 materials are shown to contain ^{11}B siting located at ^{29}Si sites *1* (Q^4), *2* (bonded with either Q^4 or Q^3 ^{29}Si site *1*), *7*,

and *8*, the first three of which belong to the external 12-MR of **MWW**-like cages, whereas the latter two of which would be accessed through internal 10-MR. Despite the similarities of framework ^{11}B sites, the two B-SSZ-70 products exhibit slightly different ^{11}B species. Specifically, the DiBI-synthesized B-SSZ-70 possesses the ^{11}B sites inserted ^{29}Si site *3* (external 12-MR). In contrast, the DiC_6I-synthesized B-SSZ-70 has ^{11}B siting located at ^{29}Si site *5* (internal 10-MR). Such differences of ^{11}B siting in DiBI- and DiC_6I-synthesized B-SSZ-70 are expected to have substantial influence on post-synthetic heteroatom exchange treatments, because the hydrated heteroatom cations (such as Al^{3+} or Ti^{4+}) would be kinetically hindered by the window sizes of 10 MR. Consequently, the heteroatoms would be very likely to replace the ^{11}B sites within 12 MR on the external surface.

Apart from the ^{11}B siting, DiBI- and DiC_6I-synthesized B-SSZ-70 are shown to have different degrees of ^{11}B atom incorporations under the same synthesis chemical compositions expect for the SDA^+ molecules. For example, the same ^{11}B contents (Si/B = 10) in reactant yield different final ^{11}B contents of DiBI- (Si/B ~25) and DiC_6I-synthesized B-SSZ-70 (Si/B ~37), as shown in Figure 3. We hypothesize that such observations are due to the different hydrophobicities of DiBI and DiC_6I SDA^+ molecules, where DiBI SDA^+ species are relatively more hydrophilic than DiC_6I ones, leading to higher efficiency of ^{11}B incorporation. The distinct hydrophobicity and hydrophilicity, together with the local environments of occluded DiBI and DiC_6I SDA^+ molecules within B-SSZ-70, may explain why DiBI-synthesized B-SSZ-70 has ^{11}B siting at ^{29}Si site *3* (on the external surface), and DiC_6I-synthesized one does not. This may be because DiC_6I SDA^+ molecules are relatively hydrophobic, and their cyclohexyl groups are much less mobile than the diisobutyl groups of DiBI SDA^+ molecules. Once DiC_6I SDA^+ molecules are occupied within the confined

space of 12 MR on the external surface, ^{11}B species are very unlikely to substitute ^{29}Si site *3*. This hypothesis is supported by considering the high solubility of boric acid (the ^{11}B source) in the water-based reaction media for B-SSZ-70 synthesis. In other words, most of hydrated ^{11}B species appear to stay in the water phase rather than the B-SSZ-70 product phase during synthesis. Consequently, ^{11}B contents are expected to increase as the synthesis time extends, because the ^{11}B species in the water phase would gradually diffuse into B-SSZ-70 framework. This is evidenced by the kinetic studies of B-SSZ-70 preparation shown in Figure 13, where the amount of Si/B ratio in product is plotted against the hydrothermal synthesis time. A general trend is observed: the longer the synthesis time is, the high ^{11}B contents would be.

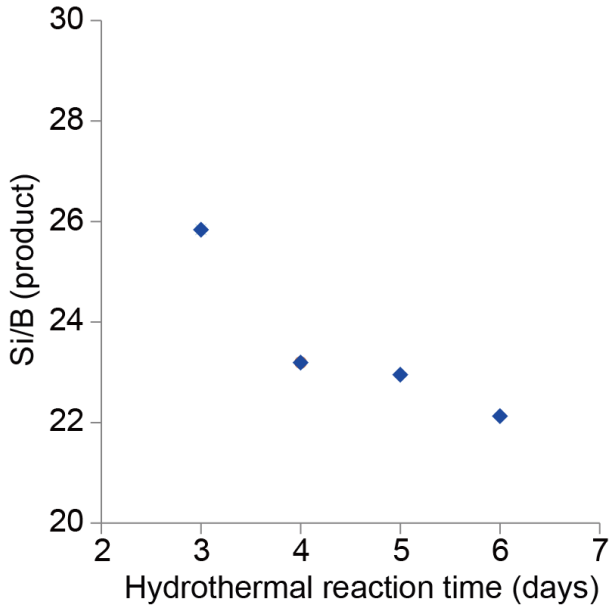

Figure 13. Kinetic studies of ^{11}B contents in DiBI-synthesized B-SSZ-70 (Si/B = 10 in reactant) as a function of reaction time.

Interestingly, the ^{11}B incorporation appears to alter the relative populations of ^{29}Si species within B-SSZ-70, obviously depending on the amount of ^{11}B contents in product. The quantitative analyses of 1D ^{29}Si single-pulse NMR spectra of DiBI- and DiC_6I-syntheiszed B-SSZ-70 (Figure 4) clearly indicate that the relative populations of Q^3 ^{29}Si species decrease from 18.2 to 13.0 % when the ^{11}B contents in B-SSZ-70 product increase from Si/B = 37 to 25 (see Table 5). The results suggest that ^{11}B atom insertion into silicate-based frameworks would consume the Q^3 ^{29}Si species, consistent with our previous observations on surfactant-directed layered borosilicates.[20] To further examine the hypothesis regarding how hydrophilicity of SDA^+ molecules could possibly affect resulting ^{11}B loading in product, as well as Q^3 and Q^4 ^{29}Si species of B-SSZ-70, we compare a series of B-SSZ-70 products synthesized via three SDA^+ molecules: diisopropyl imidazolium (DiPI), DiBI, and DiC_6I and the same Si/B ratio (Si/B = 4) in reactant. Due to the extents of hydrophilicity: DiPI > DiBI > DiC_6I, it is expected that the ^{11}B contents of B-SSZ-70 products would follow the order: DiPI- > DiBI- > DiC_6I-synthesized B-SSZ-70. This is supported by the results from elemental analysis, as shown in Table 5, where DiPI-synthesized B-SSZ-70 possesses higher ^{11}B loading (Si/B ~14) than DiBI- (Si/B ~22) and DiC_6I-synthesized B-SSZ-70 (Si/B ~32). Very interestingly, the amount of Q^3 ^{29}Si species is determined to be strongly influenced by the ^{11}B contents in final B-SSZ-70 products. Specifically, the relative populations of Q^3 ^{29}Si species in the B-SSZ-70 zeolites were found to follow the order: DiPI- (12.5 %) < DiBI- (22.6 %) < DiC_6I-synthesized B-SSZ-70 (29.2 %), which is exactly the reverse order in their ^{11}B contents. Detailed quantitative analyses are listed in Table D1. Note that the Q^3 ^{29}Si species in B-SSZ-70 prepared with Si/B = 4 in reactant are expected to have lower relative populations compared to the ones in B-SSZ-70

synthesized with Si/B = 10 in reactant, which was attributed to the limited ^{29}Si spectral resolutions (see Figure D3). Consequently, the observations and results of DiPI-, DiBI-, and DiC_6I-synthesized B-SSZ-70 again support our hypothesis regarding the influence of SDA^+ molecules on ^{11}B incorporation into borosilicate zeolites. Overall, we believe that the deep understanding of ^{11}B siting presented in this report would be very helpful in synthesizing borosilicate zeolites with targeted ^{11}B site distributions. The preferential ^{11}B site distributions within borosilicate zeolites could be post-synthetically exchanged with other heteroatoms to achieve the control of heteroatom siting in high silica zeolite catalysts.

Table 5. Dependence of SDA^+ molecules on ^{11}B contents and ^{29}Si species in B-SSZ-70.

Product	SDA^+ molecules	Si/B in reactant	Si/B in product	Q^3 ^{29}Si (%)	Q^4 ^{29}Si (%)
B-SSZ-70	DiBI	10	25	13.0	87.0
	DiC_6I	10	37	18.2	81.8
	DiPI	4	14	12.5	87.5
	DiBI	4	22	22.6	77.4
	DiC_6I	4	32	29.2	70.8

5.5 Conclusions

The molecular interactions of SDA^+ species and borosilicate zeolite frameworks as well as ^{29}Si-O-^{11}B site connectivities are established and shown to be similar in zeolite B-SSZ-70 synthesized with DiBI and DiC_6I molecules. Advanced solid-state 2D *J*- and dipolar-mediated NMR measurements resolve correlation intensities from distinct ^{29}Si-O-^{11}B site pairs and molecularly proximate ^{1}H moieties of the SDA^+ molecules with respect to ^{29}Si as well as ^{11}B species in B-SSZ-70, respectively. Specifically, both DiBI and DiC_6I molecules exhibit strong interactions with certain framework ^{29}Si and ^{11}B species in B-SSZ-

70, as established by 2D $^{29}Si\{^{1}H\}$ and $^{11}B\{^{1}H\}$ dipolar-mediated (through-space) NMR methods. Interestingly, while similar interactions between SDA^{+} molecules and framework ^{29}Si sites are identified in DiBI- and DiC_6I-synthesized B-SSZ-70, subtle differences indeed exist and they possibly indicate the distinct local environments of occluded DiBI and DiC_6I SDA^{+} molecules, consistent with the TGA profiles. More importantly, framework ^{11}B species are established to be greatly affected by DiBI and DiC_6I species, suggesting structure-directing influences of DiBI and DiC_6I species on ^{11}B site distributions in B-SSZ-70.

DiBI- and DiC_6I-synthesized B-SSZ-70 are both shown to have preferential ^{11}B site distributions, in which ^{11}B atoms are inserted into framework sites that are accessible through internal 10-MR and external 12-MR of **MWW**-like cages in B-SSZ-70. Interestingly, DiBI-synthesized B-SSZ-70 is shown to have higher ^{11}B contents in product (Si/B ~22) than DiC_6I-directed B-SSZ-70 (Si/B ~32) under otherwise synthesis compositions and conditions, which is attributed to the different hydrophobic properties of the SDA^{+} molecules. This hypothesis is further supported by the B-SSZ-70 synthesis using DiPI species that are more hydrophilic than DiBI and DiC_6I species, yielding DiPI-synthesized B-SSZ-70 with increased ^{11}B contents (Si/B ~14). The results clearly indicate that the amount of ^{11}B loading in B-SSZ-70 is strongly correlated with the hydrophilic properties of SDA+ molecules. Overall, such molecular-level understanding regarding the influences of organic SDA^{+} species on framework ^{11}B species in B-SSZ-70 is expected to aid rational synthesis of structure-directing agents and borosilicate zeolite catalysts with desired ^{11}B heteroatom site distributions.

5.6 References

1. Busca, G. Acid catalysts in industrial hydrocarbon chemistry. *Chem. Rev.* **107,** 5366–5410 (2007).

2. Corma, A. From Microporous to Mesoporous Molecular Sieve Materials and Their Use in Catalysis. *Chem. Rev.* **97,** 2373–2419 (1997).

3. Degnan, T. F. The implications of the fundamentals of shape selectivity for the development of catalysts for the petroleum and petrochemical industries. *J. Catal.* **216,** 32–46 (2003).

4. Chen, N. Y., Degnan, T. F. & Smith, C. M. *Molecular Transport and Reaction in Zeolites: Design and Application of Shape Selective Catalysis*. 328 (Wiley, 1994).

5. Van Donk, S., Janssen, A. H., Bitter, J. H. & de Jong, K. P. Generation, Characterization, and Impact of Mesopores in Zeolite Catalysts. *Catal. Rev.* **45,** 297–319 (2003).

6. Van Santen, R. A. & Kramer, G. J. Reactivity Theory of Zeolitic Broensted Acidic Sites. *Chem. Rev.* **95,** 637–660 (1995).

7. Dědeček, J., Sobalík, Z. & Wichterlová, B. Siting and Distribution of Framework Aluminium Atoms in Silicon-Rich Zeolites and Impact on Catalysis. *Catal. Rev. - Sci. Eng.* **54,** 135–223 (2012).

8. Pinar, A. B., Verel, R., Pérez-Pariente, J. & van Bokhoven, J. a. Direct evidence of the effect of synthesis conditions on aluminum siting in zeolite ferrierite: A 27Al MQ MAS NMR study. *Microporous Mesoporous Mater.* **193,** 111–114 (2014).

9. Pinar, A. B., Márquez-Álvarez, C., Grande-Casas, M. & Pérez-Pariente, J. Template-controlled acidity and catalytic activity of ferrierite crystals. *J. Catal.* **263,** 258–265 (2009).

10. Pinar, A. B., Gómez-Hortigüela, L., McCusker, L. B. & Pérez-Pariente, J. Controlling the Aluminum Distribution in the Zeolite Ferrierite via the Organic Structure Directing Agent. *Chem. Mater.* **25,** 3654–3661 (2013).

11. Gábová, V., Dědecek, J. & Cejka, J. Control of Al distribution in ZSM-5 by conditions of zeolite synthesis. *Chem. Commun. (Camb).* 1196–7 (2003). at <http://www.ncbi.nlm.nih.gov/pubmed/12778732>

12. Kennedy, G. J., Afeworki, M. & Hong, S. B. Probing the non-random aluminum distribution in zeolite merlinoite with ultra-high-field (18 . 8 T) 27 Al and Si MAS NMR. *Microporous Mesoporous Mater.* **52,** 55–59 (2002).

13. Han, O. H., Kim, C.-S. & Hong, S. B. Direct evidence for the nonrandom nature of Al substitution in zeolite ZSM-5: an investigation by (27)Al MAS and MQ MAS NMR. *Angew. Chem. Int. Ed. Engl.* **41,** 469–72 (2002).

14. Shin, J., Ahn, N. H., Camblor, M. a, Cho, S. J. & Hong, S. B. Intraframework Migration of Tetrahedral Atoms in a Zeolite. *Angew. Chem. Int. Ed. Engl.* **53,** 1–5 (2014).

15. Shin, J., Ahn, N. H., Camblor, M. a., Zicovich-Wilson, C. M. & Hong, S. B. Synthesis of Aluminosilicate Natrolites and Control of Their Tetrahedral Atom Ordering. *Chem. Mater.* **26,** 3361–3363 (2014).

16. Moliner, M., Rey, F. & Corma, A. Towards the rational design of efficient organic structure-directing agents for zeolite synthesis. *Angew. Chem. Int. Ed. Engl.* **52,** 13880–13889 (2013).

17. Jiang, J., Yu, J. & Corma, A. Extra-large-pore zeolites: bridging the gap between micro and mesoporous structures. *Angew. Chem. Int. Ed. Engl.* **49,** 3120–45 (2010).

18. Burton, A. W., Lee, G. S. & Zones, S. I. Phase selectivity in the syntheses of cage-based zeolite structures: An investigation of thermodynamic interactions between zeolite hosts and structure directing agents by molecular modeling. *Microporous Mesoporous Mater.* **90,** 129–144 (2006).

19. Burton, A. W., Zones, S. I. & Elomari, S. The chemistry of phase selectivity in the synthesis of high-silica zeolites. *Curr. Opin. Colloid Interface Sci.* **10,** 211–219 (2005).

20. Garaga, M. N. *et al.* Local Environments of Boron Heteroatoms in Non-Crystalline Layered Silicates. *In preparation*

21. Hsieh, M.-F. *et al.* Aluminum Heteroatom Distributions in Surfactant-Directed Aluminosilicates. *In preparation*

22. Pinar, A. B., Gomez-Hortiguela, L. & Perez-Pariente, J. Cooperative Structure Directing Role of the Cage-Forming Tetramethylammonium Cation and the Bulkier Benzylmethylpyrrolidinium in the Synthesis of Zeolite Ferrierite. *Chem. Mater.* **19,** 5617–5626 (2007).

23. Márquez-Alvarez, C., Pinar, A. B., García, R., Grande-Casas, M. & Pérez-Pariente, J. Influence of Al Distribution and Defects Concentration of Ferrierite Catalysts

Synthesized From Na-Free Gels in the Skeletal Isomerization of n-Butene. *Top. Catal.* **52,** 1281–1291 (2009).

24. Román-Leshkov, Y., Moliner, M. & Davis, M. E. Impact of Controlling the Site Distribution of Al Atoms on Catalytic Properties in Ferrierite-Type Zeolites †. *J. Phys. Chem. C* **115,** 1096–1102 (2011).

25. Dedecek, J., Balgova, V., Pashkova, V., Klein, P. & Wichterlová, B. Synthesis of ZSM-5 Zeolites with Defined Distribution of Al Atoms in the Framework and Multinuclear MAS NMR Analysis of the Control of Al Distribution. *Chem. Mater.* **24,** 3231–3239 (2012).

26. Xie, D. *et al.* Optimized Synthesis and Structural Characterization of the Borosilicate MCM-70. *J. Phys. Chem. C* **113,** 9845–9850 (2009).

27. Ouyang, X. *et al.* Single-Step Delamination of a MWW Borosilicate Layered Zeolite Precursor under Mild Conditions without Surfactant and Sonication. *J. Am. Chem. Soc.* **57,** 1449−1461 (2014).

28. Zones, S. I. *et al.* Studies of Aluminum Reinsertion into Borosilicate Zeolites with Intersecting Channels of 10- and 12-Ring Channel Systems. *J. Am. Chem. Soc.* **57,** 1462−1471 (2014).

29. Zones, S. I., Chen, C. Y., Benin, A. & Hwang, S.-J. Opportunities for selective catalysis within discrete portions of zeolites: The case for SSZ-57LP. *J. Catal.* **308,** 213–225 (2013).

30. Chen, C.-Y. & Zones, S. I. Method for heteroatom lattice substitution in large and extra-large pore borosilicate zeolites. (2002).

31. Tong, H. T. T. & Koller, H. Control of Al for B framework substitution in zeolite Beta by counterions. *Microporous Mesoporous Mater.* **148,** 80–87 (2012).

32. http://www.iza-structure.org/databases/.

33. Archer, R. H. *et al.* Physicochemical Properties and Catalytic Behavior of the Molecular Sieve SSZ-70. *Chem. Mater.* **22,** 2563–2572 (2010).

34. Martínez, C. & Corma, A. Inorganic molecular sieves: Preparation, modification and industrial application in catalytic processes. *Coord. Chem. Rev.* **255,** 1558–1580 (2011).

35. Burton, A. & Elomari, S. SSZ-60: a new large-pore zeolite related to ZSM-23. *Chem. Commun. (Camb).* 2618–9 (2004). doi:10.1039/b410010g

36. Burton, A. *et al.* The synthesis, characterization, and structure solution of SSZ-58: a novel two-dimensional 10-ring pore zeolite with previously unseen double 5-ring subunits. *J. Am. Chem. Soc.* **125,** 1633–1642 (2003).

37. Burton, A. *et al.* SSZ-53 and SSZ-59: two novel extra-large pore zeolites. *Chemistry* **9,** 5737–5748 (2003).

38. Elomari, S., Burton, A., Medrud, R. C. & Grosse-Kunstleve, R. The synthesis, characterization, and structure solution of SSZ-56: An extreme example of isomer specificity in the structure direction of zeolites. *Microporous Mesoporous Mater.* **118,** 325–333 (2009).

39. Elomari, S., Burton, A. W., Ong, K., Pradhan, A. R. & Chan, I. Y. Synthesis and Structure Solution of Zeolite SSZ-65. *Chem. Mater.* **19,** 5485–5492 (2007).

40. Li, Y. & Zou, X. SU-16: a three-dimensional open-framework borogermanate with a novel zeolite topology. *Angew. Chem. Int. Ed. Engl.* **44,** 2012–2015 (2005).

41. Vortmann, S., Marler, B., Gies, H. & Daniels, P. Synthesis and crystal structure of the new borosilicate zeolite RUB-13. *Microporous Mater.* **4,** 111–121 (1995).

42. Wagner, P. *et al.* Electron Diffraction Structure Solution of a Nanocrystalline Zeolite at Atomic Resolution. *J. Phys. Chem. B* **103,** 8245–8250 (1999).

43. Zones, S. I. Translating new materials discoveries in zeolite research to commercial manufacture. *Microporous Mesoporous Mater.* **144,** 1–8 (2011).

44. Ogino, I. *et al.* Heteroatom-Tolerant Delamination of Layered Zeolite Precursor Materials. *Chem. Mater.* **25,** 1502–1509 (2013).

45. Chen, C. Y. & Zones, S. I. From Borosilicate to Gallo- and Aluminosilicate Zeolites : New Methods for Lattice Substitution via Post-Synthetic Treatment. *Stud. Surf. Sci. Catal.* **135,** 211 (2001).

46. *Zeolites and Catalysis: Synthesis Reactions and Applications*. (Wiley-VCH, 2010). doi:10.1002/9783527630295

47. Ouyang, X. *et al.* Novel surfactant-free route to delaminated all-silica and titanosilicate zeolites derived from a layered borosilicate MWW precursor. *Dalton Trans.* **43,** 10417–10429 (2014).

48. Archer, R. H., Zones, S. I. & Davis, M. E. Imidazolium structure directing agents in zeolite synthesis: Exploring guest/host relationships in the synthesis of SSZ-70. *Microporous Mesoporous Mater.* **130,** 255–265 (2010).

49. Engelhardt, G. & Michel, D. *High-Resolution Solid-State NMR of Silicates and Zeolites*. (Wiley, 1987).

50. Koller, H. & Weiß, M. Solid state NMR of porous materials : zeolites and related materials. *Top. Curr. Chem.* **306,** 189–227 (2012).

51. Fyfe, C. A., Feng, Y., Grondey, H., Kokotailo, G. T. & Gies, H. One- and Two-Dimensional High-Resolution Solid-State NMR Studies of Zeolite Lattice Structures. *Chem. Rev.* **91,** 1525–1543 (1991).

Chapter 6: Controlling Aluminum Site Distributions in Delaminated Zeolite SSZ-70 by Isomorphous Substitution of Boron with Aluminum

6.1 Abstract

Aluminum atoms are shown to be reinserted into specific sites in delaminated zeolite SSZ-70 via isomorphous substitution of boron atoms in a controlled manner. Multi-dimensional solid-state nuclear magnetic resonance (NMR) spectroscopy determines distinct intra-framework interactions involving boron and aluminum, as well as silicon sites in boro- (B-SSZ-70) and alumino-silicate zeolite SSZ-70 (Al-SSZ-70), respectively. Two-dimensional (2D) *J*-mediated (through-bond) $^{11}B\{^{29}Si\}$ NMR analyses identify distinct covalently bonded boron and silicon species though bridging oxygen atoms in B-SSZ-70. The established ^{11}B-O-^{29}Si site connectivities, together with the framework structure, permit determination of boron site distributions in B-SSZ-70, where boron atoms are at framework sites accessible through 10- and 12-membered ring. Interestingly, 2D *J*-mediated $^{11}B\{^{29}Si\}$ NMR analyses show that such preferential boron site distributions in B-SSZ-70 were retained over the course of delamination. These fundamental insights allow us to predict locations of reinserted aluminum atoms, because hydrated aluminum ions would be kinetically hindered by 10-membered ring windows during reinsertion processes. Notably, the reinserted aluminum species are shown to be located at framework sites on external surface of aluminum-reinserted delaminated SSZ-70 (*i.e.*, Al-UCB-4), consistent with the

kinetic aspects of aluminum reinsertion. This result is in stark contrast with the aluminum site distributions in Al-SSZ-70, where aluminum atoms appear to be non-selectively distributed among distinct crystallographic sites based on 2D *J*-mediated $^{27}Al\{^{29}Si\}$ NMR analyses. Overall, the molecular-level insights into the isomorphous substitution of boron for aluminum in zeolite SSZ-70 are expected to establish synthesis protocols for zeolite catalysts with rationally controlled heteroatom site distributions.

6.2 Introduction

Zeolite-based catalysts are currently used in various industrial processes,[1–3] primarily due to their tunable crystalline structures and their different types of framework heteroatoms. Framework topologies are able to provide shape selectivity in zeolite-catalyzed reactions,[4–6] whereas heteroatoms impart reaction activity to zeolites.[7–10] Consequently, such understanding and observation have spur interest in synthesizing zeolite catalysts with combinations of available structures and chemical compositions.[11–15] To date, relationships between zeolite phases and synthesis compositions including conditions have been better understood since the discovery of synthetic zeolites.[14,16–20] Nevertheless, how to systematically alter locations of heteroatoms in zeolite catalysts still remains very challenging, despite the fact that substantial influence of heteroatom site distributions on acidity and reaction performances has been recognized.[21–30]

In this regard, current research interest in understanding heteroatom site distributions in zeolites has focused on preciously controlling locations of aluminum (^{27}Al) atoms in aluminosilicate zeolites, because most zeolite-catalyzed reactions belong to acid catalysis,

benefited from Brønsted acid sites associated with proton cations nearby framework ^{27}Al atoms in aluminosilicate zeolites. In addition to ^{27}Al, other types of heteroatom incorporations are continuously being developed to tune reaction activity of associated zeolite catalysts. For example, titanium (Ti) atoms can be used to prepare Ti-containing zeolites with applications in selective oxidation reactions.[31–34] Tin (Sn) incorporation results into Lewis acid sites in Sn-inserted zeolites that can be used in biomass reactions.[35–42] Interestingly, germanium (Ge) contents in synthesis indeed help discover new types of zeolite frameworks.[16,19,43] Similar to Ge, Boron (^{11}B) atoms can yield certain zeolite frameworks that are only available in borosilicate forms.[12,44–49] Furthermore, ^{11}B incorporation provides versatile routes to post-synthetically modify borosilicate zeolites, which will be described in detail below. In short, it would be impossible to highlight all the influences of heteroatoms on zeolite properties here. Nevertheless, we can know that the importance of heteroatoms in zeolite catalysts, which initiates extensive investigations that focus on understanding relationships of heteroatom site distributions in zeolite catalysts between their corresponding reaction and adsorption performances.

While the overall research objective is clear, a few reports shed light on understanding and even controlling heteroatom site distributions in zeolites. For example, ^{27}Al site distributions were shown to be altered by structure-directing agents (SDAs) or synthesis compositions and conditions.[7,50–55] However, to the best of our knowledge, a generic method of systematically controlling heteroatom site distributions in high silica zeolites has not been established yet. Most available reports concluded that heteroatoms (*e.g.*, ^{27}Al) are often randomly distributed in zeolite frameworks, except for a few extreme cases, where heteroatoms are found to be inserted into certain types of tetrahedral sites (T-sites).[41,56–58]

Such poor understanding of heteroatom site distributions in zeolites may be attributed to complicated chemistry of zeolite crystallization. This may also be because current characterization methods provide limited information regarding locations of heteroatoms in zeolites.[7,59,60] The challenges were recently overcome by our modified two-dimensional (2D) nuclear magnetic resonance (NMR) spectroscopy techniques that can *directly* probe site connectivities of ^{27}Al and ^{29}Si as well as ^{11}B and ^{29}Si through bridging oxygen atoms in alumino- and boro-silicate frameworks, respectively.[61,62] Using the new 2D NMR methods together with crystallographic information, we had previously shown that ^{11}B atoms are preferentially inserted into specific framework sites in borosilicate zeolite SSZ-70 (B-SSZ-70), which shed light on possibilities of synthesizing zeolite catalysts with controlled heteroatom site distributions. This is because framework ^{11}B atoms in borosilicate zeolites can be post-synthetically exchanged with Al, Ti, and other types of heteroatoms, which would impart various catalytic activities to resulting zeolites.[3,57,63–68]

Borosilicate zeolite SSZ-70 (B-SSZ-70) was selected as a model system herein to demonstrate the possibility of directing heteroatom site distributions in high silica zeolites, not only because it has 2D structural features, but also because it has significant industrial applications (*e.g.*, alkylation of benzenes). While the exact crystal structure of zeolite SSZ-70 has not been determined yet, we have shown that most of its topology must be very similar to zeolite MCM-22 (**MWW**[69] type). In addition, catalytic tests indicated that SSZ-70 exhibits a much slower catalyst deactivation rate than SSZ-25 (**MWW**).[70] Together with the fact that zeolite MCM-22 has been commercially used in alkylation of aromatics,[21] zeolite SSZ-70 would be considered a very promising catalyst for similar commercial applications. Furthermore, zeolite SSZ-70 has interesting 2D structures that can alleviate mass transport

limitations of zeolite catalysts via chemical/physical treatments. Similar to MCM-22,[71–73] SSZ-70 can be delaminated to expose a great number of accessible acid sites by increasing its external surface area.[65] Overall, understanding and further being able to control heteroatom site distributions in SSZ-70 are hypothesized to substantially impact on development of zeolite catalyst.

Here, we report detailed analyses of ^{11}B and ^{27}Al site distributions in zeolite SSZ-70 at the molecular level primarily using solid-state NMR spectroscopy. Interestingly, ^{11}B atoms are shown to be selectively incorporated into certain subsets of ^{29}Si sites in B-SSZ-70, whereas ^{27}Al atoms are found to appear non-selectively distributed in aluminosilicate zeolite SSZ-70 (Al-SSZ-70). These insights are consistent with our previous investigations in surfactant-directed layered boro- and alumino-silicates. Then the ^{11}B site distributions in B-SSZ-70 are monitored *ex-situ* at different synthesis stages over the course of delamination by multi-dimensional NMR techniques. Specifically, one-dimensional (1D) ^{29}Si and ^{11}B NMR results indicate a high degree of similarities of local ^{29}Si and ^{11}B environments between as-synthesized B-SSZ-70 and delaminated B-SSZ-70 (UCB-4) after a series of post-synthetic treatments. These observations are consistent with the claims previously made by Ogino and coworkers, where they showed that the modified delamination procedure enables the structural integrity and retention of heteroatom contents in SSZ-70.[65] More importantly, the ^{11}B site distributions in B-SSZ-70 at different synthesis stages were established and shown to be nearly identical using 2D *J*-mediated (through-bond) ^{11}B{^{29}Si} NMR measurements and zeolite crystallography, where ^{11}B atoms are located at sites that are accessible through internal 10-membered-ring (10-MR) and external 12-MR channels in B-SSZ-70. The understanding of ^{11}B site distributions in UCB-4 allows us to hypothesize

that locations of ^{27}Al atoms in SSZ-70 can be controlled via B-SSZ-70 synthesis followed by ^{27}Al reinsertion.

This hypothesis is supported by the case study of ^{27}Al reinserted UCB-4 prepared using delaminated B-SSZ-70 (UCB-4) for ^{27}Al reinsertion. 1D ^{27}Al NMR analysis of ^{27}Al-reinserted UCB-4, in conjunction with the information learned from ^{27}Al site distributions in Al-SSZ-70, indicates that most of ^{27}Al atoms are reinserted at framework sites accessible through external 12-MR. Furthermore, only one-third of the framework ^{11}B species in UCB-4 were replaced by ^{27}Al atoms. These results are aligned with our understanding of ^{27}Al reinsertion, in which hydrated ^{27}Al ions would be kinetically hindered by 10-MR windows. We believe that the molecular understanding of ^{11}B and ^{27}Al site distributions in SSZ-70 presented herein would shed light on influences of synthetic treatments on locations of heteroatoms in high silica zeolites. More interestingly, our case study of ^{27}Al reinserted UCB-4 is expected to provide insights into generic methods of synthesizing zeolite catalysts with controlled heteroatom site distributions.

6.3 Experimental

6.3.1 Materials.

Organic structure-directing-agent (SDA) molecules. Organic 1,3-diisobutyl imidazolium (DiBI) in the hydroxide (OH^-) form was kindly provided by Dr. Stacey Zones at the Chevron Energy Technology Company. The alkaline solutions used in zeolite preparation typically have concentrations of 0.4 ~ 1.0 M.

Zeolite synthesis. All the zeolite reactions were performed using 23 mL of poly(tetrafluoroethylene) (PTFE)-lined stainless steel Parr™ autoclaves. Reagents for B- and Al-SSZ-70 with ^{29}Si natural abundance synthesis are Cab-O-Sil M5 (scintillation grade, ACROS ORGANICS), 1N sodium hydroxide solution (NaOH, Fisher Chemical), DiBI SDA^+ OH solution, deionized water (DI H_2O), boric acid (Sigma-Aldrich), and Reheis F-2000 (50-53 wt % Al_2O_3). Detailed gel compositions and conditions are summarized in Table E1. A general description of zeolite preparation (on a 13 mmol Si basis) will be shared below as an example. First, 1N NaOH (1.3 g), DI H_2O (0.87 g), and DiBI SDA^+ OH (5.42 g, 0.48 M) were well mixed according to the gel composition (denoted as mixture *I*). For borosilicate reactions, boric acid (80 mg) and small amount of as-synthesized B-SSZ-70 (20 mg, 2.5 wt % on the silica oxide basis) were added into mixture *I* as ^{11}B sources and seed crystals, respectively. For aluminosilicate reactions, Reheis F-2000 (51 mg) and small amount of as-synthesized Al-SSZ-70 (20 mg, 2.5 wt% with respect to the silica oxide) were added into mixture *I* as ^{27}Al sources and seed crystals, respectively. In both cases, Cab-O-Sil M5 (780 mg) was then slowly added into the whole mixture under vigorous stirring. Once the whole reaction media had been well mixed, it was transferred into the 23 mL autoclaves, and the whole reaction was heated at 160 ºC and tumbled at approximate 43 rpm for several days. Reactors were open every 5 to 7 days to check if zeolite products are formed using microscopy. If the formation of product is not completed, the whole mixture was stirred and then heated again in the autoclaves for several days. Once crystallization had terminated, zeolite products were filtered, washed using excess DI H_2O, and then air dried. The synthesis of B- and Al-SSZ-70 with ~99 % ^{29}Si enrichment followed the identical

procedure described above, except for using ~99 % ^{29}Si-enriched SiO_2 (CortecNet) as ^{29}Si source.

Delamination and surfactant swelling treatments. The delamination procedure was completed by Dr. Christopher M. Lew at the Chevron Energy Technology Company, based on the previously reported one.[65]

Calcination. Calcination of delaminated B-SSZ-70 was performed in thin beds under nitrogen flowing over the product (20 ft^3/min) mixed with ~2 % of air, and followed the profile: room temperature ramp to 120 °C at 1 °C/min; hold at 120 °C for 2 h; 120 °C ramp to 500 °C at 1 °C/min; hold at 500 °C for 5 h; 500 °C ramp to 550 °C at 1 °C/min; hold at 550 °C for 5 h; then cool to room temperature.

Aluminum reinsertion into borosilicates. Al reinsertion was to use 0.15 g of delaminated & calcined B-SSZ-70 (*i.e.*, calcined UCB-4), 0.569 g of $Al(NO_3)_3 \cdot 9\ H_2O$ (≥98 %, Sigma-Aldrich), 3.8 g of DI water. All the three components were mixed in a well-sealed and thick-wall glass vial at room temperature for 1 h, after which the whole system was statically heated at 95 °C for 5 days. After heating, the system was cooled and had solids and solution separated. Then the solids were washed twice using pH = 2 HCl, prepared with 0.1 N HCl (Fisher Chemical), at room temperature to remove any solubilized Al salt. The HCl-washed solids were subsequently rinsed with excess DI water, and then air dry for characterization.

6.3.2 Characterization.

Powder X-ray diffraction (PXRD) patterns were collected using a Siemens D5000 diffractometer or a Bruker D8 Advance or Philips X'Pert MPD. Scanning electron microscopy (SEM) images were taken on a Hitachi S-570 instrument. Elemental analysis was performed either at the Galbraith Laboratories (Knoxville, TN) or at the University of California, Santa Barbara (UCSB) using Thermo jCAP 6300 model. The CHN results were obtained by the analytical lab in the Marine Science Institute (MSI) at UCSB using the CEC440HA model from Exeter Analytical, Inc. Nitrogen (N_2) adsorption/desorption isotherms were collected using the TriStar 3000 instrument. The calcined samples were degassed under continuous N_2 flow at 200 °C overnight before the N_2 adsorption/desorption measurements. Micropore volume and external surface area were calculated using the t-plot method.

Solid-state 1D and 2D NMR spectroscopy measurements were performed to characterize the molecular compositions and structures of B-SSZ-70 related (including as-synthesized, swollen, delaminated (*i.e.*, UCB-4), and delaminated & calcined forms) and Al-SSZ-70 products. Most of the solid-state magic-angle-spinning (MAS) NMR experiments were conducted at room temperature (~25 °C) under the MAS conditions of 8 kHz on a Bruker AVANCE II 500 spectrometer with a 11.7 T wide-bore superconducting magnet, operating at frequencies of 500.0, 160.4, 130.3, and 99.4 MHz corresponding to ^{1}H, ^{11}B, ^{27}Al, and ^{29}Si resonances, respectively. A 4.0 mm variable-temperature H-X-Y triple-resonance MAS NMR probehead installed with an ^{11}B-^{29}Si or ^{27}Al-^{29}Si insert was used for most NMR measurements conducted on B-SSZ-70 related or Al-SSZ-70 materials, respectively. 1D spin-echo ^{11}B and ^{27}Al NMR spectra were acquired using a recycle delay

of 2 s, half-echo delay of 0.125 ms, weak excitation pulse power, and double frequency sweep (DFS) preparation sequence to increase ^{11}B and ^{27}Al signal sensitivities, respectively. Quantitative 1D single-pulse ^{29}Si NMR experiments were acquired using a 90° pulse (corresponding to ^{29}Si nutation frequency of 16 kHz) and a recycle delay of 500 s. For all the above measurements, high power ^{1}H heteronuclear decoupling was applied during ^{29}Si, ^{27}Al, and ^{11}B signal acquisition using the pulse scheme: small-phase-incremental-alternation-with-64-steps (SPINAL-64). ^{29}Si NMR chemical shifts, ^{11}B, and ^{27}Al NMR shifts were referenced to tetrakis(trimethylsilyl)silane (TKS), borontrifluoride diethyletherate (BF_3OEt_2), and 0.5 M aluminum nitrate solution ($Al(NO_3)_3$), respectively. Quantitative analysis of 1D ^{29}Si MAS NMR spectra was performed using the Dmfit software.[74]

2D ^{11}B{^{29}Si} *J*-mediated (through-bond) heteronuclear multiple quantum coherence (HMQC) NMR spectra were acquired on ^{29}Si-enriched as-synthesized, swollen, and delaminated B-SSZ-70 at room temperature (~25 °C) and 11.7 T under the MAS conditions of 8 kHz using a recycle delay of 2 s using a 4.0 mm variable-temperature H-X-Y triple-resonance MAS NMR probehead (installed with an ^{11}B-^{29}Si insert). The half-echo delay before and after the evolution period was experimentally optimized to 11.3 ms for all B-SSZ-70 related materials, during which a 90° ^{29}Si pulse (corresponding to a ^{29}Si nutation frequency of 16 kHz) was applied to refocus the ^{11}B NMR signals right after the first evolution period. STATES mode was applied for the indirect dimension in all 2D ^{11}B{^{29}Si} *J*-mediated HMQC NMR experiments. ^{1}H heteronuclear decoupling (50 kHz) with the SPINAL-64 scheme was applied during the whole 2D ^{11}B{^{29}Si} *J*-mediated HMQC experiments. Similarly, 2D ^{27}Al{^{29}Si} *J*-mediated HMQC NMR spectrum was acquired on

^{29}Si-enriched as-synthesized Al-SSZ-70 at room temperature (~25 °C) and 11.7 T under MAS conditions of 8 kHz using a recycle delay of 2.2 s using a 4.0 mm variable-temperature H-X-Y triple-resonance MAS NMR probehead (installed with an ^{27}Al-^{29}Si insert). The half-echo delay before and after the evolution period was experimentally optimized to 4.5 ms, during which a 90° ^{29}Si pulse (corresponding to a ^{29}Si nutation frequency of 16 kHz) was applied to refocus the ^{27}Al NMR signals right after the first evolution period. STATES mode was applied for the indirect dimension in the 2D ^{27}Al{^{29}Si} *J*-mediated HMQC NMR experiments. ^{1}H heteronuclear decoupling (50 kHz) with the SPINAL-64 scheme was applied during the whole 2D ^{27}Al{^{29}Si} *J*-mediated HMQC experiments.

Solid-state 1D single-pulse ^{27}Al NMR measurements of as-synthesized Al-SSZ-70 were conducted on a Bruker AVANCE III NMR spectrometer with an 18.8 T standard-bore superconducting magnet, operating at ^{1}H and ^{27}Al frequencies of 800.4 and 208.6 MHz, respectively, using a 3.2 mm H-X-Y triple-resonance MAS NMR probehead. The experiments used a short pulse length ($\pi/12$) and a weak pulse power along with a recycle delay of 0.6 s. High power ^{1}H heteronuclear decoupling with SPINAL-64 was applied during ^{27}Al signal acquisition. ^{27}Al NMR shifts were referenced to 0.5 M aluminum nitrate solution ($Al(NO_3)_3$).

6.4 Results and Discussion

Here, our main focus is to establish the ^{11}B and ^{27}Al siting in delaminated B-SSZ-70 and Al-SSZ-70, respectively, with the intension of controlling ^{27}Al site distributions by

post-synthetically exchanging ^{11}B with ^{27}Al atoms in the SSZ-70 framework. First, long-range order of B-SSZ-70 related zeolites will be discussed to gain insights into the ^{11}B site distributions in these materials. For example, the reflections at *ca.* 3.3° and 6.6° 2θ in the powder X-ray diffraction (PXRD) pattern 1a (see Figure 1a) manifest *d*-spacing of *ca.* 26.7 and 13.4 Å in as-synthesized B-SSZ-70, respectively. These two reflections correspond to the lamellar structure that is also revealed by the SEM image (Figure E1). Other reflections, such as the ones at *ca.* 20° and 26° 2θ, show distinct long-range order in B-SSZ-70, consistent with the previously published result.[70] To prevent direct framework condensation upon calcination, as-synthesized B-SSZ-70 was intercalated using long-chain organic cetyltrimethylammonium bromide (CTAB) surfactants, and the resulting product was denoted as swollen B-SSZ-70 whose corresponding PXRD pattern 1b is shown in Figure 1b. Compared to the pattern 1a, new reflections are observed. Specifically, the reflections (labeled using asterisk) at *ca.* 2.0°, 4.0°, 6.0°, and 8.0° 2θ, associated with *d*-spacing of *ca.* 44.0, 22.0, 14.7, and 11.0 Å, respectively, demonstrate that the swollen B-SSZ-70 still exhibits the lamellar structure. A clear evidence that the B-SSZ-70 has been swollen is supported by the reflection at *ca*. 2.0° 2θ (*d*-spacing: ~44 Å), indicating that *c*-axis is expanded above 40 Å much longer than the one (~27 Å) in as-synthesized B-SSZ-70. The changes in *c*-axis are also revealed by the absence of the two reflections at *ca.* 3.3° and 6.6° 2θ. Additionally, the elemental analysis shows higher organic contents (~42 wt%) in the swollen B-SSZ-70 than the ones in the as-synthesized B-SSZ-70 (~17 wt%), where C/N ratio also increased from *ca.* 5.7 to 15.0, attributed to the presence of CTAB surfactant (Table E2). Interestingly, the other reflections in the pattern 1b (Figure 1b) become broad after surfactant swelling, suggesting that the long-range order, especially for periodicity

along *c*-axis, is no longer present in the swollen B-SSZ-70. All the above PXRD and elemental analyses support that long-range order in B-SSZ-70 was successfully modified via the CTAB surfactant swelling treatment.

The swollen B-SSZ-70 was then sonicated to separate CTAB-intercalated B-SSZ-70 sheets as far as possible, and the obtain product was denoted as delaminated B-SSZ-70 (*i.e.*, UCB-4). Consequently, the long-range order in the delaminated B-SSZ-70 is expected to be very similar to the swollen B-SSZ-70, as evidenced by their corresponding PXRD patterns 1b and c. The pattern 1c (Figure 1c, delaminated B-SSZ-70) shows the identical reflections to the pattern 1b (Figure 1b, swollen B-SSZ-70), except for the relatively weaker reflection intensities, which are attributed to slightly loss in long-range order during sonication. The final step in sample preparation was to remove surfactants and SDAs via high temperature calcination, and the resulting material was designated as delaminated & calcined B-SSZ-70 (or calcined UCB-4), whose PXRD pattern 1d is shown in Figure 1d. As expected, the reflections at *ca.* 2.0°, 4.0°, 6.0°, and 8.0° 2θ in the pattern 1d, associated with the lamellar structure induced by CTAB surfactants, disappear after calcination. Therefore, we hypothesize that the remaining reflections in the pattern 1d indeed represent the inherent long-range order in B-SSZ-70. For example, the two reflections at *ca.* 7.2° and 14.4° 2θ corresponding to *d*-spacing of ~12.2 and 6.1 Å, respectively, are believed to manifest the *c*-axis of **MWW**-like layers in B-SSZ-70 (the previous NMR data show that SSZ-70 must have similarities to **MWW**[70]), which are also supported by our NMR structural analyses (Chapter 4). The delamination treatment indeed increases substantial amount of external surface area from 89 to 133 (m^2/g), as shown in Table E3. While detailed analyses of long-

range order in the B-SSZ-70 related zeolites could be obtained, the PXRD patterns 1a-d alone are insufficient to provide information regarding the ^{11}B siting in B-SSZ-70.

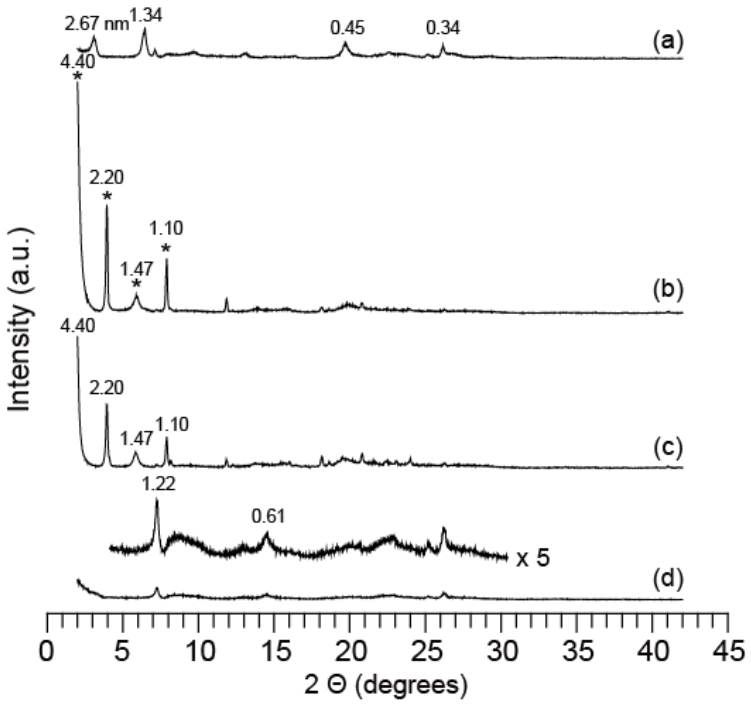

Figure 1. Powder X-ray diffraction (PXRD) patterns of (a) as-synthesized zeolite B-SSZ-70 (Si/B ~26), (b) swollen B-SSZ-70 (Si/B ~25), (c) delaminated B-SSZ-70 (Si/B ~24), and (d) delaminated & calcined B-SSZ-70 (Si/B ~24).

To understand and further monitor the ^{11}B siting in B-SSZ-70 during a series of post-synthetic treatments, solid-state magic-angle-spinning (MAS) NMR spectroscopy was employed to identify molecular ^{29}Si and ^{11}B structures, because of its high sensitivity to local nuclear and electronic environments of NMR-active nuclei. Figure 2a-d shows 1D single-pulse ^{29}Si MAS NMR spectra of as-synthesized, swollen, delaminated, and delaminated & calcined B-SSZ-70, respectively, where various Q^3 and Q^4 ^{29}Si species are manifested. Note that Q^n notations stand for a central ^{29}Si site is connected to other n ^{29}Si sites through bridging oxygen atoms (n is an integer from 0 to 4). Specifically, as-

synthesized B-SSZ-70 possesses one main Q^3 ^{29}Si signals centered at *ca.* -94, as well as several overlapping Q^4 ^{29}Si signals from -104 to -120 ppm. Despite the fact that the B-SSZ-70 used in this study was synthesized under hydroxide-mediated conditions, such Q^3 ^{29}Si signal is attributed to the inherent structural features of zeolite SSZ-70, and it is associated with the ^{29}Si sites on the edge of **MWW**-like cages. The overlapping Q^4 ^{29}Si signals correspond to the ^{29}Si site within the **MWW**-like layers. Compared to the ^{29}Si NMR spectra of as-synthesized siliceous zeolite SSZ-70,[70] the reduced spectral resolution in the ^{29}Si NMR spectrum (Figure 2a) was explained by the influence of ^{11}B atom incorporation on local ^{29}Si environments, which may be considered as indirect evidence of framework ^{11}B species.

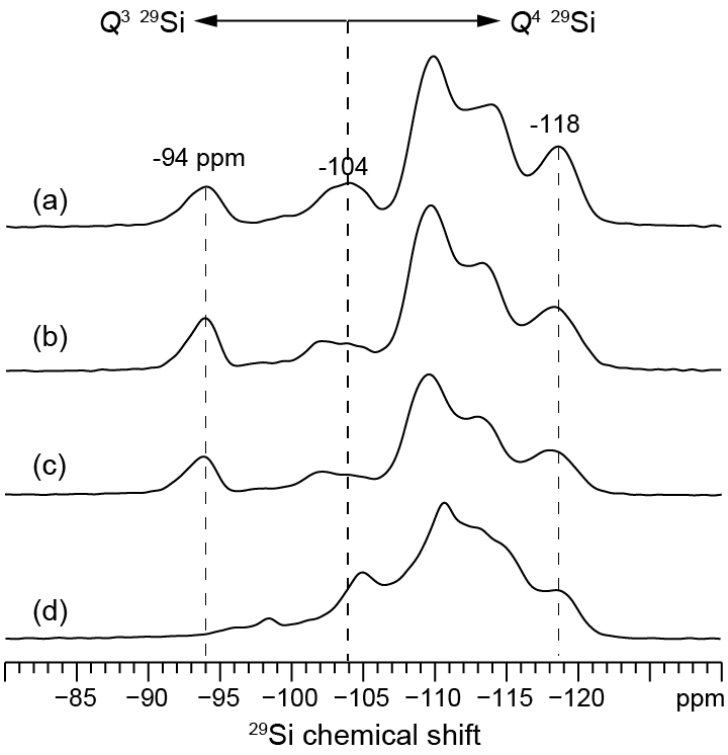

Figure 2. Solid-state 1D single-pulse ^{29}Si MAS NMR spectra of (a) as-synthesized zeolite B-SSZ-70 (Si/B ~26), (b) swollen B-SSZ-70 (Si/B ~25), (c) delaminated B-SSZ-70 (Si/B ~24), and (d) delaminated & calcined B-SSZ-70 (Si/B ~24), all of which were acquired at room temperature (~25 °C) under MAS conditions of 8 kHz.

Interestingly, the local ^{29}Si environments in swollen B-SSZ-70 are shown to be very similar to the ones in as-synthesized B-SSZ-70, based on their 1D ^{29}Si MAS NMR spectra shown in Figure 2b and a, respectively. While both ^{29}Si NMR results manifest nearly identical ^{29}Si signals: the Q^3 one at *ca*. -94 ppm and the Q^4 ones from -104 to -120 ppm, some subtle differences exist, as pointed by the Q^3 ^{29}Si signals from *ca*. -101 to -104 ppm. This is hypothesized to result from the interactions between organic CTAB surfactants and inorganic B-SSZ-70 frameworks during the swelling process. This is because the cationic head groups of CTAB surfactants should primarily interact with the edge of **MWW**-like layers in B-SSZ-70 by considering charge compensation involving cationic head groups and deprotonated Q^3 ^{29}Si species. Also, the amount of Q^3 ^{29}Si species is expected to increase, due to the presence of separated B-SSZ-70 sheets. This is supported by the quantitative analyses of 1D single-pulse ^{29}Si MAS NMR spectra, where the relative population of Q^3 ^{29}Si species increases from 13.0 to 16.1 % after the CTAB surfactant swelling procedure (see Table 1). Furthermore, the swollen B-SSZ-70 does not have any Q^2 ^{29}Si species whose expected chemical shifts will be around -90 ppm or below, consistent with the previous claims that the modified swelling procedure would retain framework integrity.[65] As expected, swollen and delaminated B-SSZ-70 exhibit nearly identical local ^{29}Si environments based on their 1D ^{29}Si MAS NMR spectra in Figure 2b and c, respectively, both of which reveal almost the same Q^3 and Q^4 ^{29}Si signals, except for the slight changes in relative populations of Q^3 and Q^4 ^{29}Si species. The Q^3 ^{29}Si species increase their relative populations from 16.1 to 17.6 % (see Table 1), which is likely due to the newly separated B-SSZ-70 sheets after the sonication. The delaminated B-SSZ-70 was then calcined to remove all possibly remaining CTAB surfactants and SDAs in structures, leading to a substantial

reduction in the amount of Q^3 ^{29}Si species from 17.6 to 8.3 % (see Table 1). The simulated ^{29}Si NMR spectra and relevant information are shown in Figure E2 and Table E4, respectively. The decrease of Q^3 ^{29}Si species is attributed to zeolite framework condensation during calcination, and the major fraction of remaining Q^3 ^{29}Si species should correspond to external surface Q^3 ^{29}Si sites, whereas a small fraction of Q^3 ^{29}Si signals may represent structural defect Q^3 ^{29}Si sites. However, it would be very challenging for us to assign quantitative contributions from external surface Q^3 ^{29}Si species with respect to the ones from structural defects. Additionally, the 1D ^{29}Si MAS NMR spectrum of the delaminated & calcined B-SSZ-70 (Figure 2d) still exhibits the main Q^4 ^{29}Si signals (*e.g.*, the one at -118 ppm) similar to the ones in the delaminated B-SSZ-70 (Figure 2c), although some of Q^4 ^{29}Si signals, such as the ones at -110 and -114 ppm, are obscure by other Q^4 ^{29}Si signals. The extremely overlapping Q^4 ^{29}Si signals prevent reliable analyses of distinguishing new Q^4 ^{29}Si sites (due to framework condensation) from the pre-existing Q^4 ^{29}Si sites in B-SSZ-70 sheets. Unlike ^{27}Al insertion whose effect on resulting ^{29}Si NMR spectra has been well recognized,[75,76] ^{11}B incorporation does not seem to displace ^{29}Si NMR signals very much, as supported by our previous NMR and computational results.[61] Similarly, the reduced ^{29}Si spectral resolution in the 1D ^{29}Si MAS NMR spectra of swollen and delaminated B-SSZ-70 zeolites (Figure 2b-c) may be attributed to the influence of ^{11}B atom incorporation. Nevertheless, the combination of PXRD patterns and 1D ^{29}Si NMR results could not provide direct understanding of local ^{11}B structures and their site distributions in B-SSZ-70.

Table 1. Relative populations of Q^3 and Q^4 ^{29}Si species in B-SSZ-70 related zeolites.

Material	Form	Q^3 ^{29}Si (%)	Q^4 ^{29}Si (%)
B-SSZ-70	As-synthesized	13.0	87.0
	Swollen	16.1	83.9
	Delaminated	17.6	82.4
	Delaminated and calcined	8.3	91.7

In contrast, local ^{11}B structures in B-SSZ-70 related products were directly probed via 1D ^{11}B MAS NMR measurements, aiming to identify various ^{11}B species. For example, the 1D ^{11}B NMR spectrum of as-synthesized B-SSZ-70 (Figure 3a) shows several ^{11}B signals at *ca.* 2.0, -0.5, -2.0, -2.8, and -3.2 ppm, all of which are assigned to four-coordinate ^{11}B species and designated as ^{11}B species *A*, *B*, *C*, *D*, and *E*, respectively. This is because of their highly symmetrical line shapes and narrow line widths (full width at half maximum (FWHM), < 0.5 ppm), as compared to the three-coordinate ^{11}B species that typically yield standard quadrupolar line shapes and broad line widths (FWHM, > 4 ppm in general).[77,78] These observations are consistent with the expected coordination number of framework ^{11}B species by considering the fact that zeolite structures are composed of four-coordinate ^{29}Si sites. Interestingly, the swollen B-SSZ-70 also possesses four-coordinate ^{11}B species, as evidenced by the ^{11}B signals at *ca.* -2.0, -2.8, and -3.2 ppm (referred to as ^{11}B species *C'*, *D'*, and *E'*, respectively) in the corresponding 1D ^{11}B NMR spectrum (Figure 3b), all of which are very similar to the ^{11}B signals in the as-synthesized B-SSZ-70 (Figure 3a). Such similarities suggest that most ^{11}B sites in B-SSZ-70 appear to be retained after the surfactant swelling process. There are subtle differences of local ^{11}B environments in as-synthesized and swollen B-SSZ-70, as indicated by the changes in the weak ^{11}B signals at 2.0 and -0.5 ppm in Figure 3a. These two ^{11}B signals appear to be affected by the swelling process,

resulting into two ^{11}B signals at -0.4 and -1.0 ppm in the 1D ^{11}B NMR spectrum of swollen B-SSZ-70 (Figure 3b), labeled as ^{11}B species *A'* and *B'*, respectively. More interestingly, the local ^{11}B structures in swollen and delaminated B-SSZ-70 are identified to be the same on the basis of their 1D ^{11}B NMR spectra shown in Figure 3b and c, respectively. The various ^{11}B signals at ~ -0.4, -1.0, -2.0, -2.8, and -3.2 ppm in Figure 3c are designated as ^{11}B species *A''*, *B''*, *C''*, *D''*, and *E''*, respectively. Furthermore, both ^{11}B NMR results (Figure 3b-c) indicate the absence of three-coordinate ^{11}B species (*i.e.*, framework ^{11}B species were not leached), and they are very similar to the ^{11}B NMR spectrum of as-synthesized B-SSZ-70 (Figure 3a). Based on the 1D ^{11}B NMR results (Figure 3a-c), it may be concluded that most of the ^{11}B siting had been retained over the course of the post-synthetic treatments, consistent with the previous claims of heteroatom retention benefited from the modified delamination treatments.[65]

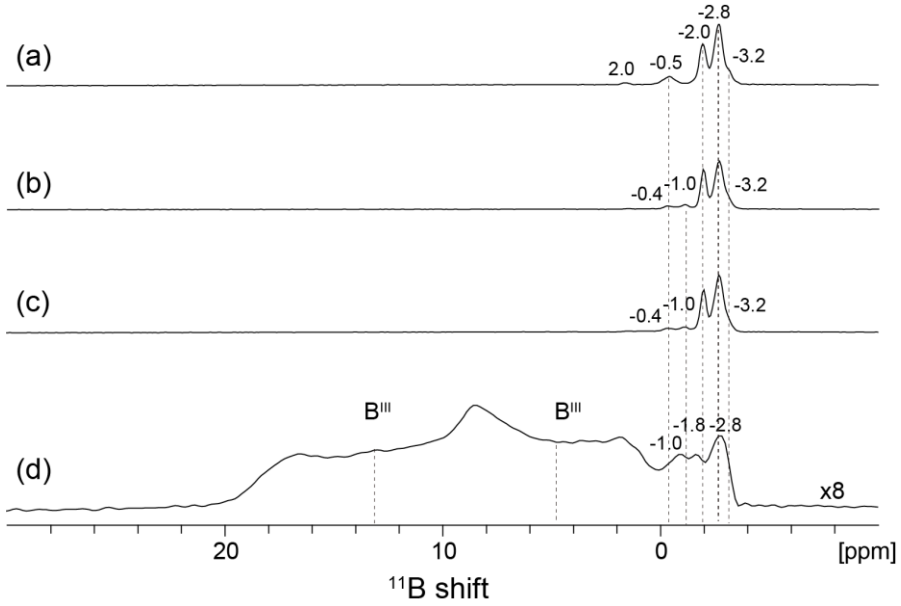

Figure 3. Solid-state 1D spin-echo ^{11}B MAS NMR spectra of (a) as-synthesized zeolite B-SSZ-70 (Si/B ~26), (b) swollen B-SSZ-70 (Si/B ~25), (c) delaminated B-SSZ-70 (Si/B ~24), and (d) delaminated & calcined B-SSZ-70 (Si/B ~24), all of which were acquired at ~25 °C under MAS conditions of 8 kHz.

The changes of local ^{11}B structures in delaminated B-SSZ-70 after calcination are revealed by the 1D ^{11}B NMR spectrum (Figure 3d), very different from B-SSZ-70 relevant zeolites before calcination (Figure 3a-c). Specifically, the ^{11}B signals from *ca.* 0 to 20 ppm exhibit classical quadrupolar line shapes and are thus assigned to two different three-coordinate ^{11}B sites that show some overlapping ^{11}B signals.[78] Other ^{11}B signals at -1.0, -1.8, and -2.8 ppm are hypothesized to be associated with four-coordinate ^{11}B species, primarily due to their ^{11}B resonances. In contrast to as-synthesized, swollen, and delaminated B-SSZ-70, a substantial fraction of four-coordinate ^{11}B sites have transformed into three-coordinate types in delaminated and calcined B-SSZ-70, and it appears that only a small fraction of original four-coordinate ^{11}B species remain intact. These observations are not very surprising and commonly seen in borosilicate zeolite catalysts.[67,78–80]

While the types of ^{29}Si and ^{11}B species in B-SSZ-70 related zeolites are nicely characterized via 1D NMR spectroscopy, two-dimensional (2D) NMR techniques can further provide deep understanding of molecular interactions between these ^{29}Si and ^{11}B components. In general, 2D NMR methods rely on two types of interactions: through-space dipolar and through-bond *J*-couplings, the former of which are often used to determine site proximities of two NMR-active nuclei, whereas the latter of which can be employed to unambiguously establish their covalent connectivities. Through-bond *J*-couplings are particularly significant, because they can identify distinct site connectivities of ^{11}B and ^{29}Si species through bridging oxygen atoms (*i.e.*, ^{29}Si-O-^{11}B) in borosilicate frameworks, based on their correspondingly $^{2}J(^{29}Si\text{-}O\text{-}^{11}B)$ couplings, which together with zeolite crystallography could essentially determine the ^{11}B site distributions. Figure 4 shows a 2D

J-mediated heteronuclear multiple quantum correlation (HMQC) $^{11}B\{^{29}Si\}$ NMR spectrum of as-synthesized B-SSZ-70 that exhibits several intensity correlations among ^{11}B and ^{29}Si signals, allowing for the determination of ^{29}Si-O-^{11}B site connectivities. For example, the ^{29}Si signal at -114 ppm corresponding to ^{29}Si site *7* shows correlated signal intensities with the ^{11}B signal at -2.8 ppm associated with ^{11}B species *D*, indicating the site connectivity of ^{29}Si site *7*-O-^{11}B site *D*. The same ^{11}B signal at -2.8 ppm is also correlated with the ^{29}Si signal at *ca.* -113 ppm associated with ^{29}Si site *8*, establishing the site connectivity of ^{29}Si site *8*-O-^{11}B site *D*. In conjunction with the understanding of crystallography, where ^{29}Si site *8* is bonded with ^{29}Si sites *7*, *8*, *8*, and *8* (Table E5) and the corresponding structure of zeolite SSZ-70 is shown in Figure E2, the two observations prove that a fraction of ^{11}B site *D* result from the ^{11}B atom inserted into ^{29}Si site *8* (designated as ^{11}B species *D-8*). Likewise, intensity correlations are clearly visible between the ^{11}B signal at *ca.* -2.7 ppm (also labeled as ^{11}B species *D*) and the ^{29}Si signal at *ca.* -108 ppm assigned to ^{29}Si site *2*, manifesting the presence of ^{29}Si site *2*-O-^{11}B site *D*. Interestingly, the same ^{11}B signal shows correlated intensities with the ^{29}Si signal at -101 ppm (Q^3 ^{29}Si site *10*). Such evidence, together with the established connectivities of ^{29}Si site *2*-O-^{11}B site *D*, allows us to identify that another portion of ^{11}B species *D* come from the ^{11}B atom incorporated into Q^4 ^{29}Si site *1* (referred to as ^{11}B species *D-1*).

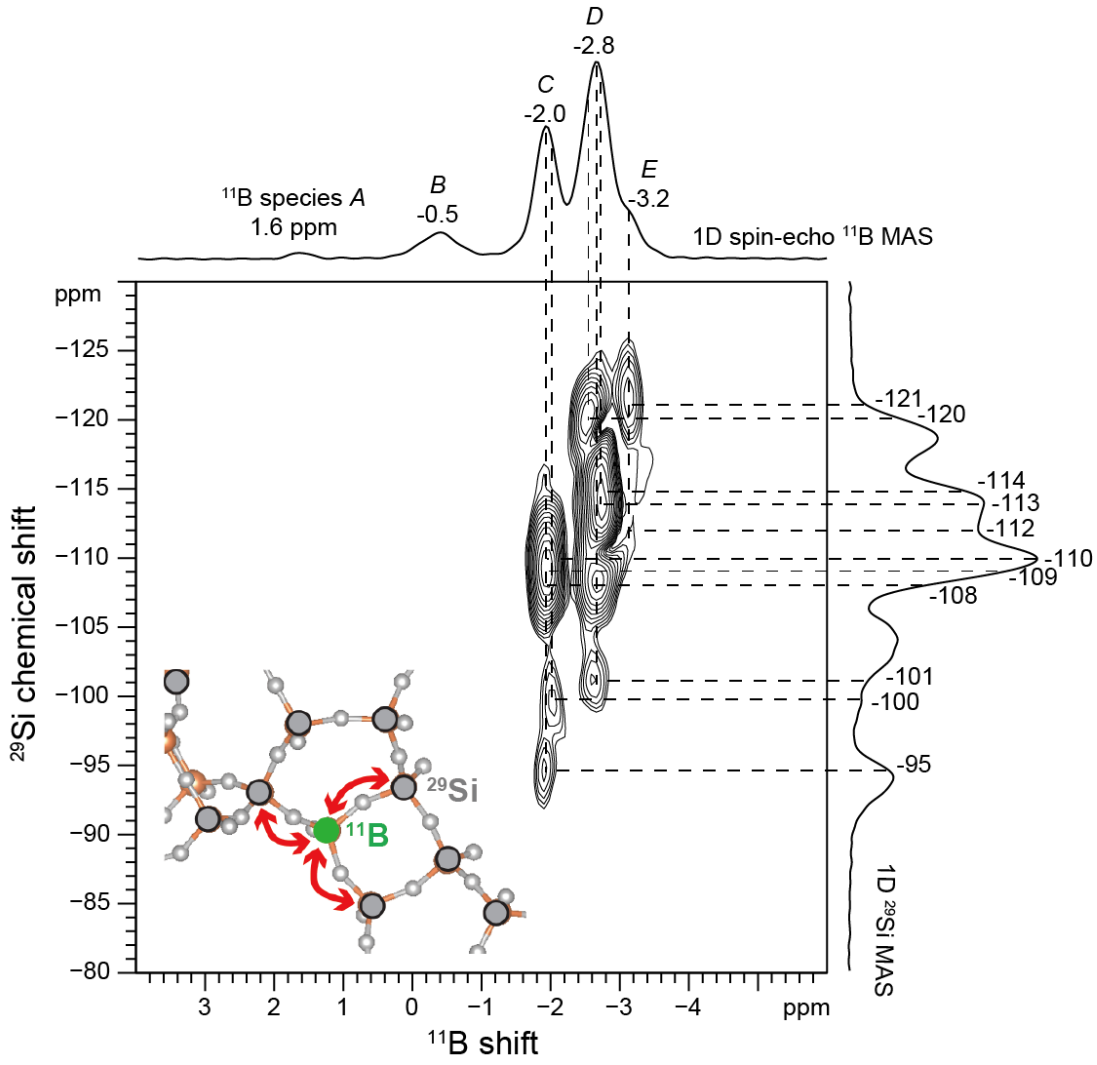

Figure 4. Solid-state 2D *J*-mediated heteronuclear multiple-quantum correlation (HMQC) ^{11}B{^{29}Si} NMR spectra of ^{29}Si-enriched as-synthesized zeolite B-SSZ-70 (Si/B = 10 in reactant), acquired at room temperature (~25 ºC) under MAS conditions of 8 kHz. Solid-state 1D single-pulse ^{29}Si and spin-echo ^{11}B MAS spectra are shown along the right vertical and the top horizontal axes, respectively.

Similarly, other ^{11}B siting in as-synthesized B-SSZ-70 can be probed using this 2D ^{11}B{^{29}Si} *J*-mediated NMR experiment. For example, the correlated signal intensities in Figure 4 between the ^{29}Si signal at -120 ppm (^{29}Si site *6*) and the ^{11}B signal at *ca*. -2.5 ppm (previously assigned to ^{11}B species *D* due to the limited resolution in the 1D ^{11}B MAS NMR spectrum, Figure 3a), indicating the presence of ^{29}Si site *6*-O-^{11}B site *D*. Furthermore, the

intensity correlations involving the ^{11}B signal at *ca.* -2.6 ppm (^{11}B species *D*) and the ^{29}Si signals at *ca.* -108 (^{29}Si site *2*) and -110 ppm (^{29}Si site *3*) manifest the connectivity of ^{11}B site *D*-O-^{29}Si site *2* and *3,* respectively, despite the fact that the corresponding ^{11}B signal is slightly shifted from *ca.* -2.5 to -2.6 ppm. Based on these ^{29}Si-O-^{11}B connectivities, it is concluded that still another fraction of ^{11}B species *D* result from the ^{29}Si site *3* substituted by ^{11}B atoms (designated as ^{11}B species *D-3*). The slightly shifted ^{11}B signal is attributed to local structural modification around the ^{11}B species *D-3* from ^{11}B incorporation. The analysis above clearly shows that it is possible for several distinct ^{11}B sites to share very similar ^{11}B shifts, which may be very difficult to be distinguished using 1D NMR spectroscopy alone.

Likewise, the ^{11}B signal at -2.0 ppm shows intensity correlations with the ^{29}Si signals at *ca.* -95, -100, -109, -110, and -110.5 ppm, suggesting the presence of at least two distinct four-coordinate ^{11}B sites, because the manifested ^{29}Si-O-^{11}B connectivities overspecify the bonding geometries for a four-coordinate ^{29}Si site. In fact, the ^{11}B signal at -2.0 ppm (^{11}B species *C*) is considered to be associated with two distinct ^{11}B sites. On one hand, a fraction of ^{11}B species *C* are hypothesized to stem from the ^{11}B atoms incorporated into Q^4 ^{29}Si site *1*, designated as ^{11}B species *C-1*, as supported by two correlation intensities between the ^{11}B signal (-2.0 ppm) and the ^{29}Si signals (-100 and -108 ppm) corresponding to ^{29}Si sites *9* and *2*, respectively. On the other hand, another faction of the ^{11}B species *C* result from the ^{11}B atoms inserted in ^{29}Si site *2* bonded with Q^3 or Q^4 ^{29}Si site *1*, referred to as ^{11}B species *C-2*' and *C-2*, respectively. This is evidenced by correlated intensities involving the ^{11}B signal at -2.0 ppm and the ^{29}Si signals at -95 (Q^3 ^{29}Si site *1*), -109 (Q^4 ^{29}Si site *1*), -110 (^{29}Si site *3*), and -110.5 ppm (^{29}Si site *4*). Lastly, the ^{11}B signal at *ca.* -3.2 ppm (^{11}B species *E*) is

assigned to the ^{11}B atoms replacing ^{29}Si site *7* (labeled as ^{11}B species *E-7*), as shown by the correlated intensities among the ^{11}B signal (*ca.* -3.2 to -3.3 ppm) and the ^{29}Si signals (-112, -114, and -121 ppm) corresponding to ^{29}Si sites *5*, *8*, and *6*, respectively. Compared to the ^{11}B species *C*, *D*, and *E*, the ^{11}B species *A* and *B* appear to be extra-framework species, due to the absence of correlated intensities involving ^{11}B signals (at 1.6 and -0.5 ppm) with any ^{29}Si signals. Overall, the detailed analysis of the 2D ^{11}B{^{29}Si} *J*-mediated NMR spectrum (Figure 4), in conjunction with the understanding of zeolite SSZ-70 structure, unambiguously determine the locations of various ^{11}B sites in as-synthesized B-SSZ-70, summarized in Table 2 and illustrated in Scheme 1.

Table 2. Summary of ^{11}B shift assignments and their corresponding ^{11}B sites in as-synthesized B-SSZ-70

^{11}B shift (ppm)	Coordination number	^{11}B species assignment	Location
1.6	4	Exfa[a]	?
-0.5	4	Exfa	?
-2.0	4	*C-1*	*1* (bonded with ^{29}Si site *9*)
-2.0	4	*C-2*	*2* (bonded with Q^4 ^{29}Si site *1*)
-2.0	4	*C-2'*	*2* (bonded with Q^3 ^{29}Si site *1*)
-2.6	4	*D-3*	*3*
-2.7	4	*D-1*	*1* (bonded with ^{29}Si site *10*)
-2.8	4	*D-8*	*8*
-3.2 ~ -3.3	4	*E-7*	*7*

[a] "Exfa" means extra-framework species.

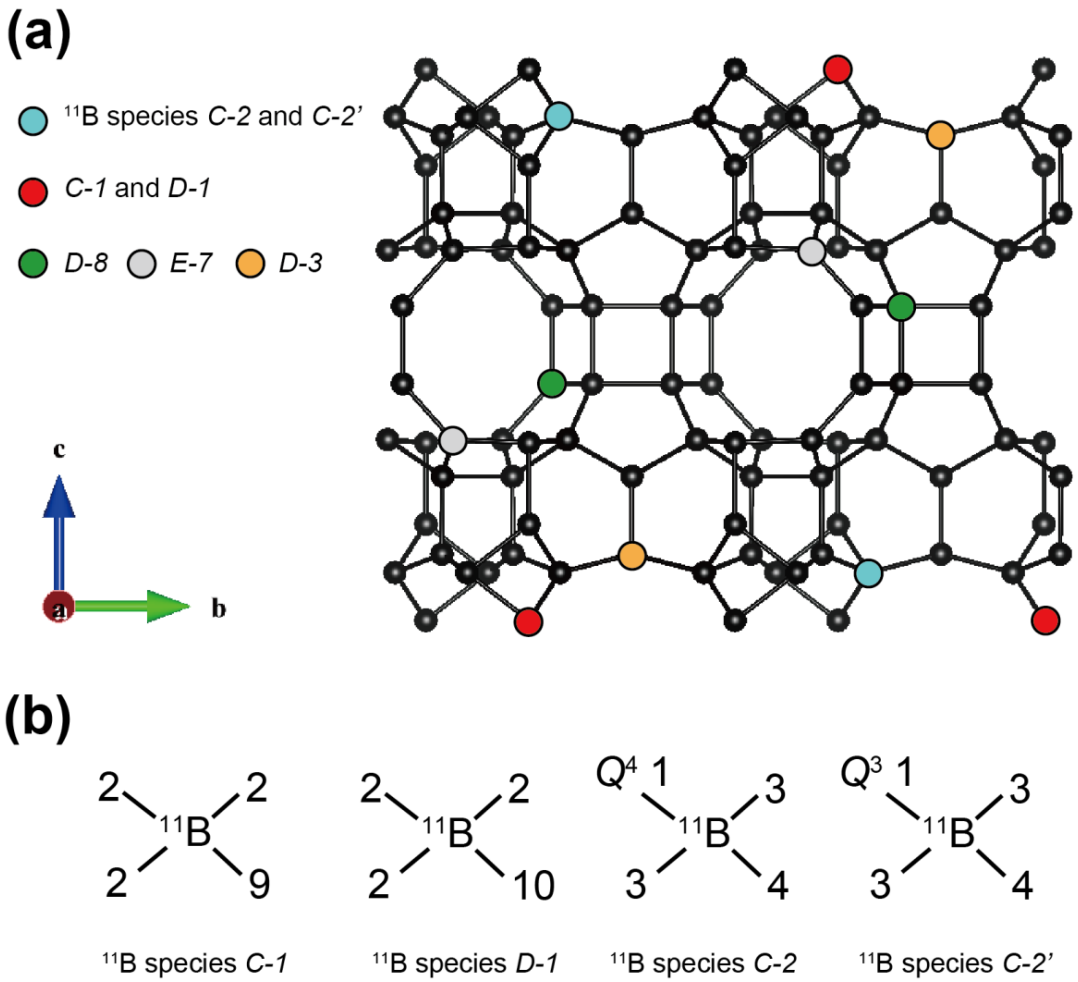

Scheme 1. (a) Schematic diagram of ^{11}B site distributions in as-synthesized B-SSZ-70, where ^{29}Si sites are shown in black, various ^{11}B sites are colored differently (see the inset for details), and bridging oxygen atoms are omitted for simplicity. Note the ^{11}B site distributions presented in this scheme are only for demonstration and may not represent the real ^{11}B contents (Si/B ~26 expected) in product. (b) Schematic illustrations of structural differences between ^{11}B species *C-1* and *D-1* as well as *C-2* and *C-2'*. The ^{29}Si-O-^{29}Si and ^{11}B-O-^{29}Si bond angles and lengths shown here may not be accurate.

On the basis of understanding regarding the ^{11}B siting in as-synthesized B-SSZ-70, it would be very interesting to monitor how these ^{11}B sites could possibly change at different synthesis stages. Figure 5 shows a 2D *J*-mediated HMQC ^{11}B{^{29}Si} NMR spectrum of swollen B-SSZ-70 (in red) that manifests several correlated intensities between ^{11}B and ^{29}Si signals, most of which are the same as the ones of as-synthesized B-SSZ-70 (Figure 4). This

suggests that most of the ^{11}B siting was retained during the CTAB surfactant swelling process. For example, the retention of ^{11}B species *D-8* is evidenced by the intensity correlations between the ^{11}B signal at *ca*. -2.8 ppm and the ^{29}Si signals at ~ -113 and -114 ppm, designated as ^{11}B species *D'-8* in swollen B-SSZ-70. Similarly, the correlated intensities involving the ^{11}B signal at *ca*. -2.6 ppm (the ^{11}B species *D'*) and the ^{29}Si signals at *ca*. -119, -110, and -109 ppm (corresponding to the ^{29}Si sites *6*, *3*, and *2*, respectively) support that the ^{11}B atoms inserted into ^{29}Si site *3* were retained, referred to as ^{11}B species *D'-3*. Likewise, the ^{29}Si site *7* substituted by ^{11}B atoms (named as ^{11}B species *E'-7*) appear to remain intact, as indicated by the ^{11}B-O-^{29}Si site connectivities based on the correlations among the ^{11}B signal at *ca*. -3.1 ppm (the ^{11}B species *E*') and the ^{29}Si signals at *ca*. -121, -113, and -115 ppm (associated with the ^{29}Si sites 6, 8, and 5, respectively). Lastly, the ^{11}B atoms incorporated into ^{29}Si site *2* bonded to Q^4 and Q^3 ^{29}Si site *1*, designated as ^{11}B species *C'-2* and *C'-2'*, respectively, are shown to be unperturbed, because of the correlated intensities between the ^{11}B signal at ~ -2.0 ppm (^{11}B species *C'*) and the ^{29}Si signals at *ca*. -97 (Q^3 ^{29}Si site *1*), -109 (Q^4 ^{29}Si site *1*), -109.5 (^{29}Si site *3*), and -110 ppm (^{29}Si site *4*). Notice that some of the above correlated ^{11}B and ^{29}Si signals may not exhibit the exact same resonances as the ones in the 2D *J*-mediated ^{11}B{^{29}Si} NMR spectrum of as-synthesized B-SSZ-70 (Figure 4), which is attributed to the influences of intercalated CTAB surfactants on local ^{11}B and ^{29}Si environments. Overall, the above 2D ^{11}B{^{29}Si} NMR result (Figure 5a) and analysis clearly indicate that a substantial fraction of framework ^{11}B sites were retained after B-SSZ-70 was intercalated with CTAB surfactants, consistent with 1D ^{11}B NMR results (Figure 3a-b), where the main ^{11}B signals at *ca.* -2.0, -2.8, and -3.2 ppm are observed in as-synthesized and swollen B-SSZ-70.

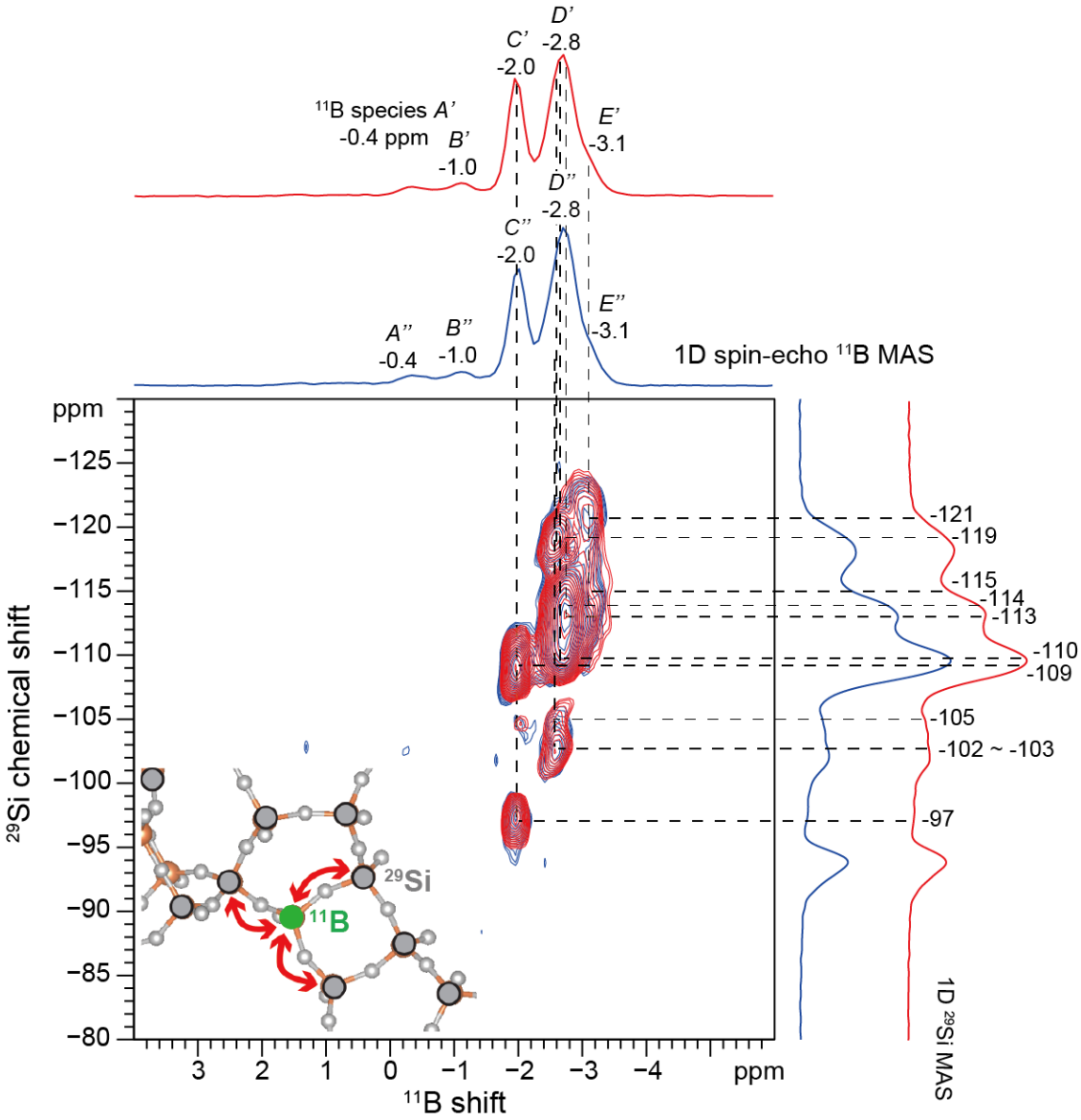

Figure 5. Solid-state 2D *J*-mediated heteronuclear multiple-quantum correlation (HMQC) $^{11}B\{^{29}Si\}$ NMR spectra of ^{29}Si-enriched swollen B-SSZ-70 (Si/B ~25 expected in product, red color) and delaminated B-SSZ-70 (Si/B ~24 expected in product, blue color), all of which were acquired at room temperature under MAS conditions of 8 kHz. Solid-state 1D single-pulse ^{29}Si and spin-echo ^{11}B MAS spectra are shown along the right vertical and the top horizontal axes, respectively.

While most framework ^{11}B species are not affected by the CTAB surfactant swelling treatment, some of the ^{11}B sites especially for the ones on the edge of **MWW**-like cages were modified, which may be due to the interactions between inorganic borosilicate

framework and organic CTAB surfactants. Specifically, the local ^{29}Si structures around ^{11}B species *D-1* in as-synthesized B-SSZ-70 appear to be slightly influenced during the swelling process, referred to as ^{11}B species *D'-1* in swollen B-SSZ-70, because the correlated ^{29}Si signals displaced from -101 and -108 ppm (Figure 4) to *ca*. -102 ~ -103 and -105 ppm (Figure 5, in red), respectively. These two shifted ^{29}Si signals (-102 ~ -103 and -105 ppm) could be reasonably assigned to the ^{29}Si sites *10* and *2*, respectively, by considering the main purpose of CTAB surfactant swelling treatment, creating breakage between adjacent **MWW**-like cages and layered (boro)silicate sheets in B-SSZ-70. Such physical separation is expected to cause structural deformation in local ^{11}B and ^{29}Si environments near the interface. Interestingly, very similar structural influence is also observed on the ^{11}B atoms inserted into Q^4 ^{29}Si site *1* bonded to ^{29}Si sites *2* and *9* (named as ^{11}B species *C-1* and *C'-1* in as-synthesized and swollen B-SSZ-70, respectively), as evidenced by the absence of the correlated intensities between the ^{11}B signal at -2.0 ppm (^{11}B species *C'*) and the ^{29}Si signal at *ca*. -100 ppm (^{29}Si site *9*). This reveals that the corresponding ^{11}B site *C'*-O-^{29}Si site *9* connectivity was broken during the swelling process, suggesting that the resulting ^{11}B site *C'-1* is still four-coordinated rather than three-coordinated, due to the absence of classical quadrupolar ^{11}B line shapes (Figure 3b). Additionally, the disappearing ^{11}B site *C'*-O-^{29}Si site *9* connectivity may imply that a small fraction of the ^{11}B species *C'-1* was lost during swelling process, consistent with previously reported elemental analyses.[65] Similar to the ^{11}B species *A* and *B* in as-synthesized B-SSZ-70, the ^{11}B species *A'* and *B'* in swollen B-SSZ-70 are shown to be extra-framework ^{11}B species, because of no intensity correlations between ^{11}B signals at -0.4 and -1.0 ppm and any ^{29}Si signals. The ^{11}B signal assignments for swollen B-SSZ-70 are summarized in Table 3 and illustrated in Scheme 2. The

comparison of 2D $^{11}B\{^{29}Si\}$ NMR results (Figures 4 and 5, in red) demonstrate the possibility of *ex-situ* monitoring ^{11}B siting in borosilicate zeolite frameworks, which had been considered a formidable task to accomplish. More importantly, the majority of the ^{11}B sites were established to be unaffected by the CTAB surfactant swelling treatment.

Table 3. Summary of ^{11}B shift assignments and their corresponding ^{11}B sites in swollen B-SSZ-70

^{11}B shift (ppm)	Coordination number	^{11}B species assignment	Location
-0.4	4	Exfa[a]	?
-1.0	4	Exfa	?
-2.0	4	*C'-1*	*1* (bonded with ^{29}Si site *9*)
-2.0	4	*C'-2*	*2* (bonded with Q^4 ^{29}Si site *1*)
-2.0	4	*C'-2'*	*2* (bonded with Q^3 ^{29}Si site *1*)
-2.6	4	*D'-3*	*3*
-2.7	4	*D'-1*	*1* (bonded with ^{29}Si site *10*)
-2.8	4	*D'-8*	*8*
-3.2	4	*E'-7*	*7*

[(a)] "Exfa" means extra-framework species.

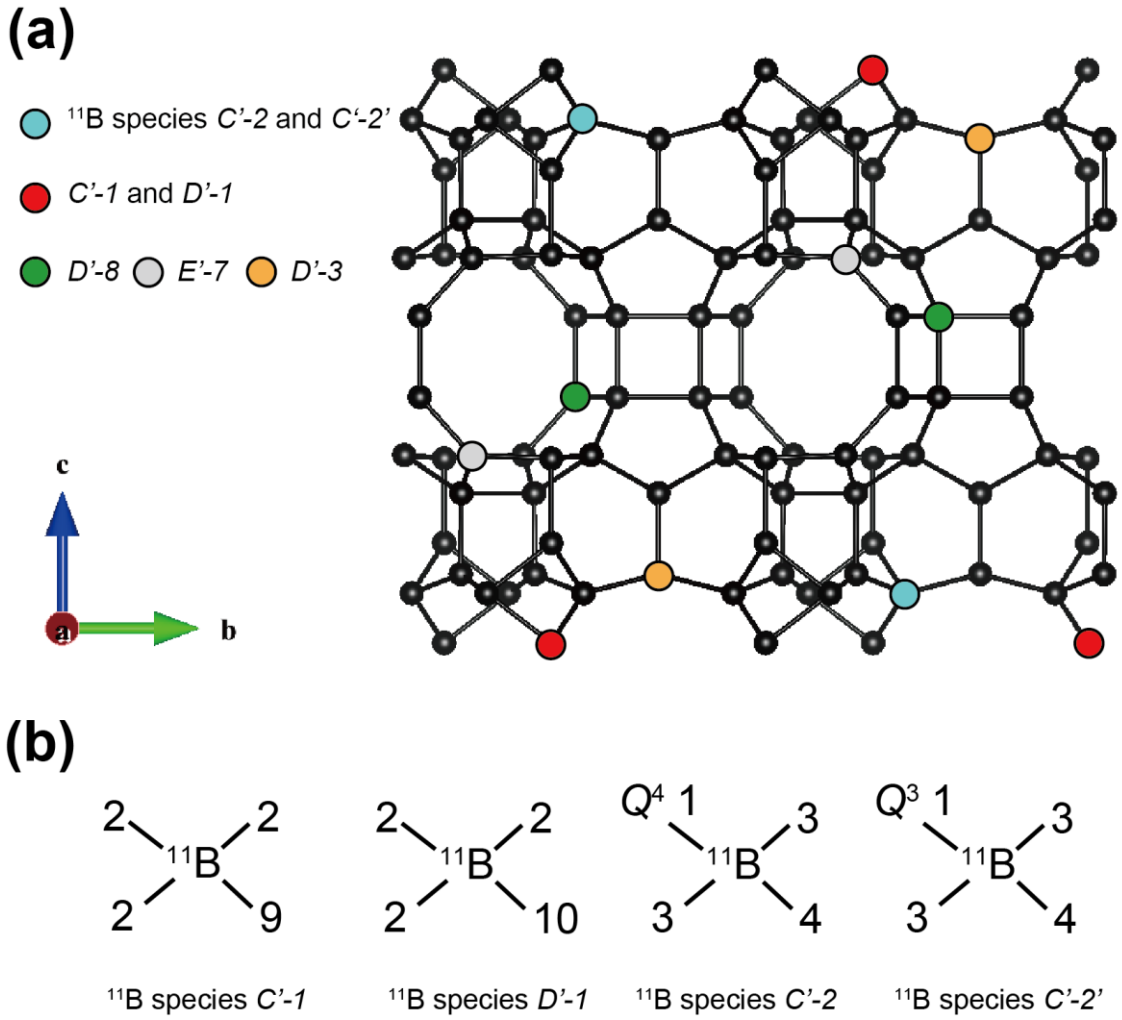

Scheme 2. (a) Schematic diagram of ^{11}B site distributions in swollen B-SSZ-70, where ^{29}Si sites are shown in black, various ^{11}B sites are colored differently (see the inset for details), and bridging oxygen atoms are omitted for simplicity. Note the ^{11}B siting presented in this scheme is only for demonstration and may not represent the real ^{11}B contents (Si/B ~25 expected) in product. (b) Schematic illustrations of structural differences between ^{11}B species *C'-1* and *D'-1* as well as *C'-2* and *C'-2'*. The ^{29}Si-O-^{29}Si and ^{11}B-O-^{29}Si bond angles and lengths shown here may not be accurate.

In addition to CTAB surfactant swelling, mechanical sonication was performed on swollen B-SSZ-70, trying to further prevent direct framework condensation upon calcination. Interestingly, the ^{11}B siting in delaminated B-SSZ-70 is established to be

identical with the one in swollen B-SSZ-70 by comparing their 2D *J*-mediated $^{11}B\{^{29}Si\}$ NMR results (Figure 5, in red and blue). For example, the ^{11}B species *D'-8* was retained after delamination, as indicated by the correlated intensities among the ^{11}B signal at -2.8 ppm (^{11}B species *D''*) and the ^{29}Si signals at *ca*. -114 (^{29}Si site *7*) and -113 ppm (^{29}Si site *8*), designated as ^{11}B species *D''-8* in delaminated B-SSZ-70. With the same 2D NMR analyses, ^{11}B species *C'-1*, *C'-2*, *C'-2'*, *D'-3*, *D'-1*, and *E'-7* in swollen B-SSZ-70 are determined to be intact after delamination, referred to as ^{11}B species *C''-1*, *C''-2*, *C''-2'*, *D''-3*, *D''-1*, and *E''-7* in delaminated B-SSZ-70, respectively, on the basis of the identical intensity correlations among various ^{11}B and ^{29}Si signals in the 2D *J*-mediated $^{11}B\{^{29}Si\}$ NMR spectra (Figure 5, in red and blue). The assignments of different four-coordinate ^{11}B species in delaminated B-SSZ-70 are listed in Table 4 and illustrated in Scheme 2. From the above detailed 2D $^{11}B\{^{29}Si\}$ NMR analyses, it can be realized how powerful such new 2D NMR methods could be in establishing distinct ^{11}B-O-^{29}Si site connectivity pairs in borosilicate frameworks, from which in conjunction with zeolite crystallography ^{11}B heteroatom siting can be identified. More importantly, the framework ^{11}B species in delaminated B-SSZ-70 are shown to be preferential distributed among certain sites. Such molecular-level understanding allows us to "predict" where the ^{27}Al or other heteroatoms would be post-synthetically reinserted, which will be discussed later together with ^{27}Al siting in Al-SSZ-70.

Table 4. Summary of ^{11}B shift assignments and their corresponding ^{11}B sites in delaminated B-SSZ-70

^{11}B shift (ppm)	Coordination number	^{11}B species assignment	Location
-0.4	4	Exfa[a]	?
-1.0	4	Exfa	?
-2.0	4	*C"-1*	*1* (bonded with ^{29}Si site *9*)
-2.0	4	*C"-2*	*2* (bonded with Q^4 ^{29}Si site *1*)
-2.0	4	*C"-2'*	*2* (bonded with Q^3 ^{29}Si site *1*)
-2.6	4	*D"-3*	*3*
-2.7	4	*D"-1*	*1* (bonded with ^{29}Si site *10*)
-2.8	4	*D"-8*	*8*
-3.2	4	*E"-7*	*7*

[a] "Exfa" means extra-framework species.

As shown by the 1D ^{11}B MAS NMR analyses (Figure 3c-d), local ^{11}B environments in delaminated B-SSZ-70 change significantly before and after calcination. Specifically, delaminated B-SSZ-70 possesses four-coordinate ^{11}B species only, whereas calcined/delaminated B-SSZ-70 contains *ca*. 83% and 17% of three- and four-coordinate ^{11}B species, respectively. Simulated ^{11}B MAS NMR spectra with deconvoluted signals for the delaminated and delaminated/calcined B-SSZ-70 are shown in Appendix E, Figure E3a-b along with detailed information summarized in Table E5 and E6, respectively. Such structural differences in the different types of ^{11}B sites leads to two questions: (i) what are the locations of the three- and four-coordinate ^{11}B sites in delaminated/calcined B-SSZ-70? and (ii) what counter cations balance the anionic framework charges of the various types of four-coordinate ^{11}B sites in the B-SSZ-70 framework before calcination? A quantitative 1D spin-echo ^{11}B MAS NMR analysis of delaminated/calcined B-SSZ-70 (Figure E3b) reveals three types of three-coordinate ^{11}B species: ^{11}B-VI (C_{qcc} = 2.5 MHz, η = 0.20, δ_{iso} = 11 ppm),

^{11}B-VII (C_{qcc} = 2.7 MHz, η = 0.13, δ_{iso} = 15 ppm), ^{11}B-VIII (C_{qcc} = 2.7 MHz, η = 0.20, δ_{iso} = 18 ppm), and ^{11}B-IX (C_{qcc} = 1.8 MHz, η = 0.20, δ_{iso} = 20 ppm), where C_{qcc}, η, and δ_{iso} refer to the quadrupolar coupling constant, asymmetry parameter, and isotropic ^{11}B chemical shift values, respectively. Based on their isotropic ^{11}B chemical shifts in the range of 10~18 ppm, the ^{11}B-VI, -VII, and -VIII species appear to correspond to framework ^{11}B sites.[78,80] By comparison, the ^{11}B-IX species seem to be associated with extra-framework ^{11}B sites, based on its isotropic ^{11}B chemical shift (20 ppm), which is similar to the values (19~20 ppm) reported for trigonal ^{11}B species in aqueous boric acid solutions and borate galsses.[80] In addition to these three-coordinate ^{11}B species, there are five types of four-coordinate ^{11}B species, labeled as ^{11}B-I, -II, -III, -IV, and -V, in delaminated/calcined B-SSZ-70. By considering their coordination number and crystallographic insights about the structure of B-SSZ-70, such four-coordinate ^{11}B species are likely associated with framework ^{11}B sites. While the ^{11}B chemical shifts, as well as the ^{11}B NMR lineshapes, allow us to identify various local ^{11}B environments, the locations of such three- and four-coordinate ^{11}B species in delaminated/calcined B-SSZ-70 still remain unknown, including whether or not all of the three-coordinate ^{11}B species are in the framework.

To assess whether most of the four- and three-coordinate ^{11}B species are still retained in the framework of B-SSZ-70 after calcination, we conducted a 1D ^{11}B{^{29}Si} *J*-mediated HMQC NMR experiment on delaminated/calcined B-SSZ-70 (Figure 6a). As discussed above for the as-synthesized B-SSZ-70, such *J*-mediated NMR experiments are sensitive only to covalently linked ^{11}B-O-^{29}Si site pairs. The intensity observed in the 1D ^{11}B{^{29}Si} *J*-mediated HMQC NMR spectrum therefore unambiguously establishes that all of the different types of three- and four-coordinate ^{11}B species, except for the ^{11}B-IX' moieties,

four covalently bonds with silicate moieties, reflecting their retaintion in the framework after calcination. The absence of intensity for the ^{11}B-IX' moieties indicate that they are extra-framework species. To determine the locations and bonding of specific ^{11}B-O-^{29}Si site pairs requires a 2D ^{11}B{^{29}Si} *J*-mediated experiment. However, this approach is infeasible, due to the weak ^{11}B-^{29}Si *J*-mediated interactions, which result in low NMR signal sensitivity and unreasonably long measurement times.

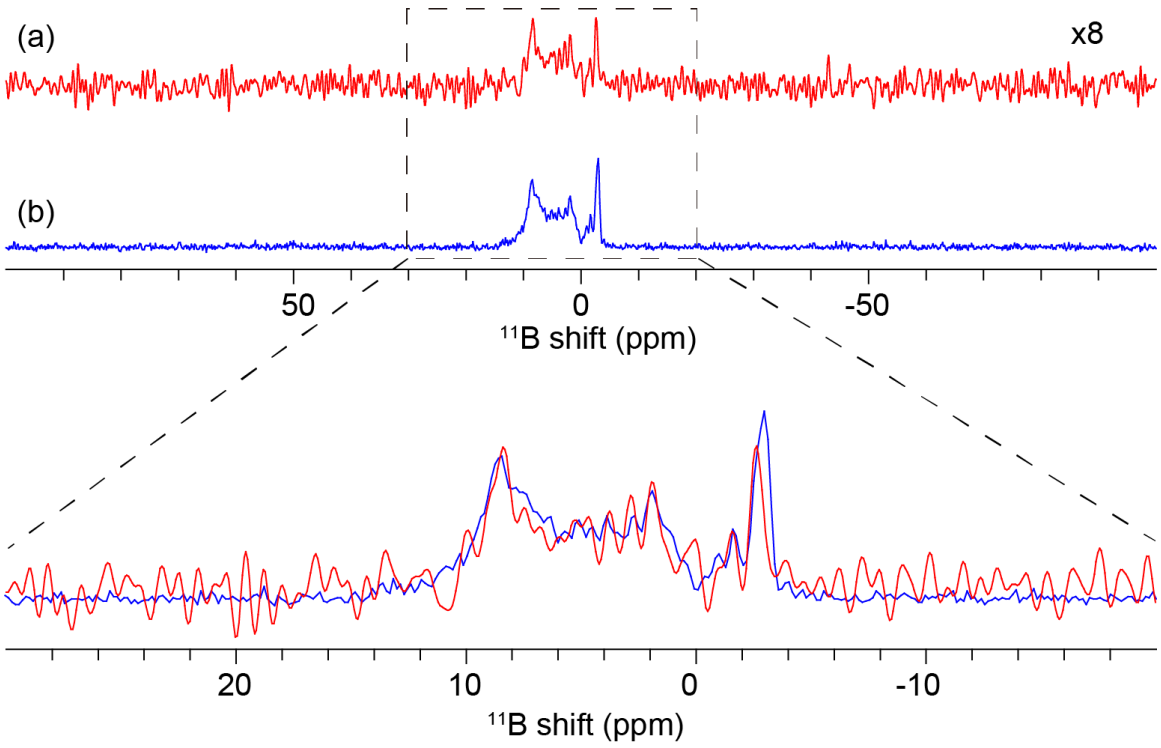

Figure 6. Comparison of (a) 1D ^{11}B{^{29}Si} *J*-mediated HMQC NMR spectrum and (b) 1D ^{11}B projection extracted from 2D ^{11}B{^{29}Si} dipolar-mediated HMQC NMR spectrum, both of which were acquired on delaminated & calcined B-SSZ-70 with *ca*. 99% ^{29}Si enrichment (Si/B ~24 expected in product).

Nevertheless, ^{11}B{^{29}Si} dipolar-mediated experiments with very short recoupling times exhibit greater NMR signal sensitivity and can be used to resolve only nearest-neighbor ^{11}B-O-^{29}Si pairs in the B-SSZ-70 framework. Consequently, 2D ^{11}B{^{29}Si} dipolar-mediated

HMQC NMR correlation measurements can be conducted to elucidate through-space interactions between nearest-neighbor ^{11}B and ^{29}Si species in the framework of B-SSZ-70. Figure 7 shows a 2D $^{11}B\{^{29}Si\}$ dipolar-mediated HMQC NMR spectrum of delaminated/calcined B-SSZ-70, where correlated intensities are revealed among various ^{11}B and ^{29}Si signals. Specifically, the ^{11}B signal (^{11}B-I species) at *ca*. -2.6 ppm is correlated with the ^{29}Si signals at *ca*. -113 to -114 ppm that are assigned to ^{29}Si sites 7 and 8, respectively, indicating that ^{11}B-I species are ^{11}B atoms in framework site 8. Similarly, ^{11}B-II species are concluded to arise from ^{11}B atoms at framework sites 1 and/or 2, as evidenced by the correlated intensities between the ^{11}B signal at -1.7 ppm and the ^{29}Si signals centered around -109 ppm. Furthermore, ^{11}B-III species appear to result from ^{11}B atoms inserted into framework sites 1, 2, and 8, because of the intensity correlations between the ^{11}B signal at *ca*. -0.9 ppm and the ^{29}Si signals at -101, -109, and -114 ppm. Interestingly, a fraction of ^{11}B-I, -II, and -III species appear to share the same type of framework ^{11}B sites given their locations. However, the distinct ^{11}B shifts suggest that these ^{11}B sites are subtly different, even though they may originate from ^{11}B atoms inserted into the same type of framework sites, and these differences will be discussed in combinations with associated counter cations that balance negative charges near framework ^{11}B sites.

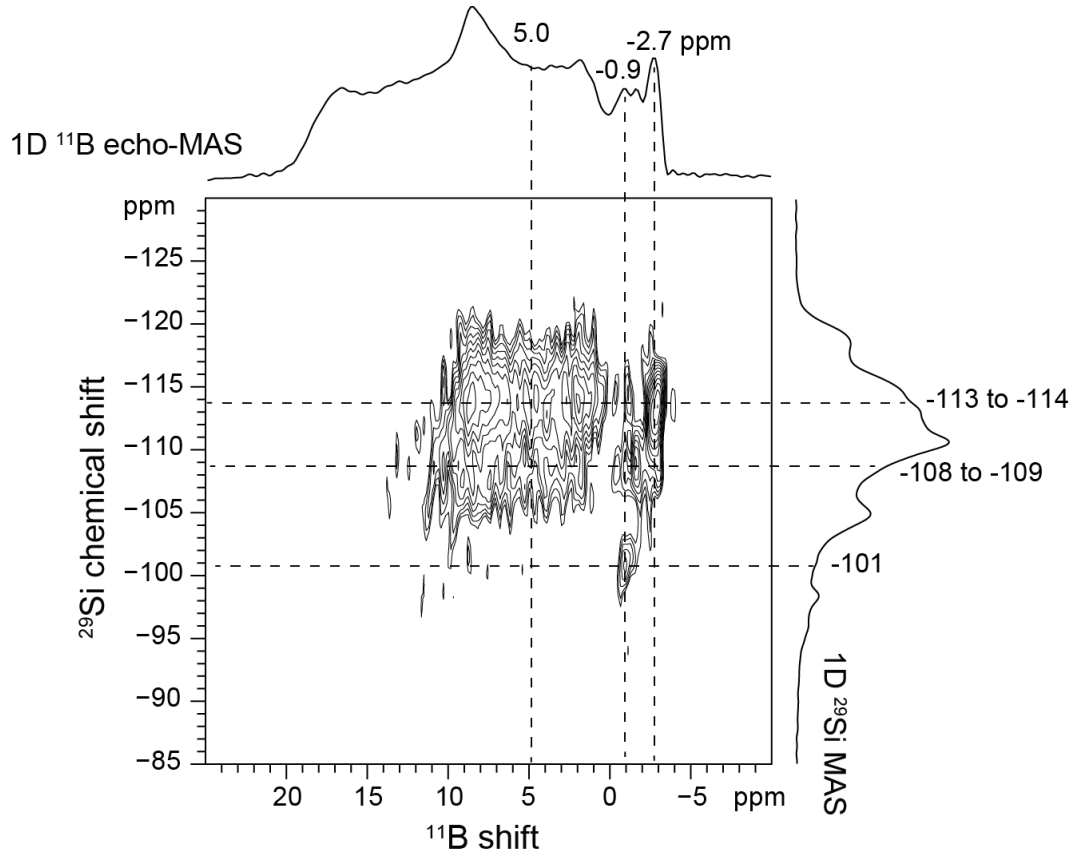

Figure 7. Solid-state 2D dipolar-mediated heteronuclear multiple-quantum correlation (HMQC) ^{11}B{^{29}Si} NMR spectrum of delaminated & calcined B-SSZ-70 with *ca*. 99% ^{29}Si enrichment (Si/B ~24 expected in product), which was acquired at room temperature under MAS conditions of 8 kHz. Solid-state 1D single-pulse ^{29}Si and spin-echo ^{11}B MAS NMR spectra are shown along the right vertical and the top horizontal axes, respectively.

In addition to four-coordinate ^{11}B species (*e.g.*, ^{11}B-I', -II', and –III'), a portion of three-coordinate ^{11}B species are identified to be framework ^{11}B sites by the 2D ^{11}B{^{29}Si} dipolar-mediated HMQC NMR analysis. Specifically, ^{11}B-VI' species is shown to result from ^{11}B atoms inserted into framework site 8, because of the correlated ^{11}B signal centered around 5 ppm and the ^{29}Si signals at approximately -113 to -114 ppm. Similarly, the intensity correlations involving the partially resolved ^{11}B signals centered around 8 ppm and the ^{29}Si signals spread between -108 to -110 ppm clearly indicate that ^{11}B-VII' and –VIII' species

are associated with ^{11}B atoms incorporated into framework sites 1 and 2. It is possible that ^{11}B-VII' and –VIII' species may correspond to other framework ^{11}B sites, but the associated ^{11}B signals overlap with the ^{11}B signal centered around 5 ppm, which prevents detailed site assignments. Very interestingly, different from ^{11}B-VI', -VII', and –VIII' species, the 2D ^{11}B{^{29}Si} dipolar-mediated HMQC NMR analysis shows that no correlated intensities between the corresponding ^{11}B signal centered around 15 ppm and any ^{29}Si signals (Figure 7), based on which it is determined that the ^{11}B-IX' species are non-framework ^{11}B sites. Such molecular-level insights into framework and non-framework ^{11}B sites, as well as the substantial changes of various ^{11}B sites in the B-SSZ-70 framework after calcination, allow us to propose possible mechanisms that account for such greatly altered local ^{11}B environments.

Based on the advanced 1D and 2D NMR analyses, framework ^{11}B sites can be divided into two types. The first type refers to ^{11}B sites (*i.e.*, ^{11}B-IV' and –V' species) that remain four-coordinated in the B-SSZ-70 framework after calcination. By comparison, the second type are ^{11}B sites (*i.e.*, ^{11}B-I', -II', and –III' species) that transform from their four- to three-coordination in the same B-SSZ-70 framework upon calcination. We hypothesize that different mechanisms are responsible for such distinct structural transformations between the two types of ^{11}B sites, which are likely to depend on associated counter cations that balance negative framework charges. Specifically, sodium cations (Na^+) appear to compensate for negative charges near the first group of framework ^{11}B sites, and such charge balancing Na^+ cations are retained even after calcination. The corresponding mechanism is depicted in Scheme 3. Interestingly, previous studies have revealed that Na^+ cations can protect framework ^{11}B species against severe structural changes in calcined

borosilicate zeolites,[78,80] which can be supported by the Na content from elemental analysis. However, our NMR data here are insufficient to determine molecular proximities between Na^+ and ^{11}B-IV' and –V' species, which could be probed in detail using advanced NMR methods, such as Rotational-Echo DOuble-Resonance (REDOR) NMR.[80]

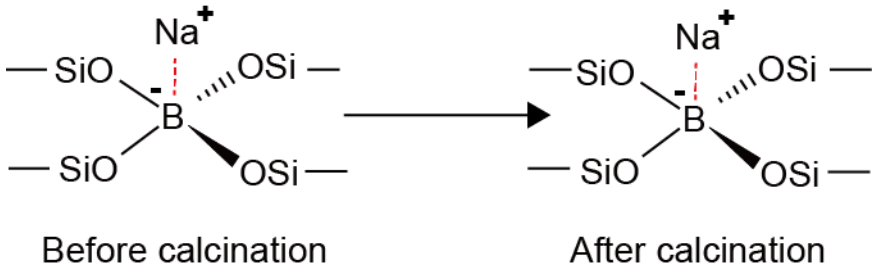

Scheme 3. Mechanism responsible for negative charges near framework ^{11}B sites balanced by sodium cations (Na^+) in the delaminated B-SSZ-70 framework before and after calcination.

In contrast, positively charged SDA^+ molecules are hypothesized to balance negative charges near the second type of framework ^{11}B sites. In the case of delaminated B-SSZ-70, SDA^+ species can be a combination of $DiBI^+$ and $CTAB^+$ molecules that were removed during calcination, as illustrated in Scheme 4a. Consequently, the counter cations would become protons, and such framework ^{11}B species would be surrounded by water molecules simultaneously, due to the resulting hydrophilicity of Brønsted acid sites. Interestingly, these Si-O-B bonds would be influenced by extent of hydration, very different from aluminosilicate zeolites whose Si-O-Al bonds have higher tolerance of hydration than Si-O-B ones in borosilicate zeolites.[81] In other words, the presence of water can greatly influence bonding configuration of framework ^{11}B sites, which would hydrolyze Si-O-B bonds and change the corresponding coordination number for ^{11}B sites from four to three (Scheme 4b). Such three-coordinate ^{11}B species could be potentially extracted from borosilicate

framework (*i.e.*, deboronation process) if calcined borosilicate zeolites are treated under extreme hydration conditions (Scheme 4d).[82] Additionally, it has been observed in the borosilicate glasses that the ^{11}B signals of three-coordinate ^{11}B species are displaced to higher frequencies as the number of Si-O-B bonds decreases.[83] Based on the correlations observed in borosilicate glasses, we thus assign ^{11}B-VI', -VII', -VIII', and –IX' species to $B(OSi)_3$ (B[3]-1), $B(OSi)_2(OH)$ (B[3]-2), $B(OSi)(OH)_2$ (B[3]-3), and $B(OH)_3$ (B[3]-NF) moieties, respectively, as illustrated in Scheme 4e. Very interestingly, the three-coordinate framework ^{11}B species (*i.e.*, $B(OSi)_3$, $B(OSi)_2(OH)$) would interact with water molecules, because of Lewis acid-base interactions, which would yield four-coordinate ^{11}B species shown in Scheme 4c.

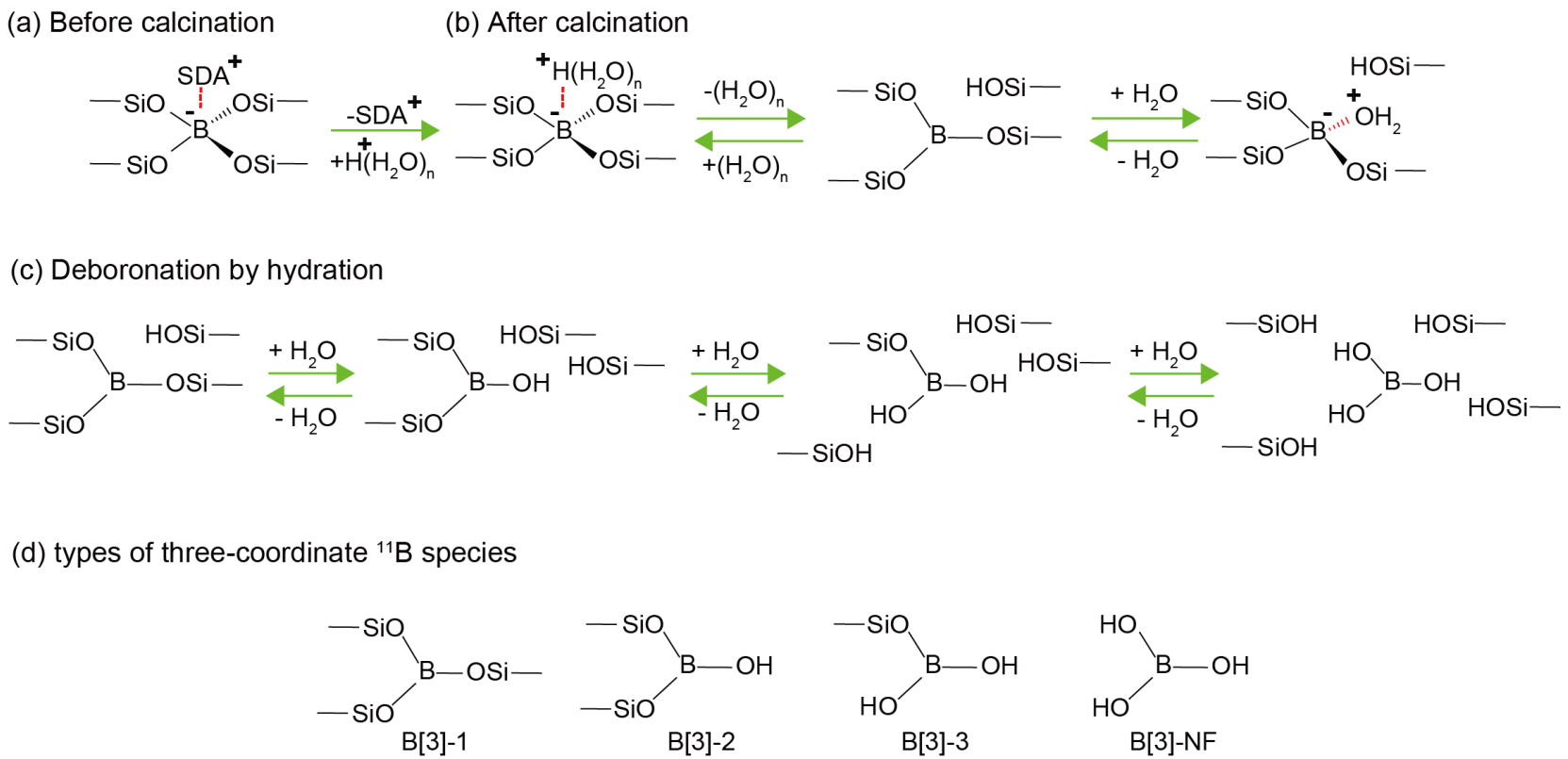

Scheme 4. Counter cation and hydration effects on local boron structural environments in delaminated B-SSZ-70 (a) before and (b) after calcination. (c) Deboronation occurs in delaminated/calcined B-SSZ-70 upon dehydration. (d) types of three-coordinate ^{11}B species that may be present in delaminated/calcined B-SSZ-70.

Local -B environments in the B-SSZ-70 framework are significantly influenced by hydration, which have been observed in other types of borosilicate zeolites.[78–80,84,85] Figure 8 shows three 1D ^{11}B echo-MAS NMR spectra acquired on the same delaminated/calcined B-SSZ-70 material stored under ambient conditions at different times after calcination, which clearly shows that relative populations of three- and four-coordinate ^{11}B species change by different extents of hydration. Overall, the total population of four-coordinate ^{11}B sites increases from *ca*. 17% to 34% at the expense of three-coordinate ^{11}B species (around 83% to 66%) over 14 months, supporting our hypothesis that water molecules would be anchored to three-coordinate framework ^{11}B sites. Simulated 1D ^{11}B echo-MAS NMR spectrum with components of delaminated & calcined B-SSZ-70 under mild hydration for 10 months is shown in Appendix E, Figure E3c, and the associated quantitative information is summarized in Table E7. The formation of four-coordinate ^{11}B-I' species is hypothesized to result from ^{11}B-VI' species anchored with water. The associated ^{11}B signal centered approximately 0.7 ppm exhibits relatively broad linewidth (FWHM ~2 ppm) compared with typical four-coordinate ^{11}B moieties (FWHM < 1 ppm), which may be due to the not highly symmetric local environments of ^{11}B-VI' species. Interestingly, the relative population of ^{11}B signals spanned between *ca*. 1.0 and 4.0 ppm gradually increases during mild hydration. Similarly, we hypothesize that ^{11}B-II' and –III' species correspond to water interacting framework ^{11}B[3]-2 and -3 sites, respectively, mainly based on the isotropic ^{11}B chemical shifts from quantitative analyses (Table E6-8). To further reduce the efforts of second order quadrupolar coupling (C_{qcc}) on 1D ^{11}B NMR results, two 1D ^{11}B NMR spectra acquired on the same delaminated and calcined B-SSZ-70 at 11.7 and 18.8 T are compared (Figure E4) and the quantitative analyses are summarized in Appendix E, Table E8 and E9, respectively.

However, the resolution of the ^{11}B NMR spectra is not greatly improved. Furthermore, the ^{11}B signals spread from *ca*. -2 to 14 ppm make identification of various four- and three-coordinate ^{11}B sites to be very challenging, which we hypothesize a distributions of four- and three-coordinate ^{11}B species interacting with water molecules, respectively. Nevertheless, we have at least demonstrated that presence of three-coordinate framework ^{11}B species as well as the influences of hydration on local ^{11}B environments in delaminated & calcined B-SSZ-70.

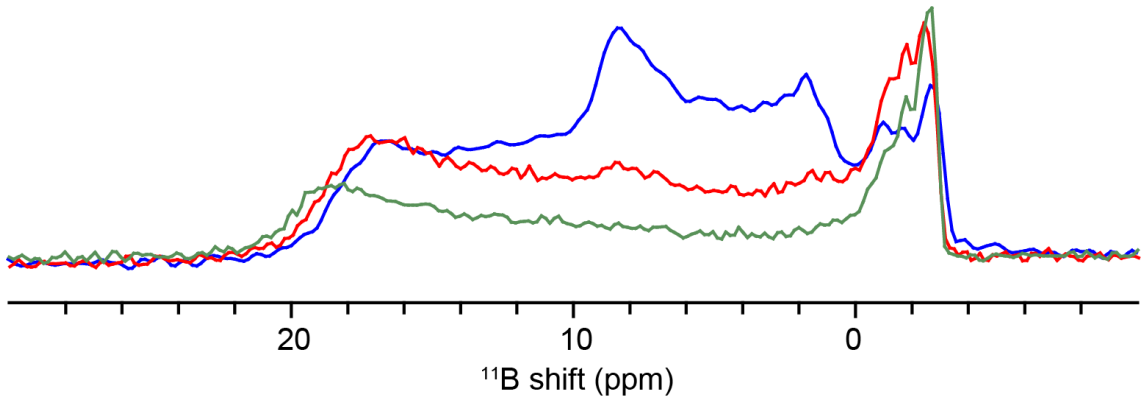

Figure 8. Comparison of 1D ^{11}B echo-MAS NMR spectra acquired on the same delaminated/calcined B-SSZ-70 material (Si/B ~24) stored under ambient condition (mild hydration) after calcination for 1.5 (in blue), 10 (in red), and 14 months (in green).

According to the discussion above, two types of counter cations (*i.e.*, Na^+ and SDA^+) can possibly balance negative charges near framework ^{11}B sites, which lead to substantial structural transformation after calcination. In principle, solid-state quantitative 1D ^{11}B MAS NMR spectroscopy can allow us to quantify the two types of framework ^{11}B species, primarily based on their change balancing cations. However, the associated ^{11}B NMR signals exhibit very similar ^{11}B shifts, which make precise quantification very challenging. In this regard, we could only estimate the relative distributions of ^{11}B sites, assessed through 10- and 12-MR rings in the delaminated B-SSZ-70 before calcination, using the molecular

insights gained from the 2D $^{11}B\{^{29}Si\}$ *J*-mediated HMQC NMR spectrum shown in Figure 5. The stimulated 1D ^{11}B MAS NMR spectrum with components of delaminated B-SSZ-70 is provided in Appendix E, Figure E3a, and the detailed information is summarized in Table E5. Such an analysis indicates that ^{11}B sites accessible through 12- and 10-MR in the B-SSZ-70 constitute approximately 34% and 56% of the total boron content, respectively. This information suggests that post-synthetic heteroatom insertion into B-SSZ-70 could replace about 33% of ^{11}B species at most, because targeted heteroatom cations would be kinetically hindered by the window size of 10-MR.

Despite the fact that the substantial influences of ^{27}Al siting in aluminosilicate zeolite catalysts on zeolite-based applications has been well recognized, understanding ^{27}Al site distributions still remains a very difficult problem to elucidate, which can be now addressed by these powerful 2D NMR methods. The fundamental and technological importance of ^{27}Al incorporation has motivated us to determine the ^{27}Al siting in Al-SSZ-70 using the modified NMR methods, and then compare the obtained information with the ^{11}B siting in B-SSZ-70. First, the long-range order of Al- and B-SSZ-70 is compared by considering the distinct sizes among ^{11}B, ^{29}Si, and ^{27}Al atoms, which may lead to local structural changes. While such changes may be manifested in the long-range structural order of B- and Al-SSZ-70, the corresponding PXRD patterns (Figures 1a and 9) show nearly identical reflections for as-synthesized B- and Al-SSZ-70, respectively. For example, the same *002* reflection at 2θ values of *ca.* 6.6° in Figures 1a and 6, associated with *d*-spacing of 13.4 Å, indicates that both B- and Al-SSZ-70 have lamellar structures. Other reflections, such as at 2θ values of 20° and 26° 2θ, show the same long-range order of B- and Al-SSZ-70, consistent with previous reports.[65,70] Although these PXRD pattenrs may be simulated to obtain the B or Al

and Si atom coordination, the resulting information may be insufficient to precisely identify ^{11}B or ^{27}Al heteroatom locations in boro- or aluminosilicate frameworks, in part due to the limited resolution of the PXRD patterns. Furthermore, the derived heteroatom location is averaged, which may be unable to provide site specific information, especially important in understanding heteroatom distributions.

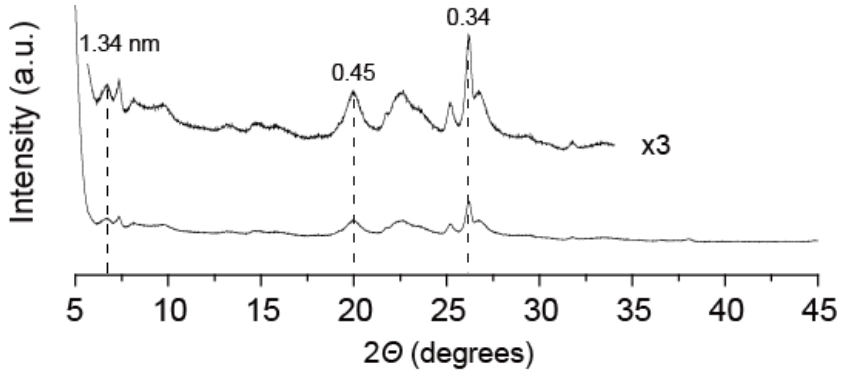

Figure 9. PXRD patterns of as-synthesized Al-SSZ-70 (Si/Al ~21).

In contrast to X-ray diffraction, solid-state NMR is highly sensitive to short-range order of NMR-active nuclei, as discussed above. Similarly, 1D ^{29}Si MAS NMR measurements were used to characterize the ^{29}Si molecular structures of as-synthesized Al-SSZ-70. Distinct from framework ^{11}B species, the presence of ^{27}Al atoms is known to influence their nearby ^{29}Si environments, leading to displacements of ^{29}Si signals.[75,76,86] Nevertheless, Figure 10 shows a 1D ^{29}Si NMR spectrum of as-synthesized Al-SSZ-70 that reveals some similar ^{29}Si signals to the ones observed in as-synthesized B-SSZ-70 (Figure 2a). For example, the ^{29}Si signal at *ca*. -94 ppm corresponds to Q^3 ^{29}Si species, revealing the unusual feature of zeolite SSZ-70. Additionally, the ^{29}Si signals at *ca*. -104, -110, -115, -119 ppm, associated with various Q^4 ^{29}Si sites in zeolite SSZ-70 frameworks, indicating that as-synthesized Al-SSZ-70 appears to possess similar ^{29}Si environments to the as-synthesized

B-SSZ-70. Very interestingly, ^{27}Al atoms does not seem to be inserted into any ^{29}Si sites connected with Q^3 ^{29}Si species, because of the absence of ^{29}Si signals corresponding to any ^{29}Si Q^3(1Al) species whose expected ^{29}Si chemical shifts would be around -90 ppm or below (highlighted in Figure 10).[76] Moreover, careful comparisons between the two 1D ^{29}Si NMR results (Figures 2a and 10) suggest that subtle differences exist between the B- and Al-SSZ-70, such as the ^{29}Si signals in the range of *ca*. -110 to -115 ppm, which may be attributed to the distinct heteroatom siting. Based on the information learned from the 1D ^{29}Si MAS NMR analysis alone, it is very unlikely to identify ^{27}Al atom locations in Al-SSZ-70, although the dependence of the number of ^{27}Al atoms on the resulting ^{29}Si signals has been recognized, in which ^{29}Si signals would be displaced to roughly 5 ppm toward downfield per ^{27}Al atom present in the first nearest neighbor of a given ^{29}Si site.[62,75,76,86]

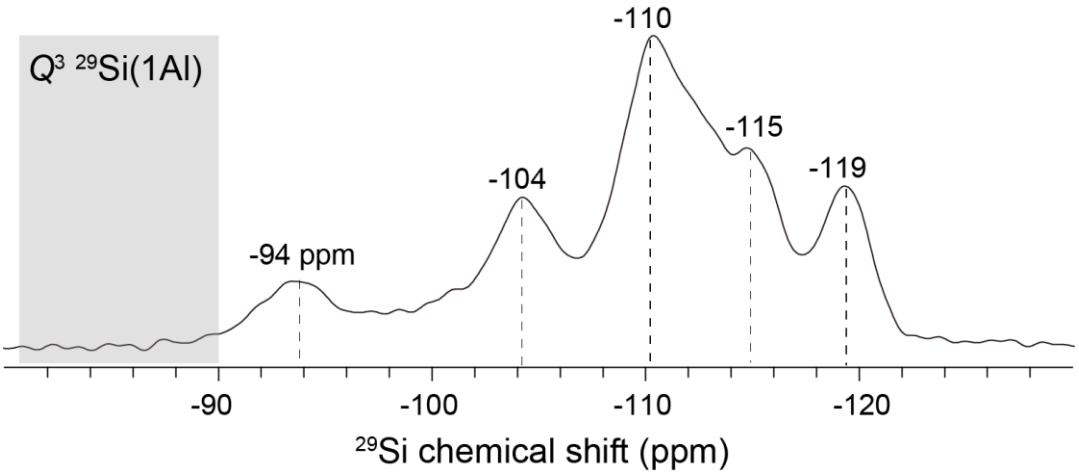

Figure 10. Solid-state 1D single-pulse ^{29}Si MAS NMR spectra of ^{29}Si-enriched as-synthesized Al-SSZ-70 (Si/Al ~21 expected), acquired at room temperature (~25 °C) under MAS conditions of 8 kHz. The highlighted region in grey shows the expected range for ^{29}Si signals associated with Q^3 ^{29}Si(1Al) species.

Similar to ^{11}B heteroatoms, ^{27}Al species are expected to become four-coordinated after inserted into zeolite frameworks mainly composed of four-coordinate ^{29}Si sites. 1D spin-echo ^{27}Al MAS NMR spectroscopy was used to understand the local ^{27}Al structures in Al-

SSZ-70. Figure 11a shows a 1D spin-echo ^{27}Al MAS NMR spectrum of as-synthesized Al-SSZ-70 that exhibits main ^{27}Al signals at *ca*. 49 and 55 ppm, both of which are associated with four-coordinate ^{27}Al species. Furthermore, no ^{27}Al signals at around 0 ppm are observed in Figure 11a, indicating the absence of six-coordinate ^{27}Al species. In other words, as-synthesized Al-SSZ-70 primarily possesses framework ^{27}Al sites. Interestingly, the two ^{27}Al signals at *ca*. 48 and 55 ppm could correspond to at least two distinct types of four-coordinate ^{27}Al sites, as suggested by the overlapping ^{27}Al signals. Such overlapping ^{27}Al signals may also be due to the strong second-order quadrupolar interactions of ^{27}Al nuclei, which could be reduced by conducting ^{27}Al NMR measurements at higher magnetic fields. Figure 8b shows a 1D single-pulse ^{27}Al MAS NMR spectrum that was acquired on the same as-synthesized Al-SSZ-70 at 18.8 T instead of 11.7 T. Very interestingly, the 1D ^{27}Al NMR result (Figure 11b) still exhibits two main ^{27}Al signals at *ca*. 48 and 56 ppm as well as no ^{27}Al signals at around 0 ppm, demonstrating again that as-synthesized Al-SSZ-70 contains framework ^{27}Al sites only. Comparisons of the two ^{27}Al NMR spectra acquired at different magnetic fields clearly support that such overlapping ^{27}Al signals in Figure 11a are in part due to the strong second order quadrupolar interactions of ^{27}Al nuclei. Consequently, the remaining ^{27}Al signals could be reasonably hypothesized to be because of a distribution of ^{27}Al shifts, which may be associated with distinct four-coordinate ^{27}Al species in Al-SSZ-70.

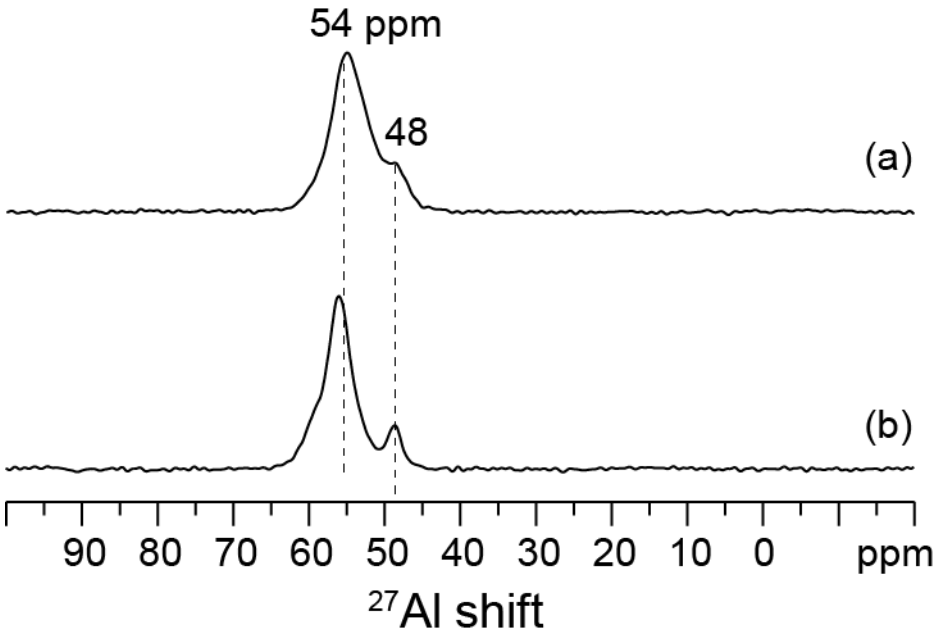

Figure 11. Solid-state 1D (a) spin-echo and (b) single-pulse ^{27}Al MAS NMR spectra of as-synthesized zeolite Al-SSZ-70 (Si/Al ~21), acquired at 11.7 and 18.8 T under MAS conditions of 8 kHz and room temperature (~25 °C), respectively.

The 2D *J*-mediated NMR methods are capable of determining not only distinct ^{11}B-O-^{29}Si site connectivities in B-SSZ-70, as extensively discussed above, but also various ^{27}Al-O-^{29}Si site connectivities in Al-SSZ-70. The resulting ^{27}Al siting is particularly interesting, because it may be used to establish correlations between such molecular understanding and bulk reaction and/or adsorption properties of zeolite catalysts in a variety of zeolite-catalyzed applications. Figure 12 shows a 2D *J*-mediated ^{27}Al{^{29}Si} HQMC NMR spectrum of as-synthesized Al-SSZ-70, where correlated intensities are observed among several ^{27}Al and ^{29}Si signals, all of which represent distinct ^{27}Al-O-^{29}Si site pairs. For example, the ^{27}Al signal at *ca*. 48 ppm (four-coordinate ^{27}Al species, labeled as ^{27}Al species *A*) is strongly correlated with the ^{29}Si signal at *ca*. -108 ppm (Q^4 ^{29}Si (1Al) species), corresponding to the connectivity of ^{27}Al site *A*-O-^{29}Si site *8* (1Al), because the presence of ^{27}Al species *A* would displace the ^{29}Si chemical shift of their next-nearest-neighbor (NNN) ^{29}Si site *8* from ~ -113

to -108 ppm. In addition, the same ^{27}Al signal (^{27}Al species *A*) exhibits intensity correlations with the ^{29}Si signal at *ca*. -110 ppm (assigned to ^{29}Si site *7* (1Al) based on a similar hypothesis of how ^{27}Al species affect the ^{29}Si chemical shifts of their NNN ^{29}Si sites), indicating the ^{27}Al site *A*-O-^{29}Si site *7* (1Al) connectivity. These two ^{27}Al-O-^{29}Si site pairs, together with the understanding of SSZ-70 structure, unambiguously establish that a fraction of ^{27}Al species *A* result from the ^{27}Al atoms inserted into ^{29}Si site *8* (designated as ^{27}Al species *A*-*8*).

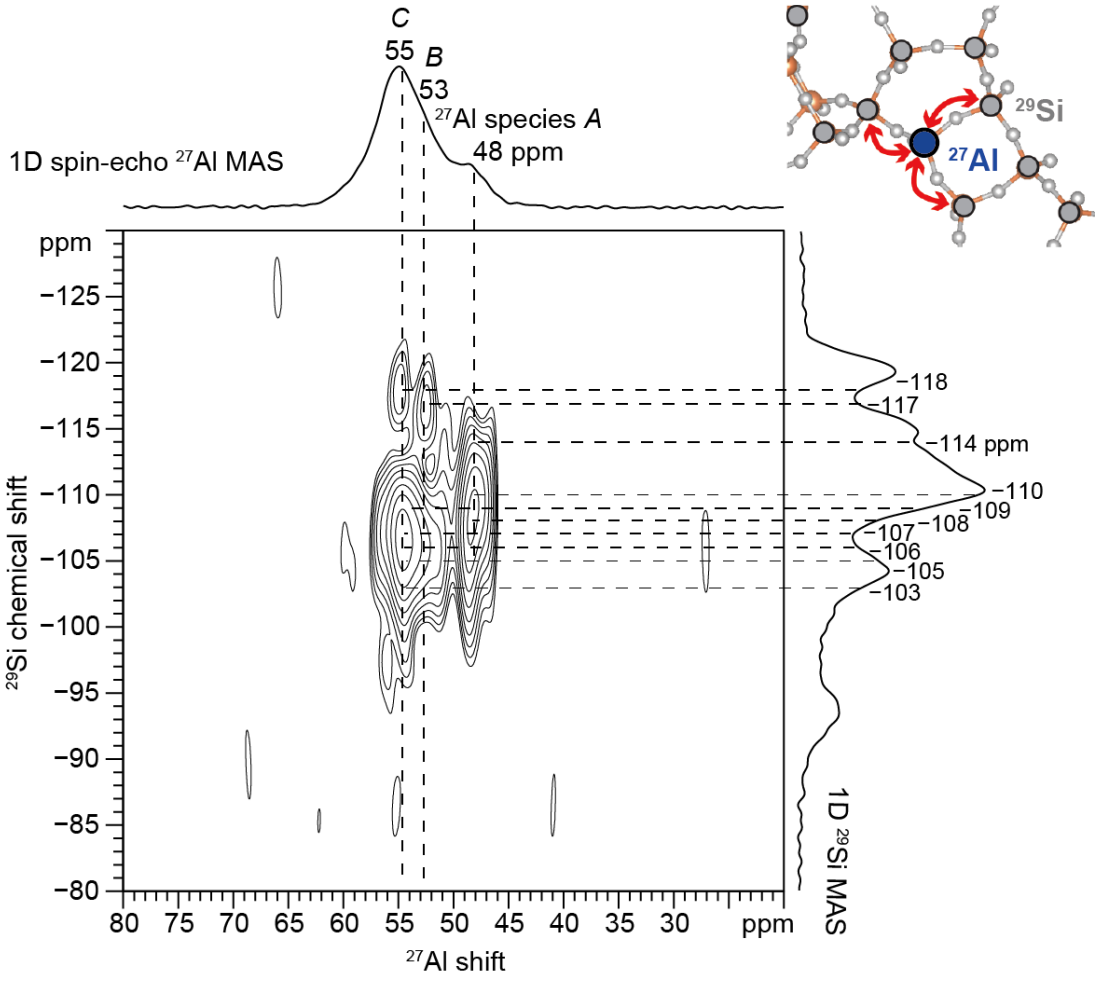

Figure 12. Solid-state 2D *J*-mediated heteronuclear multiple-quantum correlation (HMQC) ^{27}Al{^{29}Si} NMR spectrum of ^{29}Si-enriched as-synthesized Al-SSZ-70 (Si/Al ~21 expected), acquired at room temperature under MAS conditions of 8 kHz. Solid-state 1D single-pulse

^{29}Si and spin-echo ^{27}Al MAS spectra are shown along the right vertical and the top horizontal axes, respectively.

Furthermore, ^{27}Al species *A* is shown to represent at least two distinct ^{27}Al sites that share very similar ^{27}Al shifts, very difficult to distinguish using 1D NMR spectroscopy measurements. For example, the correlated intensities involving the ^{27}Al signal at 48 ppm (^{27}Al species *A*) and the ^{29}Si signals at *ca.* -106 (^{29}Si site *4* (1Al)) and -110 ppm (^{29}Si site *7* (1Al)) show the connectivities of ^{27}Al site *A*-O-^{29}Si site *4* and ^{27}Al site *A*-O-^{29}Si site *7*, respectively, which indicates the a portion of ^{27}Al species *A* come from the ^{27}Al atoms inserted into ^{29}Si site *5* (referred to as ^{27}Al species *A-5*). Similarly, still a fraction of ^{27}Al species *A* are believed to result from the ^{29}Si site *7* substituted by ^{27}Al atoms, named as ^{27}Al species *A-7*, as supported by the correlated pairs of ^{27}Al signal (48 ppm, ^{27}Al species *A*) ↔ ^{29}Si signal (~-107 ppm, ^{29}Si site *5* (1Al)), ^{27}Al signal (48 ppm, ^{27}Al species *A*) ↔ ^{29}Si signal (~-114 ppm, ^{29}Si site *6* (1Al)), and ^{27}Al signal (48 ppm, ^{27}Al species *A*) ↔ ^{29}Si signal (~-108 ppm, ^{29}Si site *8* (1Al)). Other ^{27}Al-O-^{29}Si site connectivities can also be determined based on the 2D *J*-mediated ^{27}Al{^{29}Si} HMQC NMR spectrum (Figure 12). For example, the ^{27}Al signal at *ca.* 53 ppm (^{27}Al species *B*) appears to be contributed by the ^{27}Al atoms incorporated into ^{29}Si site *3* (designated as ^{27}Al species *B-3*), as evidenced by the intensity correlations between the ^{27}Al signal at 53 ppm (^{27}Al species *B*) as well as the ^{29}Si signals at *ca*. -103 (^{29}Si site *2* (1Al)), -105 (^{29}Si site *3* (1Al)), and -117 ppm (^{29}Si site *6* (1Al)).

Interestingly, the observation of distinct ^{27}Al sites exhibiting very similar ^{27}Al shifts takes place on other ^{27}Al signals in as-synthesized Al-SSZ-70. For instance, the ^{27}Al signal at *ca*. 55 ppm (^{27}Al species *C*) shows correlated intensities with several ^{29}Si signals, such as the ones at *ca*. -103, -105, -106, -107, and -109 ppm, each of which corresponds to a distinct ^{27}Al-O-^{29}Si site connectivity. Obviously, the number of different ^{27}Al-O-^{29}Si site pairs

overspecifies the bonding configuration of a single ^{29}Si site. Thus, it is hypothesized that the ^{27}Al signal at *ca*. 55 ppm is associated with at least two types of four-coordinate ^{27}Al species. Specifically, the ^{27}Al signal at ~55 ppm (^{27}Al species *C*) is correlated with the ^{29}Si signals at *ca*. -103 and -107 ppm associated with the ^{29}Si sites *2* (1Al) and *5* (1Al), respectively, determining that a fraction of ^{27}Al species *C* stems from the ^{27}Al atoms inserted into ^{29}Si site *4* (named as ^{27}Al species *C-4*). Furthermore, the same ^{27}Al signal (^{27}Al species *C*) exhibits correlated intensities with the ^{29}Si signals at -104 (^{29}Si site *1* (1Al)), -105 (^{29}Si site *3* (1Al)), and -106 ppm (^{29}Si site *4* (1Al)), showing that a portion of ^{27}Al species *C* were contributed by the ^{29}Si site *2* substituted by ^{27}Al atoms (designated as ^{27}Al species *C-2*). Additionally, the presence of the ^{27}Al atoms inserted into ^{29}Si site *6* is supported by the intensity correlations between the ^{27}Al signal at ~55 ppm (^{27}Al species *C*) and the ^{29}Si signals at -105 (^{29}Si site *3* (1Al)), -109 (^{29}Si site *7* (1Al)), and -118 ppm (^{29}Si site *6* (1Al)), which is referred to as ^{27}Al species *C-6*. Lastly, some ^{27}Al atoms appear to be incorporated into Q^3 ^{29}Si site *1* (named as ^{27}Al species *C-1*), as evidenced by the correlated the ^{27}Al signal at around 55 ppm with the ^{29}Si signal at *ca.* -103 ppm (^{29}Si site *2* (1Al)). Very interestingly, ^{27}Al atoms are shown to be connected with Q^4 ^{29}Si sites only, forming Q^4 ^{29}Si (1Al) species. This is consistent with the 1D ^{29}Si NMR result (Figure 10), where no Q^3 ^{29}Si (1Al) species are detected. All the ^{27}Al signal assignments are illustrated in Scheme 5 and summarized in Table 5.

Table 5. Summary of ^{27}Al shift assignments and their corresponding ^{27}Al sites in as-synthesized Al-SSZ-70

^{27}Al shift (ppm)	Coordination number	^{27}Al species assignment	Location
48	4	*A-5*	*5*
48	4	*A-8*	*8*
48	4	*A-7*	*7*
53	4	*B-3*	*3*
55	4	*C-1*	Q^3 site *1*
55	4	*C-2*	*2* (bonded with Q^4 ^{29}Si site *1*)
55	4	*C-4*	*4*
55	4	*C-6*	*6*

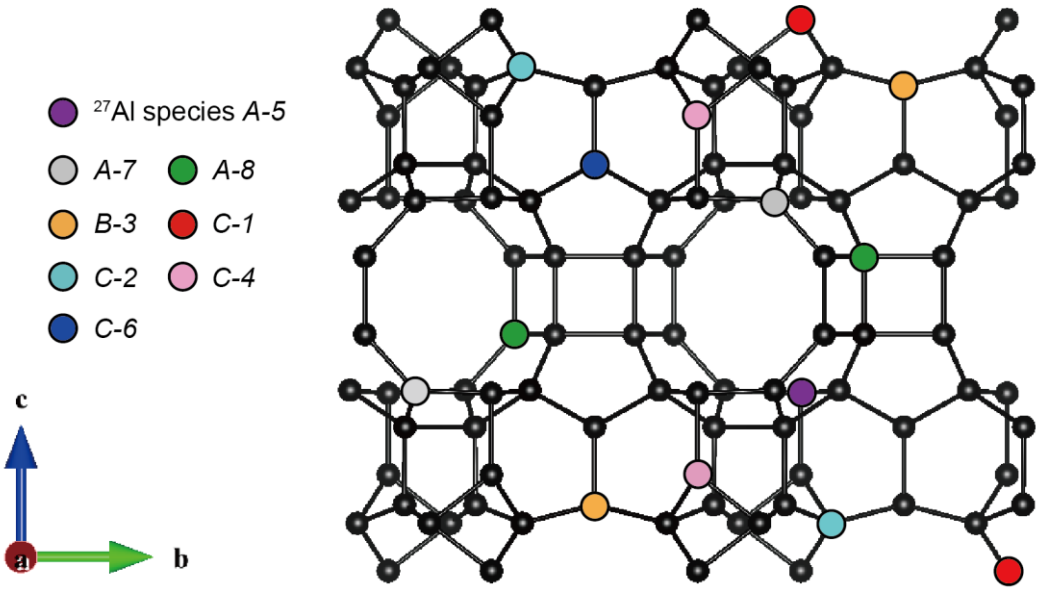

Scheme 5. Schematic diagram of ^{27}Al site distributions in as-synthesized Al-SSZ-70, where ^{29}Si sites are shown in black, various ^{27}Al sites are colored differently (see the inset for details), and bridging oxygen atoms are omitted for simplicity. Note the ^{27}Al siting presented in this scheme is only for demonstration and may not represent the real ^{27}Al contents (Si/Al ~21 expected) in product. The ^{29}Si-O-^{29}Si and ^{27}Al-O-^{29}Si bond angles and lengths shown here may not be accurate.

The detailed analyses of the 2D *J*-mediated ^{27}Al{^{29}Si} NMR result (Figure 9) suggest that various ^{27}Al sites are non-selectively distributed among nearly all ^{29}Si sites in Al-SSZ-70, very different from the ^{11}B siting in B-SSZ-70, where ^{11}B atoms are shown to be inserted into certain ^{29}Si sites only. Very interestingly, despite the fact that ^{27}Al atoms appear to go everywhere in Al-SSZ-70, they are not incorporated into any ^{29}Si sites neighboring Q^3 ^{29}Si species. This may be also because that ^{27}Al incorporation would possibly introduce ^{29}Si framework condensation on any ^{29}Si sites in the NNN of ^{27}Al species. While our studies here are insufficient to understand the main causes of why ^{11}B and ^{27}Al heteroatoms are very differently distributed in zeolite SSZ-70, the resulting ^{11}B and ^{27}Al siting in zeolite SSZ-70 shed light on possibilities of controlling heteroatom site distributions in high silica zeolites.

Specifically, such a synthesis protocol would start with preparation of B-SSZ-70, where ^{11}B atoms are established to be preferentially inserted into specific ^{29}Si sites. Then the as-synthesized B-SSZ-70 could be directly calcined or be delaminated to increase its external surface area and calcined, both of which will be next used in post-synthetic heteroatom exchange treatments. Several types of heteroatoms could be utilized in the exchange processes,[57,63–67,87] during which framework ^{11}B species would dissolve and desorb from borosilicate frameworks in reaction media, resulting into silanol defects (also viewed as vacancies). Such silanol defects would serve as potential locations for heteroatom reinsertion in the post-synthetic exchange processes. Our studies of the ^{11}B siting in B-SSZ-70 indicate that framework ^{11}B sites are distributed within the internal 10-MR and the external 12-MR of **MWW**-like cages. Among these different vacancies after deboration, heteroatoms would be particularly reinserted into the ones within the external 12-MR of

MWW-like cages, based on the sizes of hydrated heteroatom ions. For example, Figure 13 shows a 1D ^{27}Al NMR spectrum of Al-reinserted UCB-4 (*i.e.*, delaminated and calcined B-SSZ-70) that exhibits ^{27}Al signals at *ca*. 48 and 55 ppm. While the ^{27}Al signals are similar to the ones observed in Al-SSZ-70 (Figure 11), they appear to be slightly broader, which may be attributed to relatively less uniform local ^{27}Al environments of Al-reinserted UCB-4, because the host inorganic framework was swollen, delaminated, and calcined, as compared to the as-synthesized Al-SSZ-70 without any treatments. Specifically, the ^{27}Al signal at *ca.* 55 ppm could be reasonably assigned to the ^{27}Al atoms inserted into ^{29}Si sites *1* and/or *2* on the basis of ^{27}Al signal assignments in Al-SSZ-70, referred to as ^{27}Al species *A'-1* and *A'-2*, respectively. Additionally, the ^{27}Al signal at ~53 ppm (embedded among the ^{27}Al signals at 48 and 55 ppm) is attributed to the ^{29}Si site *3* reinserted with ^{27}Al atoms, designated as ^{27}Al species *B'-3*.

Interestingly, the ^{27}Al signal at ~48 ppm is hypothesized to result from the ^{27}Al atoms reinserted to ^{29}Si sites *7* and *8* in the internal 10-MR within **MWW**-like cages, based on the ^{27}Al species *A-7* and *A-8* exhibit similar ^{27}Al shifts (*ca.* 48 ppm) in Al-SSZ-70 (see Table 5), named as ^{27}Al species *C'-7* and *C'-8* in Al-reinserted UCB-4, respectively.. This is unexpected, because the Al reinsertion would be expected to occur only on external silanol defects.[57,63,64,88] This result suggests that a fraction of the **MWW**-like cages may not be well retained during the swelling and delamination treatments, resulting into "broken" **MWW**-like cages.[89] Such "broken" MWW-like cages are very likely to provide exposed 10-MR within MWW-like cages that were previously thought to be inaccessible. Despite the powerful 2D NMR methods demonstrated in this report, the limited ^{29}Si spectral resolution in 1D ^{29}Si MAS NMR spectrum of Al-reinserted UCB-4 (Figure E4) prevents reliable signal

assignments to locate the reinserted ^{27}Al atoms. Additionally, the not well resolved ^{27}Al signals in the 1D ^{27}Al MAS NMR spectrum (Figure 11) also make quantitative analysis of these ^{27}Al species to be formidable. Nevertheless, we are still able to compare the molecular-level information of Al-reinserted UCB-4 with the ^{27}Al siting in Al-SSZ-70, yielding the understanding of the ^{27}Al site distributions within Al-reinserted UCB-4. The relevant ^{27}Al siting and signal assignments in are illustrated and summarized in Scheme 6 and Table 6, respectively. More importantly, the synthesis protocol, post-synthetic Al reinsertion, and 2D NMR methods clearly demonstrate that it is possible to control heteroatom siting in high silica zeolite catalysts, which has been considered as a formidable task to accomplish. Furthermore, as mentioned above, such heteroatom reinsertion is not only limited to ^{27}Al, which could be extended to other heteroatoms, aiming for imparting new catalytic properties to zeolite SSZ-70. For example, tin (Sn) reinsertion would enable biomass applications of SSZ-70, whereas titanium (Ti) would broaden applications of SSZ-70 to oxidation processes.[87] Overall, we believe that the understanding of ^{11}B and ^{27}Al heteroatom siting in SSZ-70 as well as the 2D NMR methods, presented in this report, would be very helpful in designing boro- and aluminosilicate zeolite catalysts with engineered heteroatom site distributions.

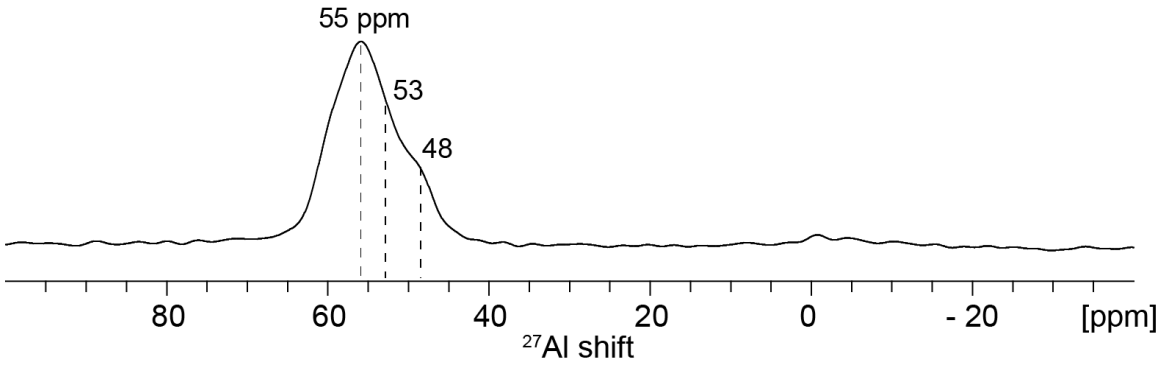

Figure 13. Solid-state 1D spin-echo ^{27}Al MAS NMR spectra of Al-reinserted-UCB-4 (Si/Al ~89), acquired at room temperature (~25 °C) and 11.7 T under MAS conditions of 8 kHz.

Table 6. Summary of ^{27}Al shift assignments and their corresponding ^{27}Al sites in Al-reinserted-UCB-4

^{27}Al shift (ppm)	Coordination number	^{27}Al species assignment	Location
55	4	*A'-1*	*1*
55	4	*A'-2*	*2*
53	4	*B'-3*	*3*
48	4	*C'-7*	*7*
48	4	*C'-8*	*8*

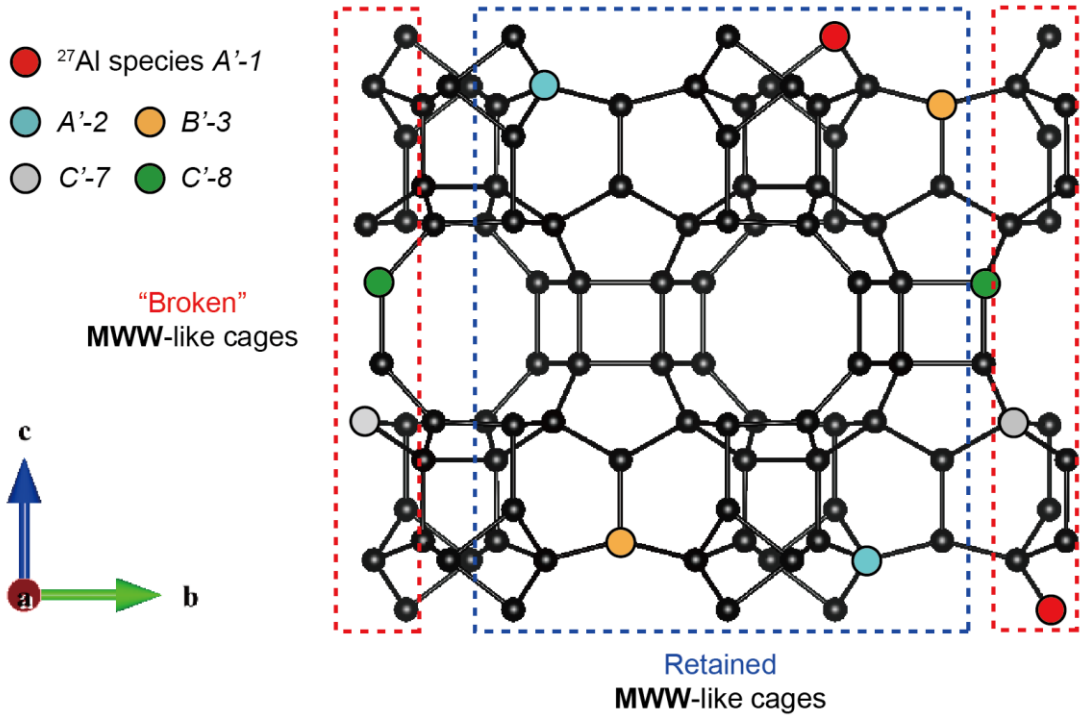

Scheme 6. Schematic diagram of ^{27}Al site distributions in Al-reinserted-UCB-4, where ^{29}Si sites are shown in black, various ^{27}Al sites are colored differently (see the inset for details), and bridging oxygen atoms are omitted for simplicity. Retained and "broken" MWW-like cages are highlighted with blue and red boxes, respectively. Note the ^{27}Al siting presented in this scheme is only for demonstration and may not represent the real ^{27}Al contents (Si/Al ~89) in product. The ^{29}Si-O-^{29}Si and ^{27}Al-O-^{29}Si bond angles and lengths shown here may not be accurate.

6.5 Conclusions

The molecular interactions between ^{11}B/^{27}Al and ^{29}Si species in boro-/aluminosilicate zeolite SSZ-70 are established primarily using solid-state 2D NMR techniques. Interestingly, the corresponding heteroatom site distributions in B- and Al-SSZ-70 are shown to be substantially different, as identified by the crystallographic information and the solid-state 2D *J*-mediated (through-bond) ^{11}B{^{29}Si} and ^{27}Al{^{29}Si} NMR measurements, where various ^{11}B-O-^{29}Si or ^{27}Al-O-^{29}Si site connectivities are determined in B- and Al-SSZ-70 frameworks, respectively. Specifically, the ^{11}B heteroatoms are shown to be preferentially

inserted into certain framework sites that are accessible by internal 10-MR and external 12-MR in B-SSZ-70, whereas ^{27}Al atoms appear to be distributed among all types of sites in Al-SSZ-70. Such significant differences shed light on the possibilities of controlling heteroatom site distributions in high silica zeolite catalysts, because framework ^{11}B species in B-SSZ-70 could be post-synthetically exchanged with other types of heteroatoms. Furthermore, SSZ-70 possesses lamellar structural features that can be delaminated to alleviate mass transport limitation of zeolite catalysts in reactions involving bulky molecules, which motivated us to monitor *ex-situ* ^{11}B site distributions in B-SSZ-70 over the course of delamination by 2D *J*-mediated ^{11}B{^{29}Si} NMR techniques. Importantly, the NMR results and analyses clearly indicate that locations of ^{11}B species in delaminated B-SSZ-70 (UCB-4) are retained after a series of post-synthetic treatments. In other words, ^{11}B sites are accessible through internal 10-MR and external 12-MR in UCB-4.

With the understanding regarding locations of ^{11}B species in UCB-4, we propose a synthesis protocol to control heteroatom siting in high silica zeolite catalysts. This protocol is established by borosilicate zeolite synthesis in conjunction with heteroatom reinsertion, as supported by the investigations of Al-reinserted UCB-4 in this work. 1D ^{27}Al NMR result indicate that Al-reinserted UCB-4 has a distribution of four-coordinate ^{27}Al species, most of which are assigned to ^{27}Al atoms in sites accessible by external 12-MR, whereas a small portion of ^{27}Al signals are hypothesized to stem from ^{27}Al atoms in sites near internal 10-MR, based on the site-specific information learned from ^{27}Al site distributions in Al-SSZ-70. Such 1D ^{27}Al NMR analyses are consistent with the kinetic aspects of ^{27}Al reinsertion and the elemental results of Al-reinserted UCB-4, showing that only *ca.* one third of framework ^{11}B species were replaced with ^{27}Al atoms. In addition, the ^{27}Al reinsertion into sites

accessible by internal 10-MR was hypothesized to result from "broken" **MWW**-like cages formed during delamination. Overall, the molecular-level comparisons of ^{11}B and ^{27}Al site distributions in boro- and aluminosilicate SSZ-70 and the proposed synthesis protocol are expected to provide insights into rational design of zeolite catalyst synthesis with controlled heteroatom site distributions.

6.6 References

1. Degnan, T. F. The implications of the fundamentals of shape selectivity for the development of catalysts for the petroleum and petrochemical industries. *J. Catal.* **216,** 32–46 (2003).

2. Martínez, C. & Corma, A. Inorganic molecular sieves: Preparation, modification and industrial application in catalytic processes. *Coord. Chem. Rev.* **255,** 1558–1580 (2011).

3. *Zeolites and Catalysis: Synthesis Reactions and Applications*. (Wiley-VCH, 2010). doi:10.1002/9783527630295

4. Davis, M. E. Ordered porous materials for emerging applications. *Nature* **417,** 813–821 (2002).

5. Corma, A. From Microporous to Mesoporous Molecular Sieve Materials and Their Use in Catalysis. *Chem. Rev.* **97,** 2373–2419 (1997).

6. Gounder, R. & Iglesia, E. The catalytic diversity of zeolites: confinement and solvation effects within voids of molecular dimensions. *Chem. Commun. (Camb).* **49,** 3491–509 (2013).

7. Dědeček, J., Sobalík, Z. & Wichterlová, B. Siting and Distribution of Framework Aluminium Atoms in Silicon-Rich Zeolites and Impact on Catalysis. *Catal. Rev. - Sci. Eng.* **54,** 135–223 (2012).

8. Cundy, C. S. & Cox, P. A. The hydrothermal synthesis of zeolites: history and development from the earliest days to the present time. *Chem. Rev.* **103,** 663–702 (2003).

9. Cundy, C. S. & Cox, P. A. The hydrothermal synthesis of zeolites: Precursors, intermediates and reaction mechanism. *Microporous Mesoporous Mater.* **82,** 1–78 (2005).

10. Barrer, R. M. *Hydrothermal Chemistry of Zeolites*. (Academic Pr, 1982).

11. Moliner, M., Martinez, C. & Corma, A. Synthesis Strategies for Preparing Useful Small Pore Zeolites and Zeotypes for Gas Separations and Catalysis. *Chem. Mater.* **26,** 246–258 (2014).

12. Zones, S. I. & Hwang, S.-J. A novel approach to borosilicate zeolite synthesis in the presence of fluoride. *Microporous Mesoporous Mater.* **146,** 48–56 (2011).

13. Zones, S. I. *et al.* The fluoride-based route to all-silica molecular sieves; a strategy for synthesis of new materials based upon close-packing of guest–host products. *Comptes Rendus Chim.* **8,** 267–282 (2005).

14. Zones, S. I. & Davis, M. E. Zeolite materials: recent discoveries and future prospects. *Curr. Opin. Solid State Mater. Sci.* **1,** 107–117 (1996).

15. Corma, A. & Davis, M. E. Issues in the Synthesis of Crystalline Molecular Sieves: Towards the Crystallization of Low Framework-Density Structures. *ChemPhysChem* **5,** 304–313 (2004).

16. Jiang, J., Yu, J. & Corma, A. Extra-large-pore zeolites: bridging the gap between micro and mesoporous structures. *Angew. Chem. Int. Ed. Engl.* **49,** 3120–45 (2010).

17. Jackowski, A., Zones, S. I., Hwang, S.-J. & Burton, A. W. Diquaternary ammonium compounds in zeolite synthesis: cyclic and polycyclic N-heterocycles connected by methylene chains. *J. Am. Chem. Soc.* **131,** 1092–100 (2009).

18. Burton, A. W. & Zones, S. I. Organic Molecules in Zeolite Synthesis: Their preparaion and Structure-Directing Effects. *Stud. Surf. Sci. Catal.* **168,** 137–179 (2007).

19. Zones, S. I. Translating new materials discoveries in zeolite research to commercial manufacture. *Microporous Mesoporous Mater.* **144,** 1–8 (2011).

20. Burton, A. W., Lee, G. S. & Zones, S. I. Phase selectivity in the syntheses of cage-based zeolite structures: An investigation of thermodynamic interactions between zeolite hosts and structure directing agents by molecular modeling. *Microporous Mesoporous Mater.* **90,** 129–144 (2006).

21. Busca, G. Acid catalysts in industrial hydrocarbon chemistry. *Chem. Rev.* **107,** 5366–5410 (2007).

22. Van Santen, R. A. & Kramer, G. J. Reactivity Theory of Zeolitic Broensted Acidic Sites. *Chem. Rev.* **95,** 637–660 (1995).

23. Xu, B., Bordiga, S., Prins, R. & van Bokhoven, J. a. Effect of framework Si/Al ratio and extra-framework aluminum on the catalytic activity of Y zeolite. *Appl. Catal. A Gen.* **333,** 245–253 (2007).

24. Mikovsky, R. J. & Marshall, J. F. Random aluminum-ion siting in the faujasite lattice. *J. Catal.* **44,** 170–173 (1976).

25. Pine, L. A., Maher, P. J. & Wachter, W. A. Prediction of cracking catalyst behavior by a zeolite unit cell size model. *J. Catal.* **476,** 466–476 (1984).

26. Beagley, B., Dwyer, J., Fitch, F. R., Mann, R. & Walters, J. Aluminum Distribution and Properties of Faujasites. Basis of Models and Zeolite Acidity. *J. Phys. Chem.* **88,** 1744–1751 (1984).

27. Jones, A. J., Carr, R. T., Zones, S. I. & Iglesia, E. Acid strength and solvation in catalysis by MFI zeolites and effects of the identity, concentration and location of framework heteroatoms. *J. Catal.* **312,** 58–68 (2014).

28. Schallmoser, S. *et al.* Impact of the local environment of Brønsted acid sites in ZSM-5 on the catalytic activity in n-pentane cracking. *J. Catal.* **316,** 93–102 (2014).

29. Vjunov, A. *et al.* Quantitatively probing the Al distribution in zeolites. *J. Am. Chem. Soc.* **136,** 8296–8306 (2014).

30. Ogura, M. *et al.* Stabilization of bare divalent Fe(II) cations in Al-rich beta zeolites for superior NO adsorption. *J. Catal.* **315,** 1–5 (2014).

31. Wu, P. A Novel Titanosilicate with MWW Structure: II. Catalytic Properties in the Selective Oxidation of Alkenes. *J. Catal.* **202,** 245–255 (2001).

32. Wu, P. *et al.* Methodology for synthesizing crystalline metallosilicates with expanded pore windows through molecular alkoxysilylation of zeolitic lamellar precursors. *J. Am. Chem. Soc.* **130,** 8178–87 (2008).

33. Taramasso, M., Perego, G. & Notari, B. Preparation of porous crystalline synthetic material comprised of silicon and titanium oxides. (1983).

34. Notari, B. Microporous Crystalline Titanium Silicates. *Adv. Catal.* **41,** 253–334 (1996).

35. Bermejo-Deval, R. *et al.* Metalloenzyme-like catalyzed isomerizations of sugars by Lewis acid zeolites. *Proc. Natl. Acad. Sci. U. S. A.* **109,** 9727–32 (2012).

36. Bermejo-Deval, R., Gounder, R. & Davis, M. E. Framework and Extraframework Tin Sites in Zeolite Beta React Glucose Di ff erently. *ACS Catal.* **2,** 2705–2713 (2012).

37. Luo, H. Y. *et al.* Synthesis and catalytic activity of Sn-MFI Nanosheets for the Baeyer-Villiger oxidation of cyclic ketones Supplementary information 1 Synthesis of materials.

38. Román-Leshkov, Y., Moliner, M., Labinger, J. a & Davis, M. E. Mechanism of glucose isomerization using a solid Lewis acid catalyst in water. *Angew. Chem. Int. Ed. Engl.* **49,** 8954–7 (2010).

39. Román-Leshkov, Y. & Davis, M. E. Activation of Carbonyl-Containing Molecules with Solid Lewis Acids in Aqueous Media. *ACS Catal.* **1,** 1566–1580 (2011).

40. Pacheco, J. J. & Davis, M. E. Synthesis of terephthalic acid via Diels-Alder reactions with ethylene and oxidized variants of 5-hydroxymethylfurfural. *Proc. Natl. Acad. Sci.* **111,** 8363–8367 (2014).

41. Bare, S. R. *et al.* Uniform catalytic site in Sn-beta-zeolite determined using X-ray absorption fine structure. *J. Am. Chem. Soc.* **127,** 12924–32 (2005).

42. Corma, a, Nemeth, L. T., Renz, M. & Valencia, S. Sn-zeolite beta as a heterogeneous chemoselective catalyst for Baeyer-Villiger oxidations. *Nature* **412,** 423–5 (2001).

43. Moliner, M., Rey, F. & Corma, A. Towards the rational design of efficient organic structure-directing agents for zeolite synthesis. *Angew. Chem. Int. Ed. Engl.* **52,** 13880–13889 (2013).

44. Burton, A. *et al.* SSZ-53 and SSZ-59: two novel extra-large pore zeolites. *Chemistry* **9,** 5737–5748 (2003).

45. Burton, A. & Elomari, S. SSZ-60: a new large-pore zeolite related to ZSM-23. *Chem. Commun. (Camb).* 2618–9 (2004). doi:10.1039/b410010g

46. Elomari, S., Burton, A., Medrud, R. C. & Grosse-Kunstleve, R. The synthesis, characterization, and structure solution of SSZ-56: An extreme example of isomer specificity in the structure direction of zeolites. *Microporous Mesoporous Mater.* **118,** 325–333 (2009).

47. Elomari, S., Burton, A. W., Ong, K., Pradhan, A. R. & Chan, I. Y. Synthesis and Structure Solution of Zeolite SSZ-65. *Chem. Mater.* **19,** 5485–5492 (2007).

48. Vortmann, S., Marler, B., Gies, H. & Daniels, P. Synthesis and crystal structure of the new borosilicate zeolite RUB-13. *Microporous Mater.* **4,** 111–121 (1995).

49. Wagner, P. *et al.* Guest/Host Relationships in the Synthesis of the Novel Cage Based Zeolites SSZ-35, SSZ-36, and SSZ-39. *J. Am. Chem. Soc.* **122,** 263–273 (2000).

50. Gábová, V., Dědecek, J. & Cejka, J. Control of Al distribution in ZSM-5 by conditions of zeolite synthesis. *Chem. Commun. (Camb).* 1196–7 (2003). at <http://www.ncbi.nlm.nih.gov/pubmed/12778732>

51. Pinar, A. B., Verel, R., Pérez-Pariente, J. & van Bokhoven, J. a. Direct evidence of the effect of synthesis conditions on aluminum siting in zeolite ferrierite: A 27Al MQ MAS NMR study. *Microporous Mesoporous Mater.* **193,** 111–114 (2014).

52. Márquez-Alvarez, C., Pinar, A. B., García, R., Grande-Casas, M. & Pérez-Pariente, J. Influence of Al Distribution and Defects Concentration of Ferrierite Catalysts Synthesized From Na-Free Gels in the Skeletal Isomerization of n-Butene. *Top. Catal.* **52,** 1281–1291 (2009).

53. Pinar, A. B., Gómez-Hortigüela, L., McCusker, L. B. & Pérez-Pariente, J. Controlling the Aluminum Distribution in the Zeolite Ferrierite via the Organic Structure Directing Agent. *Chem. Mater.* **25,** 3654–3661 (2013).

54. Pinar, A. B., Márquez-Álvarez, C., Grande-Casas, M. & Pérez-Pariente, J. Template-controlled acidity and catalytic activity of ferrierite crystals. *J. Catal.* **263,** 258–265 (2009).

55. Román-Leshkov, Y., Moliner, M. & Davis, M. E. Impact of Controlling the Site Distribution of Al Atoms on Catalytic Properties in Ferrierite-Type Zeolites †. *J. Phys. Chem. C* **115,** 1096–1102 (2011).

56. Xie, D. *et al.* Optimized Synthesis and Structural Characterization of the Borosilicate MCM-70. *J. Phys. Chem. C* **113,** 9845–9850 (2009).

57. Zones, S. I. *et al.* Studies of Aluminum Reinsertion into Borosilicate Zeolites with Intersecting Channels of 10- and 12-Ring Channel Systems. *J. Am. Chem. Soc.* **57,** 1462−1471 (2014).

58. Van Bokhoven, J. A. *et al.* Determining the aluminium occupancy on the active T-sites in zeolites using X-ray standing waves. *Nat. Mater.* **7,** 551–555 (2008).

59. Sklenak, S. *et al.* Aluminium siting in the ZSM-5 framework by combination of high resolution 27Al NMR and DFT/MM calculations. *Phys. Chem. Chem. Phys.* **11,** 1237–47 (2009).

60. Sazama, P. *et al.* Effect of aluminium distribution in the framework of ZSM-5 on hydrocarbon transformation. Cracking of 1-butene. *J. Catal.* **254,** 180–189 (2008).

61. Garaga, M. N. *et al.* Local Environments of Boron Heteroatoms in Non-Crystalline Layered Silicates. *In preparation*

62. Hsieh, M.-F. *et al.* Aluminum Heteroatom Distributions in Surfactant-Directed Aluminosilicates. *In preparation*

63. Chen, C. Y. & Zones, S. I. From Borosilicate to Gallo- and Aluminosilicate Zeolites : New Methods for Lattice Substitution via Post-Synthetic Treatment. *Stud. Surf. Sci. Catal.* **135,** 211 (2001).

64. Zones, S. I., Chen, C. Y., Benin, A. & Hwang, S.-J. Opportunities for selective catalysis within discrete portions of zeolites: The case for SSZ-57LP. *J. Catal.* **308,** 213–225 (2013).

65. Ogino, I. *et al.* Heteroatom-Tolerant Delamination of Layered Zeolite Precursor Materials. *Chem. Mater.* **25,** 1502–1509 (2013).

66. Ouyang, X. *et al.* Single-Step Delamination of a MWW Borosilicate Layered Zeolite Precursor under Mild Conditions without Surfactant and Sonication. *J. Am. Chem. Soc.* **57,** 1449−1461 (2014).

67. Tong, H. T. T. & Koller, H. Control of Al for B framework substitution in zeolite Beta by counterions. *Microporous Mesoporous Mater.* **148,** 80–87 (2012).

68. Senapati, S., Zimdars, J., Ren, J. & Koller, H. Post-synthetic modifications of as-made zeolite frameworks near the structure-directing agents. *J. Mater. Chem. A* **2,** 10470–10484 (2014).

69. http://www.iza-structure.org/databases/.

70. Archer, R. H. *et al.* Physicochemical Properties and Catalytic Behavior of the Molecular Sieve SSZ-70. *Chem. Mater.* **22,** 2563–2572 (2010).

71. Corma, A., Fornes, V., Pergher, S. B., Maesen, T. L. M. & Buglass, J. G. Delaminated zeolite precursors as selective acidic catalysts. *Nature* **396,** 353–356 (1998).

72. Roth, W. J., Nachtigall, P., Morris, R. E. & Cejka, J. Two-Dimensional Zeolites: Current Status and Perspectives. *Chem. Rev.* **114,** 4807–4837 (2014).

73. Roth, W. J., Gil, B. & Marszalek, B. Comprehensive system integrating 3D and 2D zeolite structures with recent new types of layered geometries. *Catal. Today* **227,** 9–14 (2013).

74. Massiot, D. *et al.* Modelling one- and two-dimensional solid-state NMR spectra. *Magn. Reson. Chem.* **40,** 70–76 (2002).

75. Engelhardt, G. & Michel, D. *High-Resolution Solid-State NMR of Silicates and Zeolites*. (Wiley, 1987).

76. Koller, H. & Weiß, M. Solid state NMR of porous materials : zeolites and related materials. *Top. Curr. Chem.* **306,** 189–227 (2012).

77. Du, L.-S. & Stebbins, J. F. Solid-state NMR study of metastable immiscibility in alkali borosilicate glasses. *J. Non. Cryst. Solids* **315,** 239–255 (2003).

78. Hwang, S.-J., Chen, C.-Y. & Zones, S. I. Boron Sites in Borosilicate Zeolites at Various Stages of Hydration Studied by Solid State NMR Spectroscopy. *J. Phys. Chem. B* **108,** 18535–18546 (2004).

79. Koller, H., Fild, C. & Lobo, R. F. Variable anchoring of boron in zeolite beta. *Microporous Mesoporous Mater.* **79,** 215–224 (2005).

80. Fild, C., Shantz, D. F., Lobo, R. F. & Koller, H. Cation-induced transformation of boron-coordination in zeolites. *Phys. Chem. Chem. Phys.* **2,** 3091–3098 (2000).

81. Stavet, M. S. & Nicholas, J. B. DENSITY-FUNCTIONAL STUDIES OF ZEOLITES .2. STRUCTURE AND ACIDITY OF [T]-ZSM-5 MODELS (T=B, AL, GA, AND FE). *J. Phys. Chem.* **99,** 15046–15061 (1995).

82. De Ruiter, R., Kentgens, A. P. M., Grootendorst, J., Jansen, J. C. & van Bekkum, H. Calcination and deboronation of [B]-MFI single crystals. *Zeolites* **13,** 128–138 (1993).

83. Martens, R. & Müller-Warmuth, W. Structural groups and their mixing in borosilicate glasses of various compositions – an NMR study. *J. Non. Cryst. Solids* **265,** 167–175 (2000).

84. Fild, C., Eckert, H. & Koller, H. Charge-Induced Partial Ordering of Boron around Structure Directing Agents in Zeolites Observed by 13C{11B} Rotational Echo Double Resonance NMR. *J. Am. Chem. Soc.* **122,** 12590–12591 (2000).

85. Fild, C., Eckert, H. & Koller, H. Tetrahedral BO 4 Units with Na ‡ and of Trigonal BO 3 Units with H ‡ in Dehydrated Zeolite. *Angew. Chem. Int. Ed. Engl.* **37,** 2505–2507 (1998).

86. Fyfe, C. A., Feng, Y., Grondey, H., Kokotailo, G. T. & Gies, H. One- and Two-Dimensional High-Resolution Solid-State NMR Studies of Zeolite Lattice Structures. *Chem. Rev.* **91,** 1525–1543 (1991).

87. Ouyang, X. *et al.* Novel surfactant-free route to delaminated all-silica and titanosilicate zeolites derived from a layered borosilicate MWW precursor. *Dalton Trans.* **43,** 10417–10429 (2014).

88. Chen, C.-Y. & Zones, S. I. Method for heteroatom lattice substitution in large and extra-large pore borosilicate zeolites. (2002).

89. Runnebaum, R. C. *et al.* Role of Delamination in Zeolite-Catalyzed Aromatic Alkylation: UCB - 3 versus 3 - D Al-SSZ-70. *ACS Catal.* **4,** 2364–2368 (2014).

Chapter 7: Conclusions

My Ph.D. research focuses on characterizing, understanding, and controlling heteroatom site distributions in zeolite and layered boro- and alumino-silicate frameworks. Motivation for this study was driven by the significant influences that heteroatoms and their distributions have on adsorption and catalytic properties of zeolite catalysts. Despite the strong dependence of these catalytically relevant properties on heteroatom distributions, an understanding of these site distributions in zeolite frameworks has remained largely elusive, because the complicated order and disorder in proximity to heteroatom sites make such systems very difficult to characterize by conventional methods alone. By comparison, solid-state NMR spectroscopy is highly sensitive to the local environments of NMR-active nuclei and therefore can provide detailed information related to heteroatom sites, their local environments, and distributions. Specifically, 1D NMR methods are capable of identifying various heteroatom species and quantifying their relative populations. Furthermore, 2D NMR techniques enable determination of site proximities and connectivities to nuclei of interest, based on through-space dipolar and through-bond *J*-coupled interactions, respectively. In particular, 2D *J*-mediated NMR methods are powerful *keys* for understanding heteroatom site distributions in zeolites, because they can establish distinct covalently bonded sites.

Consequently, we hypothesized that through-bond *J*-couplings between ^{11}B/^{27}Al and ^{29}Si species (*i.e.*, $^{2}J(^{11}B\text{-}O\text{-}^{29}Si)$ and $^{2}J(^{27}Al\text{-}O\text{-}^{29}Si)$ couplings), in conjunction with zeolite crystallography, can unambiguously determine the positions of ^{11}B and ^{27}Al heteroatoms in boro- and alumino-silicate frameworks. We investigated both $C_{16}H_{33}N^{+}Me_3$- and $C_{16}H_{33}N^{+}Me_2Et$-directed layered frameworks which are known to possess two and five

distinct ^{29}Si sites, respectively, and therefore provide relatively simple platforms for investigating ^{11}B and ^{27}Al incorporation. Newly modified 2D NMR methods, designed for probing $^{2}J(^{11}\text{B-O-}^{29}\text{Si})$ and $^{2}J(^{27}\text{Al-O-}^{29}\text{Si})$ couplings, were applied to two types of surfactant-directed layered boro- and aluminosilicates to establish ^{11}B and ^{27}Al site distributions. Interestingly, ^{11}B heteroatoms were non-selectively distributed among two ^{29}Si sites in the $C_{16}H_{33}N^{+}Me_3$-directed borosilicates, creating newly cross-linked ^{29}Si sites in the next-nearest-neighbor ^{11}B atoms, whereas ^{11}B species were exclusively inserted into specific ^{29}Si sites in the $C_{16}H_{33}N^{+}Me_2Et$-directed borosilicates without substantially altering the framework structures. To our knowledge, these are the first accounts in which ^{11}B heteroatom site distributions are established in borosilicate frameworks. In contrast, ^{27}Al atoms non-selectively distribute in the $C_{16}H_{33}N^{+}Me_3$- and $C_{16}H_{33}N^{+}Me_2Et$-directed aluminosilicates, suggesting that ^{11}B and ^{27}Al species participate differently in the formation of boro- and aluminosilicates, respectively. More importantly, these molecular-level insights into ^{11}B site distributions in borosilicates enable investigations into controlling heteroatom distributions in zeolite frameworks.

On the basis of ^{11}B and ^{27}Al siting gained from surfactant-directed boro- and alumino-silicate materials, we aim to generalize the modified 2D NMR methods to establish heteroatom siting in zeolites, with a particular focus on SSZ-70 as an example. This zeolite was chosen for study not only due to its structural features, which alleviate mass transport limitations of zeolite catalysts, but also because of its broad usage in production of benzene derivatives. SSZ-70 possesses an unusual zeolite structure composed of MWW-like cages with disordered silicate units between these cages, as evidenced by the 2D *J*-mediated (through-bond) solid-state NMR, X-ray diffraction, and electron microscopy results. Such

crystallographic information provides a fundamental basis to determine ^{11}B and ^{27}Al siting in B- and Al-SSZ-70, respectively. For these systems, ^{11}B atoms preferentially incorporate into specific crystallographic sites accessible by internal 10-MR and external 12-MR of MWW-like cages in B-SSZ-70, whereas ^{27}Al atoms appear to be distributed among nearly all types of sites in Al-SSZ-70. Interestingly, these results are consistent with the previous observations of surfactant-directed boro and alumino-silicates.

Presence of ^{11}B or ^{27}Al atoms in zeolite frameworks is known for imparting hydrophilic properties to zeolite catalysts. In this regard, we were interested in investigating how the hydrophobicity of organic structure-directing agent (SDA) molecules influences ^{11}B site distributions in B-SSZ-70. While SDA hydrophobicity has little influence on ^{11}B site distributions, which are very similar (*i.e.*, ^{11}B sites accessible by internal 10-MR and external 12-MR) to that observed in B-SSZ-70, the ^{11}B loadings are strongly affected. That is, SDA molecules with enhanced hydrophilicity will increase ^{11}B contents in B-SSZ-70. Interestingly, ^{11}B loadings are closely correlated with the amount of incompletely cross-linked ^{29}Si sites (Q^3 ^{29}Si), consistent with our observations of the $C_{16}H_{33}N^+Me_2Et$-directed borosilicates where ^{11}B atoms inserted into Q^3 ^{29}Si sites.

Based on the understanding of ^{11}B site distributions in B-SSZ-70, we developed a synthesis protocol that allows control of heteroatom siting in high silica zeolites by using delaminated B-SSZ-70 as a case study. This zeolite was chosen, because it can be delaminated to expose additional external surface area for reactions involving bulky molecules. The ^{11}B siting in B-SSZ-70 was monitored *ex-situ* at different synthesis stages during delamination via 2D NMR methods, and framework ^{11}B sites are shown to be intact, where ^{11}B atoms incorporate into specific crystallographic sites accessible by internal 10-

MR and external 12-MR in B-SSZ-70. This information allows locations of reinserted ^{27}Al heteroatoms to be predicted, because hydrated ^{27}Al ions would be kinetically hindered by 10-MR windows during reinsertion. Notably, the reinserted ^{27}Al species are shown to be located at external (surface) sites in aluminum-reinserted delaminated SSZ-70. Such a distribution is significantly different from the ^{27}Al site distributions in as-synthesized Al-SSZ-70 (*i.e.*, ^{27}Al being internally and externally located). The particular example demonstrates that our synthesis protocol enables the systematic alternation of heteroatom site distributions in high silica zeolite catalysts. In conclusion, the molecular insights about heteroatom site distributions of these materials presented in my Ph.D. dissertation are interesting and useful for the zeolite community, which has sought to prepare zeolite catalysts with controlled heteroatom site distributions.

Appendix A

Local Environments of Boron Heteroatoms in Non-Crystalline Layered Silicates

Table A1. Description of pseudopotentials used for planewave-based DFT calculations. [Courtesy: Dr. Sylvian Cadars and Dr. Zalfa Nour]

Atom	Core-states	Local channel	r_{loc} (a.u.)	r_{nonloc} (a.u.)	r_{aug} (a.u.)	Pseudopotential projectors	PAW projectors
H		p	0.8	0.8	0.6	2x2s	2x2s
B	1s	d	1.4	1.4	1.0	2x2s, 2x2p	2x2s, 2x2p
C	1s	d	1.4	1.4	1.0	2x2s, 2x2p	2x2s, 2x2p
N	1s	d	1.5	1.5	1.0	2x2s, 2x2p	2x2s, 2x2p
O	1s	d	1.3	1.3	0.9	2x2s, 2x2p	2x2s, 2x2p
Si	1s, 2s, 2p	d	1.8	1.8	1.3	2x3s, 2x3p	2x3s, 2x3p, 2x3d
Pseudopotentials used for calculations on reference crystalline systems (see below)							
Li		p	1.2	1.2	0.8	1x1s, 2x2s	1x1s, 2x2s
Na	1s	d	1.3	1.3	1.0	1x2s, 2x2p, 1x3s	1x2s, 2x2p, 1x3s
Mg	1s, 2s	d	1.6	2.0	1.4	2x3s,1x2p, 2x3p	2x3s, 1x2p, 2x3p, 2x3d
Al	1s, 2s,2p	d	2.0	2.0	1.4	2x3s, 2x3p	2x3s, 2x3p, 2x3d
P	1s, 2s, 2p	d	1.8	1.8	1.3	2x3s, 2x3p	2x3s, 2x3p,2x3d
Ca	1s	f	1.6	2.0	1.4	1x3s, 2x3p, 1x4s	1x3s, 2x3p, 1x4s

where r_{loc} is the pseudisation radius for the local component of the pseudopotential, r_{nonloc} is the pseudisation radius for the non-local components of the pseudopotential, and r_{aug} is the pseudisation radius for the charge augmentation functions.

The corresponding Materials Studio castep on-the-fly strings used to generate these potentials are:

```
H 1|0.8|3.675|7.35|11.025|10UU(qc=6.4)[]
Li 1|1.2|11|13.2|15|10U:20UU(qc=5.5)[]
B 2|1.4|9.187|11.025|13.965|20UU:21UU(qc=5.5)[]
C  2|1.4|9.187|11.025|12.862|20UU:21UU(qc=6)[]
N  2|1.5|11.025|12.862|14.7|20UU:21UU(qc=6)[]
O 2|1.3|16.537|18.375|20.212|20UU:21UU(qc=7.5)[]
Na 2|1.3|1.3|1|11.8|13.6|15.3|20U=-2.07:30U=-0.105:21U=-1.06U=+0.25[]
Mg 2|1.6|2|1.4|6|7|8|30NH:21U:31UU:32LGG(qc=4.5)[]
Al 2|2|3.675|5.512|7.717|30UU:31UU:32LGG[]
Si 2|1.8|3.675|5.512|7.35|30UU:31UU:32LGG[]
P 2|1.8|3.675|5.512|6.982|30UU:31UU:32LGG[]
Ca 3|1.6|2.0|1.4|7|9|10|30U:40U:31:32U=+0@+0.12U=+1.0@+0.12
```

The pseudopotential of Ca used the correction described by Profeta *et al.*[3]

Table A2. Calculated shielding (σ_{iso}) and experimental chemical shifts (δ_{iso}) of reference systems of known crystal structure. [Courtesy: Dr. Sylvian Cadars and Dr. Zalfa Nour]

Nucleus	Compound, formula	Site #	Experimental shift (ppm)	Reference	Calculated shielding (ppm)
^{29}Si	α-quartz SiO_2	1	-107.4	[4]	429.6
	Cristoballite SiO_2	1	-108.5	[4]	430.9
	albite $NaAlSi_3O_8$	3	-105	[5]	428.0
		2	-97		419.0
		1	-93		414.4
	datolite $CaBSiO_4(OH)$	1	-83	[4]	404.4
	danburite $CaB_2Si_2O_8$	1	-89	[4]	410.1
	Pyrophyllite $Si_4Al_2O_{10}(OH)_2$	1	-94	[5]	416.7
	Talc $Si_4Mg_3O_{10}(OH)_2$	1	-97	[5]	420.0
	Na_2SiO_3	1	-76.8	[4]	396.9
	α-$Na_2Si_2O_5$	1	-93.6	[6]	416.5
	β-$Na_2Si_2O_5$	1	-85.6	[6]	406.5
		2	-87.5		408.0
	δ-$Na_2Si_2O_5$	1	-90.6	[7]	411.7
		2	-90.2		411.2
^{11}B	Reedmegnerite $NaBSi_3O_8$	1	-1.9	[5]	96.31
	Datolite $CaBSiO_4(OH)$	1	1.0	[5]	93.38
	Danburite $CaB_2Si_2O_8$	1	0.7	[5]	95.45
	BN cubic	1	1.6	[5]	94.80
	BN hexagonal	1	30.4	[5]	66.40
	diomignite $Li_2B_2O_7$	1	17.9	[5]	76.22
	dilithium tetraborate	2	1.7		92.04
	BPO_4	1	-3.3	[5]	98.23
	Sassolite $B(OH)_3$	1	18.8	[5]	74.70

Calculations of shieldings for crystalline model systems of known structure and experimental shifts are used to accurately calculate the isotropic ^{29}Si and ^{11}B chemical shifts (δ_{iso}) from calculated ^{29}Si and ^{11}B shieldings (σ_{iso}). This procedure compensates for possible systematic errors of the DFT calculations. All calculations were conducted on structures previously optimized with fixed unit cell parameters. The series of compounds listed in Table A2 led to the following relationships: $\delta_{iso}(ppm) = -0.920*\sigma_{iso} + 288.45$ for ^{29}Si ; and $\delta_{iso}(ppm) = -1.0*\sigma_{iso} + 95.3$ for ^{11}B.

Table A3. Estimated perturbation range of framework ^{11}B species on ^{29}Si environments [Courtesy: Dr. Sylvian Cadars and Dr. Zalfa Nour]

Materials	Si/B	Perturbation range (Å)	Number of ^{29}Si neighbors affected [a]	% of ^{29}Si signal affected [b]
$C_{16}H_{33}\mathbf{Me}_3N^+$-directed layered borosilicates	140	4	3.5	2.5
		5	10	7
		6	13.5	10
		7	16.5	12
		8	28	20
$C_{16}H_{33}\mathbf{Me_2Et}N^+$-directed layered borosilicates	70	4	3.9	8
		5	9.3	18
		6	14.2	27
		7	18.7	36
		8	29.3	56

[a] The number of ^{29}Si sites affected by their nearby ^{11}B atoms was calculated as follows. For a given model of either $C_{16}H_{33}\mathbf{Me_3}N^+$- or $C_{16}H_{33}\mathbf{Me_2Et}N^+$-directed silicates adapted from previous references[1,2], one ^{29}Si site was manually replaced by a ^{11}B atom, and the number of ^{29}Si atoms within the chosen perturbation range was calculated. This procedure was repeated for ^{11}B substituting each type of distinct ^{29}Si sites in $C_{16}H_{33}\mathbf{Me_3}N^+$- and $C_{16}H_{33}\mathbf{Me_2Et}N^+$-directed silicates that have two and five distinct ^{29}Si sites, respectively. In the case of the $C_{16}H_{33}\mathbf{Me_2Et}N^+$-directed silicates, three indistinguishable candidate structures were all considered. The values shown in the table are the average number of ^{29}Si sites counted in all cases.

[b] The fraction of influenced ^{29}Si signals were calculated as the number of affected ^{29}Si sites based on the Si/B ratios.

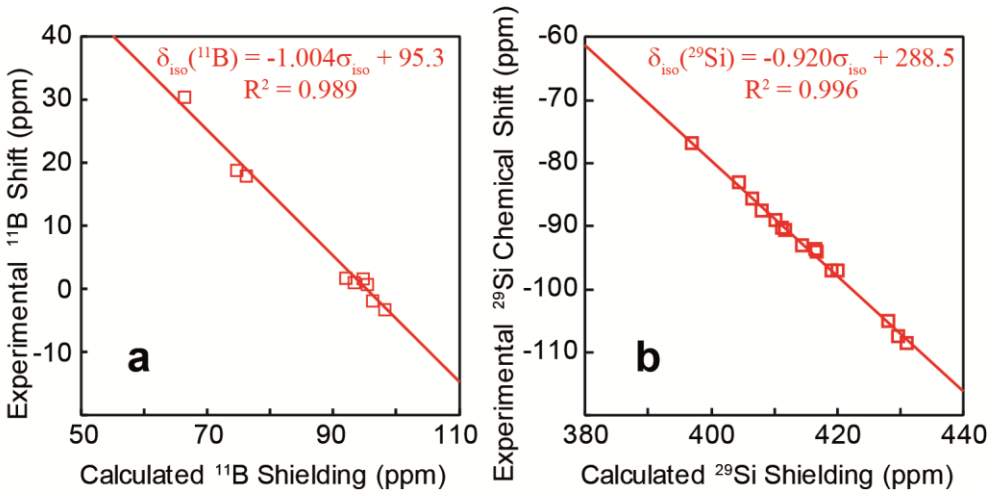

Figure A1. Correlation plots between experimental isotropic chemical shifts and isotropic shielding calculated by DFT for a series of reference crystals with known structures summarized in Table A3. The figures (a) and (b) correspond to ^{11}B and ^{29}Si NMR data, respectively. [Courtesy: Dr. Sylvian Cadars and Dr. Zalfa Nour]

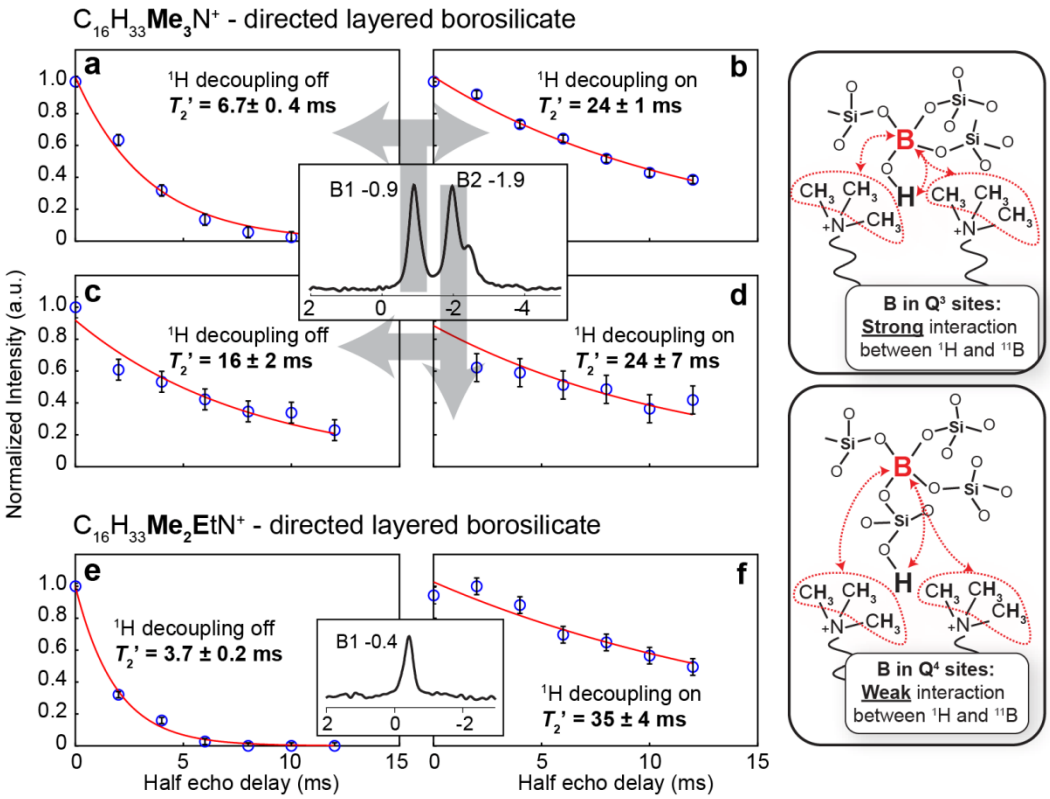

Figure A2. Transverse ^{11}B dephasing time (T_2') measurements conducted on (a-d) $C_{16}H_{33}Me_3N^+$- and (e, f) $C_{16}H_{33}Me_2EtN^+$- directed layered borosilicates (a, c, e) without and (b, d, f) with heteronuclear ^1H-^{11}B decoupling during the ^{11}B signal acquisition to make distinction between Q^3 and Q^4 ^{11}B environments. The ^{11}B signals associated with Q^3 ^{11}B sites dephase much more rapidly without heteronuclear ^1H decoupling than the ones with heteronuclear ^1H decoupling, due to their closer proximity of ^1H moieties. By comparison, Q^4 ^{11}B sites are not substantially affected, because their dipolar couplings to the protons are relatively weak. [Courtesy: Dr. Mounesha Garaga]

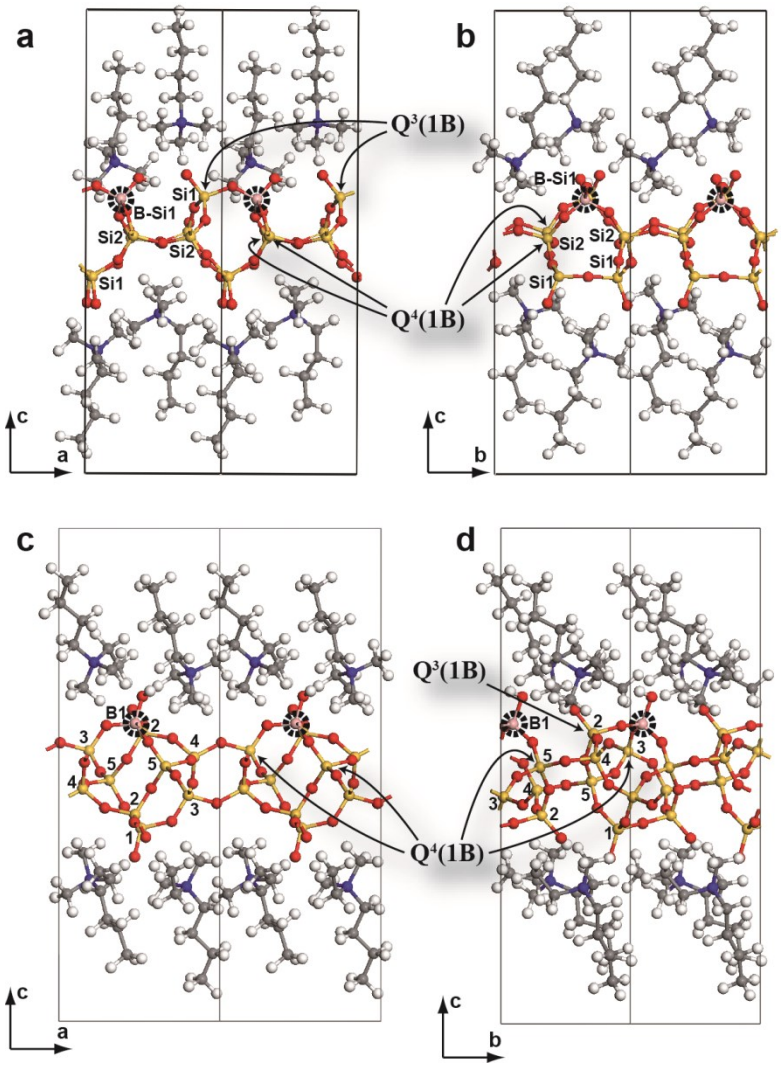

Figure A3. Examples of structural models of $C_4H_9\mathbf{Me_3}N^+$- and $C_4H_9\mathbf{Me_2Et}N^+$-directed layered borosilicates, optimized using planewave-based DFT calculation. Specifically, in the case of (a, b) $C_4H_9\mathbf{Me_3}N^+$-directed borosilicates, one ^{11}B atom was manually inserted into one Q^3 ^{29}Si site out of 8 T-sites per unit cell. Similarly, in the case of (c, d) $C_4H_9\mathbf{Me_2Et}N^+$-directed borosilicates, one ^{11}B atom was manually inserted into one ^{29}Si site 1 (Q^3 ^{29}Si) out of 10 T-sites per unit cell, where each type of ^{29}Si site is given a number from 1 to 5. The negative charge nearby the ^{11}B atom is balanced by a ^1H that was directly added onto the Q^3 ^{11}B site in these models. The black lines delimit the unit cell in each case. [Courtesy: Dr. Sylvian Cadars and Dr. Zalfa Nour]

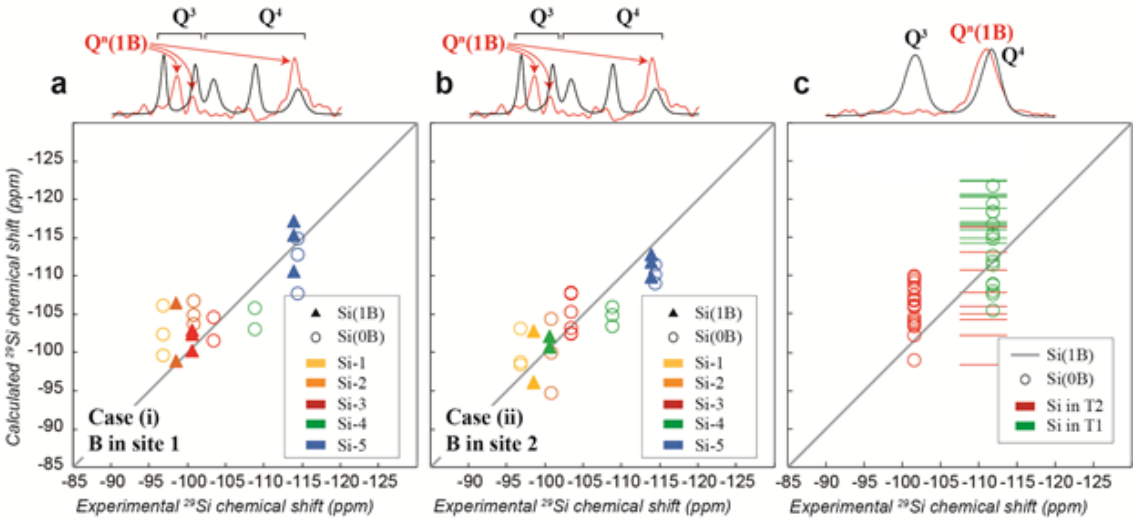

Figure A4. Comparisons of experimental ^{29}Si chemical shifts and isotropic chemical shifts calculated by DFT for all the models of (a, b) C_4H_9**Me$_2$Et**N^+- and (c) C_4H_9**Me$_3$**N^+-directed borosilicates. The corresponding 1D ^{29}Si{^{1}H} CP-MAS spectra (in black) and the 1D ^{29}Si projections extracted from 2D *J*-mediated ^{11}B{^{29}Si} NMR spectra (in red) are shown along with the top horizontal axis, the latter of which reveal Q^n(1B) ^{29}Si environments. The symbol (○) in plots (a), (b), and (c) corresponds to ^{29}Si atoms that are not connected to a ^{11}B atom, whose experimental ^{29}Si chemical shifts are expected to contribute to a majority of ^{29}Si signals and to be identical to the ones of siliceous counterparts. Plots (a) and (b) correspond to two distinct situations of ^{11}B incorporation into C_4H_9**Me$_2$Et**N^+-directed borosilicates, where ^{11}B atoms are inserted into either (a) crystallographic ^{29}Si site 1 or (b) ^{29}Si site 2. The resulting calculated ^{29}Si shifts associated with Q^n (1B) ^{29}Si species are shown using the symbol (▲). In the case of C_4H_9**Me$_3$**N^+-directed borosilicates, calculated ^{29}Si shifts corresponding to Q^n (1B) ^{29}Si sites are displayed as horizontal lines in plot (c). Models studied here are based on the three candidate structures of the $C_{16}H_{33}$**Me$_2$Et**N^+-directed layered silicates and the reported framework structure of octosilicate RUB-18 for the $C_{16}H_{33}$**Me$_3$**N^+-directed layered silicates. In all cases, all possible situations of ^{11}B incorporation as well as different mechanisms for the charge compensation of negative charges nearby ^{11}B atoms were considered. Different charge compensation mechanisms used in the calculation include the addition of surfactant molecules with shorted alkyl chains (*e.g.*, C_4H_9**Me$_3$**N^+) than real surfactants (*e.g.*, $C_{16}H_{33}$**Me$_3$**N^+) in the interlayer space or the addition of a ^{1}H atom on the non-bridging oxygen of the ^{11}B (for ^{11}B in Q^3) or one of the connected Q^3 Si atoms (for ^{11}B in Q^4). Note that the strategy concerning surfactants is only available in the case of C_4H_9**Me$_3$**N^+-directed borosilicates, because the headgroup sizes of C_4H_9**Me$_2$Et**N^+-directed borosilicates cannot fit in the interlayer space of C_4H_9**Me$_2$Et**N^+-directed borosilicates. [Courtesy: Dr. Sylvian Cadars and Dr. Zalfa Nour]

Table A4. Summary for calculated ^{11}B chemical shift values using DFT performed on the structural models of C_4H_9**Me$_2$Et**N^+-directed borosilicates. [Courtesy: Dr. Sylvian Cadars and Dr. Zalfa Nour]

Material model	^{29}Si site replaced by ^{11}B atoms	Range of calculated isotropic ^{11}B chemical shifts (ppm) [a]	Experimental ^{11}B shift (ppm) [b]
C_4H_9**Me$_2$Et** N^+ - layered borosilicate	Si1(Q^3)	-1.1 to -0.8	-0.4
	Si2(Q^3)	-1.3 to 0.4	
	Si3(Q^4)	-1.9 to -1.6	
	Si4(Q^4)	-3.5 to -2.1	
	Si5(Q^4)	-3.9 to -2.2	

[a] The values listed here include the results obtained using the models built from different reference silicate structures (candidate structures no. 2, 3, or 4 in ref.[2]) or using different mechanisms for the charge-compensation of the ^{11}B atom and non-bridging O atoms (H^+ to form as BOH or SiOH moieties or C_4H_9**Me$_2$Et**N^+ surfactant-mimicking molecule).

[b] Position of ^{11}B signal at 17.6 T. This value should be close to the actual chemical shift value because the quadrupolar interaction, and thus the corresponding contribution to the isotropic shift of these $^{11}B^{(IV)}$ is particularly small (< 1 MHz, as predicted from DFT calculations).

Table A5. ^{11}B chemical shift values calculated with DFT for the model structures of the $C_{16}H_{33}Me_3N^+$-layered borosilicate material with $C_4H_9Me_3N^+$ surfactant-mimicking molecules. [Courtesy: Dr. Sylvian Cadars and Dr. Zalfa Nour]

Model composition and charge	B/Si substitution site	New framework connectivity	BOH/SiOH groups	Supercell size	Calculated $\delta_{iso}(^{11}B)$ (ppm)	Experimental ^{11}B shift (ppm)[a]
$(BSi_7O_{18})^{5-} \cdot 5(C_4H_9Me_3N^+)$	Si1(Q^3) as BO^-	None		1x1x1	-0.7	-0.9
$(BSi_{15}O_{36})^{9-} \cdot 9(C_4H_9Me_3N^+)$	Si1(Q^3) as BO^-	None		1x2x1	-0.1	-0.9
$(BSi_7O_{18}H)^{4-} \cdot 4(C_4H_9Me_3N^+)$	Si1(Q^3) as BOH	None	1 BOH	1x1x1	-0.6	-0.9
$(BSi_{15}O_{36}H_8)^- \cdot (C_4H_9Me_3N^+)$	Si1(Q^3) as BOH	None	1 BOH / 7 SiOH	1x2x1	-1.2	-0.9
$(BSi_7O_{18})^{5-} \cdot 5(C_4H_9Me_3N^+)$	Si2(Q^4)	None		1x1x1	-1.9	-2.5
$(BSi_{15}O_{36})^{9-} \cdot 9(C_4H_9Me_3N^+)$	Si2(Q^4)	None		1x2x1	-1.7	-2.5
$(BSi_7O_{18}H)^{4-} \cdot 4(C_4H_9Me_3N^+)$	Si2(Q^4)	None	1 SiOH	1x1x1	-2.7	-2.5
$(BSi_{15}O_{36}H_8)^- \cdot (C_4H_9Me_3N^+)$	Si2(Q^4)	None		1x2x1	-2.4	-2.5
Models with additional Si-O-Si connectivities						
$(BSi_{23}O_{53}H)^{10-} \cdot 0(C_4H_9Me_3N^+)$	Si1(Q^3)	1 Si-O-Si	1 BOH	1x3x1	0.1	-0.9
$(BSi_{31}O_{53}H_{10})^- \cdot (C_4H_9Me_3N^+)$	Si1(Q^3)	1 Si-O-Si	1 BOH / 9 SiOH	2x2x1	-0.4	-0.9
$(BSi_{47}O_{107}H_{22})^- \cdot (C_4H_9Me_3N^+)$	Si1(Q^3)	1 Si-O-Si	1 BOH / 21 SiOH	2x3x1	0.1	-0.9
$(BSi_{31}O_{71}H)^{14-} \cdot 14(C_4H_9Me_3N^+)$	Si2(Q^4)	1 Si-O-Si	1 SiOH	2x2x1	-2.3, -3.3 [b]	-2.5
$(BSi_{31}O_{71})^{15-} \cdot 15(C_4H_9Me_3N^+)$	Si2(Q^4)	1 Si-O-Si		2x2x1	-2.2, -3.6 [b]	-2.5
$(BSi_{31}O_{70})^{13-} \cdot 13(C_4H_9Me_3N^+)$	Si2(Q^4)	2 Si-O-Si		2x2x1	-4.0	-1.9
$(BSi_{31}O_{70}H_{12})^- \cdot (C_4H_9Me_3N^+)$	Si2(Q^4)	2 Si-O-Si	12 SiOH	2x2x1	-3.4	-1.9

[a] The ^{11}B experimental shift corresponds to the position of the experimental peak that gives the best match between all available experimental and calculation constraints.

[b] depending on the position of the additional ^{29}Si-O-^{29}Si connectivity.

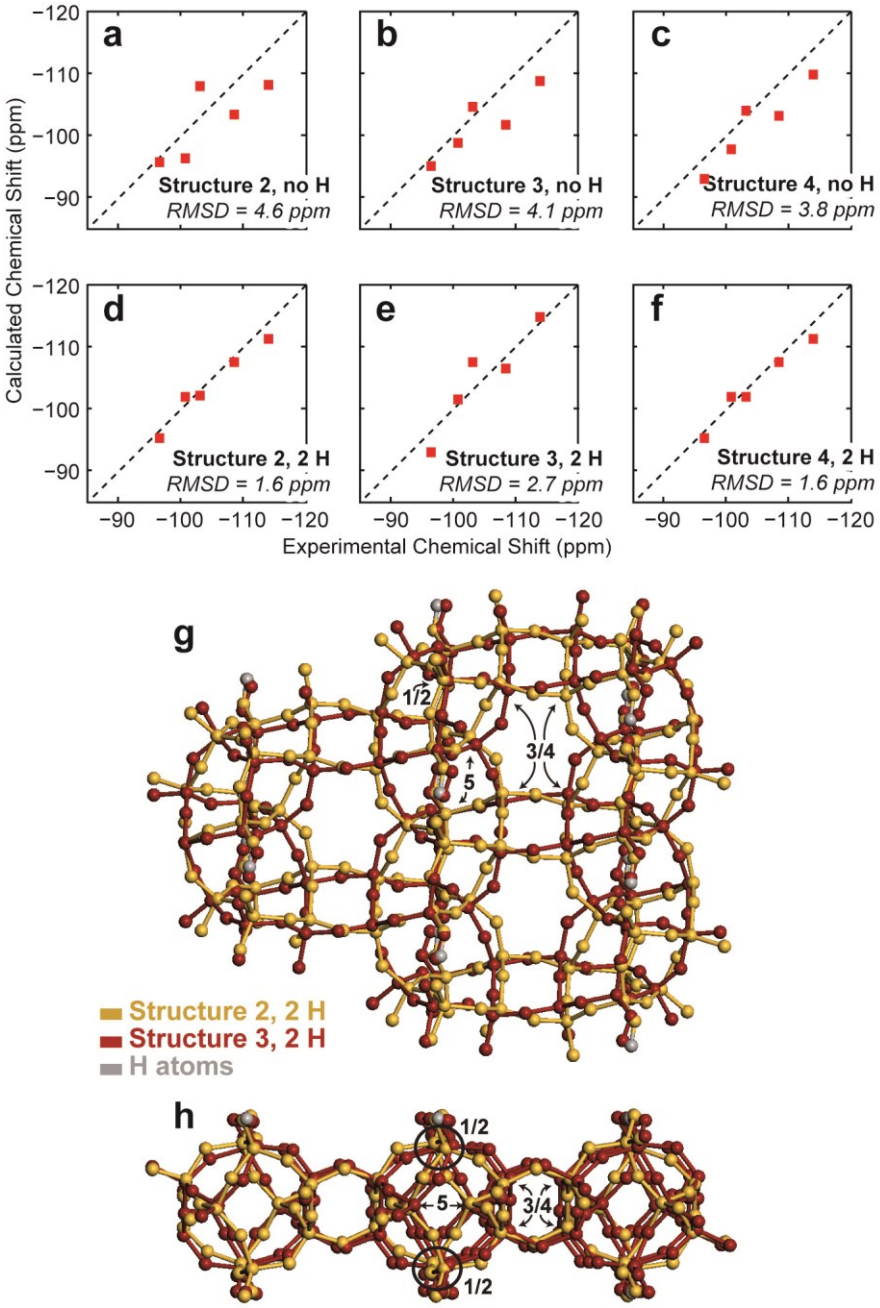

Figure A5. (a-f) Comparisons between experimental and calculated chemical shifts for candidate model structures of the $C_{16}H_{33}$**Me$_2$Et**N^+-directed (pure-)silicate reference material. All structures optimized of the original structures labeled 2, and 4 reported in ref.[22], with (a-c) no or (d-f) only 2 protons compensating the negative charges associated with non-bridging O atoms per supercell (consisting of 10 Si atoms and 22 O atoms), as compared to 4 H atoms the original structures. Other charges are compensated by positive charges homogeneously distributed across the entire supercell. Best agreement between calculated and experimental ^{29}Si chemical shifts are obtained for the structures with 2 H per cell, which are superimposed and viewed from the top and from the side of the layer in (g) and (h).

Structure 4 turns out to be identical to structure 2 when optimized under such conditions, and is consequently not shown. [Courtesy: Dr. Sylvian Cadars]

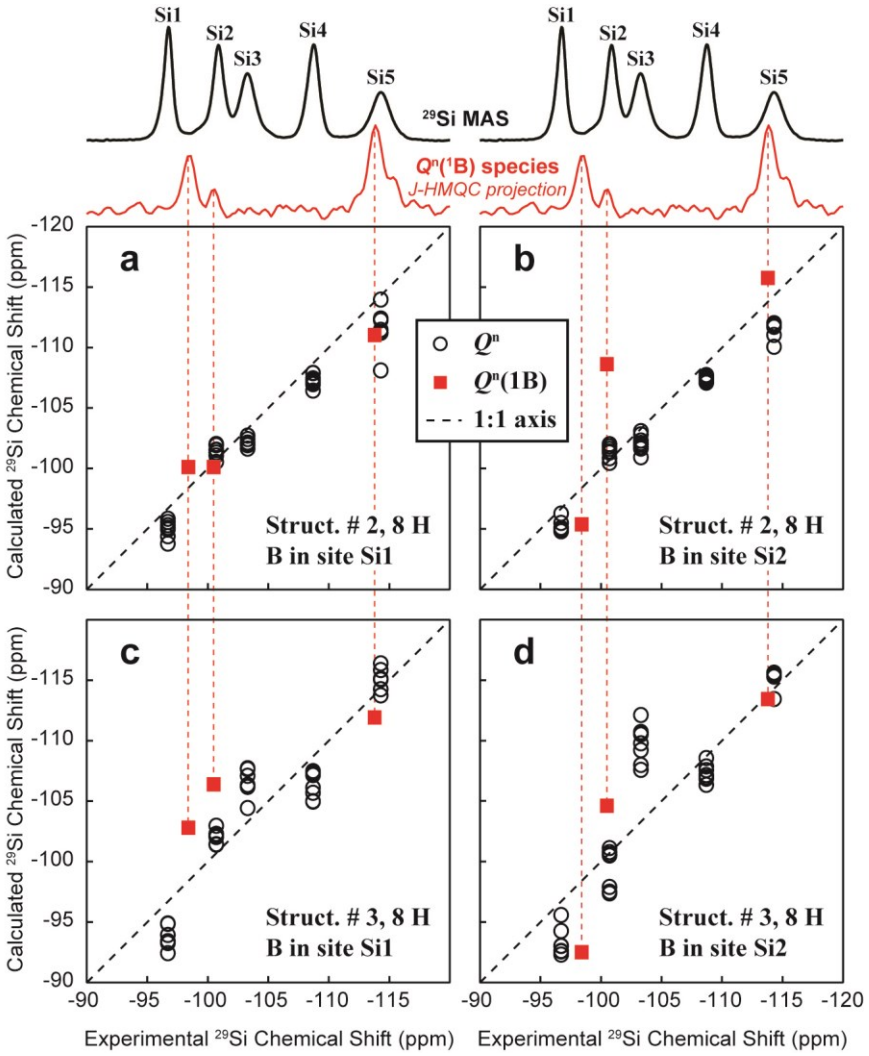

Figure A6. Comparisons are shown between experimental and calculated ^{29}Si chemical shifts for 4 distinct DFT-optimized models of the $C_{16}H_{33}$**Me$_2$Et**N^+-directed borosilicate material. All structures were obtained from pure-silicate structures # 2 and 3 above (Figure A4), by considering a 2x2x1 supercell and replacing one Q^3 ^{29}Si atom (site Si1 or Si2) by a ^{11}B atom. Surfactants are omitted in these models and simply replaced by positive charges homogeneously distributed across the entire supercell. Black circles and red squares correspond to the ^{29}Si chemical shifts of Q^n and Q^n(1B) ^{29}Si sites, respectively. Experimental ^{29}Si chemical shift values for Q^n(1B) ^{29}Si sites are obtained from the projection of the *J*-mediated ^{11}B-^{29}Si correlation NMR spectrum (shown in red above the plots), which selectively reveals ^{29}Si sites connected (via a bridging O atom) to a ^{11}B atom. The positions of the red squares are derived from the assignment giving the best agreement between experimental and calculated ^{29}Si chemical shifts for these sites. The model that is most representative of experimental NMR data is the one corresponding to the plot in (a), also shown in Figure 3a in the main text, with a ^{11}B atom substituting a ^{29}Si atom at site Si1 in model structure no. 2. [Courtesy: Dr. Sylvian Cadars]

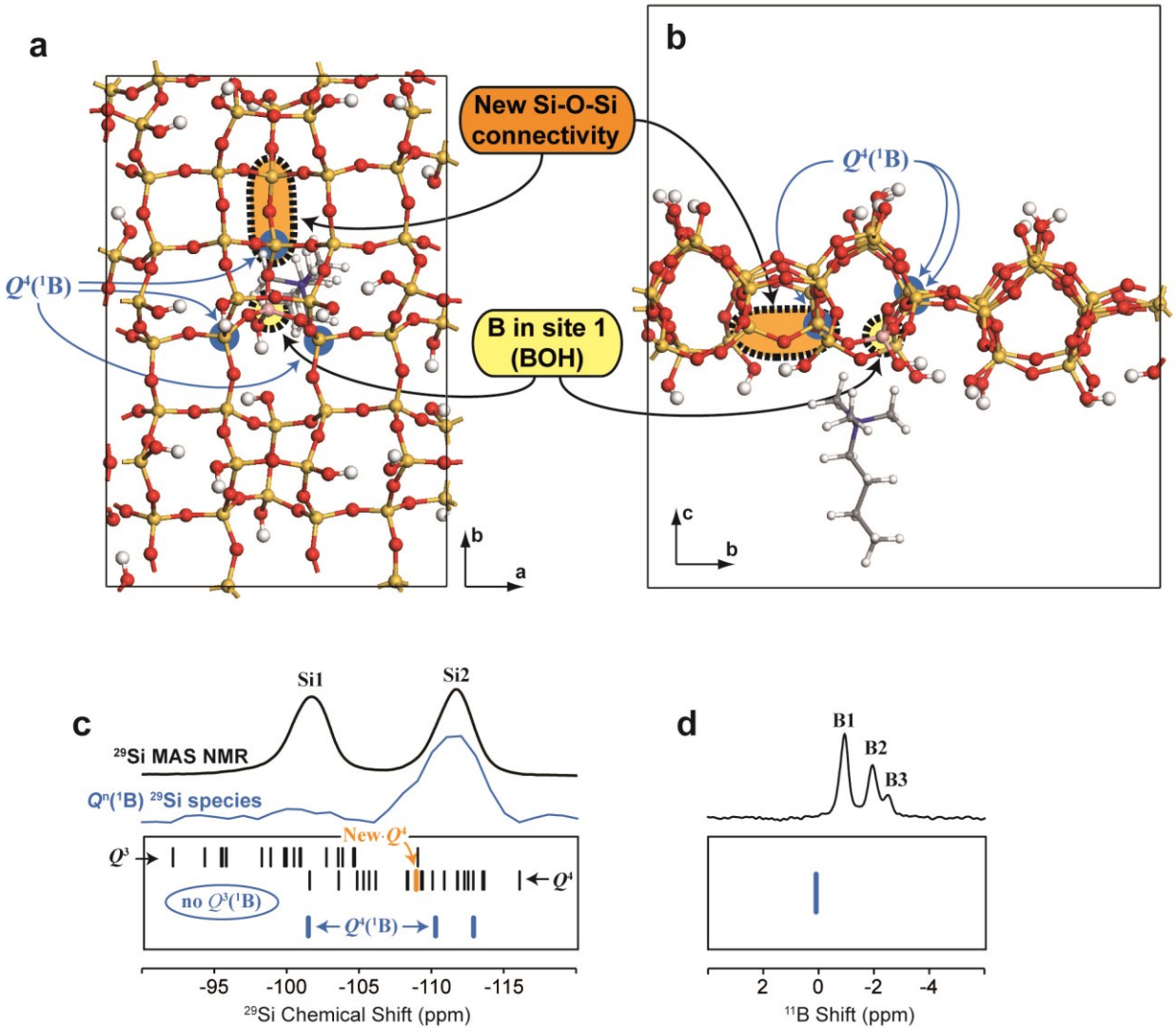

Figure A7. (a) Top and (b) side-views of a DFT-optimized model structure of the $C_{16}H_{33}\mathbf{Me_3}N^+$-directed borosilicate material constructed with a 2x3x1 supercell and one ^{11}B atom in substitution of Q^3 ^{29}Si site Si1, with one additional ^{29}Si-O-^{29}Si connectivity created between two adjacent (originally) Q^3 ^{29}Si sites. All surfactant molecules but one were omitted in this model and replaced by one H^+ added to each non-bridging O atom to form 21 SiOH groups and one BOH group. The remaining negative charge (associated with the B/Si substitution) was compensated by adding a single surfactant-mimicking $C_4H_9\mathbf{Me_3}N^+$ molecule. This led to the following composition: $(BSi_{47}O_{107}H_{22})^- \cdot (C_4H_9\mathbf{Me_3}N^+)$. (c) Comparisons of experimental (c) ^{29}Si and (d) ^{11}B NMR spectra (in black) with isotropic chemical shifts calculated for different types of Si atoms and for the B atom in the model shown in (a) and (b). The spectrum shown in blue in (c) selectively displays the contributions from Q^n(1B) ^{29}Si environments. [Courtesy: Dr. Sylvian Cadars]

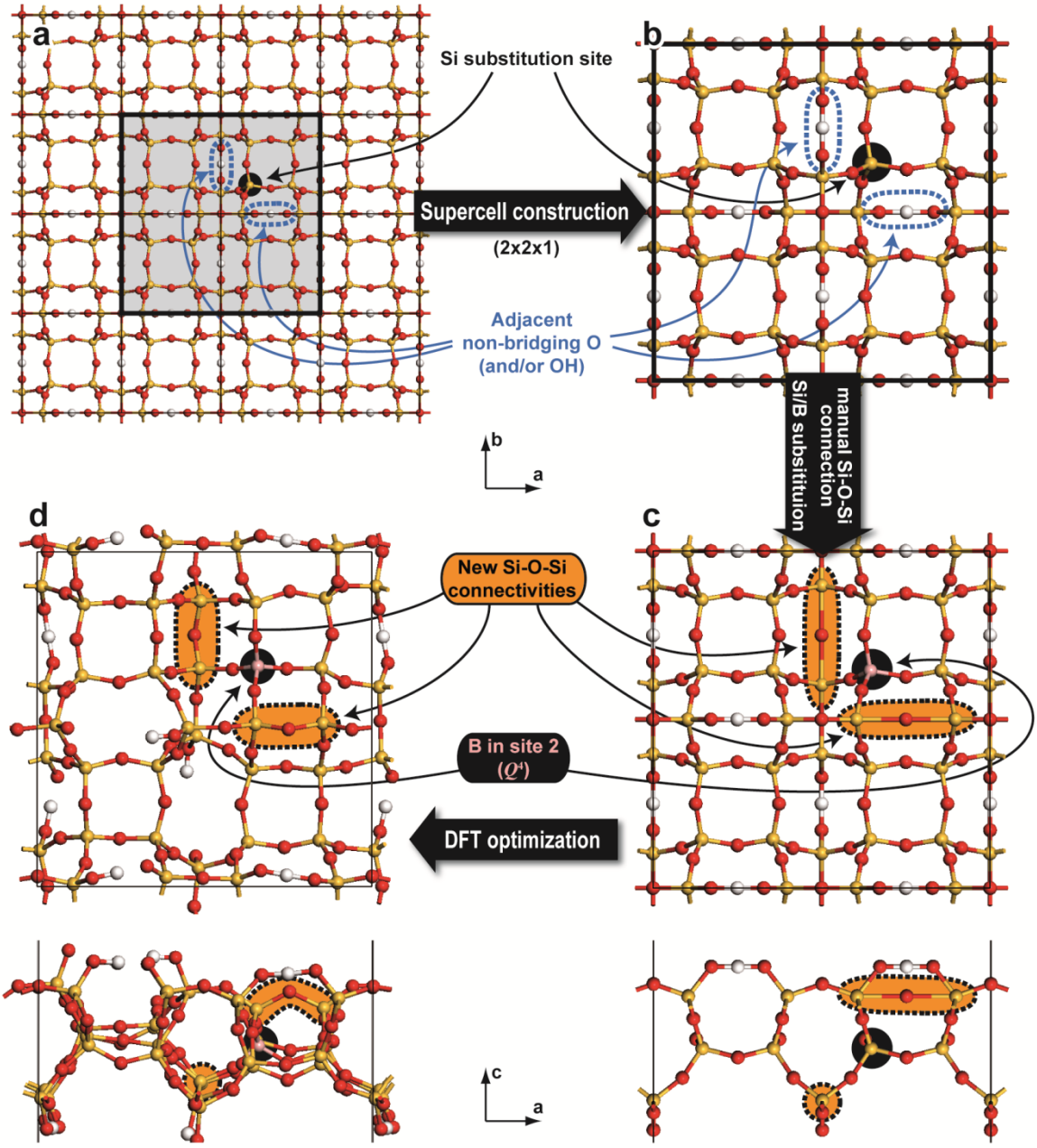

Figure A8. Schematic representation of the detailed procedure used to construct models of $C_{16}H_{33}\mathbf{Me_3}N^+$-directed borosilicates, where two new ^{29}Si-O-^{29}Si connectivities are formed between Q^3 ^{29}Si sites that are in the next-nearest-neighbors of the framework ^{11}B atom. Such a consequence can explain the absence of Q^3(1B) ^{29}Si sites in $C_{16}H_{33}\mathbf{Me_3}N^+$-directed borosilicates. The DFT-optimized model at the bottom was obtained by manually replacing two pairs of adjacent non-bridging oxygen atoms in a 2x2x1 supercell with a single oxygen atom located at the center of mass of the corresponding ^{29}Si atoms for each pair. [Courtesy: Dr. Sylvian Cadars]

References:

(1) Wolf, I.; Gies, H.; Fyfe, C. A. *The Journal of Physical Chemistry B* **1999**, *103*, 5933.

(2) Brouwer, D. H.; Cadars, S.; Eckert, J.; Liu, Z.; Terasaki, O.; Chmelka, B. F. *J. Am. Chem. Soc.* **2013**.

(3) Profeta, M.; Benoit, M.; Mauri, F.; Pickard, C. J. *J. Am. Chem. Soc.* **2004**, *126*, 12628.

(4) Stebbins, J. F. In *Handbook of Physical Constants*; Ahrens, T. J., Ed.; American Geophysical Union: Washington D.C., 1995; Vol. 2.

(5) Mackenzie, K. J. D.; Smith, M. E. *multinuclear solid-state NMR of inorganic materials*; Pergamon Press: Oxford, 2002.

(6) Koller, H.; Engelhardt, G.; Kentgens, A. P. M.; Sauer, J. *J. Phys. Chem.* **1994**, *98*, 1544.

(7) Martel, L.; Cadars, S.; Véron, E.; Massiot, D.; Deschamps, M. *Solid State Nucl. Mag.* **2012**, *45–46*, 1.

Appendix B

Aluminum Heteroatom Distributions in Surfactant-Directed Aluminosilicates

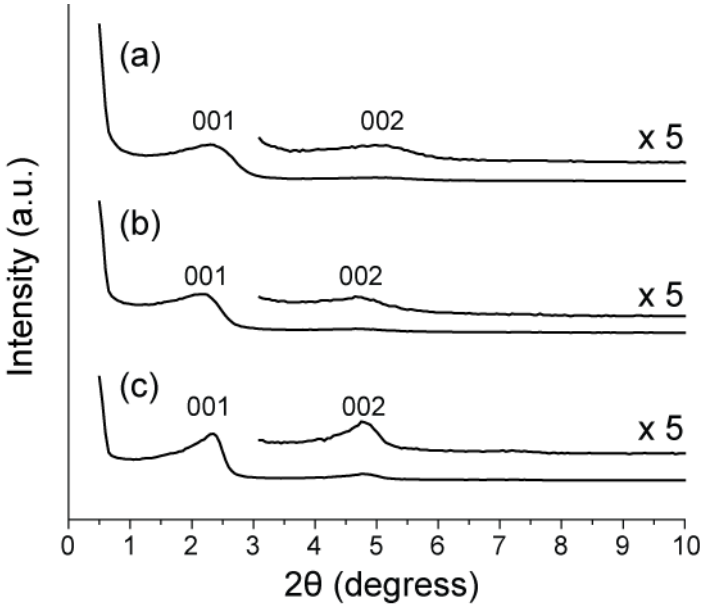

Figure B1. Small-angle powder X-ray diffraction (XRD) patterns of as-synthesized $C_{16}H_{33}N^{+}\mathbf{Me_3}$-directed aluminosilicates as a function of Al loadings: Si/Al ~ (a) 11.1, (b) 25.3, and (c) 42.6.

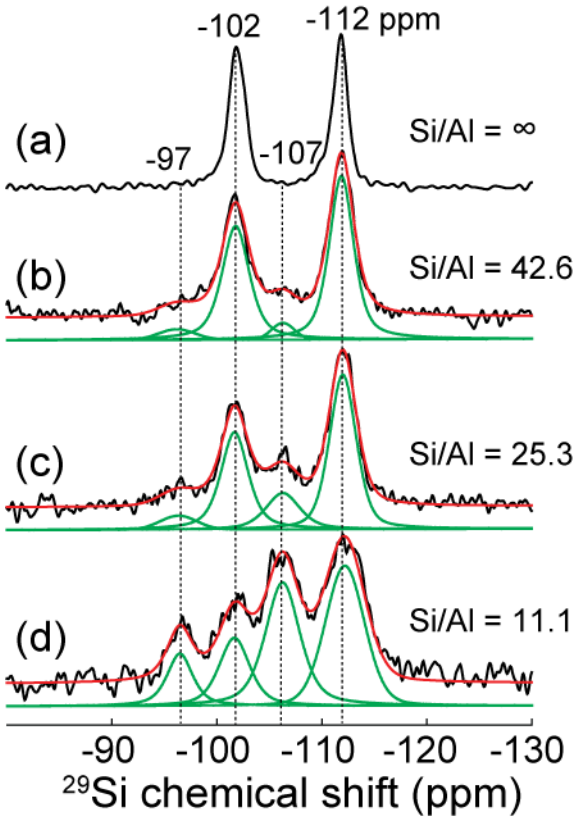

Figure B2. Solid-state 1D single-pulse ^{29}Si MAS NMR spectra acquired at 9.4 T, 25 °C, 10 kHz MAS for as-synthesized $C_{16}H_{33}N^{+}$**Me$_3$**-directed aluminosilicates as a function of ^{27}Al loadings: Si/Al ~ (a) ∞, (b) 42.6, (c) 25.3, and (d) 11.1. Simulated ^{29}Si MAS NMR spectra are shown in red, and their convoluted components are presented in green. [Courtesy: Dr. Mounesha Garaga]

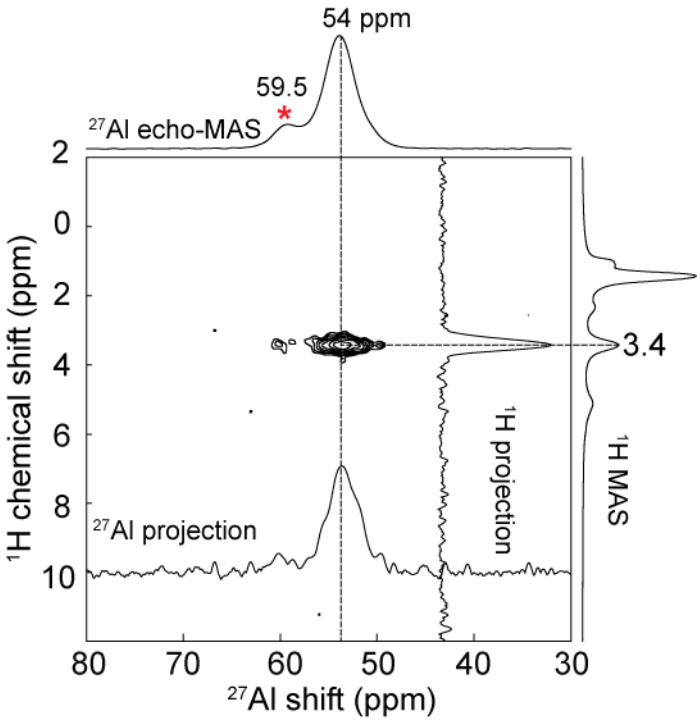

Figure B3. Solid-state 2D HETCOR (dipolar-mediate) $^{27}Al\{^{1}H\}$ NMR spectrum of as-synthesized $C_{16}H_{33}N^{+}$**Me$_3$**-directed aluminosilicates (Si/Al ~11.1), which was collected at 20.0 T, 25 °C, 10 kHz MAS, and contact time of 200 μs. Solid-state 1D ^{27}Al echo and ^{1}H MAS are shown along the top horizontal and right vertical axis, respectively. [Courtesy: Dr. Mounesha Garaga]

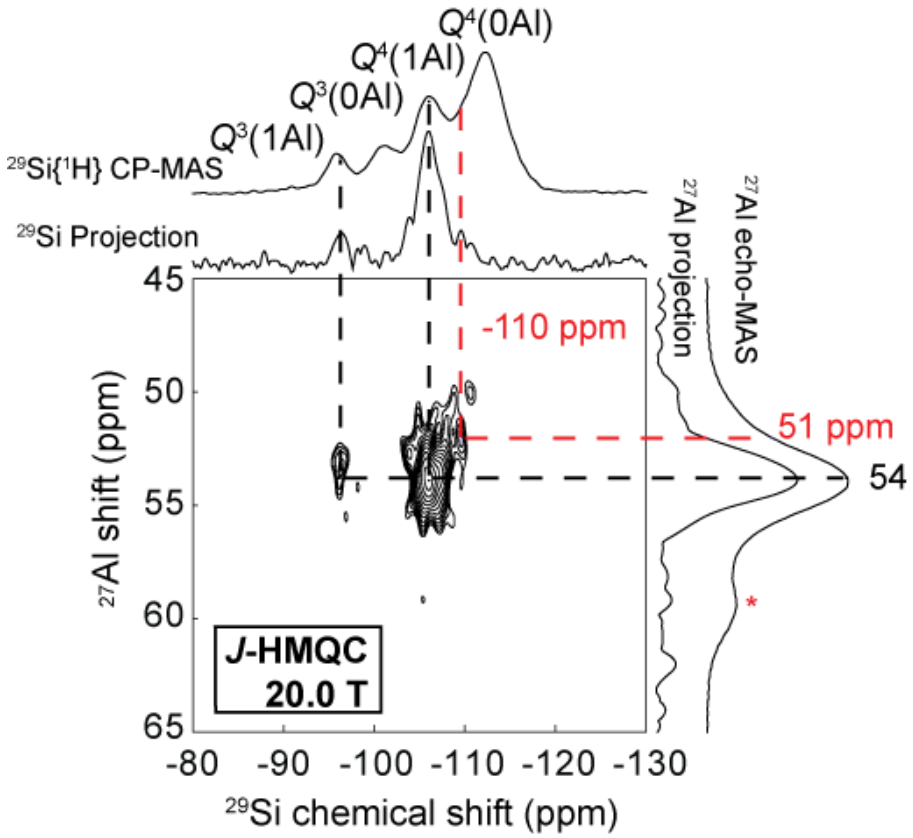

Figure B4. Solid-state 2D *J*-mediated HMQC $^{29}Si\{^{27}Al\}$ NMR spectrum of as-synthesized $C_{16}H_{33}N^{+}$**Me$_3$**-directed aluminosilicates with *ca.* 99% ^{29}Si enrichment (Si/Al ~11 expected), which was collected at 20.0 T, 25 °C and 14 kHz MAS. Solid-state 1D ^{27}Al echo-MAS NMR spectrum and ^{27}Al projection are shown along the right vertical axis, whereas a solid-state 1D $^{29}Si\{^{1}H\}$ CP-MAS NMR spectrum and ^{29}Si projection are demonstrated along the top horizontal axis. [Courtesy: Dr. Mounesha Garaga]

Table B1. Number of Q^n and Q^n(1Al) species and surfactant molecules added for $C_4H_9N^+$**Me$_3$-**directed aluminosilicate models shown in Figure 7.

Model	Supercell	Si/Al ratio(ICP)	Number of crystallographic Si sites				Total number of surfactants
			Q^3	Q^4	Q^3(1Al)	Q^4(1Al)	
Pure-silicate	1x1x1	∞	16	16	0	0	16
(i)	1x2x1	42.6	10	12	2	6	14
(ii)	1x2x1	25.3	10	12	2	6	14
(iii)	2x2x1	11.1	12	15	0	4	13

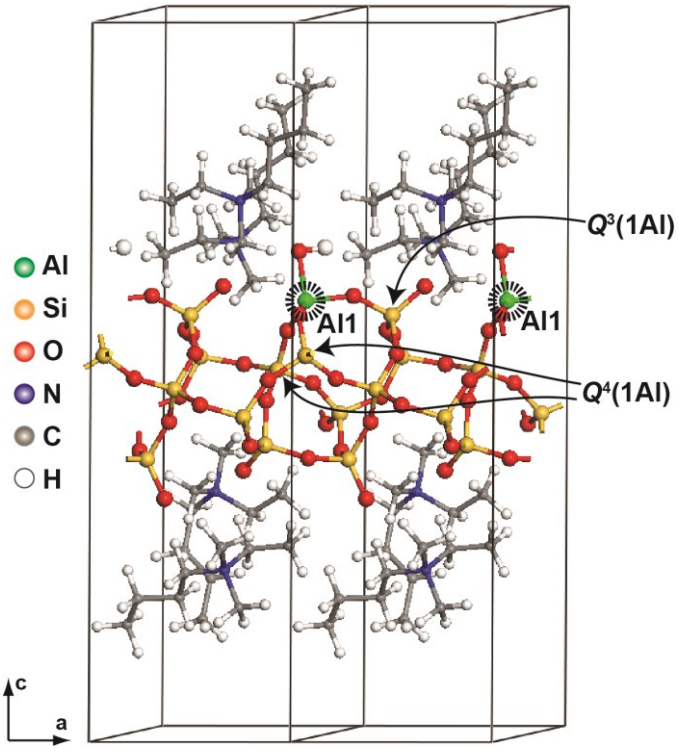

Figure B5. Structural model of $C_4H_9N^+$**Me$_2$Et-**directed aluminosilicates optimized using plane wave-based DFT calculations, where one ^{27}Al atom is manually inserted into one Si1 site (Q^3 ^{29}Si) among the 10 T-sites in structural model per unit cell. Framework negative charges near ^{27}Al species are compensated by H^+ species directly added to ^{27}Al sites. The black lines delimitate the unit cell. [Courtesy: Dr. Zalfa Nour]

Appendix C

Combined Solid-State NMR and Scattering Structural Analyses of the Layered Siliceous Zeolite SSZ-70

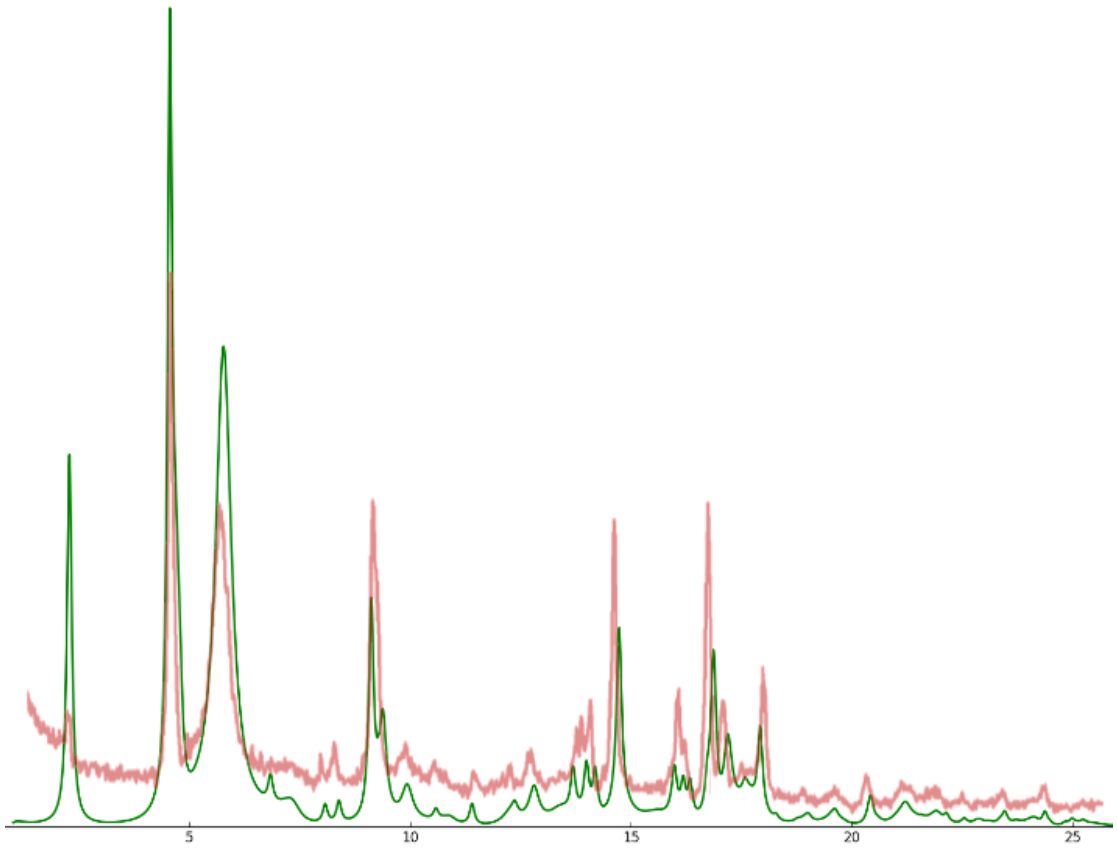

Figure C1. Experimental (in red) and simulated (in green) powder X-ray diffraction pattern of calcined SSZ-70. [Courtesy: Stef Smeets, Dr. Catherine Dejoie, Prof. Christian Baerlocher, and Prof. Lynne McCusker]

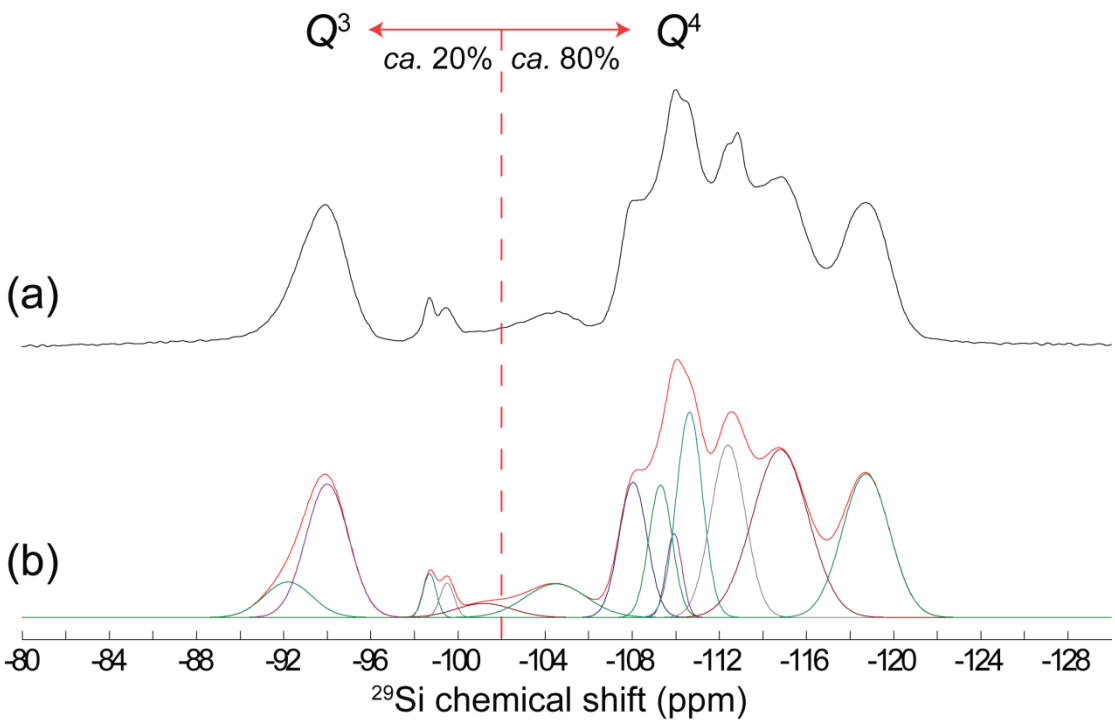

Figure C2. (a) Experimental and (b) simulated (with Gaussian deconvolution) solid-state 1D single-pulse ^{29}Si MAS NMR spectra of as-synthesized SSZ-70.

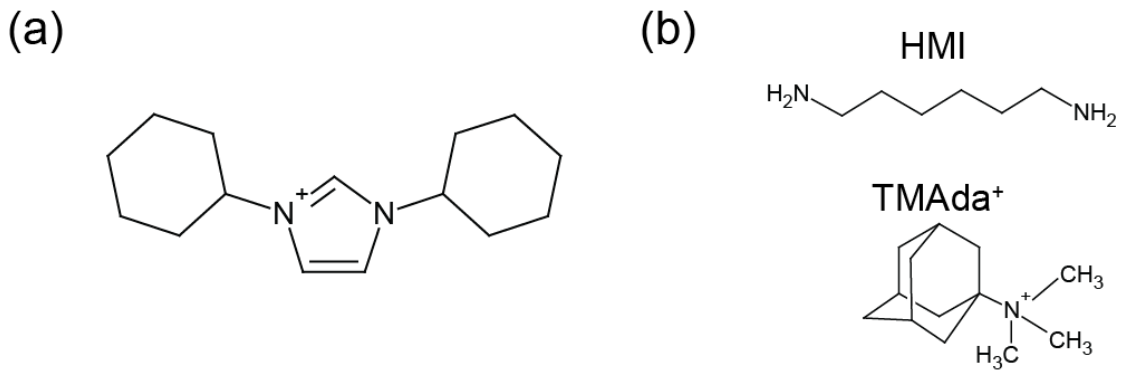

Figure C3. Organic structure-directing agents (a) 1,3-dicyclohexyl imidazolium and (b) hexamethyleneimine (HMI) and trimethyladamantammnoium ($TMAda^+$) used for synthesizing zeolite SSZ-70 and ITQ-1, respectively.

Appendix D

Influences of Structure-Directing Species on Boron Site Distributions in Borosilicate Zeolite SSZ-70 Catalysts

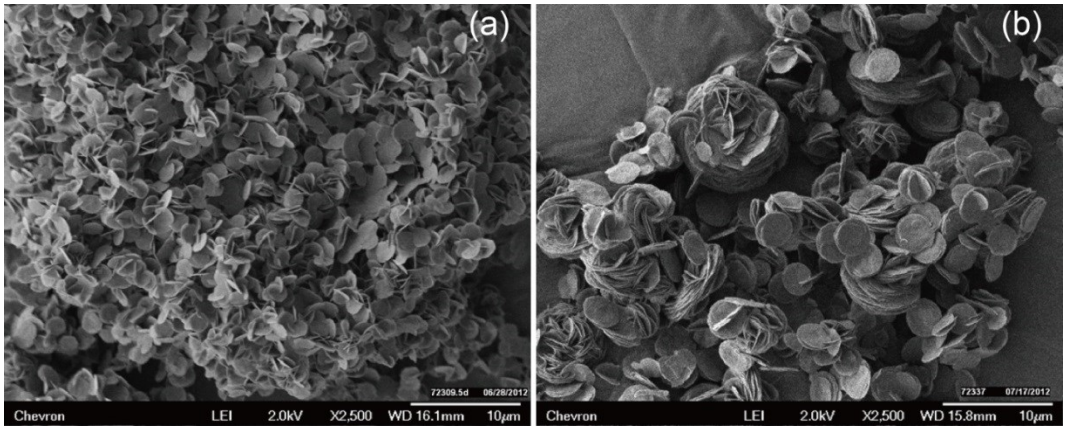

Figure D1. Representative SEM images of as-synthesized B-SSZ-70 prepared with (a) DiBI and (b) DiC_6I SDA^+ molecules.

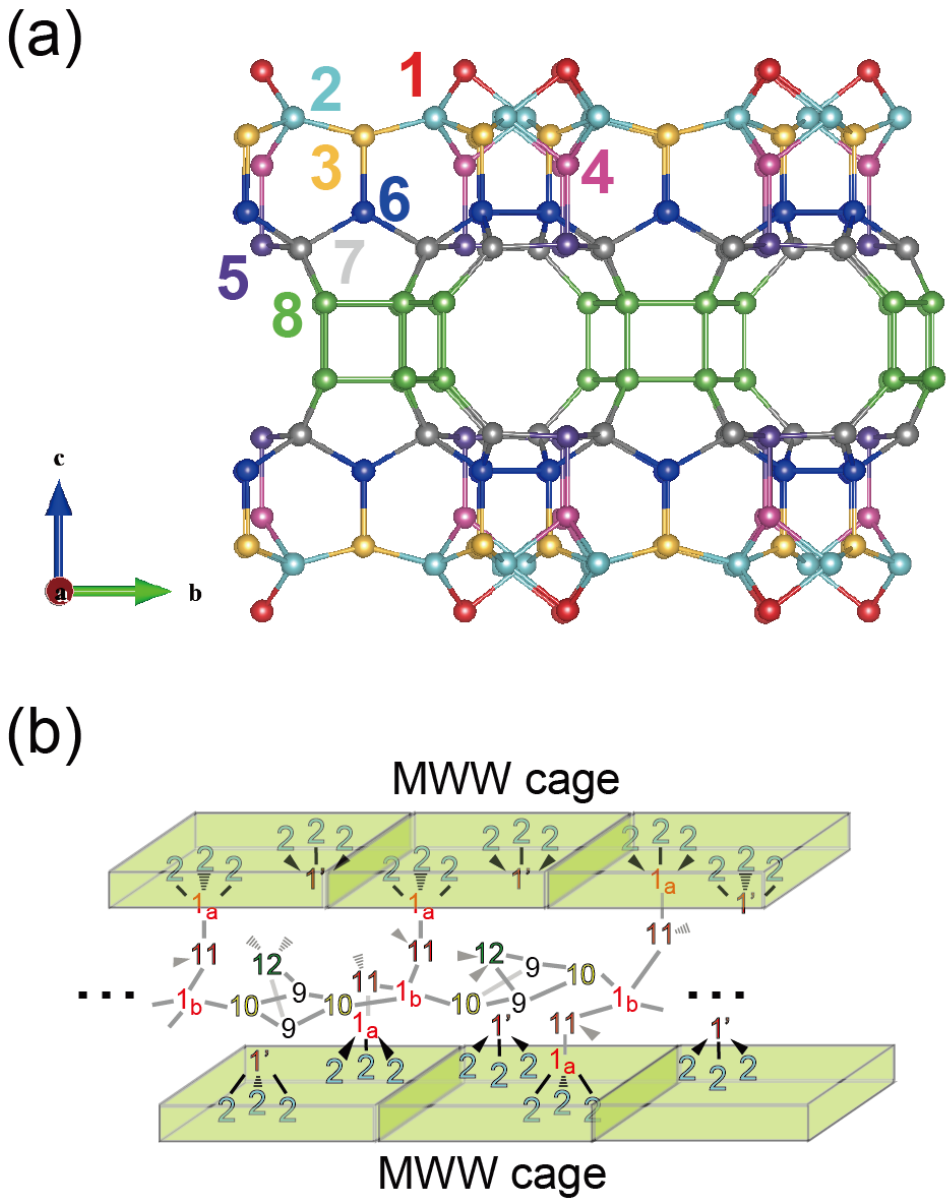

Figure D2. Schematic representation of (a) MWW-like cages in zeolite SSZ-70 adapted from one of Dr. Dan Xie's models (S2_2-4_model-4-1_Ortho), where distinct ^{29}Si site is colored accordingly, and (b) silicate layers between MWW-like cages within zeolite SSZ-70. Oxygen atoms are omitted for simplicity.

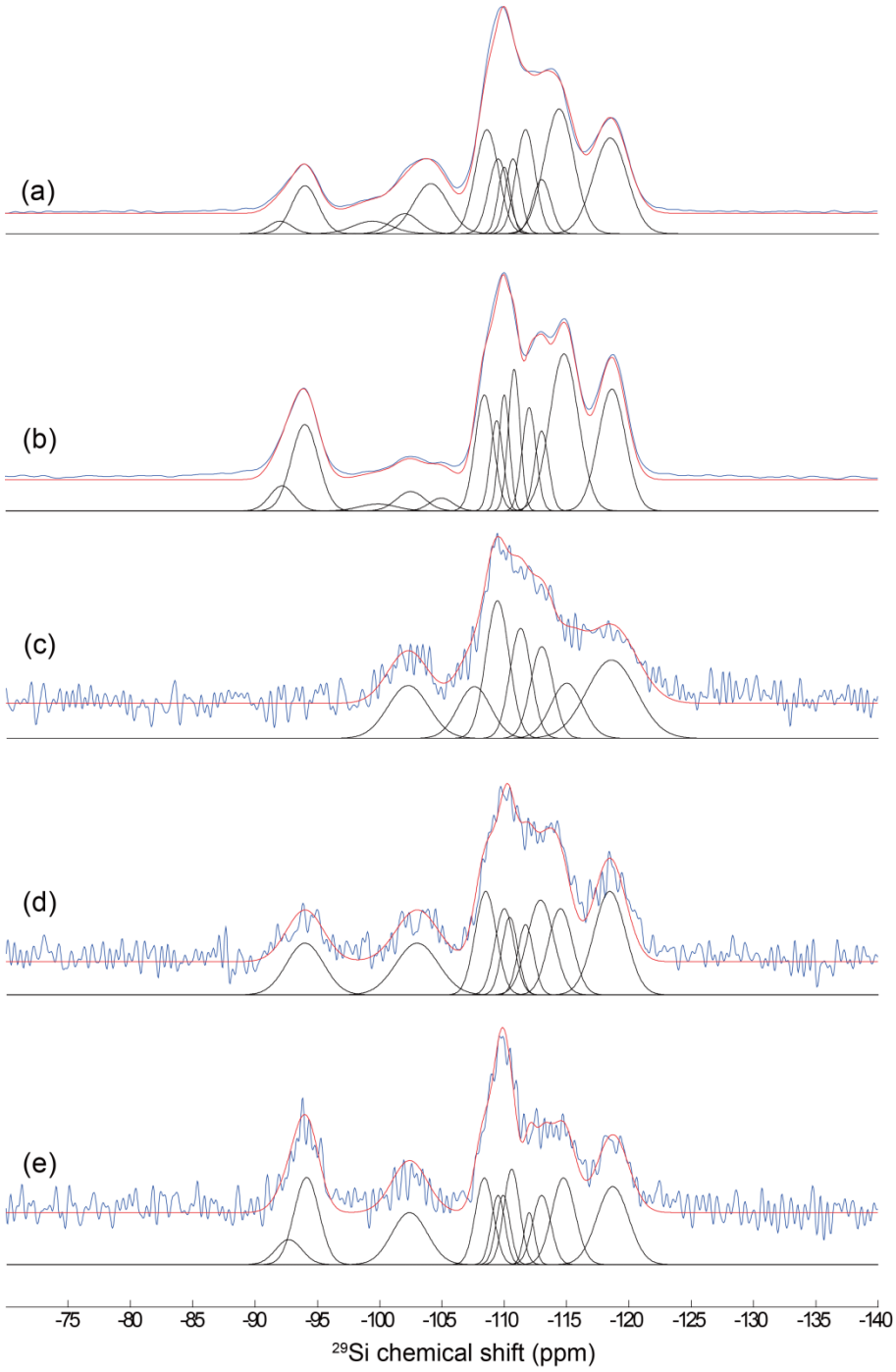

Figure D3. Solid-state 1D single-pulse ^{29}Si MAS NMR spectra of (a) ^{29}Si-enriched DiBI-synthesized (Si/B = 10), (b) ^{29}Si-enriched DiC_6I-synthesized (Si/B = 10), (c) DiPI-synthesized (Si/B = 4), (d) DiBI-synthesized (Si/B = 4), and (e) DiC_6I-synthesized (Si/B = 4) B-SSZ-70 zeolites, where experimental results, simulated spectra, and components are shown in blue, red, and black, respectively. Note all Si/B ratios refer to the ones in reactant.

Table D1. ^{29}Si NMR signal assignments and their relative populations estimated from solid-state 1D single-pulse ^{29}Si NMR experiments performed on various B-SSZ-70 zeolites.

^{29}Si-enriched DiBI-synthesized B-SSZ-70 (Si/B = 10)		
^{29}Si chemical shift (ppm)	Type	Relative population (%)
-92.0	Q^3	1.5
-94.0	Q^3	6.3
-99.4	Q^3	2.4
-102.0	Q^3	2.9
-104.1	Q^4	8.7
-108.6	Q^4	12.1
-109.5	Q^4	7.1
-110.0	Q^4	4.2
-110.7	Q^4	5.5
-111.7	Q^4	9.9
-113.0	Q^4	4.9
-114.4	Q^4	18.5
-118.5	Q^4	16.2

Table D1. (Continued)

^{29}Si-enriched DiC_6I-synthesized B-SSZ-70 (Si/B = 10)		
^{29}Si chemical shift (ppm)	Type	Relative population (%)
-92.2	Q^3	3.0
-94.0	Q^3	11.4
-99.9	Q^3	1.2
-102.5	Q^3	2.7
-104.9	Q^4	1.5
-108.4	Q^4	10.3
-109.4	Q^4	5.6
-110.0	Q^4	6.0
-110.8	Q^4	8.0
-112.0	Q^4	6.9
-113.0	Q^4	5.4
-114.8	Q^4	21.8
-118.6	Q^4	16.3

DiPI-synthesized B-SSZ-70 (Si/B = 4)		
^{29}Si chemical shift (ppm)	Type	Relative population (%)
-102.3	Q^3	12.5
-107.6	Q^4	9.9
-109.4	Q^4	18.8
-110.3	Q^4	13.7
-113.0	Q^4	12.0
-115.0	Q^4	10.3
-118.6	Q^4	22.9

Table D1. (Continued)

DiBI-synthesized B-SSZ-70 (Si/B = 4)		
^{29}Si chemical shift (ppm)	Type	Relative population (%)
-94.0	Q^3	10.5
-103.0	Q^3	12.1
-108.5	Q^4	12.1
-110.0	Q^4	9.0
-110.4	Q^4	6.8
-111.7	Q^4	6.1
-112.9	Q^4	13.8
-114.5	Q^4	11.6
-118.5	Q^4	18.1

DiC_6I-synthesized B-SSZ-70 (Si/B = 4)		
^{29}Si chemical shift (ppm)	Type	Relative population (%)
-92.7	Q^3	4.1
-94.1	Q^3	13.6
-102.4	Q^3	11.5
-108.4	Q^4	9.8
-109.5	Q^4	6.0
-109.9	Q^4	6.0
-110.6	Q^4	9.5
-112.0	Q^4	3.5
-113.0	Q^4	7.8
-114.8	Q^4	12.7
-118.7	Q^4	15.6

Appendix E

Controlling Aluminum Site Distributions in Delaminated Zeolite SSZ-70 by Isomorphous Substitution of Boron with Aluminum

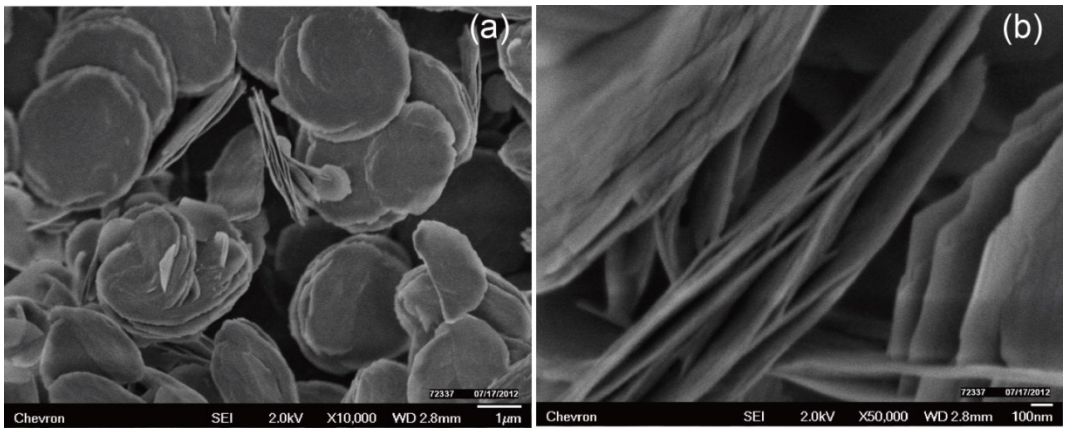

Figure E1. Representative SEM images of as-synthesized B-SSZ-70.

Table E1. Phases obtained from boro- and aluminosilicate hydroxide conditions

SDA^+	Si/B	Si/Al	SDA^+/SiO_2	H_2O/SiO_2	$NaOH/SiO_2$	Temperature (°C)	Product
DiBI	10	∞	0.2	30	0.1	160 °C, 43 rpm	B-SSZ-70
	∞	25	0.2	30	0.1	160 °C, 43 rpm	Al-SSZ-70

Note: all ratios in Table E1 refer to molar rations.

Table E2. Results from elemental analysis performed on B-SSZ-70 related products.

Material	C (wt%)	H (wt%)	N (wt%)	C/N
As-synthesized B-SSZ-70	12.6	2.0	2.6	5.7
Swollen B-SSZ-70	33.1	6.0	2.6	15.0

Table E3. Results from N_2 adsorption/desorption measurements of B-SSZ-70 related products.

Material	External surface area (m^2/g)
Calcined B-SSZ-70	89
Calcined UCB-4	133

Table E4. ^{29}Si chemical shift assignments in as-synthesized siliceous SSZ-70

^{29}Si chemical shift (ppm)	Type	Assignment	Connectivities
-94.0	Q^3	*1'*	*2* (x3)
-94.0	Q^3	*11*	*1* (x3)
-98.8	Q^3	*9*	*10* (x2), *12*
-99.5	Q^3	*10*	*1, 9* (x2)
-105	Q^4	*?*	*?*
-108.2	Q^4	*2*	*1, 3* (x2), *4*
-110.0	Q^4	*1*	*2* (x3), *9* or *10* or *11*
-110.2	Q^4	*3*	*2* (x2), *3, 6*
-110.8	Q^4	*4*	*2* (x3), *5*
-112.0	Q^4	*5*	*4, 7* (x3)
-113.0	Q^4	*8*	*7, 8* (x3)
-113.0	Q^4	*12*	*9* or *10* (x4)
-114 ~ -115	Q^4	*7*	*5, 6* (x2), *8*
-118.8	Q^4	*6*	*3, 6, 7* (x2)

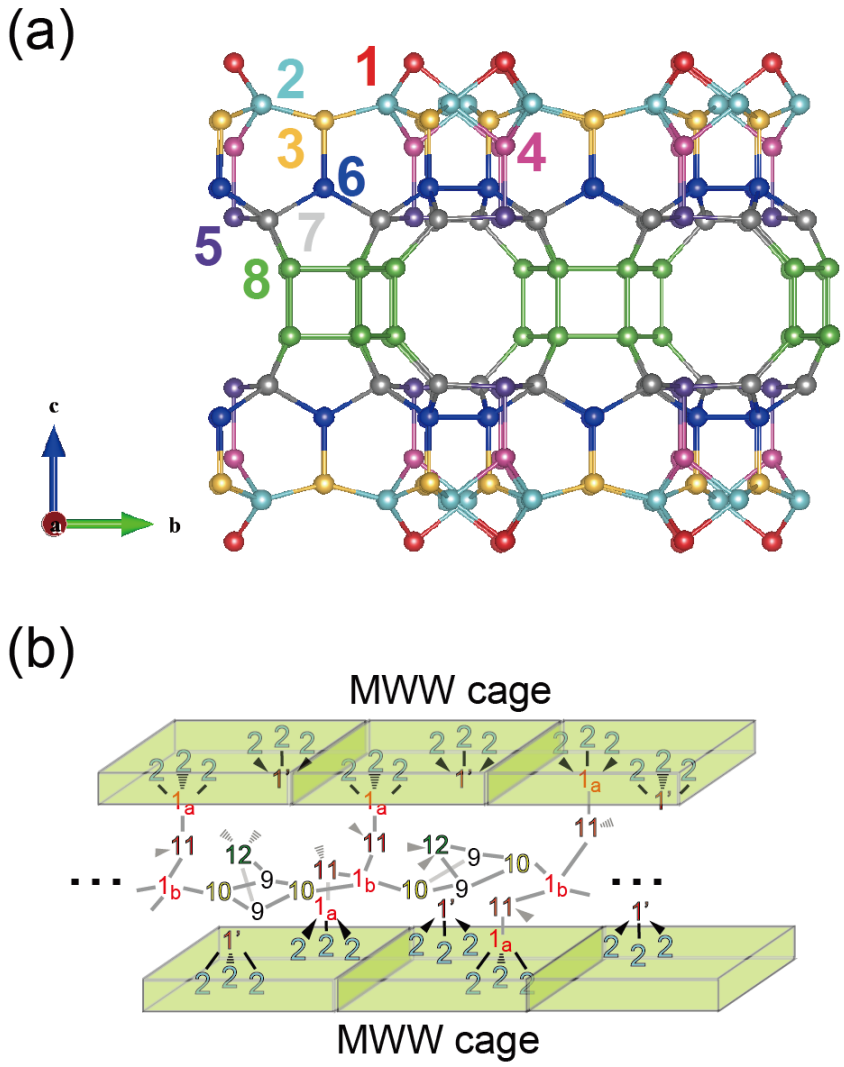

Figure E2. Schematic representation of (a) MWW-like cages in zeolite SSZ-70 adapted from one of Dr. Dan Xie's models (S2_2-4_model-4-1_Ortho), where distinct ^{29}Si site is colored accordingly, and (b) silicate layers between MWW-like cages within zeolite SSZ-70. Oxygen atoms are omitted for simplicity.

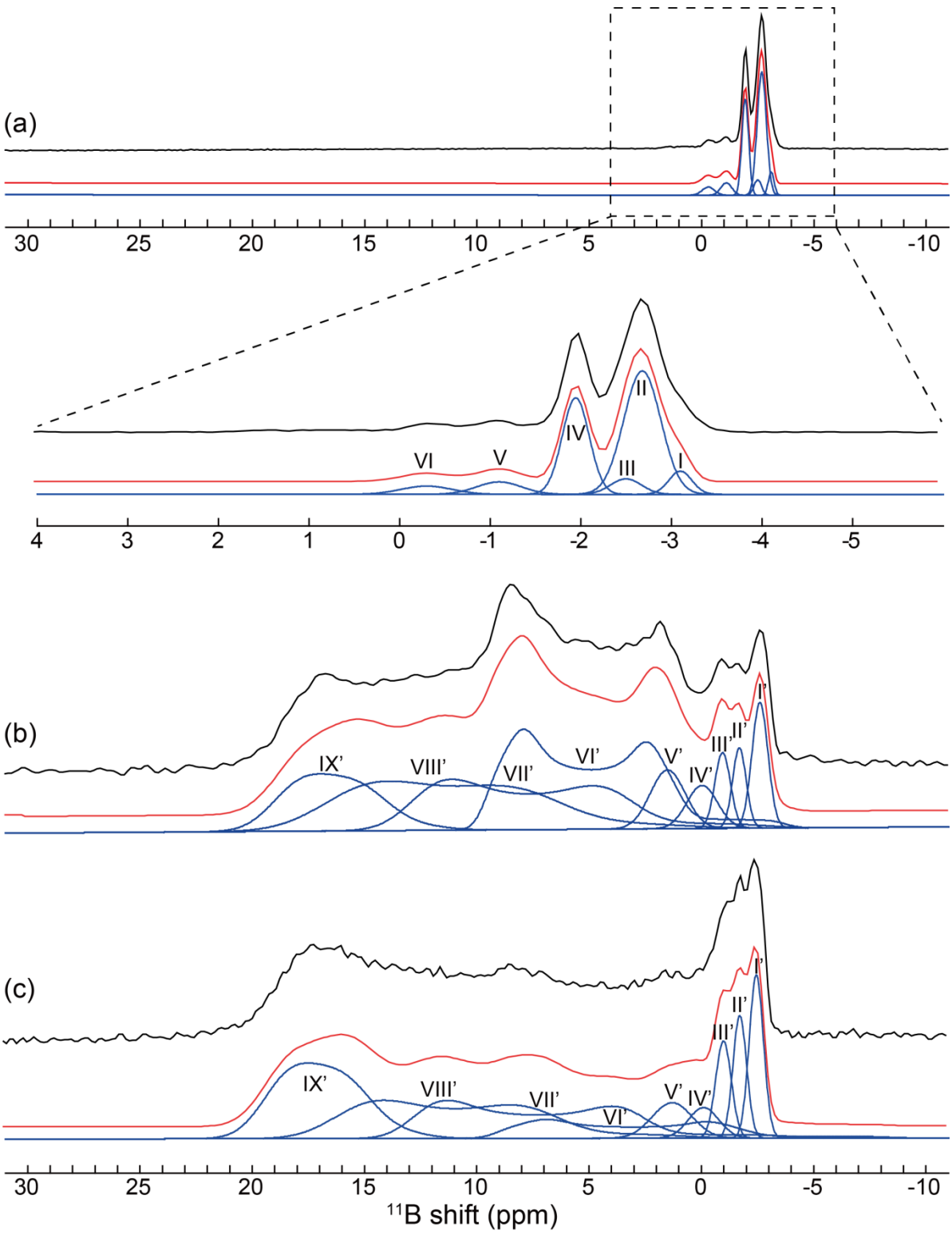

Figure E3. Experimental (in black) and simulated 1D ^{11}B MAS NMR spectra (in red) with components (in blue) of (a) delaminated B-SSZ-70 and delaminated & calcined B-SSZ-70

stored under mild hydration for (b) 1.5 and (c) 10 months, all of which were acquired on 11.7 T.

Table E5. Summary of 1D quantitative ^{11}B MAS NMR analysis (11.7 T) of delaminated B-SSZ-70

^{11}B shift (ppm)	Type (coordination)	Component, assignment	Relative population (%)
-3.1	4	I, 10-MR	5.6
-2.7	4	II, 10-MR	50
-2.5	4	III, 12-MR	5.2
-2.0	4	IV, 12-MR	28
-1.1	4	V, Non-framework	6.0
-0.3	4	VI, Non-framework	4.5

Table E6. Summary of 1D quantitative ^{11}B MAS NMR analysis (11.7 T) of delaminated & calcined B-SSZ-70 stored under mild hydration for 1.5 months after calcination

Component	Isotropic ^{11}B chemical shift (ppm)	Type (coordination)	C_{qcc} (MHz)	η	Relative population (%)
I’	-2.3	4	0.52	0.90	4.6
II’	-1.4	4	0.50	0.95	2.5
III’	-0.6	4	0.50	0.90	2.7
IV’	0.6	4	0.70	0.95	3.0
V’	2.3	4	0.80	0.95	4.7
VI’	10.9	3	2.45	0.20	27.8
VII’	14.8	3	2.70	0.13	19.7
VIII’	18.4	3	2.70	0.20	22.5
IX’	19.6	3	1.80	0.20	12.5

Table E7. Summary of 1D quantitative ^{11}B MAS NMR analysis (11.7 T) of delaminated & calcined B-SSZ-70 stored under mild hydration for 10 months after calcination

Component	Isotropic ^{11}B chemical shift (ppm)	Type (coordination)	C_{qcc} (MHz)	η	Relative population (%)
I’	-2.1	4	0.52	0.90	7.6
II’	-1.4	4	0.50	0.95	5.4
III’	-0.7	4	0.50	0.90	4.9
IV’	0.5	4	0.70	0.90	3.0
V’	2.1	4	0.80	0.95	4.6
VI’	10.8	3	2.80	0.20	9.7
VII’	15.0	3	2.80	0.13	20.3
VIII’	18.1	3	2.68	0.20	22.3
IX’	20.0	3	1.75	0.20	22.2

Table E8. Summary of 1D quantitative ^{11}B MAS NMR analysis (11.7 T) of delaminated & calcined B-SSZ-70 stored under mild hydration for 14 months after calcination

Component	Isotropic ^{11}B chemical shift (ppm)	Type (coordination)	C_{qcc} (MHz)	η	Relative population (%)
I’	-2.2	4	0.52	0.90	14.3
II’	-1.4	4	0.50	0.95	8.9
III’	-0.7	4	0.50	0.90	5.9
IV’’	0.3	4	N.A.	N.A.	7.3
VIII’	11.3	3	N.A.	N.A.	41.8
IX’	21.1	3	1.68	0.20	21.8

Table E9. Summary of 1D quantitative ^{11}B MAS NMR analysis (18.8 T) of delaminated & calcined B-SSZ-70 stored under mild hydration for 14 months after calcination

Component	Isotropic ^{11}B chemical shift (ppm)	Type (coordination)	C_{qcc} (MHz)	η	Relative population (%)
I’	-3.4	4	0.52	0.90	9.5
II’	-2.6	4	0.50	0.95	8.1
III’	-1.8	4	0.50	0.90	5.3
IV’’	-0.5	4	N.A	N.A	5.0
V’’	10.0	3	N.A	N.A	26.3
?	16.5	3	N.A	N.A	32.2
IX’	19.8	3	1.68	0.13	13.5

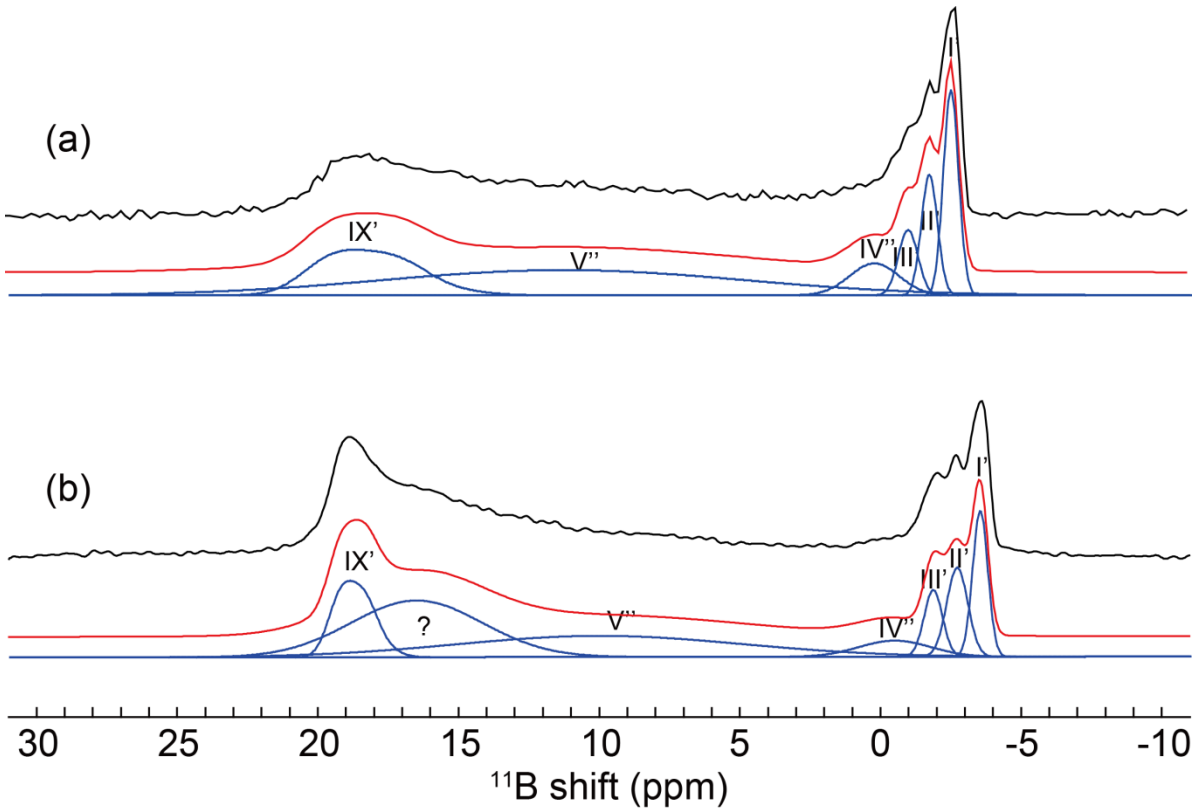

Figure E4. Experimental (in black) and simulated 1D ^{11}B MAS NMR spectra (in red) with components (in blue) of delaminated & calcined B-SSZ-70 under mild hydration for 14 months, which were acquired at (a) 11.7 and (b) 18.8 T, respectively.

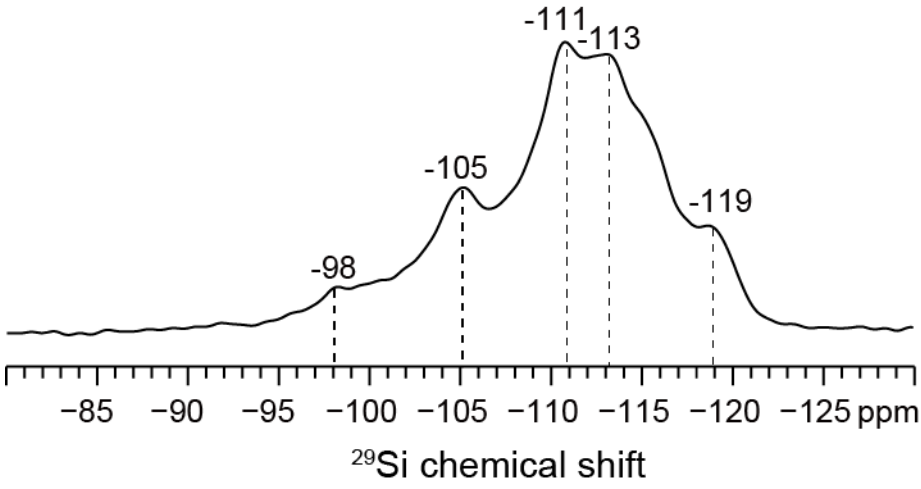

Figure E5. Solid-state 1D single-pulse ^{29}Si MAS NMR spectra of Al-reinserted-UCB-4 (Si/Al ~89), acquired at room temperature (~25 °C) and 11.7 T under MAS conditions of 8 kHz.